Astronomical, Atmospheric and Laboratory Studies Related to Lunar Ultraviolet Radiation

by

Richard Searcy O'Brien B.Sc.(Hons.)

Department of Physics

A thesis
presented for the degree of
Doctor of Philosophy
in the
University of Adelaide

November 1973

CONTENTS

	Page
SUMMARY	(vii)
PREFACE	(x)
ACKNOWLEDGEMENTS	(xi)
CHAPTER 1 OZONE IN THE ATMOSPHERE	
1.1 Photochemistry in the Atmosphere from 30-100 Kilometres	1
1.1.1 Introduction	1
1.1.2 The Solar Spectrum	2
(a) The Infra-red Region	2
(b) The Ultra-violet Region	3
1.2 Photochemical Processes Involving Ozone	3
1.2.1 Oxygen Atmosphere	4
1.2.2 Hydrogen-Oxygen Atmosphere	4
1.2.3 Effects of Nitrogen and Nitrogen Compounds	6
1.2.4 The Ozone Absorption Cross-sections	6
1.3 Measurement of Atmospheric Constituents other than Ozone	8
1.3.1 Absorption Measurements	8
1.3.2 Mass Spectrometer Measurements	9
1.3.3 Chemical Methods	10
1.3.4 Emission Measurements	10
1.4 Methods of Measurement of Ozone Concentration in the Upper Atmosphere	11
1.4.1 The Umkehr Method	11
1.4.2 Chemical Methods	13
(a) Reaction of Ozone with Potassium Iodide Solution	13
(b) The Chemiluminescent Method	14
1.4.3 The Atmospheric Radiance Method	15
1.4.4 Measurement by Atmospheric Absorption	17
1.5 Atmospheric Models	20
1.5.1 Introduction	20
1.5.2 The Equilibrium State	22
1.5.3 Slight Deviations from Equilibrium	23
1.5.4 The Non-Equilibrium State	24

Page

CHAPTER 2 DESIGN AND CALIBRATION OF THE FLIGHT PHOTOMETERS

2.1 Introduction 26

2.2 The Photometers 26
2.2.1 Filters 26
2.2.2 The Photomultiplier Type and Mounting 27

2.3 Electronics 28
2.3.1 Amplifiers 28
2.3.2 High Tension Supplies 29
2.3.3 Protection Against Dynode Vibration 30

2.4 The Rocket Vehicles 30
2.4.1 Description of the Vehicles 30
2.4.2 Distribution of the Payload 31
2.4.3 Pre-flight Checks of Equipment 33

2.5 Calibration of the Flight Photometers 33
2.5.1 Calibration of HAD 313 33
2.5.2 Calibration of C104 35
2.5.3 Calibration of C105 37
2.5.4 Calibration of C1014 37

2.6 Aspect Correction 38

2.7 Design and Calibration of Aspect Sensors 39

CHAPTER 3 OZONE DENSITIES DEDUCED FROM ROCKET FLIGHTS

3.1 Details of Location and Times of Rocket Flights 43

3.2 Reduction of Data 44
3.2.1 Tracking Records Available 44
3.2.2 Form of the Telemetered Data Received 44
3.2.3 Determination of the Height versus Time Relation 45
3.2.4 Variation of Aspect Angles During Flight 46
3.2.5 Reduction of Data to Give Curves of Incident Flux versus Height 47

3.3 Methods of Calculating the Nocturnal Ozone Distributions 48
3.3.1 The Effective Cross-Section Method 48
3.3.2 The Selective Absorption Method 50
3.3.3 Comparison of Results Obtained by the Effective Cross-Section and Selective Absorption Methods 53

Page

3.4 Comparison with Results of Other Measurements of Atmospheric Ozone 55

3.5 Effects of Rayleigh Scattering on the Aspect Sensors 57

3.6 Effects of Airglow on the Ultraviolet Sensors 63

3.7 Theoretical Computations of Airglow Intensities 67

CHAPTER 4 THE ULTRAVIOLET REFLECTIVITY OF THE LUNAR SURFACE

4.1 Introduction 76

4.2 Measured Values of Ultraviolet Radiation from the Moon 78

4.3 The Lunar Ultraviolet Albedo 80

4.4 Comparison with Other Measurements of Lunar Albedo 81

4.5 Wavelength Dependence of Lunar Albedo 83

CHAPTER 5 DESIGN OF AN EXPERIMENT TO MEASURE THE ULTRAVIOLET REFLECTIVITY OF SOME TERRESTRIAL MATERIALS

5.1 Introduction 84

5.2 The Reflection Chamber 85
5.2.1 The Original Reflection Chamber 85
5.2.2 Modifications to the Reflection Chamber 86

5.3 The Electronic Dividing Unit 87

5.4 Experimental Procedure 88

CHAPTER 6 RESULTS OF LABORATORY SPECTRAL REFLECTIVITY MEASUREMENTS

6.1 Introduction 91

6.2 Selection and Description of the Samples 93

		Page
6.3	Preparation of the Specimens	99
6.4	Analysis of Experimental Data	100
6.5	Reflectivities and Transmissivities of Lithium Fluoride, Sapphire and Silica	102
6.6	Results of Measurements of the Angular Distribution of Reflected Radiation	103
6.7	Results of Measurements of the Spectral Reflectivity of Some Terrestrial Materials	103
6.8	Further Measurements of Spectral Reflectivity	105
6.9	The Effect of Surface Roughness on Spectral Reflectivity	107
6.10	Comparison of Rock Measurements with the Lunar Albedo	108
6.11	Conclusions	110
CHAPTER 7	THEORY OF REFLECTION FROM A ROUGH SURFACE	
7.1	Introduction	112
7.2	Reflection from Smooth Surfaces	112
7.3	Reflection from Rough Surfaces	113
	7.3.1 Lambert's Law	114
	7.3.2 The Lommel-Seeliger Law	115
	7.3.3 Rough Surface Models	116
7.4	Basic Theory and Notation	117
7.5	The Distribution Function	126
7.6	Specular and Diffuse Reflection	127
7.7	The Shadowing Function	128
7.8	The Normally Distributed Surface	130
7.9	Range of Validity of the Theory	135
7.10	Comparison with Other Theories	136

Page

7.11 Applications of the Solution 137
7.11.1 Reflection from Smooth Surfaces 137
7.11.2 Reflection from Slightly Rough Surfaces 138
7.11.3 Reflection from Moderately Rough Surfaces 138
7.11.4 Reflection from Very Rough Surfaces 140

7.12 Conclusions 143

APPENDIX 1 SOME ATMOSPHERIC PROCESSES AFFECTING OZONE

A.1.1 Dry Atmosphere 145

A.1.2 Hydrogen-Oxygen Atmosphere 146

A.1.3 Reactions Involving Nitrogen and Nitrogen Compounds 149

APPENDIX 2 ELECTRONIC CIRCUITS FOR NIGHT ROUND PHOTOMETERS

A.2.1 Circuits for HAD 313 150
A.2.1.1 High Tension and Dynode Modulator Supplies 150
A.2.1.2 Dynode Chain Circuits 150
A.2.1.3 A.C. Amplifiers 151

A.2.2 Circuits for C104, C105 and C1014 152
A.2.2.1 High Tension Supply 152
A.2.2.2 Dynode Chains 152
A.2.2.3 Amplifiers 153
A.2.2.4 Aspect Sensor Amplifiers 154

APPENDIX 3 THE LOGARITHMIC DIVIDING UNIT

A.3.1 The Power Supplies 155

A.3.2 The Integrator and Inverter Circuits 155

A.3.3 The Logarithmic Amplifiers 156

A.3.4 The Subtractor 156

A.3.5 The Sample and Hold Circuit 157

A.3.6 The Control Pulse Circuitry 158

Page

APPENDIX 4 SOME USEFUL MATHEMATICAL RESULTS

A.4.1 Calculation of the Energy Reflected from a Smooth, Perfectly Reflecting Surface 159

A.4.2 Calculation of Averages for Normal Processes 162

APPENDIX 5 PUBLICATIONS 168

BIBLIOGRAPHY 169

SUMMARY

This thesis describes a series of experiments carried out to study the phenomena related to lunar ultraviolet radiation. The work was divided into two parts:-

(i) a series of rocket-borne experiments, using photomultipliers as detectors, to measure the lunar ultraviolet reflectivity and nocturnal ozone densities.

(ii) a laboratory study, both theoretical and experimental, of the reflection of light from rough surfaces at ultraviolet wavelengths.

The ozone distributions were measured using the absorption spectroscopy technique in the region of the Hartley absorption bands from 2000Å to 3000Å. The design and calibration of the detectors are described, together with a discussion of the determination of the aspect and height of the rocket vehicles during flight.

The light source for these measurements was solar ultraciolet radiation reflected from the moon. Since the photometers were absolutely calibrated the reflectivity of the lunar surface could be calculated by assuming that absorption of radiation by ozone was negligible above 70 kilometres. The values of lunar reflectivity were found to be consistent with those of other workers at different wavelengths.

The nocturnal ozone densities from 30 to 70 kilometres were derived using both an approximate technique and a more accurate technique which took into account the variation of the ozone absorption cross-section with wavelength. The results of these calculations were consistent with those of other workers over the height range 30 to 70 kilometres.

The results of one of the rocket flights showed unusual variations in the flux versus height curves. These anomalies were explained in terms of an additional source of ultraviolet radiation, consisting of a thin emitting layer in the earth's atmosphere.

The experimental laboratory studies necessitated the design and construction of an electronic unit capable of manipulating very low signals with a poor signal-to-noise ratio. The results obtained were self-consistent and indicated the soundness of the design.

The samples used in the reflectivity measurements were chosen to cover a wide range of chemical compositions and modes of formation. A comparison of the results with those for a number of pure samples indicated that measurements of the ultraviolet reflectivity of rough surfaces were not easy to correlate with the chemical composition of the samples. A comparison of the results with the lunar albedo between 1000Å and 7000Å showed that some terrestrial rocks have albedos very similar to that of the lunar surface over this wavelength range; this suggests

that the sharp rise in the lunar spectral albedo between 2000Å and 4000Å may be due to the chemical composition of the lunar surface material.

The theoretical study of the reflection of light from rough surfaces was based on the Kirchhoff approximation for the reflected field. The discussion was carried a stage further than by other workers to include the effects of the surface correlation function. The results obtained agreed qualitatively with the experimental results but showed that there is some doubt as to the general validity of the Kirchhoff approximation, particularly at large angles of incidence and/or reflection.

PREFACE

This thesis contains no material which has been accepted for the award of any other degree or diploma in any University. To the best of the author's knowledge and belief it contains no material previously published or written by another person, except where due reference is made in the text.

R. S. O'Brien

ACKNOWLEDGEMENTS

The rocket experiments described in this thesis were carried out in co-operation with the Flight Projects and Upper Atmosphere Research Groups of the Weapons Research Establishment. The author would like to thank all personnel involved in the preparation and launching of the rocket vehicles.

The author would like to thank Messrs. R. Hurn and R. Walker of the Physics Department for designing and constructing the electronic circuitry for the rocket experiments, and Mr. S. Dowden of the Physics Department for his technical assistance in the laboratory work.

Sincere thanks are due to Dr. A. W. Kleeman of the Geology Department, University of Adelaide, for his help in selecting and preparing the rock samples used in the laboratory measurements, and for providing the data on the locality and mode of formation of the rocks from which the samples were taken.

The author would sincerely like to thank his supervisors, Professor J. H. Carver and Dr. D. G. McCoy, for their guidance and encouragement during the course of this work and the writing of this thesis. Special thanks are also due to Dr. B. H. Horton for his enthusiastic support of the work described in this thesis.

The author gratefully acknowledges the support provided by a C.S.I.R.O. Postgraduate Studentship and a full-time Demonstrating position with the University of Adelaide.

CHAPTER 1

OZONE IN THE ATMOSPHERE

1.1 Photochemistry of the Atmosphere from 30-100 Kilometres

1.1.1 Introduction

As the atmosphere exerts a profound influence upon man's way of life, its structure, composition and movements have been studied for many years. Until twenty-five years ago the region from 40-100 kilometres (the chemosphere) was difficult to study because it could not be reached by balloons and radio exploration was only effective above approximately 70 kilometres. The recent use of rockets and satellites as instrument platforms has made it possible to study the chemosphere in some detail, e.g. temperature, composition, the densities of its constituents, and other properties, and this in turn has aided man in his attempts to understand, and perhaps one day control, his environment.

One extremely important constituent of the chemosphere and lower atmosphere is ozone, the triatomic form of oxygen. The importance of ozone is due primarily to its absorption of solar radiation in the region 2000-3000 Angstroms. If it were not for this absorption man could not easily survive on the earth's surface. Hence a knowledge of the properties of ozone and its abundance in the atmosphere is of great importance.

1.1.2 The Solar Spectrum

The primary source of energy for most atmospheric phenomena is the sun. It is, therefore, most important to know the energy spectrum of solar radiation and how this radiation reacts with the atmosphere.

The atmosphere is largely transparent in the visible part of the spectrum but is almost opaque in the ultraviolet region for wavelengths less than about 3000 Angstroms. There is also a great deal of atmospheric absorption in the infra-red region for wavelengths longer than 9000Å, so that we have to consider these two main regions of interaction between the atmosphere and solar radiation.

(a) The Infra-red Region

In this part of the spectrum there are a number of alternating "windows" and absorption bands; infra-red absorption is mainly due to induced vibrational and rotational transitions in diatomic and polyatomic molecules. The main absorbing gases are water vapour, CO_2 and O_2; this fact can be determined by comparing the absorption spectra of these gases with the solar spectrum at sea level. Such a comparison, by Howard (1961) is shown in Fig. 1.1.

In spite of this absorption the overall effect of absorption and emission in the lower atmosphere is a loss of heat, due to the effect of heated gases rising from the earth's surface. However this effect does not apply at all latitudes.

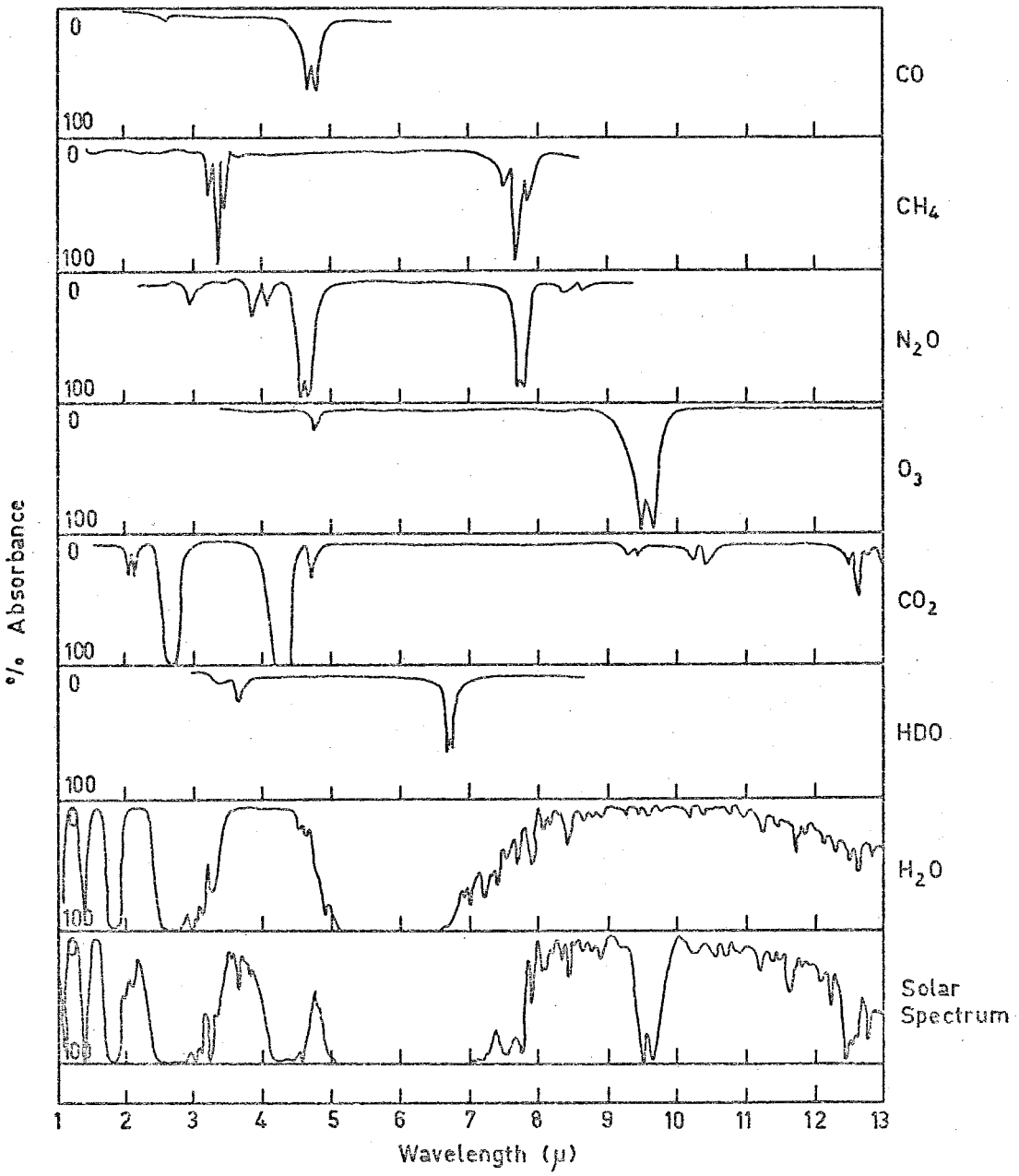

Figure 1.1 Comparison of absorption by atmospheric gases with the infrared spectrum of the sun. (ex. Howard, 1961)

Infra-red absorption has little effect on the formation and maintenance of the atmosphere but it does have a marked influence on energy transport mechanisms in the atmosphere.

(b) The Ultraviolet Region

This can be divided into two regions

(1) > 1350Å - in this region solar radiation reacts with the principle constituents of the atmosphere to produce molecular excitation and dissociation.

(2) < 1350Å - radiation in this region produces molecular ionization and dissociation and atomic excitation and ionization. The height associated with these reactions varies with wavelength.

In terms of energy interchange in the atmosphere the most important region of the spectrum is that between 2000Å and 3000Å, due to the sharp increase in the energy content of the solar spectrum over this region coupled with the large absorption coefficient of ozone, the triatomic form of oxygen. The solar spectrum in the region 2000-3600Å is shown in Fig. 1.2. The values of solar flux are due to Furakawa et al. (1967), who quote an uncertainty in their results of 20-30 per cent.

1.2 Photochemical Processes Involving Ozone

As has already been mentioned, ozone is the main absorber of radiant energy in the spectral region 2000-3000Å and is therefore responsible for the peak in the atmospheric temperature

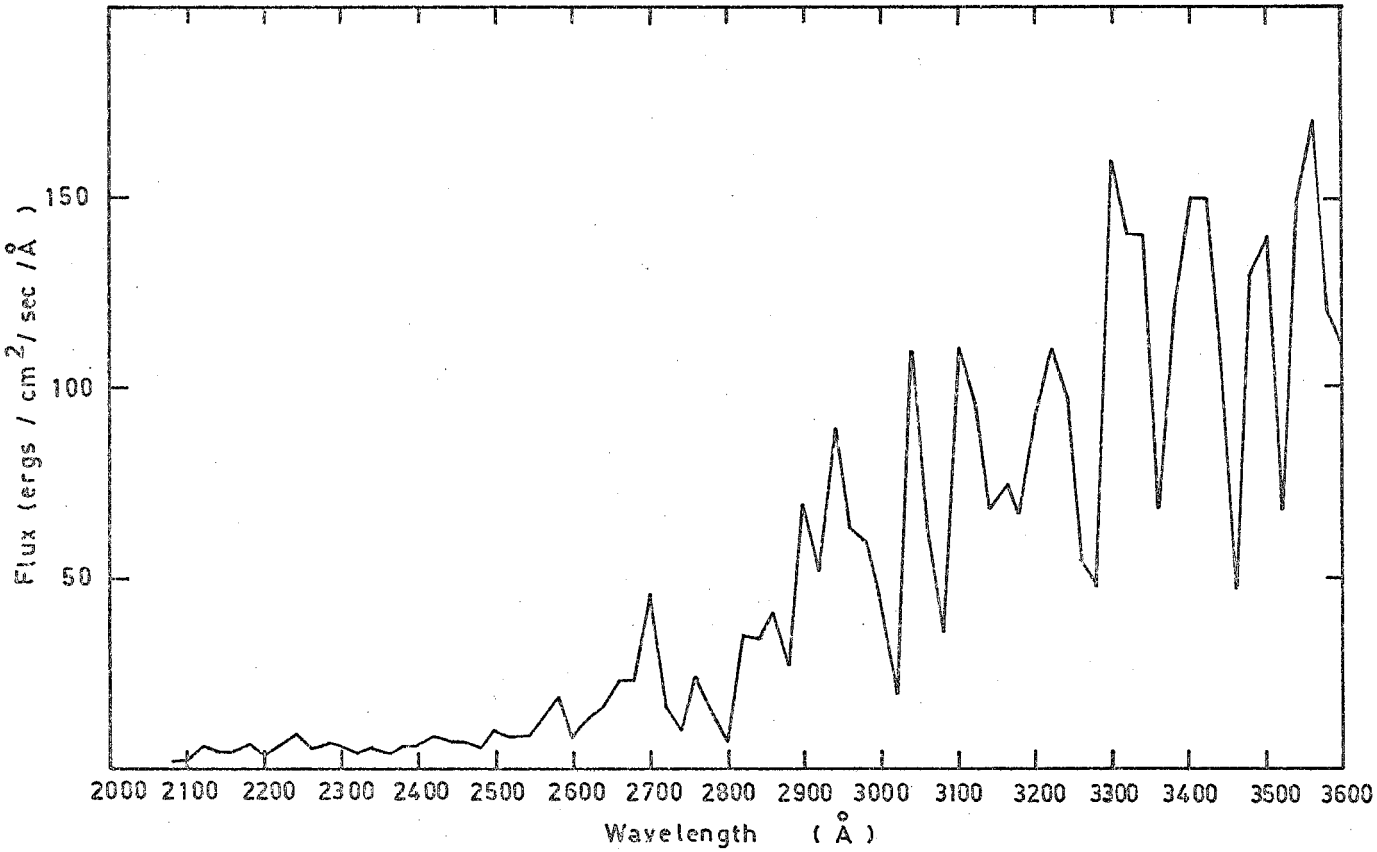

Figure 1.2 The solar spectrum (ex Furukawa et al., 1967).

curve at about 50 kilometres (Murgatroyd, 1957). Thus ozone plays a major part in the atmospheric heat budget.

1.2.1 Oxygen Atmosphere

Most authors begin by considering the reactions involving ozone in a dry atmosphere (no water vapour or hydrogen compounds). The reactions to be considered in this case are listed in Appendix A.1.1, together with the rate coefficients.

From the reactions listed in Appendix A.1.1 the time rate of change of ozone in a dry atmosphere is given by

$$\frac{d}{dt}[O_3]_o = -\alpha_3 q_3[O_3] - \alpha_4 q_4[O_3] + k_1[M][O(^3P)][O_2]$$

$$- k_2[O(^3P)][O_3] - k_4[O(^1D)][O_3] \quad \ldots (1.1)$$

where q_3 and q_4 are the quanta of radiation absorbed by O_3 in the wavelength regions $3100\text{Å} < \lambda < 11800\text{Å}$ and $\lambda < 3100\text{Å}$ respectively, and [ ] denotes the concentration of the species enclosed in the bracket.

1.2.2 Hydrogen-Oxygen Atmosphere

As soon as we consider the effects of hydrogen the situation becomes much more complicated. One could reasonably expect that, because of its low mass, hydrogen would tend to diffuse upwards so that hydrogen reactions would become more important at high altitudes and this appears to be the case. Some of the hydrogen reactions which are important in the chemistry of ozone are listed in Appendix A.1.2.

For the case of a hydrogen-oxygen atmosphere the time rate of change of ozone concentration is given by

$$\left(\frac{d}{dt}[O_3]\right)_{H,O} = \frac{d}{dt}[O_3] - k_7[O_3][H] - k_{25}[O_3][HO_2] \quad \ldots (1.2)$$

Thus the presence of hydrogen appears to lower the rate at which ozone is formed but, as mentioned before, this effect should only become appreciable at high altitudes. The hydrogen is present in molecular form and also as a result of the dissociation of water vapour.

From equations (1.1) and (1.2) we can deduce that the ozone concentration should increase at night (i.e. in the absence of sunlight); this effect should be more pronounced at high altitudes for two reasons:

(i) mixing and diffusion effects, which would tend to reduce any increase in ozone concentration, are much more pronounced at lower altitudes.

(ii) as far as absorption of radiation is concerned the ozone at high altitudes provides a shielding effect on that at lower levels.

It can be seen from this that there is a need to determine the nocturnal ozone concentration in the region 30-100 kilometres to test the validity of these theories.

1.2.3 Effects of Nitrogen and Nitrogen Compounds

Dutsch (1968) and Crutzen (1971) have considered the effect of several nitrogen compounds, e.g. HNO_3, HNO_2, NO, NO_2, NO_3, N_2O_5, N_2O_4, N_2O. Some of the more important reactions involving these compounds are listed in Appendix A.1.3.

The overall effects of all these minor constituents is to decrease the ozone concentration. However a great deal of work is needed to determine how important these effects are; the abundances of these minor constituents need to be determined accurately, as do the rate coefficients for the various reactions.

The atmospheric constituents which appear to exert the greatest influence on the photochemistry of ozone are water vapour, OH, O_2 and O, together with NO and CH_4. Techniques for measuring some of these constituents will be discussed later. It is also extremely important to know the cross-sections for the absorption of radiation by O_3, O_2, H_2O and CH_4.

1.2.4 The Ozone Absorption Cross-sections

Since ozone plays a major part in the absorption of solar radiation by the atmosphere it is most important to know the ozone absorption cross-section. This is difficult to calculate theoretically since ozone is a polyatomic molecule, and is also difficult to measure experimentally because of the difficulty involved in measuring the ozone concentration during any experiment.

The principal regions of the ozone absorption spectrum, as summarized by Horton (1968) are listed below:

Wavelength region	Form	References
1050-1500Å	Bands and Continuum	Tanaka, Inn and Watanabe
1500-2000Å	Continuum	Tanaka, Inn and Watanabe
2000-3000Å (Hartley Bands)	Continuum with suggestion of structure	Inn and Tanaka
3000-3500Å (Huggins Bands)	Bands	Inn and Tanaka
4350-7550Å (Chappuis Bands)	Continuum with suggestion of structure	Inn and Tanaka
3.3μ, 3.6μ, 4.8μ, 5.7	Vibration-rotation bands	M. Griggs
9.0μ-9.6μ	Strong vibration-rotation bands	Clough and Kneizys

Between 1000Å and 2000Å the large absorption cross-section of ozone cannot be used because absorption in this region is dominated by molecular oxygen.

The bands in the near ultraviolet and visible are suitable for absorption measurements and have been used, e.g. by Carver et al. (1966). The value of the absorption cross-section from 2000Å to 3500Å is shown in Figures 1.3 and 1.4, and the value from 4500Å to 7500Å is shown in Figure 1.5. The Huggins bands have been shown in a study by Vassy (1937), to be temperature dependent. This makes them unsuitable for use in atmospheric absorption studies because of the uncertainty in the atmospheric temperature versus height profile at any par-

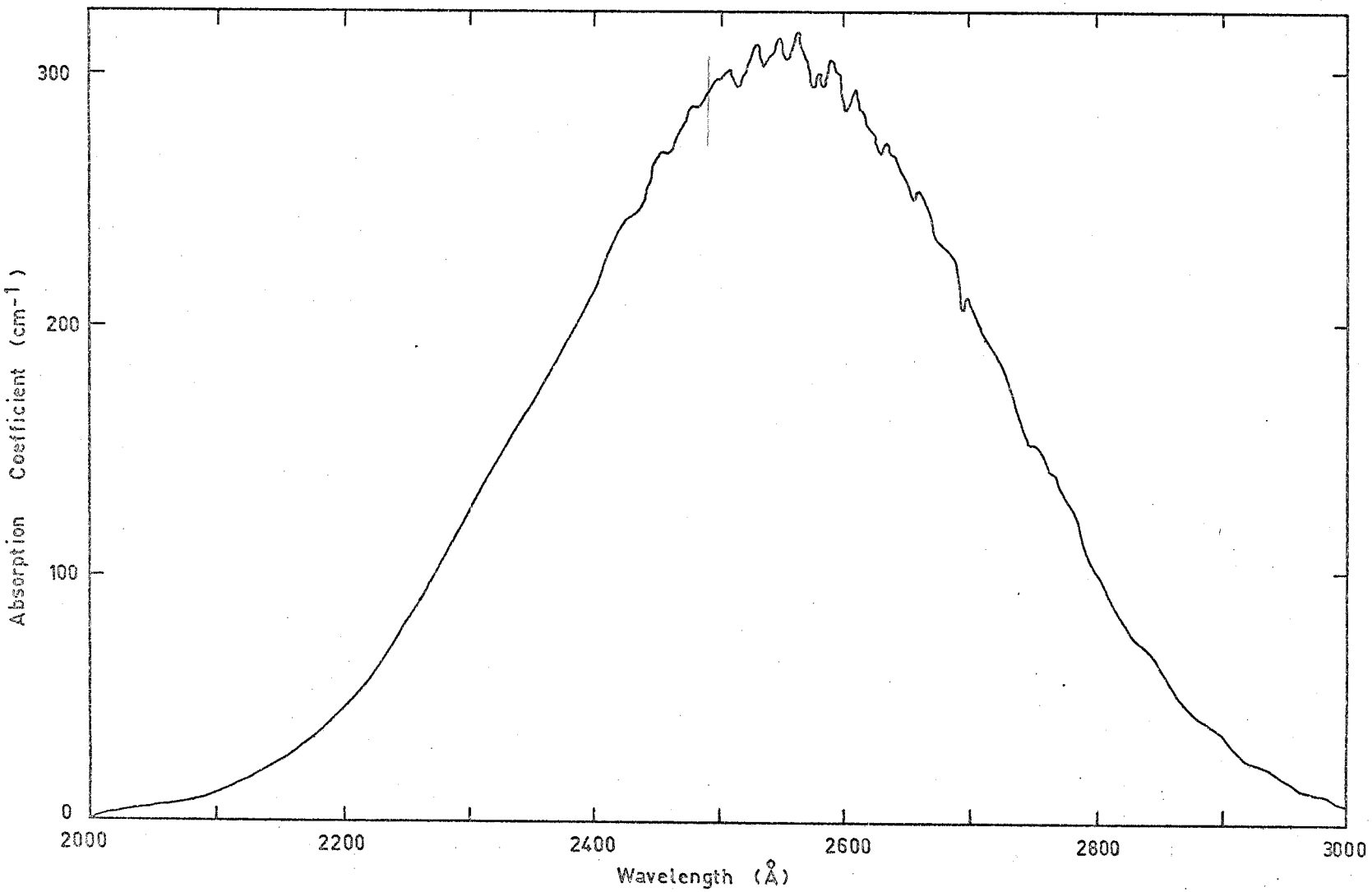

Figure 1.3 Absorption coefficient of O_3 (after Inn and Tanaka, (1959)).

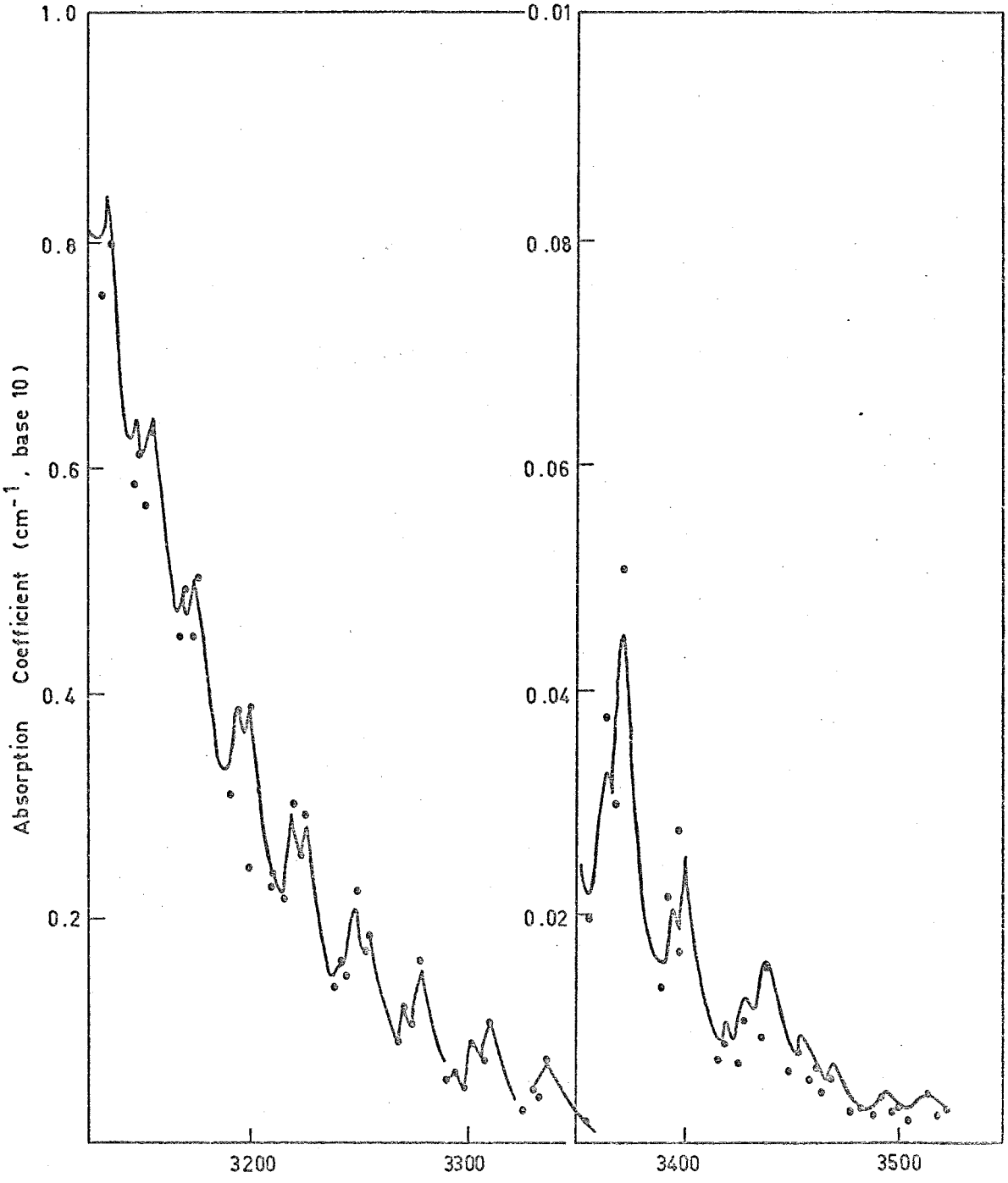

Figure 1.4 The Huggins absorption bands. The curves show the values of Inn and Tanaka while the points are those of Vigroux. (after Inn and Tanaka, (1959))

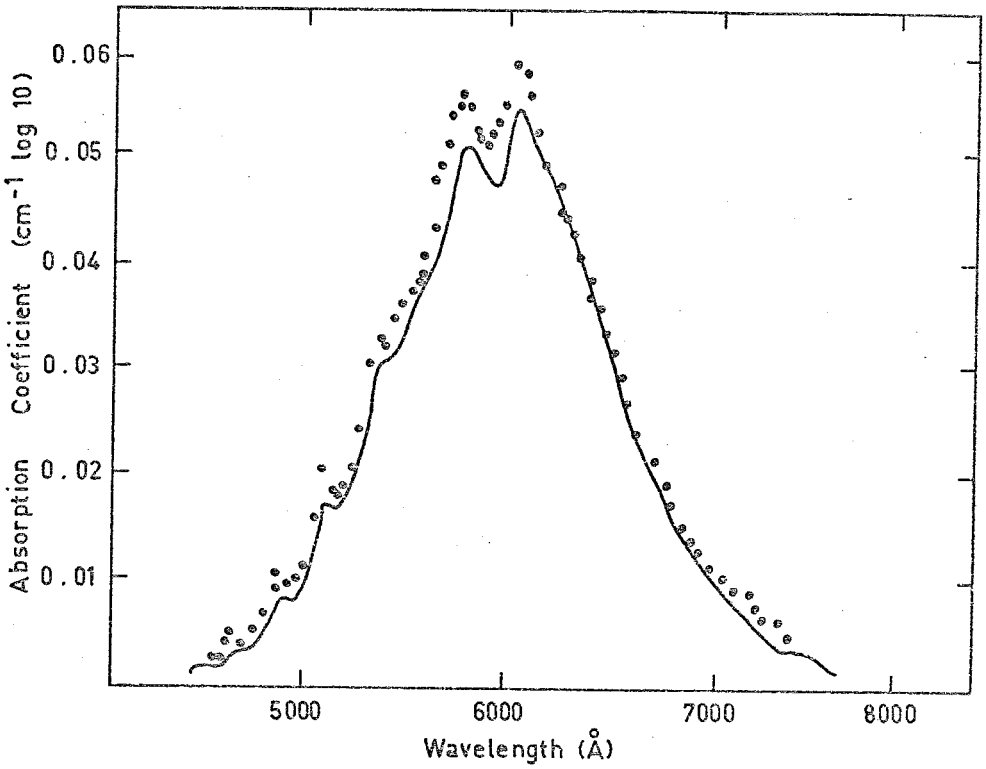

Figure 1.5 The structure of the Chappuis absorption bands. The points shown are by Vigroux and the curve by Inn and Tanaka. (after Inn and Tanaka, (1959))

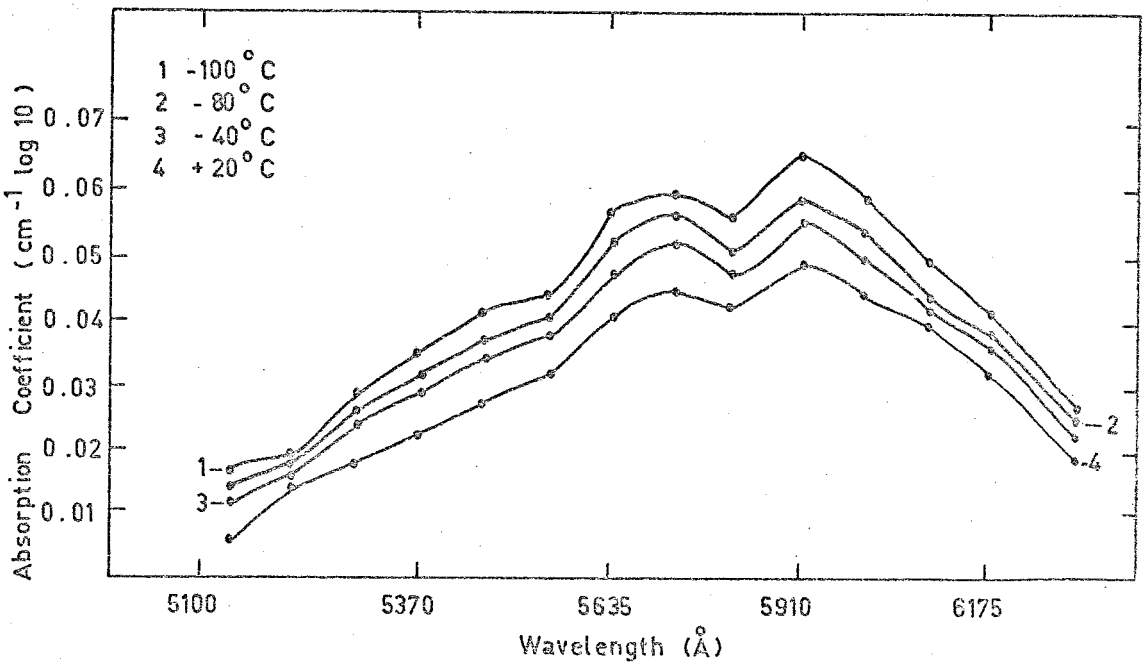

Figure 1.6 Variation of absorption in the Chappuis bands with temperature. (after Vassy, (1937))

ticular moment. In addition, the Huggins bands are too small to clearly define structure, which makes them difficult to use in absorption measurements unless very long path lengths are used, as in the Umkehr method (see section 1.4.1).

The Chappuis bands in the visible have also been shown by Vassy to be temperature dependent, so they are unsuitable for atmospheric measurements for the reason already mentioned. The effects of temperature on the Chappuis bands is shown in Figure 1.6.

The bands in the infra-red are very temperature dependent and are unsuitable for absorption measurements. However, because of their strength they are important in atmospheric heating processes.

The temperature dependence study by Vassy showed that the Hartley bands between 2700Å and 3000Å were not temperature dependent over the range from 0°C to -80°C. Atmospheric absorption measurements by Carver et al. (1966) have shown that these bands are suitable for absorption measurements above about 30 kilometres. Inn and Tanaka (1959) have suggested, on the basis of comparison of their own results with those of other authors, that the uncertainty in the values shown in Figure 1.3 is approximately 10 per cent.

1.3 Measurements of Atmospheric Constituents other than Ozone

1.3.1 Absorption Measurements

Molecular oxygen densities have been measured by Friedman

et al. (1964), Smith and Weeks (1965), Carver et al. (1965), Weeks and Smith (1968a), Wildman et al. (1969) and Subbaraya et al. (1972), using ion chambers with various combinations of windows and filling gases. This method has only been used above 60 kilometres because the instruments used did not have sufficient range to measure the low intensities (much reduced by atmospheric absorption) below this height.

Aro (1972) has measured water vapour concentrations by combining infra-red absorption measurements with radio-sonde data, while Grobecker (1971) has used ion chambers with Mylar and Aluminium or Nickel windows (producing passbands of 8-20Å and 44-60Å respectively) to measure total densities ($n(O_2) + n(O) + n(N_2)$) from X-ray absorption profiles.

1.3.2 Mass Spectrometer Measurements

Mass spectrometers have been used by Schaefer and Nichols (1964) to measure $\frac{O}{O_2}$ and $\frac{N}{N_2}$ number density ratios, by Barth (1966) to measure NO concentration, by Offerman et al. (1972) to measure CO_2, NO, N and H_2O concentrations, by Philbrick et al. (1972) to measure N_2, O, O_2, Ar, CO_2, O_3 and other minor constituents, and by Johannessen et al. (1972) to measure the concentration of water cluster ions, $H^+(H_2O)_n$. In addition Hickman and Nier (1972) have measured N, N_2, O, O_2, H_e, Ar, H_2O and CO_2 number densities in the range 120 to 185 kilometres.

This method seems to be applicable to most atmospheric constituents but suffers from the disadvantage that the

instrumentation is complex and the passage of the rocket through the atmosphere disturbs the concentration of the species under test.

1.3.3 Chemical Methods

Henderson (1971) and Thomas (1972) have flown chemical detectors to measure atomic oxygen densities. These detectors consist of a silver film, which only reacts to any measurable extent with atomic oxygen. The rate of oxidation of the film is proportional to the rate at which atomic oxygen reaches the film surface, and can be determined by measuring the change in the electrical resistance of the film since silver is a much better electrical conductor than silver oxide. The rate at which atomic oxygen reaches the film surface can be related to the local concentration by considering the dynamics of the sampling process.

The results of some of these measurements are shown in Figure 1.7 where the experimental results are compared with theoretical calculations made by Hunt (1971), Barth (1966).

1.3.4 Emission Measurements

Packer (1961) and Tavasova (1963) have measured the emission by OH and Hunt (1966) has calculated OH emission rates for theoretically derived number densities. The comparison between theory and experiment is shown in Figure 1.8.

Williamson and Houghton (1965), and Bazhulin et al. (1966)

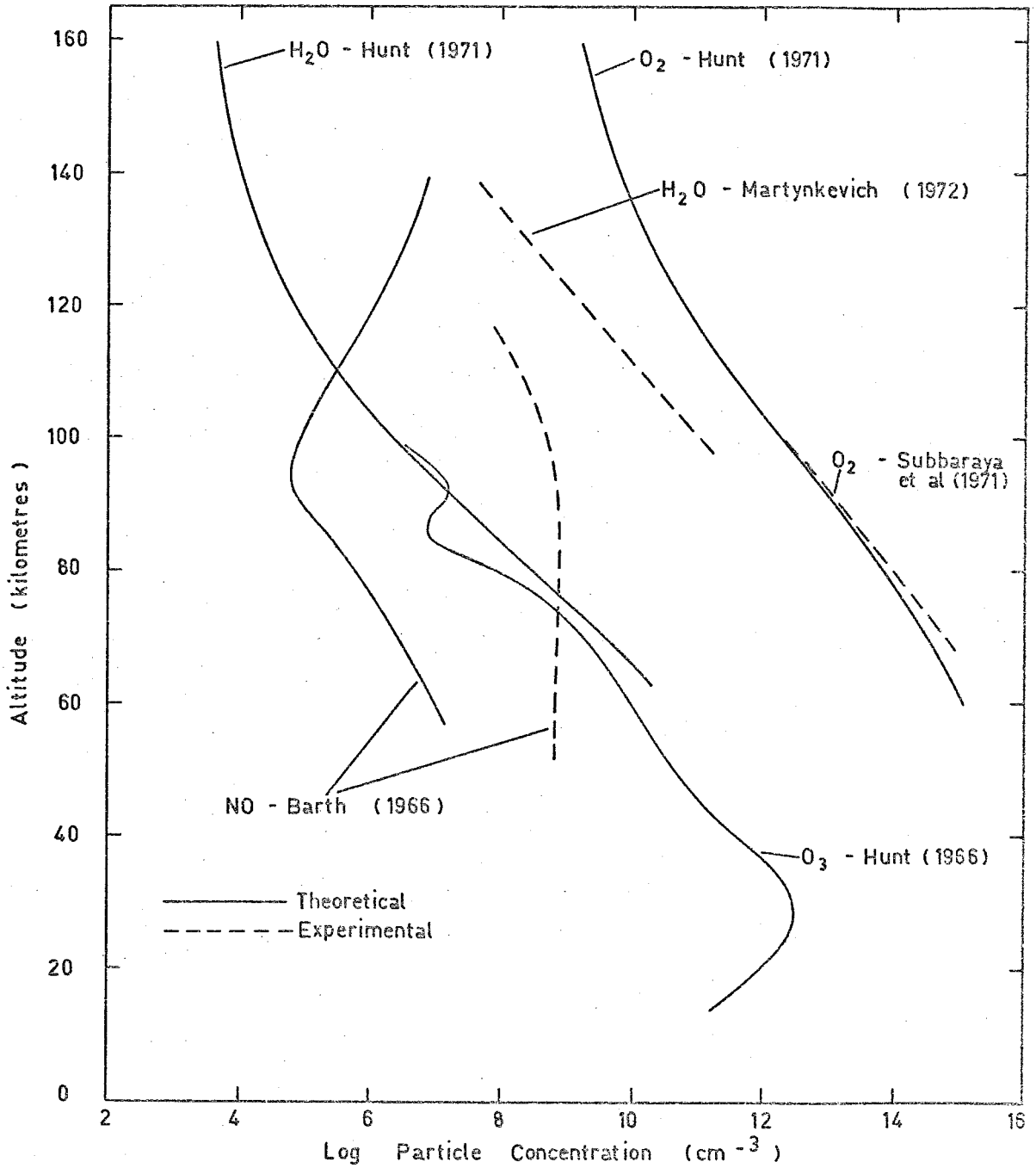

Figure 1.7 Comparison of experimental and calculated number densities for some atmospheric constituents.

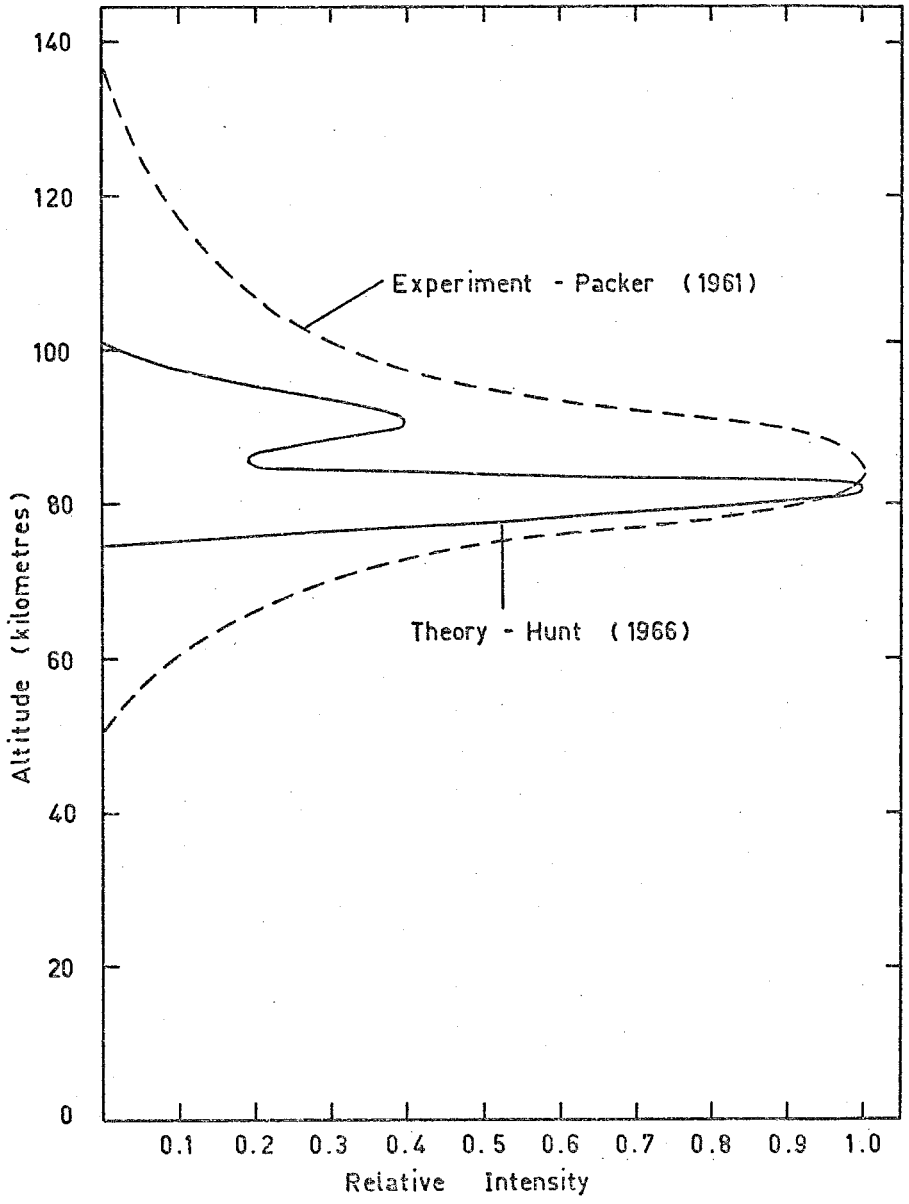

Figure 1.8 Theoretical and experimental OH airglow profiles.

have measured water vapour concentrations above 30 kilometres by measuring the intensity of the 6.3 micron radiation from water vapour, but the measured intensities were considerably higher than expected. The excess radiation has been attributed to some other atmospheric constituent, say OH, NO or N_2O.

1.4 Methods of Measurement of Ozone Concentration in the Upper Atmosphere

1.4.1 The Umkehr Method

This method uses the signals received at ground level from two narrow-band-pass photometers centred at two wavelengths in the relatively weak Huggins absorption bands of ozone in the region 3000-3500Å. The pass-bands are chosen such that one covers a region of almost zero absorption while the other covers a region of relatively strong absorption. The ratio of the signals received is recorded as a function of solar zenith angle. The relationship is of the form (Craig, 1965)

$$\frac{I(\lambda_1)}{I(\lambda_2)} = \frac{K(\lambda_1)F\infty(\lambda_1)\int_0^\infty \rho\tau_{oz}(\lambda_1)\tau_{z\infty}(\lambda_1)dz}{K(\lambda_2)F\infty(\lambda_2)\int_0^\infty \rho\tau_{oz}(\lambda_2)\tau_{z\infty}(\lambda_2)dz} \quad \ldots (1.3)$$

where $I(\lambda_i)$ = measured intensity at wavelength λ_i

$K(\lambda_i)$ = Rayleigh scattering coefficient at wavelength λ_i

$F\infty(\lambda_i)$ = solar flux at wavelength λ_i at the limits of the earth's atmosphere

ρ = air density at height z

$\tau_{\alpha\beta}(\lambda_i)$ = transmissivity of a slant air column between altitudes α and β at wavelength λ_i

The transmissivities $\tau_{oz}(\lambda)$ and $\tau_{z\infty}(\lambda)$ are given by

$$\tau_{oz}(\lambda) = \exp\left[-k(\lambda)\int_o^z \rho_3 dz - K(\lambda)\int_o^z \rho dz\right] \quad \ldots (1.4)$$

$$\tau_{z\infty}(\lambda) = \exp\left[-k(\lambda)\int_z^\infty \rho_3 \sec\psi dz - K(\lambda)\int_z^\infty \rho \sec\psi dz\right] \quad \ldots (1.5)$$

where ψ = angle between the solar beam and the local vertical at height h

ρ_3 = ozone density

$k(\lambda)$ = absorption coefficient for ozone

In these last two expressions the first term accounts for absorption by ozone and the second term accounts for Rayleigh scattering. Thus the values of $\tau_{\alpha\beta}(\lambda_i)$ are functions of zenith angle, altitude and the absorption coefficient of ozone in the pass band of the photometer.

Umkehr measurements are made at large zenith angles (50-90 degrees), so one cannot assume ψ is constant and equal to the zenith angle Z at the point of observation. In addition this method is not very suitable for use at high altitudes because it assumes that there is zero ozone concentration above some fixed level.

The Umkehr method is suitable (and is used) for monitoring ozone levels in the region of maximum ozone concentration at about 25-30 kms. The geometry of the method is shown in Figure 1.9.

Kulkarni and Pittock (1970) have made extensive Umkehr measurements and also chemiluminescent measurements. In addition Dutsch and Ling (1969) have made a critical comparison of these two techniques. Walton (1957) and Ramahathan and Dave (1957) have given numerical methods for the derivation of profiles from Umkehr measurements.

1.4.2 Chemical Methods

(a) Reaction of Ozone with Potassium Iodide Solution

Chemical methods fall into several types; the height to which these detectors must be lifted depends on the type of detector. One of the major types which was discussed in great detail by Brewer and Milford (1960) depends on the reaction

$$O_3 + 2KI + H_2O \rightarrow 2KOH + O_2 + I_2$$

The number of ozone molecules taking part in the reaction is measured by electrolysis of the iodine formed in the solution. If a potential difference is maintained in the non-reacting solution the electrodes are polarized and no current flows. When iodine is released by the reaction above then, at the cathode,

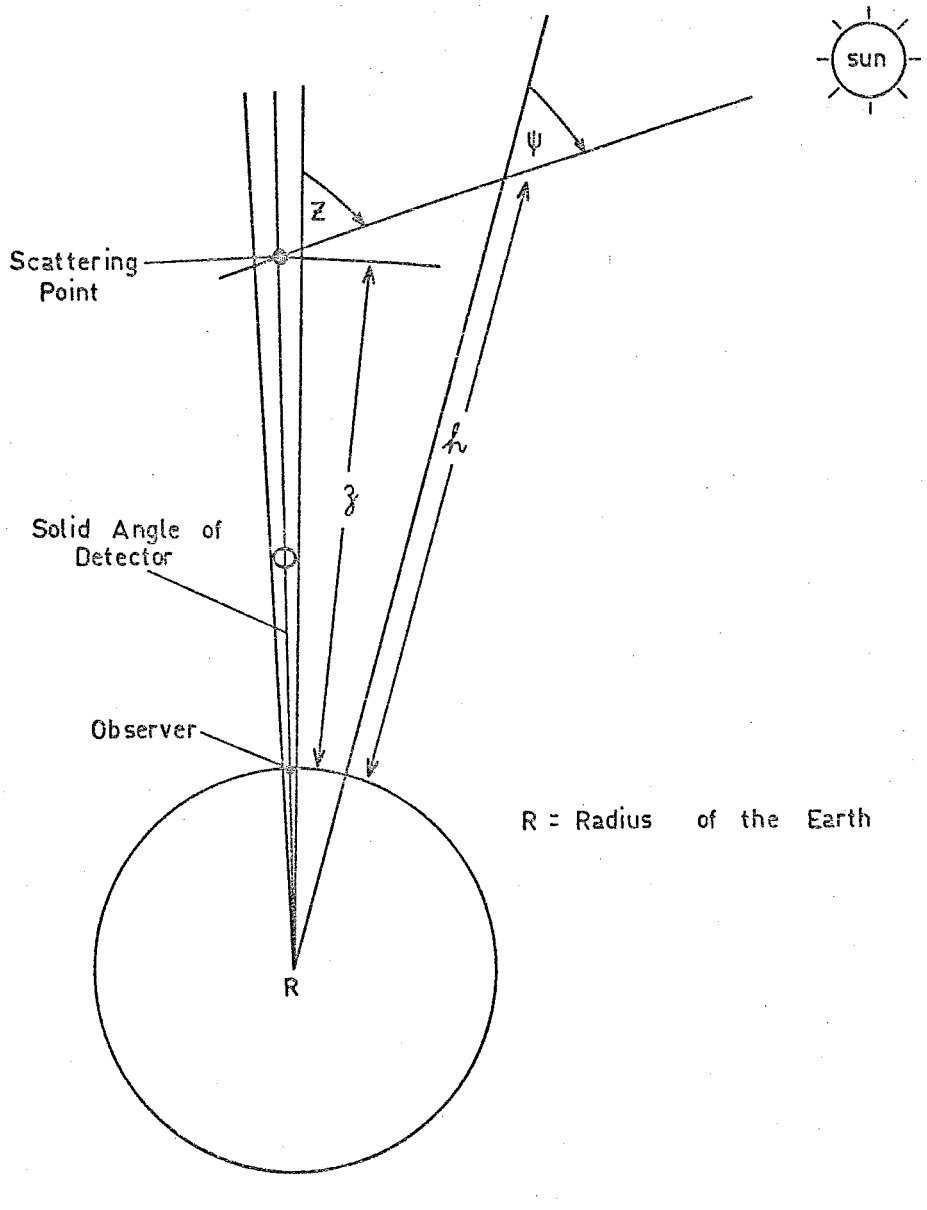

Figure 1.9 Geometry of the Umkehr and absorption methods.

$$I_2 + 2e^- \rightarrow 2I^-$$

These negative ions drift to the anode, where the reaction

$$2I^- \rightarrow 2e^- + I_2$$

takes place, so that for each ozone molecule involved two electrons flow into the circuit.

Brewer and Milford (1960) developed two sensors for measuring this current; in one the KI solution is first dripped through the ozone atmosphere onto the cathode and then flows down an insulating rod to the anode, while in the other the ozone atmosphere is bubbled through the solution at a constant rate and the iodine reacts with the special anode material to form an insoluble salt and so is removed from the solution.

These systems can give information about the ozone distribution up to heights of approximately 40 kms.

(b) The Chemiluminescent Method

Another chemical method due to Regener (1960) depends on the chemiluminescent reaction of ozone with the luminescent material "Luminol". Samples of air are drawn past a "Luminol"-coated disc and the radiation resulting from the reaction is proportional, in intensity, to the ozone content in the air sample.

Experiments using this technique have been reported by Hering and Barden (1964) while variations of the method have

been used by Hodgeson et al. (1970) for low altitude measurements, and by Randhawa (1966, 1970, 1971) and Hilsenrath (1971) for making measurements from rockets.

This method appears to be one of the most sensitive methods known for detecting ozone but suffers from the disadvantage that the sensitivity of the surface slowly decays and has to be periodically recalibrated. However the method is suitable for use over a wide range of altitudes.

Hodgeson et al. (1970) suggest that there are also problems associated with "residual signals", that is this type of detector has a finite response time, so that it may introduce problems when used to measure rapid changes in ozone concentration. In addition there are problems associated with measuring the rate of flow of air past the chemiluminescent surface which can only be overcome by taking great care in the physical design of the apparatus. This method, if used in rockets or balloons, also suffers from the fact that the air samples obtained may not be truly representative of the atmospheric conditions at the sampling point, due to the disturbing effect of the motion of the balloon or rocket.

1.4.3 The Atmospheric Radiance Method

This is an indirect approach formulated by Twomey (1961) involving the use of measurements of the scattering of solar radiation by the atmosphere as a function of the solar zenith

angle and the observation angle together with the expected depth of penetration of the atmosphere as a function of wavelength.

The method considers the following model-: an atmosphere consisting of a preponderance of molecules of polarizability a, and containing a small proportion of a highly absorbing constituent such as ozone with concentration $\varepsilon(p)$ centimetres (at STP) per millibar at the pressure level p. If absorption by the scattering molecules and scattering by the absorbing molecules are neglected, then the energy flux per square centimetre at level p is

$$E_\lambda(p) = E_\lambda(o)\exp\left[-k(\lambda)\int_o^p \varepsilon(p)dp\right] \qquad \ldots (1.6)$$

where $E_\lambda(o)$ is the incident flux density at the top of the atmosphere at wavelength λ and $k(\lambda)$ is the absorption coefficient (cm^{-1}) at wavelength λ.

From the theory of Rayleigh Scattering it can be shown that the backscattered energy (for vertical incidence) in the wavelength region λ to $\lambda+\Delta\lambda$ reaching the optical system in a solid-angle increment $\Delta\omega$ from unit area between p and $p+\Delta p$ is given by (viewing from above the atmosphere)

$$\Delta E = \left(\frac{2\pi}{\lambda}\right)^4 \frac{|a|}{mg}^2 E_\lambda(O)\exp\left[-2k(\lambda)\int_o^p \varepsilon(p)dp\right]\Delta p\Delta\lambda\Delta\omega \qquad \ldots (1.7)$$

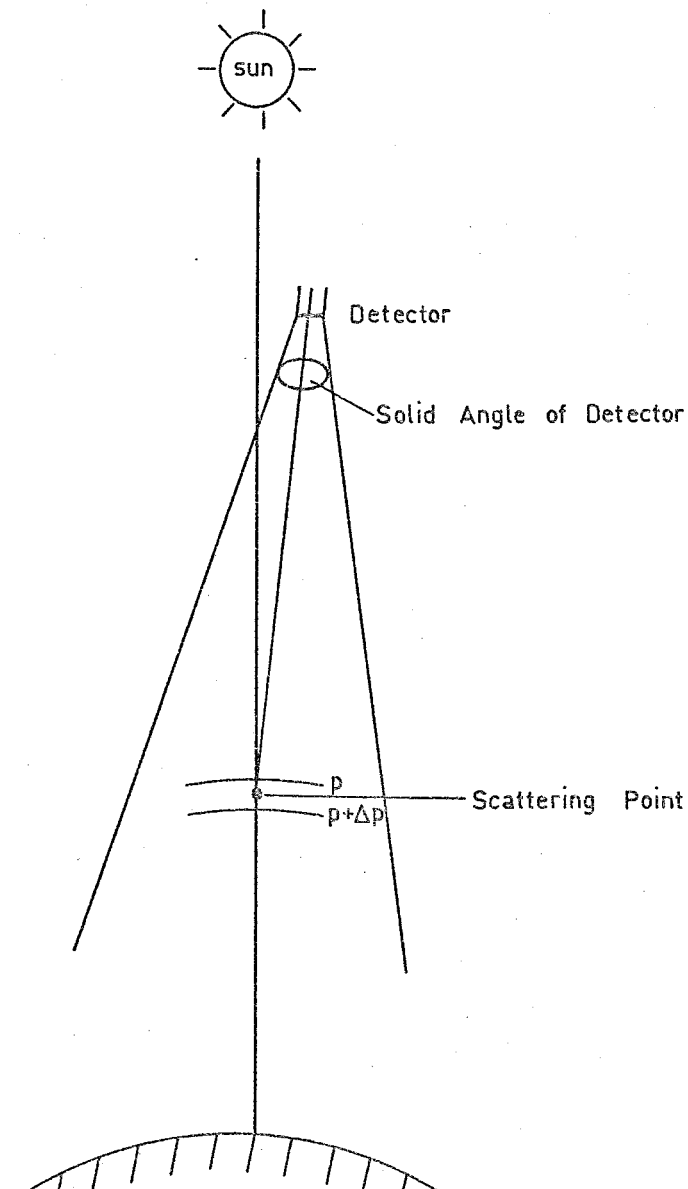

Figure 1.10 Geometry of Twomey's atmospheric radiance method.

where m = mass of a single molecule

g = acceleration due to gravity

and the factor 2 in the square bracket accounts for the fact that the radiation scattered at level p is further attenuated by absorption on its way out of the atmosphere. The geometry of the situation is shown in Figure 1.10.

Twomey's method of solution consists of inverting equation (1.7) to find p as a function of height x and then comparing observed radiance values with those expected from perturbation calculations made using a model atmosphere as a starting point.

This method has been used by Friedman et al. (1963) but is not particularly suitable for obtaining ozone profiles because of the complex mathematical treatment required and the nature of the assumptions which must be made.

1.4.4 Measurement by Atmospheric Absorption

This method uses the effect of absorption of radiation by the ozone in the atmosphere. A detector which can be carried in a balloon, rocket or satellite measures the solar flux in the region of the ultraviolet where ozone absorbs strongly. By measuring the rate of change of flux with height the vertical distribution of the ozone can be deduced.

The geometry of this method is the same as that for the Umkehr method, shown in Figure 1.9, except that in the absorption case we want to measure the intensity of the radiation reaching height z.

The intensity of radiation reaching height z is given by

$$I_\lambda(z) = I_\lambda(\infty)\exp\left[-\sigma(\lambda)\int_z^\infty n(h)\sec\psi\,dh\right] \qquad \ldots (1.8)$$

where $I_\lambda(\infty)$ is the flux above the atmosphere, at wavelength λ

ψ is the local zenith angle at height h along the line of sight of the detector

$n(h)$ is the ozone concentration at height h

$\sigma(\lambda)$ is the absorption coefficient at wavelength λ

If Z is the zenith angle of the line of sight at the detector then, from Figure 1.9

$$\frac{R+h}{\sin Z} = \frac{R+z}{\sin\psi} \qquad \ldots (1.9)$$

$$\therefore \quad \sec\psi = \left(1 - \left(\frac{R+h}{R+z}\right)^2 \sin^2 Z\right)^{-\frac{1}{2}} \qquad \ldots (1.10)$$

so that

$$I_\lambda(z) = I_\lambda(\infty)\exp\left[-\sigma(\lambda)\int_z^\infty \frac{n(h)\,dh}{\left[1-\left(\frac{R+h}{R+z}\right)^2 \sin^2 Z\right]^{\frac{1}{2}}}\right] \qquad \ldots (1.11)$$

Green et al. (1966) have developed a method for handling the singularity at $Z = 90°$, $z = h$. Equation (1.11) is greatly simplified if $Z \lesssim 65°$, in which case it is quite easy to show that the above expression reduces to

$$I_\lambda(z) = I_\lambda(\infty)\exp\left[-\sigma(\lambda)\sec Z\int_z^\infty n(h)\,dh\right] \qquad \ldots (1.12)$$

This expression can easily be inverted to obtain $\int_z^\infty n(h)dh$ as a function of z - differentiation then gives n(z) as a function of z.

Several experimental techniques have been developed for absorption measurements. Regener et al. (1954) and Johnson et al. (1952) have used spectrographic data to obtain ozone densities up to 40/70 kilometres in the wavelength region 2000-3500Å. Paetzold (1961) developed an ozonesonde which uses a quartz sphere lined with magnesium oxide as a light collector. The radiation is passed through a filter to a photocell which gives an output current proportional to the intensity of the incident radiation. This method has also been used by Sissons (1970) in both balloon- and rocket-borne experiments.

Miller and Stewart (1965), Reed and Scolnik (1964), Reed (1968) and Carver et al. (1966) have used photometers consisting of photomultipliers mounted behind broad-band interference filters, while Miller and Stewart have also used a simple prism spectrophotometer for satellite measurements.

Most absorption measurements have been made using a radiation source outside the atmosphere. The measurements of Reed and Scolnik are interesting in that they use the UV nightglow as the source of radiation. The significance of this will be discussed later.

The absorption method suffers from several disadvantages, the main one being that it can only give accurate results when

the ozone concentration is changing fairly rapidly and where the total amount of ozone between the detector and the source is not too great to completely absorb the incident radiation. This means that use of this method is restricted to heights above 35 kms.

The main advantage of this method is that the detectors used are fairly rugged, compact, and light in weight, making them suitable for satellite or rocket experiments. This means that they can easily be lifted into the region of the atmosphere (30-100 kms) where this technique is most suitable for use.

1.5 Atmospheric Models

1.5.1 Introduction

The main purpose of atmospheric modelling is to construct a mathematical model of the atmosphere which can be used to describe the behaviour of the atmosphere and to make extrapolations into the past or future. Until recently, most models have been purely static and have neglected effects such as turbulence, convective mass transport due to absorption of solar radiation by atmospheric gases, and mass transport due to diffusion.

Hunt (1965, 1966, 1971) has considered the case of a pure oxygen atmosphere, a moist atmosphere, and the effects of diffusion. In the first two cases he finds an increase in ozone concentration at night at altitudes around 70-90 kilometres, which is consistent with the simple argument presented

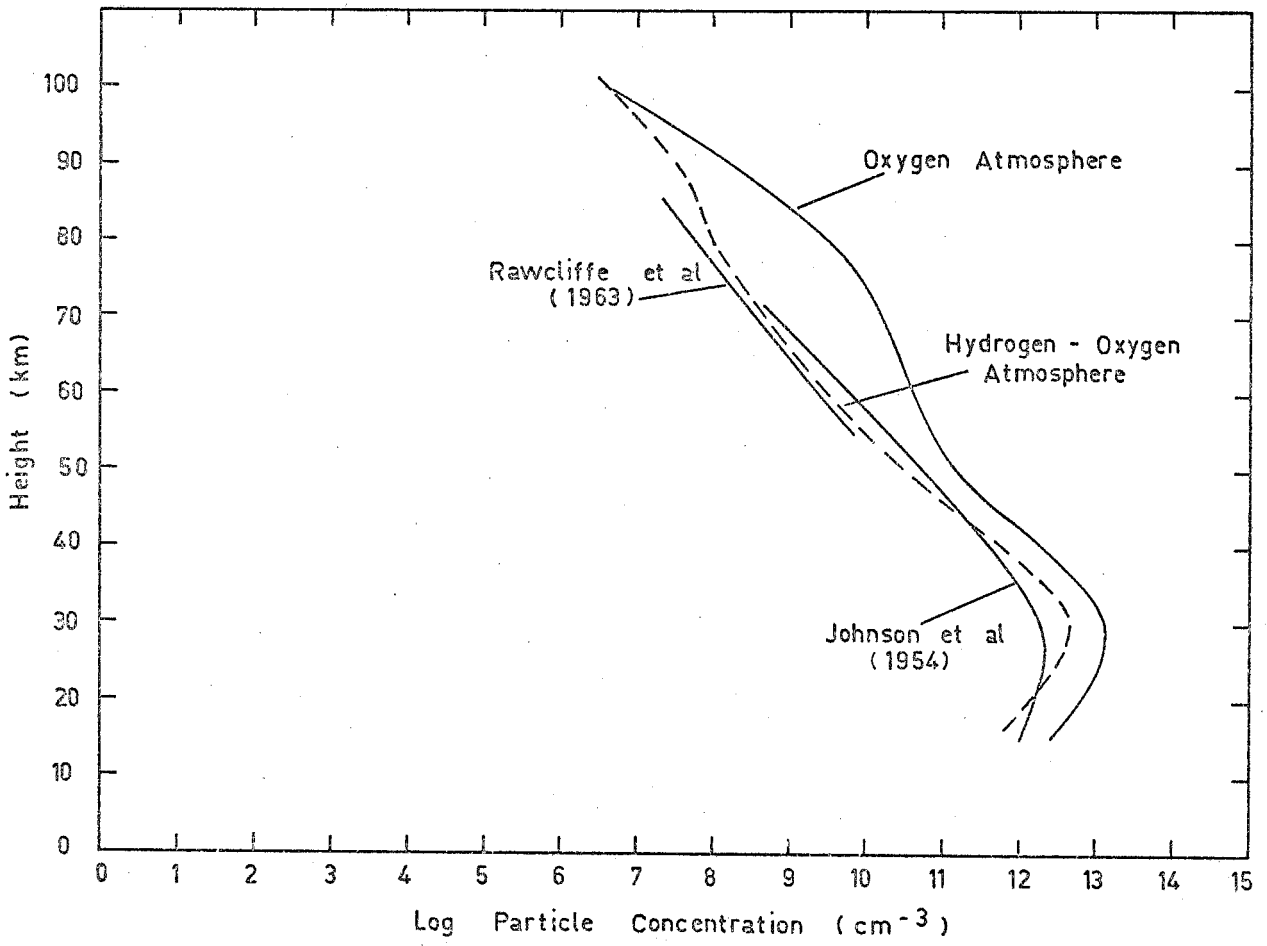

Figure 1.11 Equilibrium ozone profiles for an oxygen atmosphere and a hydrogen - oxygen atmosphere. (after Hunt (1964, 1966)). The experimental results are due to Rawcliffe et al (1963) and Johnson et al (1954).

in Section 1.2. The equilibrium profiles for ozone as predicted by Hunt for an oxygen atmosphere and a hydrogen-oxygen atmosphere are shown in Figure 1.11, where they are compared with some experimental results.

Keneshea (1967) has considered the basic oxygen-only atmosphere plus a number of other constituents, viz., NO, NO_2, N_2O, NO^+, NO_2^-, O_3^-, O^-, O^+, O_2^+ and N_2^+, but on the basis of his calculations he concludes that the effect of these constituents on the ozone concentration is negligible. He has also calculated reaction rates as a function of altitude - these calculations show that the absence of sunlight should have more effect at high altitudes.

Most atmospheric models are constructed using the same basic procedure. The problem is to solve a set of simultaneous differential equations to find the concentrations of the various constituents as a function of time and altitude. If we consider the case of a dry oxygen atmosphere the photo-chemical reactions involved are

$$O + O_2 + M \xrightarrow{a_1} O_3 + M$$

$$O + O + M \xrightarrow{a_2} O_2 + M$$

$$O + O_3 \xrightarrow{a_3} O_2 + O_2$$

$$O_2 + h\nu(I_2) \xrightarrow{\sigma_2} O + O$$

$$O_3 + h\nu(I_3) \xrightarrow{\sigma_3} O + O_2$$

From these, neglecting the effects of turbulence and transport, we obtain the following set of differential equations:-

$$\frac{d}{dt}[O] = - a_1[O][O_2][M] - 2a_2[O]^2[M] - a_3[O][O_3] + 2\sigma_2 I_2[O_2] + \sigma_3 I_3[O_3] \quad \ldots (1.13)$$

$$\frac{d}{dt}[O_2] = - a_1[O][O_2][M] + a_2[O]^2[M] + 2a_3[O][O_3] - \sigma_2 I_2[O_2] + \sigma_3 I_3[O_3] \quad \ldots (1.14)$$

$$\frac{d}{dt}[O_3] = a_1[O][O_2][M] - a_3[O][O_3] - \sigma_3 I_3[O_3] \quad \ldots (1.15)$$

where a_1, a_2, a_3 are rate coefficients

σ_2 and σ_3 are the absorption cross-sections for O_2 and O_3 respectively

I_2 and I_3 are the radiation intensities (in units of numbers of photons) absorbed by O_2 and O_3.

In addition most authors make the assumption M = constant.

These differential equations are non-linear and cannot be solved analytically. However some approximations can be made which enable estimates of concentrations to be obtained. Some of these approximations will now be discussed.

1.5.2 The Equilibrium State

The first step is to assume that the different species are in equilibrium. This means that

$$\frac{d}{dt}[O] = \frac{d}{dt}[O_2] = \frac{d}{dt}[O_3] = 0 \qquad \ldots (1.16)$$

Under these conditions equations (1.13) to (1.15) can be solved. This gives an estimate of the number densities one might expect at various levels.

1.5.3 Slight Deviations from Equilibrium

If we now assume that one of the species undergoes a slight deviation from equilibrium we can calculate the characteristic (half-restoration) time for that species; this is the time for the change in number density to be reduced to e^{-1} of its original value.

For example suppose $\frac{d}{dt}[O] = \frac{d}{dt}[O_2] = 0 \qquad \ldots (1.17)$

and $[O_3] = [O_3]_o + \Delta_3$, where $\frac{d}{dt}[O_3]_o = 0 \qquad \ldots (1.18)$

($[O_3]_o$ is the equilibrium ozone concentration).

Dutsch (1956) has shown that the characteristic time for $[O_3]$ in this case is given by

$$\tau_3 = \left(\frac{a_1[M]}{16a_3\sigma_2\sigma_3 I_2 I_3}\right)^{\frac{1}{2}} = \frac{a_1[O_2][M]}{4a_3\sigma_3 I_3[O_3]_o} \qquad \ldots (1.19)$$

Similarly, by assuming $[O_2]$ and $[O_3]$ to be in equilibrium the characteristic time for $[O]$ is given by Dutsch as

$$\tau_1 = \frac{\sigma_3 I_3}{2\sigma_2 I_2 a_3[O_2] - 4a_1 a_3[O_2][M][O]_o} \qquad \ldots (1.20)$$

The time available during the day in which [O] and [O_3] can attain equilibrium with the incident solar radiation is about 10^4 seconds, so if τ_1 and/or $\tau_3 > 10^4$ seconds the corresponding constituent will probably not be in equilibrium. Also, if the concentration of a species varies at night it will probably not reach its equilibrium concentration during the day if its characteristic time is greater than 10^4 secs. Hunt (1964) has shown that atomic oxygen above 65 kms and ozone below 35 kms will probably not be in equilibrium.

These results can also be used to show that the ozone concentration below 50 kms does not change much during the night because the atomic oxygen concentration is very low at these altitudes (Griggs, 1966).

1.5.4 The Non-Equilibrium State

Using the concentrations obtained by assuming the atmosphere to be in equilibrium as a starting point the equations 1.13 to 1.15 can be numerically integrated to determine the concentrations for the various species when the atmosphere is not in equilibrium. Hunt (1965, 1966) has used a Runge-Kutta integration technique, while Keneshea (1967) has used a Kutta-Merson method to save computer time. Hunt (1971) has also developed a model which takes diffusion into account but he points out that there are still a number of very fundamental problems which have to be solved before these models can give an accurate picture of the different processes occurring in the atmosphere.

The most pressing need appears to be for accurate measurements of reaction rates and number densities. There is also a need for more information about processes in the atmosphere such as diffusion, absorption of radiation, energy and momentum transport, atmospheric circulation, etc. As more detailed knowledge of these processes becomes available from experimental work the accuracy of atmospheric models should be greatly improved.

CHAPTER 2

DESIGN AND CALIBRATION OF THE FLIGHT PHOTOMETERS

2.1 Introduction

The relative merits of the different methods of measuring ozone concentrations have been discussed in Chapter 1. The absorption method was chosen for this work because it has the advantage of not disturbing the part of the atmosphere under test and because of the relatively simple equipment needed.

The photometers used for the present series of measurements consisted of thin film interference filters mounted in front of photomultiplier tubes. The currents from these were passed through amplifiers and the voltages produced were applied to a telemetry system and transmitted to a ground receiving station and recorded. The details of each part of the equipment will now be given.

2.2 The Photometers

2.2.1 Filters

The interference filters used were obtained commercially and had nominal peak wavelengths of 2500Å, 2700Å and 2900Å. The transmission of each filter was checked on a Perkin Elmer Type 137 Ultraviolet Visible Spectrophotometer. Graphs of log absorbance versus wavelength, as obtained by this instrument, are shown in Figs. 2.1, 2.2 and 2.3. The transmission of the

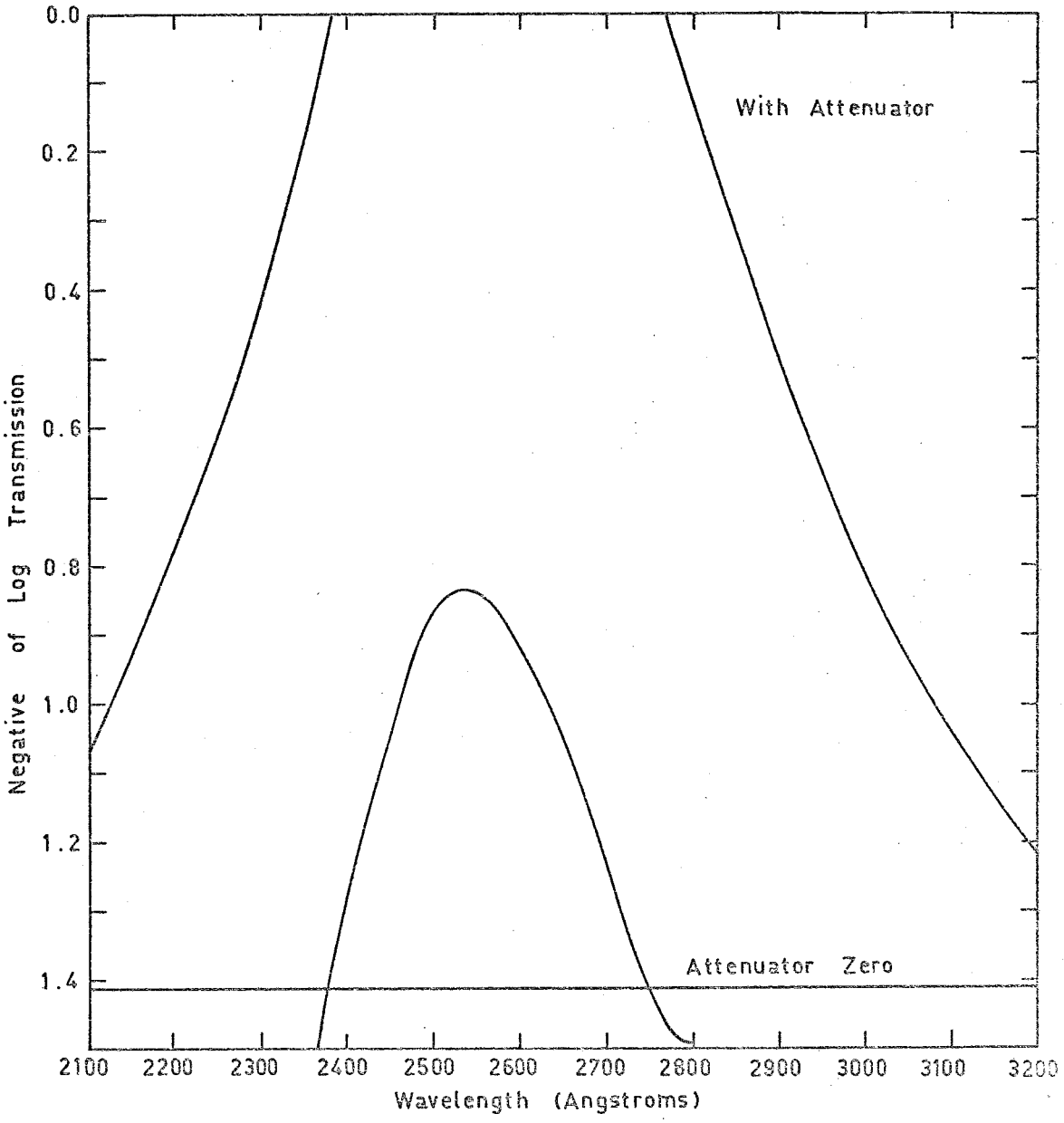

Figure 2.1 Transmission of filter at 2500 Å. The value of the curve with attenuator should be added to the value of the attenuator zero.

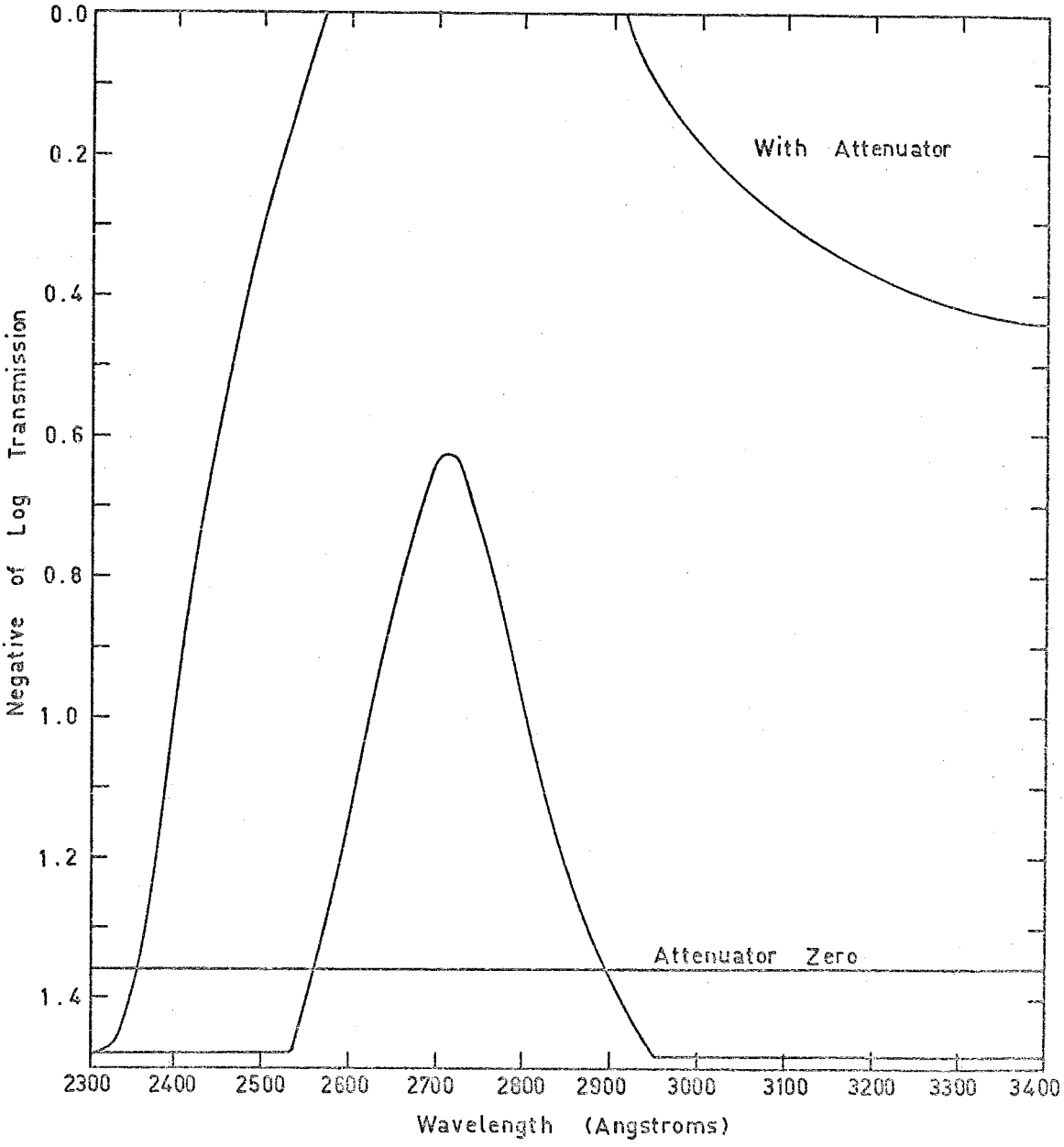

Figure 2.2 Transmission of filter at 2700 Å. The value of the curve with attenuator should be added to the value of the attenuator zero.

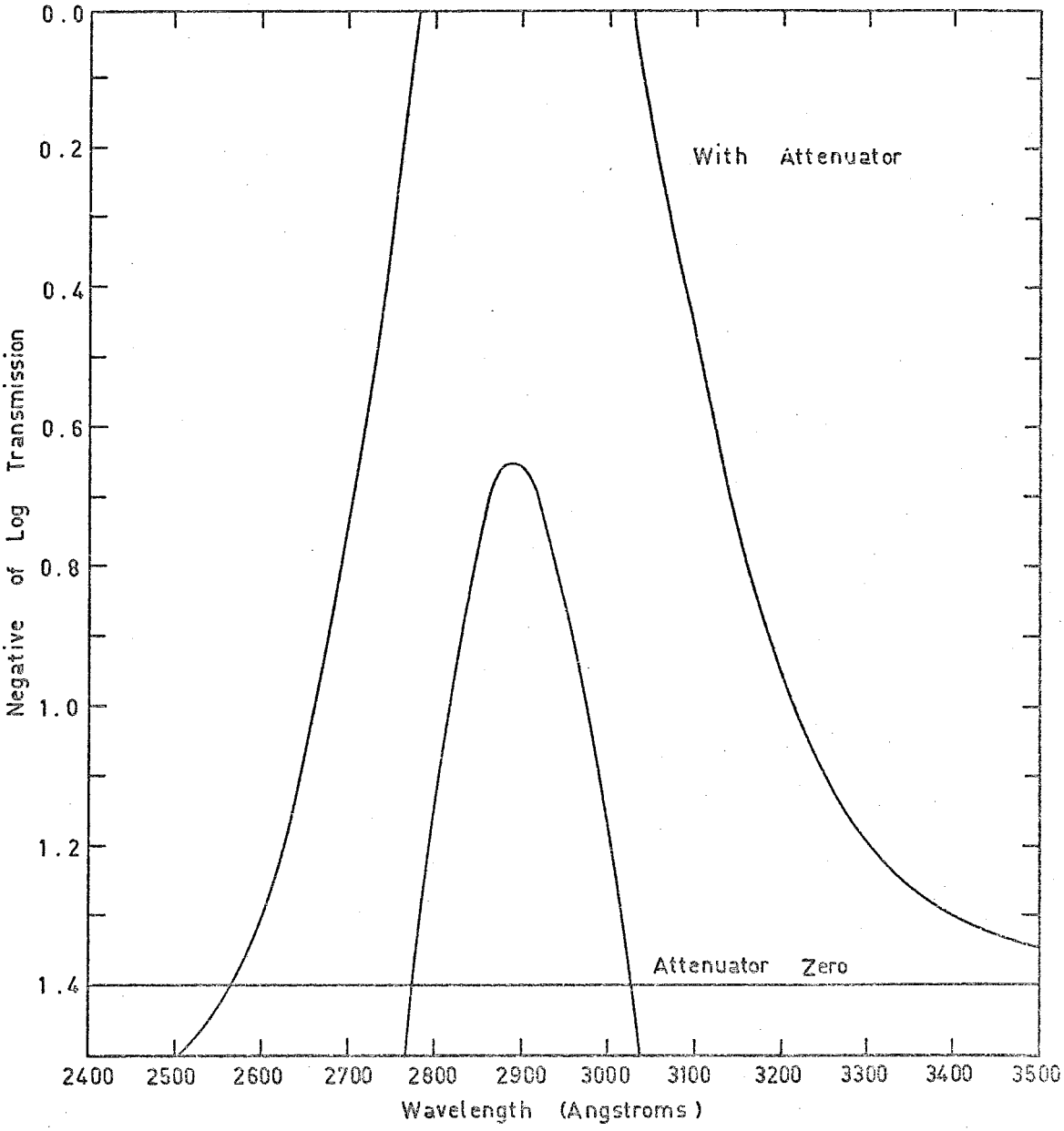

Figure 2.3 Transmission of filter at 2900 Å. The value of the curve with attenuator should be added to the value of the attenuator zero.

filters as a function of the angle of incidence was also measured. Results for a typical filter are shown in Figure 2.4.

One difficulty associated with interference filters is the transmission of lower order pass-bands at longer wavelengths. To check the effect of such transmission all photometers were exposed to moonlight at ground level; in all cases the signal, due to transmission through the filter in the visible region of the spectrum between 5000Å and 6000Å, was found to be only slightly above noise level and, in most cases, more than two orders of magnitude less than the signal expected in flight due to ultraviolet radiation.

The mounting system used for the filters in HAD 313 is shown in Figure 2.5a. The design was changed on the three later rounds (C104, C105 and C1014) because of space requirements. The system used on these rounds is shown in Figure 2.5b. Both types of mounting were arranged to clamp to the main instrumentation block by means of the mounting screws shown in the diagrams.

2.2.2 The Photomultiplier Type and Mounting

The photomultipliers used in HAD 313 were R.C.A. Type 1P28. The 1P28 is a side-window tube with a Cs-Sb cathode and an envelope of Corning 9741 glass which is capable of transmitting ultraviolet. The photomultipliers used in C104, C105 and C1014 were E.M.I. Type 9734QB. The 9734QB is an end-window tube with a CsSbO cathode and a Spectrosil window. This tube

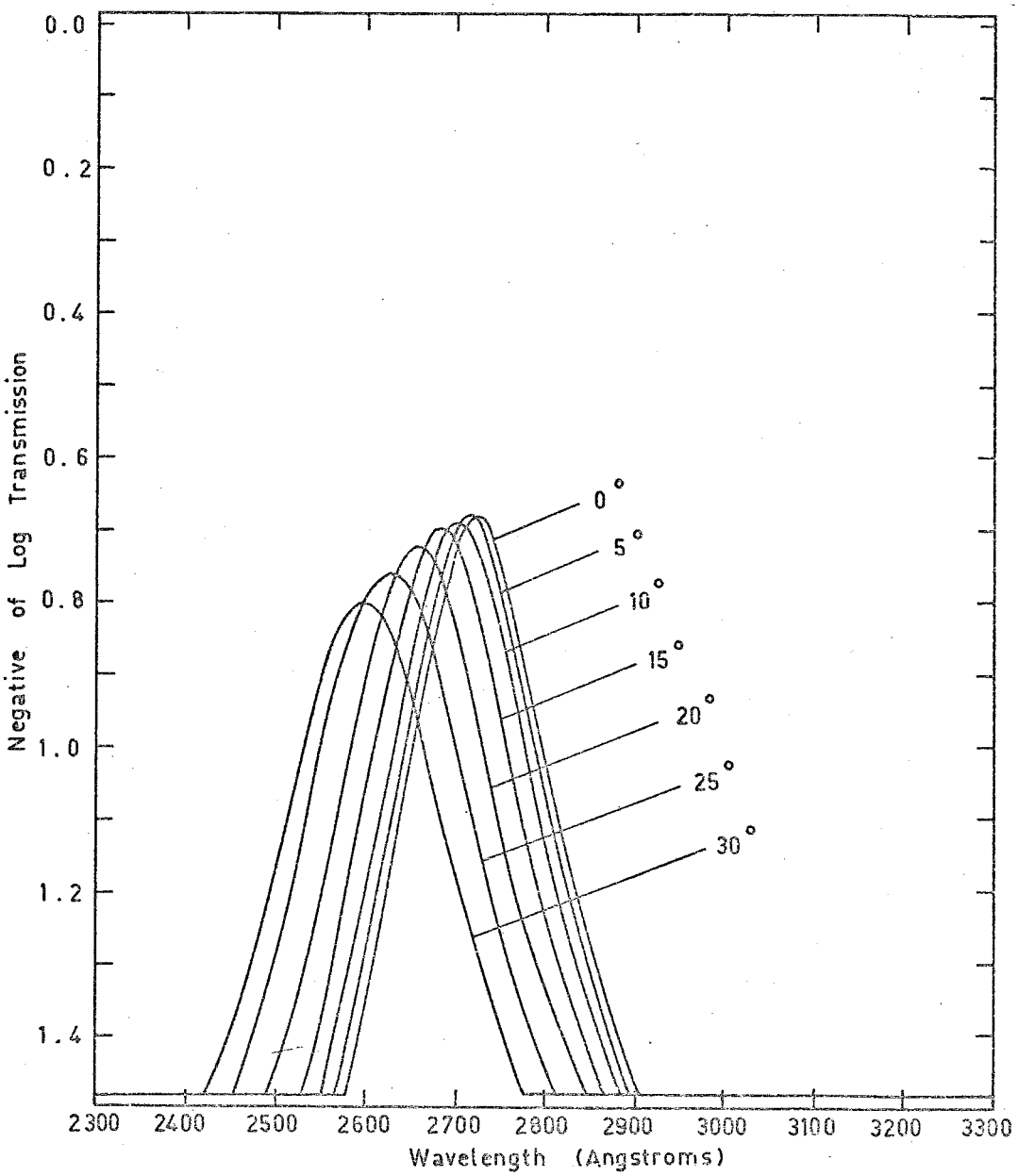

Figure 2.4 Transmission of a 2700 Å filter as a function of angle of incidence. The curves with the attenuator (as in Figs. 2.1, 2.2, 2.3) have been omitted for clarity.

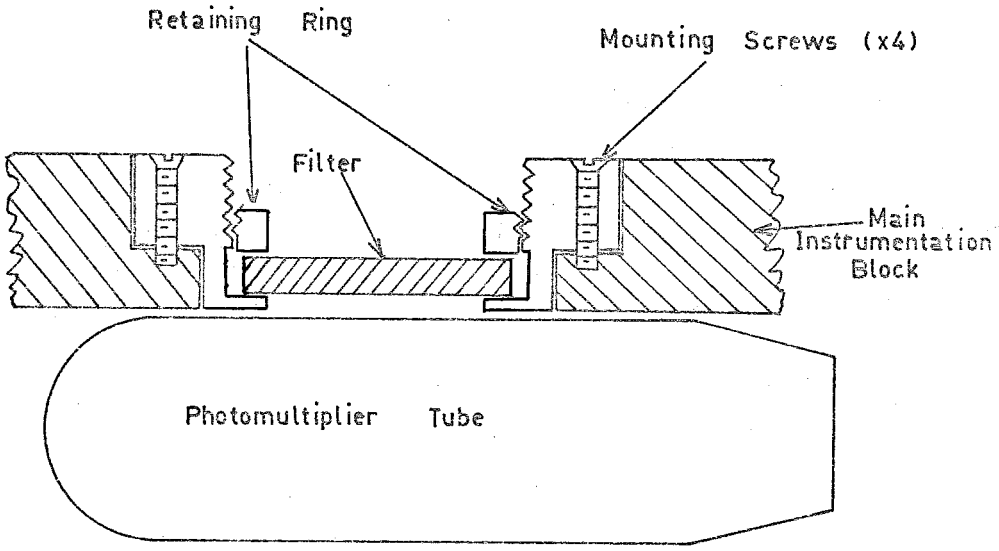

Figure 2.5a Side view of filter mount used on HAD313 (not to scale).

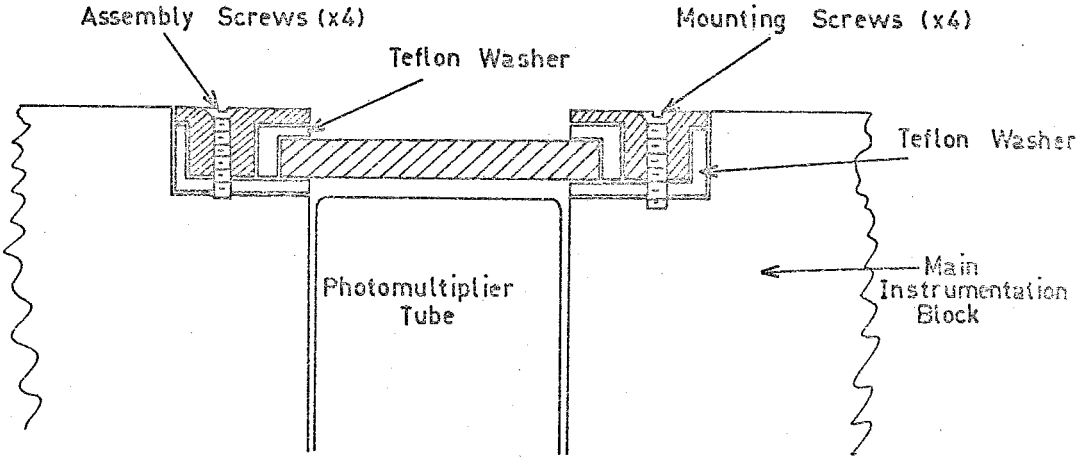

Figure 2.5b Side view of filter mount used on C104, C105 and C1014 (not to scale).

was chosen to replace the 1P28 because of its small physical size (4 inches in length, overall), its better spectral response in the wavelength region of interest, and its better dark current characteristics.

2.3 Electronics

2.3.1 Amplifiers

The amplifiers used on HAD 313 were A.C. amplifiers. These were used to guard against drifts in output voltage levels with change in temperature. To obtain the A.C. condition of output current from the photomultipliers, the signal was modulated by changing the gain of the tube in a periodic way. This was done by varying the potential of one of the dynodes with respect to the value that would exist in a normal D.C. chain. The choice of configuration for the modulation circuit was based on tests carried out by Horton (1968). The circuit for the dynode modulation system is shown in Appendix 2.

The A.C. dynode modulation system and A.C. amplifiers were not used on C104, C105 and C1014 because solid state D.C. amplifiers which were extremely stable with temperature had become available. The use of these D.C. amplifiers also led to simplification of the design of the power supplies and dynode resistor chains used with the photomultipliers.

On HAD 313, C104 and C105 three-stage amplifiers were used to amplify the signals from the photomultiplier tubes. The

first stage had a variable gain which could be adjusted by changing a single resistor, while the second and third stages each had a gain of 10. Each stage had its own output which was monitored by the telemetry system. The wide range of the system was necessary to record the change in signal as the rocket passed upwards through the atmosphere; the results of Carver et al. (1966) showed that the lunar flux should increase by a factor of about 100 during flight. Circuit diagrams, and a description of the operation of these amplifiers, are given in Appendix 2.

On C1014 each photometer was limited to a single telemetry channel so a logarithmic amplifier with a dynamic range of six decades was used. To ensure that heating effects due to the motion of the rocket through the atmosphere did not affect the gain of the amplifier the logarithmic element was mounted on a temperature-controlled oven. The temperature of the oven was kept at 60°C; from data supplied by thermistors carried on previous rockets this was considered to be well above the temperature reached inside the rocket during flight. The circuits for the logarithmic amplifiers and the oven are shown and discussed in Appendix 2.

2.3.2 High Tension Supplies

The high tension voltage for the operation of the photomultipliers was supplied from a D.C. to D.C. converter. The

circuits used for the different rockets are shown in Appendix 2. The output voltage from the power supply was dropped across the resistor chains used to supply the dynode potentials to the photomultiplier tubes. The magnitude of the resistors used in these chains had to be balanced between two requirements. The first was that the chain current had to be some two orders of magnitude higher than the expected signal current, while the second requirement was that the power dissipated in the resistor chains had to be within the tolerance of the transistors used in the power supply. The circuits used for the dynode chains are shown in Appendix 2.

2.3.3 Protection Against Dynode Vibration

Previous vibration tests had shown that the photomultiplier tubes were susceptible to dynode vibration. To minimize the effects of this vibration a simple timing circuit was built into the electronic package. This timing circuit switched on the high tension unit after the second stage motor had finished burning, i.e. when the vehicle was free of vibration.

2.4 The Rocket Vehicles

2.4.1 Description of the Vehicles

The vehicle used for the first flight (HAD 313) was a HAD (High Altitude Density) vehicle, while the vehicle used for later flights was the COCKATOO vehicle. Both types of vehicle

were provided by the Australian Department of Supply. They are both two stage vehicles, each stage having solid fuel motors, both burning for approximately 3 seconds with burnout of the second stage occurring approximately 25 seconds after launch at an altitude of about 20 kilometres. The second stage is partially spin stabilized by the action of fins but no other form of stabilization is provided. The only difference between these two vehicles is that the COCKATOO uses a larger first stage motor which increases the altitude capability of the vehicle.

2.4.2 Distribution of the Payload

The instrumentation head consists of four main sections which are listed below

a) Telemetry
b) Sensors
c) Acquisition aid
d) Firing and timing

Sections c) and d) were part of the rocket itself and were associated with the firing and subsequent radar tracking of the vehicle. The telemetry system was a W.R.E. 465 system. This consisted of a switch motor which was a 24 pin head with a wiper arm which rotated at 80 revs/sec. The voltages, from the different sensors and monitoring circuits, which appeared on each of the 24 pins were sampled in turn by the wiper arm and were applied to a voltage controlled oscillator which

varied between 130 kHz and 160 kHz as the voltage from the wiper arm varied between 0 and 1.5 volts. This frequency modulated signal then amplitude modulated a 465 MHz power oscillator which fed two quarter-wave dipoles for transmission to a ground receiving station.

Section b) carried the photomultipliers; for HAD 313 the tubes were mounted across the section, to one side of the axis, such that the photocathodes were as close to the surface of the rocket as the length of the tube allowed. A filter mount was in front of each photocathode and was screwed to the inner instrument casing. For C104 and C105 the photomultipliers were mounted diametrically across the section with the filter mount in front of the photocathode. The arrangements used for the two different types of photomultiplier tubes are shown in Figures 2.6a and 2.6b. The complete assembly for C105 is shown in Figure 2.7.

The general layout of the instrumentation section is shown in Figures 2.8 and 2.9.

For C1014 the telemetry section was moved to the rear to allow a special experiment to be placed well forward in the round.

All the power necessary for the operation of the electronics associated with the sensors was supplied from batteries. For HAD 313, C104 and C105 the batteries were mounted below the sensors while for C1014 the batteries were mounted right in the nose cone.

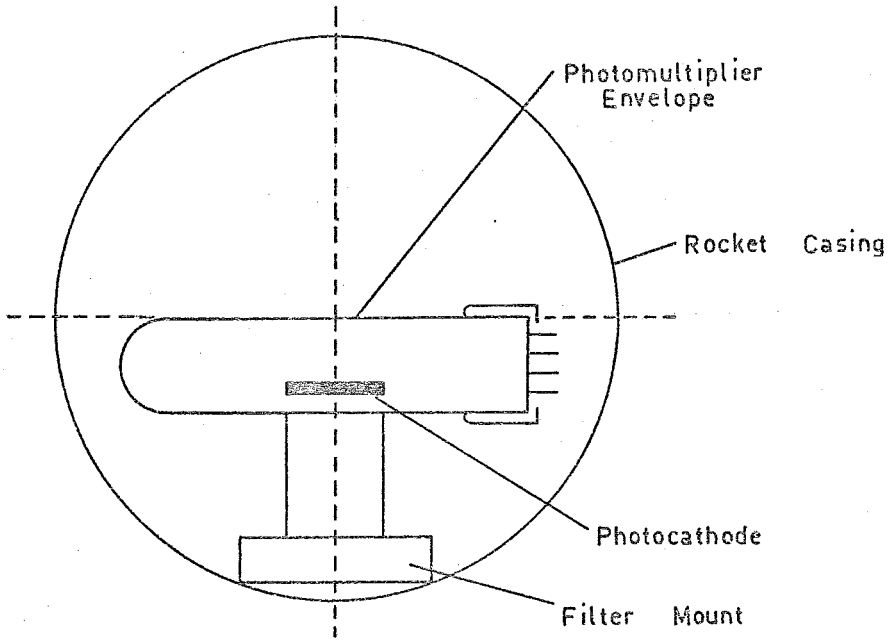

Figure 2.6a Layout for IP28 photomultipliers in HAD313.

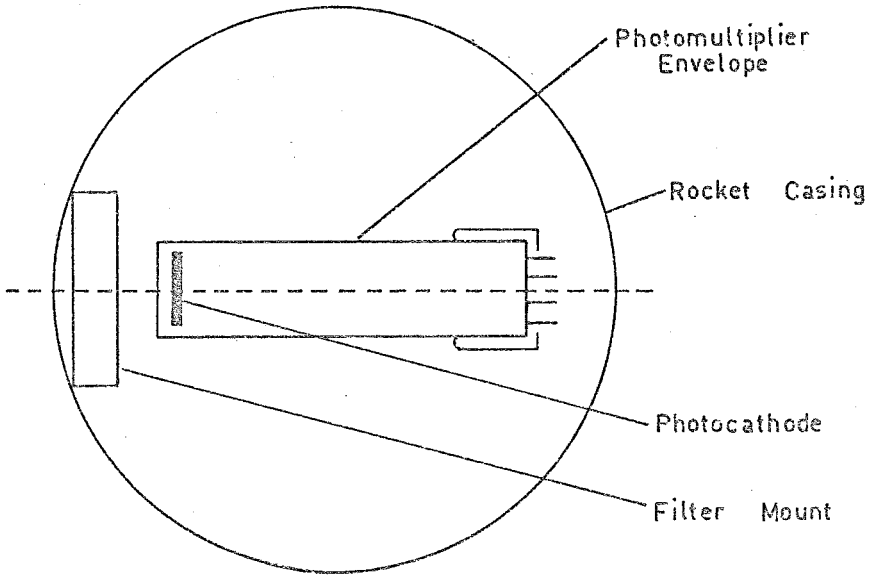

Figure 2.6b Layout for 9734QB photomultipliers in C104 and C105.

FIGURE 2.7 The complete experimental package for C105

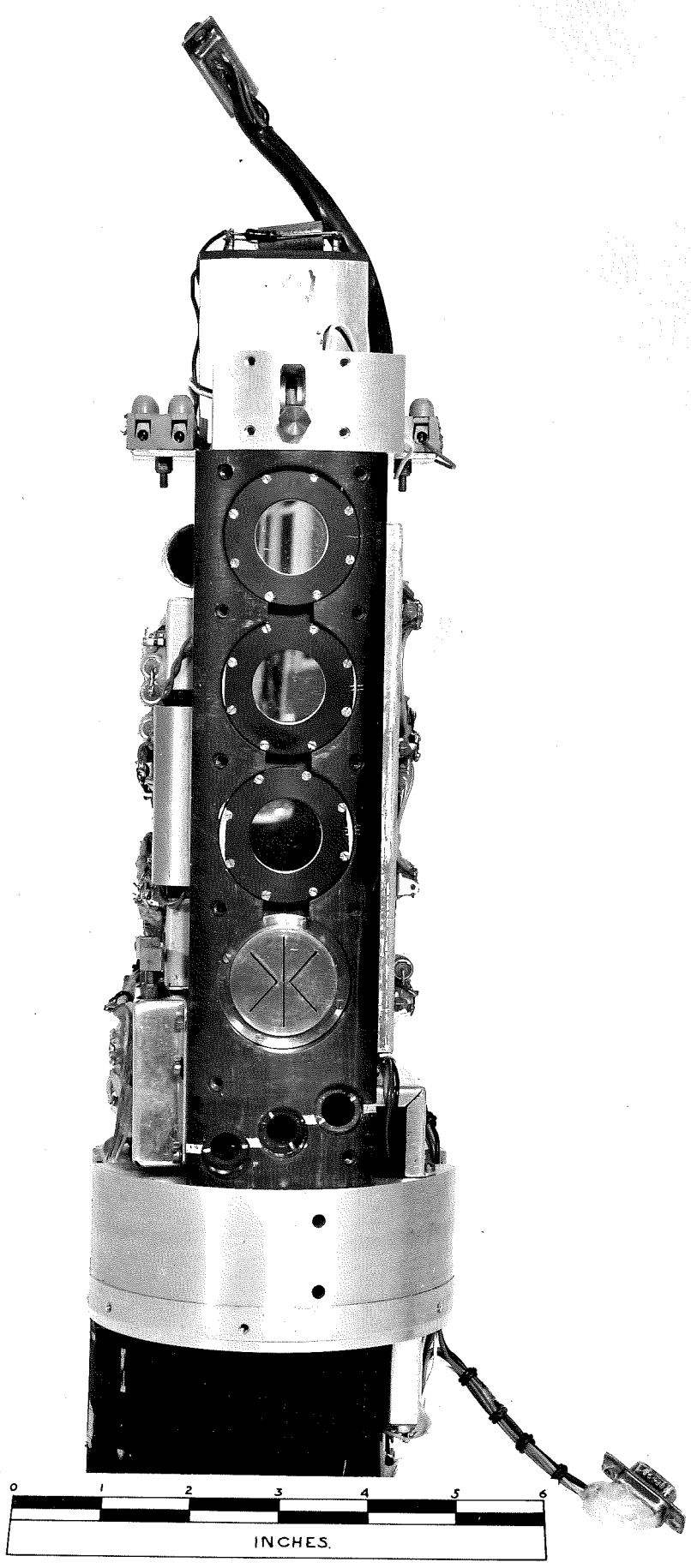
0
1
2
3
4
5
6
INCHES.

FIGURE 2.8 A typical HAD instrumentation head, showing distribution of the payload

a - Telemetry
b - Sensors
c - Acquisition aid
d - Firing and timing

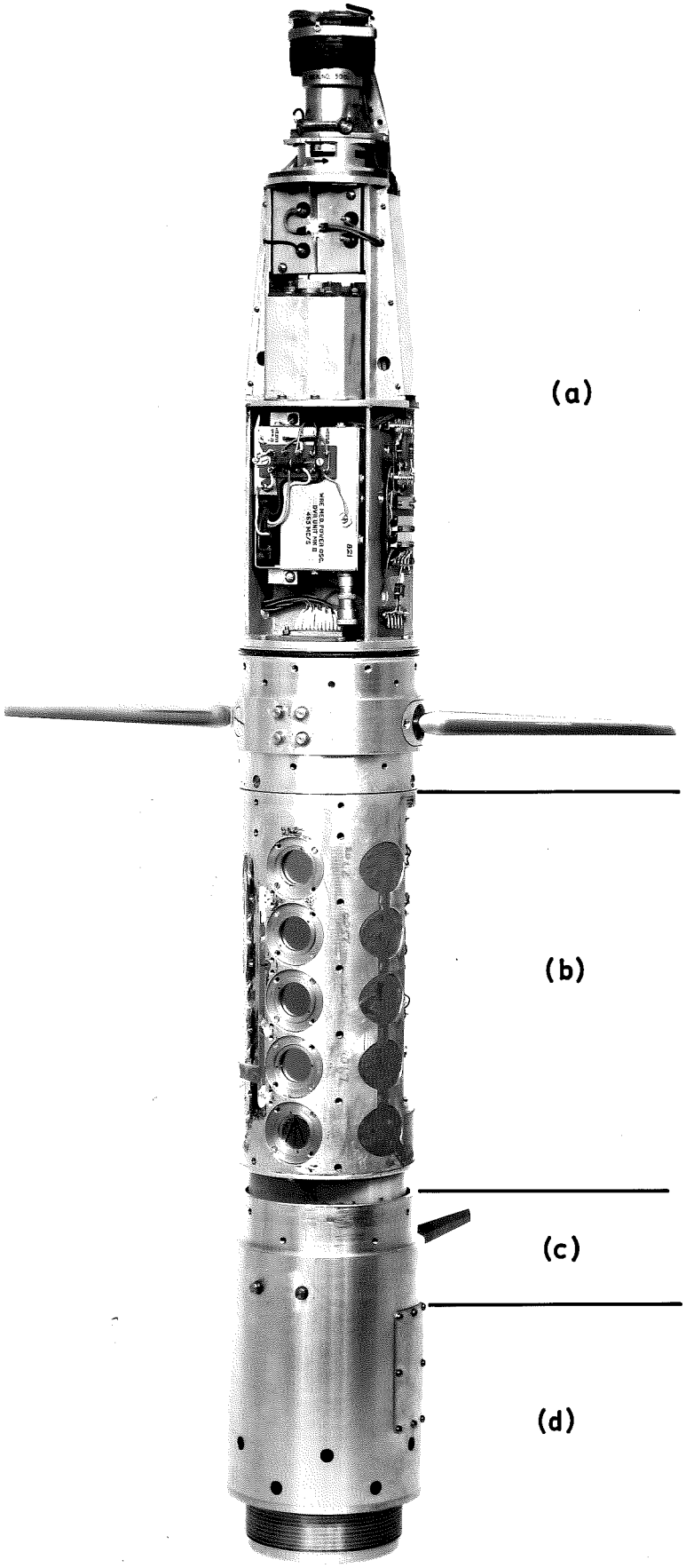
(a)
(b)
(c)
(d)

FIGURE 2.9 Complete instrumentation head of an HAD rocket vehicle

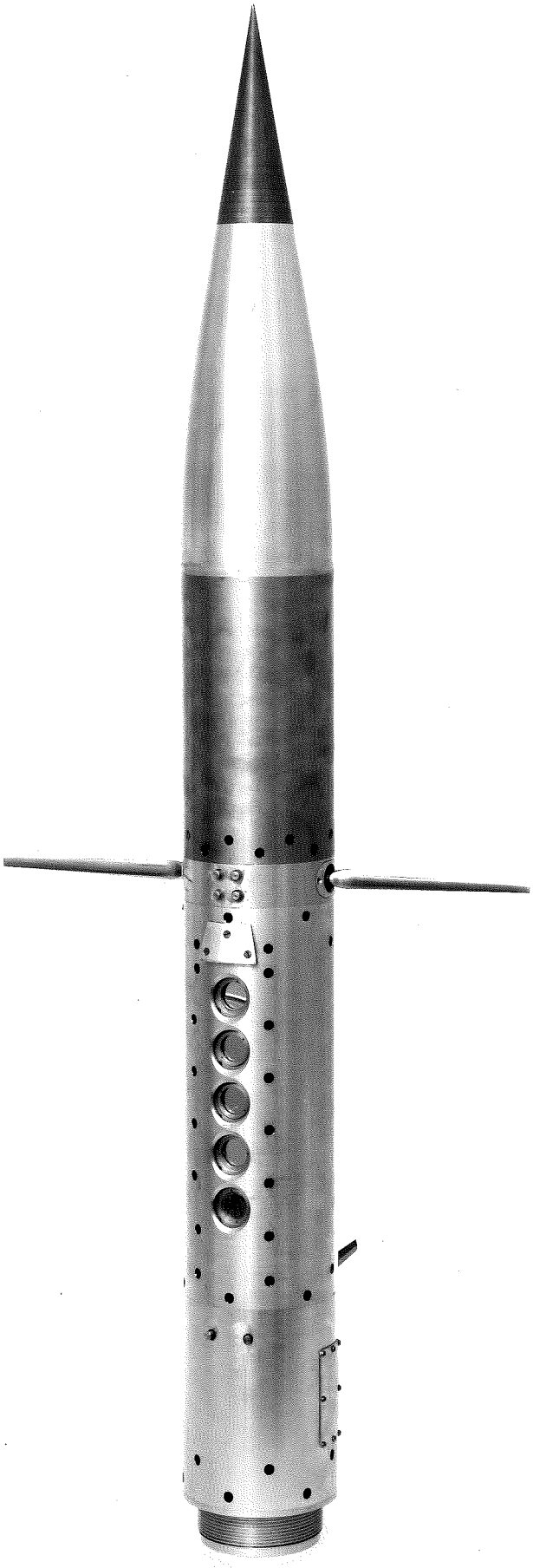

All photomultipliers and their associated electronics were potted in Dow Corning Silastic 850RTV Rubber, both as a protection against mechanical shock and for electrical insulation.

2.4.3 Pre-flight Checks of Equipment

The main pre-flight checks consisted of two parts. The electronic circuits and dynode chains, after being potted, were checked under vacuum to ensure that no corona discharge occurred. If this had occurred it was known, from previous tests, that a marked change in the current drain of the appropriate power supply would occur, enabling the fault to be detected and corrected.

The second test was a sensor and telemetry check, carried out using the facilities of the Weapons Research Establishment of the Department of Supply. The complete head was operated and the telemetry received at a remote station. Operation of all sensors and monitoring circuits was checked and checks were made of the channel allocations and the efficiency of the voltage limiting circuits. This latter check was also carried out at the Woomera range and also as part of the immediate pre-launch sequence.

2.5 Calibration of the Flight Photometers

2.5.1 Calibration of HAD 313

The two photometers were calibrated using the system shown

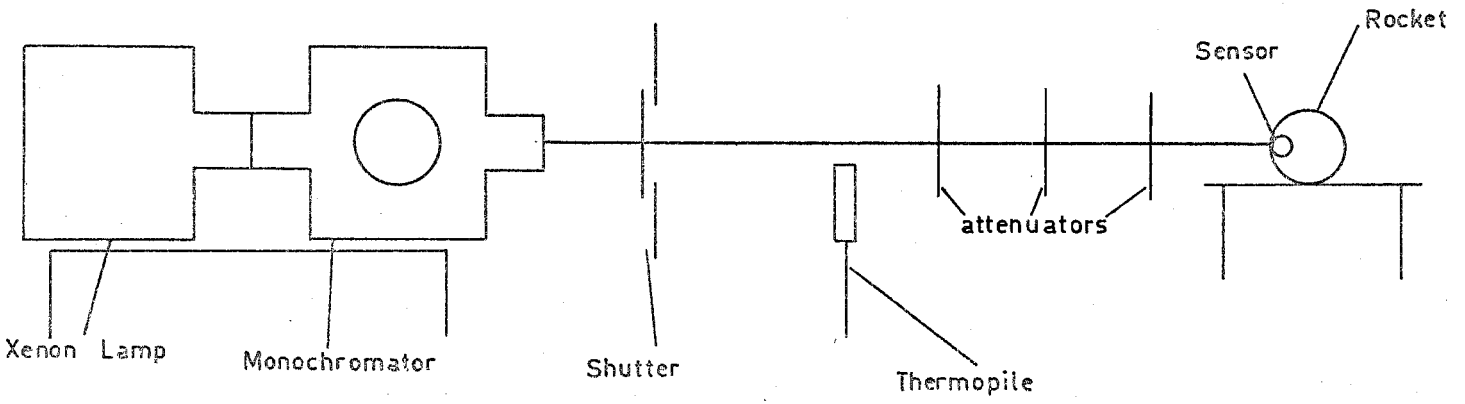

Figure 2 . 10 Calibration system for HAD313 photometers.

in Figure 2.10. The light source used was a Bausch and Lomb Xenon lamp. The beam was passed through a Bausch and Lomb monochromator and the exit slit of the monochromator was taken as the source.

The detector to be calibrated was mounted at a distance of 200 cms from the source and the Reeder thermopile at a distance of 25 cms from the source in such a way that enough of the beam passed the thermopile to fully illuminate the sensor. To test for uniformity across the beam the thermopile was first moved into the part of the beam that would by-pass it during calibration. The beam was found to be uniform to within ten per cent. Since the intensity of the beam at the detector was still too high three Perkin Elmer attenuators with a total transmission of 4×10^{-5} were placed in the beam as shown; the positions chosen were such that the diffraction patterns of the attenuators were smoothed out before the beam reached the next attenuator or the detector. One of the attenuators was removed for calibration of the 2500Å detector to give a total transmission of 5×10^{-4}.

The set of slits used on the monochromator gave a pass band of 110Å. The centre wavelength was changed in steps of 50Å and the output of the detector was recorded as a function of wavelength, together with the thermopile reading at that wavelength. A curve of output voltage versus incident flux was then plotted for each detector. The total sensitivity of

each detector was found from this response curve by measuring the area under the curve and dividing by the full-width-half maximum of the response curve. The curves obtained for HAD 313 are shown in Figure 2.11. The sensitivities of the detectors flown in HAD 313, calibrated as stated above were as listed below. The error applied to these calibrations was 20 per cent.

Wavelength at Centre	Sensitivity of First Stage
2450	.040 volts/10^{-6} ergs/an^2/sec/Å
2780	.047 volts/10^{-6} ergs/an^2/sec/Å

2.5.2 Calibration of C104

The calibration system used for HAD 313 had several disadvantages. One of these was that the thermopile was not protected from any draughts caused by movement of the experimenter. Another was that the Perkin Elmer attenuators used to attenuate the beam incident on the detector produced pronounced diffraction effects which could only be overcome by placing the attenuators a long way apart. In addition the Xenon discharge lamp used as a light source frequently changed its intensity and this required regular checking, which, because the thermopile and detector were some 2 metres apart was most inconvenient because, as already mentioned, any movement affected the thermopile.

To overcome these problems the system shown in Figures

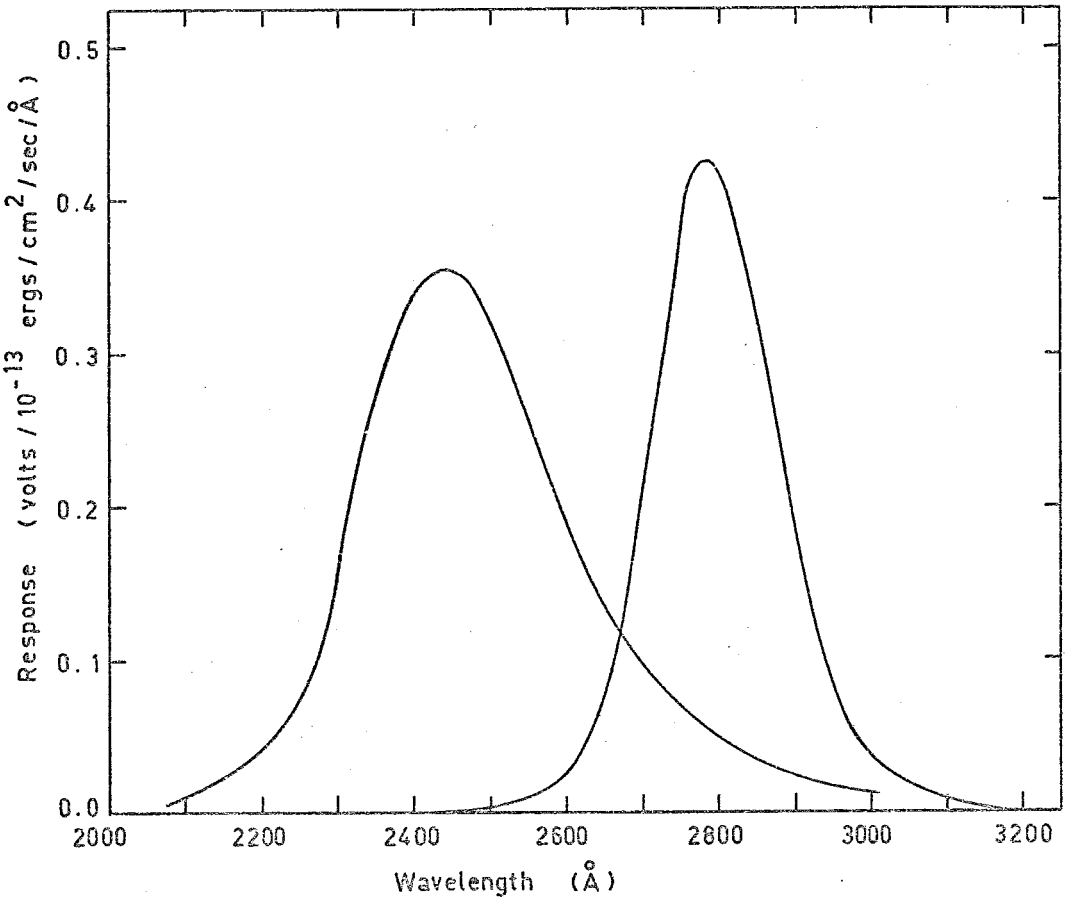

Figure 2.11 Spectral responses of detectors flown in HAD 313.

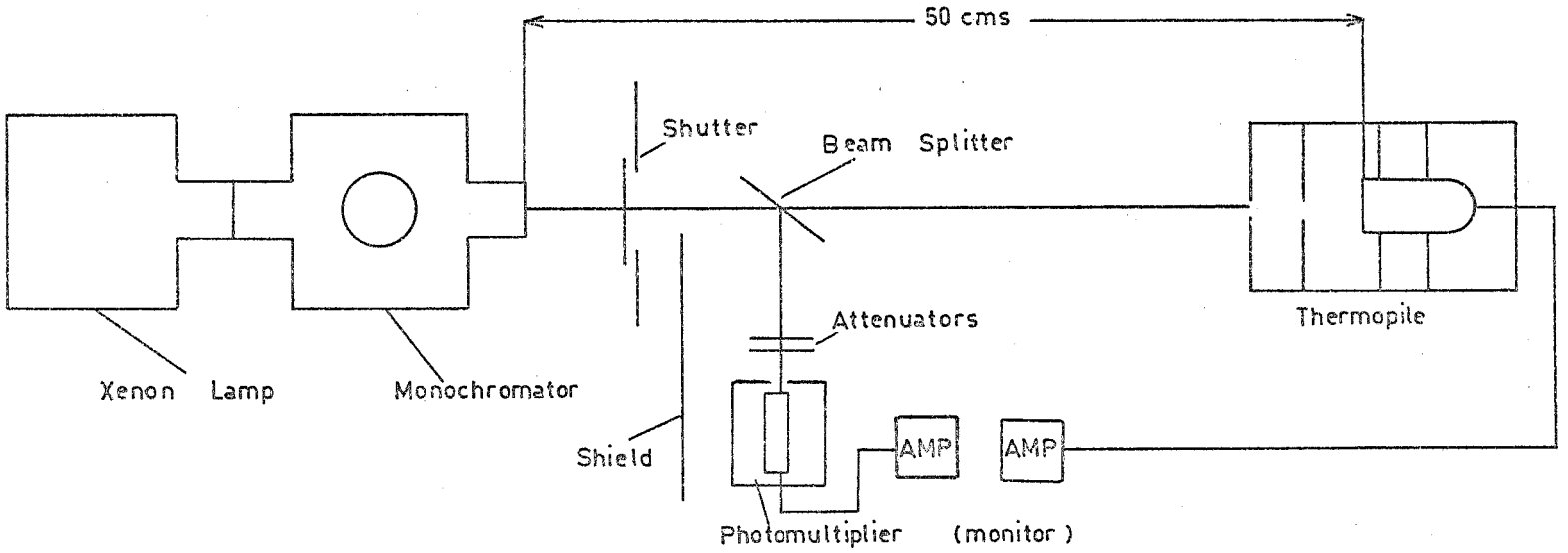

Figure 2 . 12 a First stage of calibration procedure for C104.

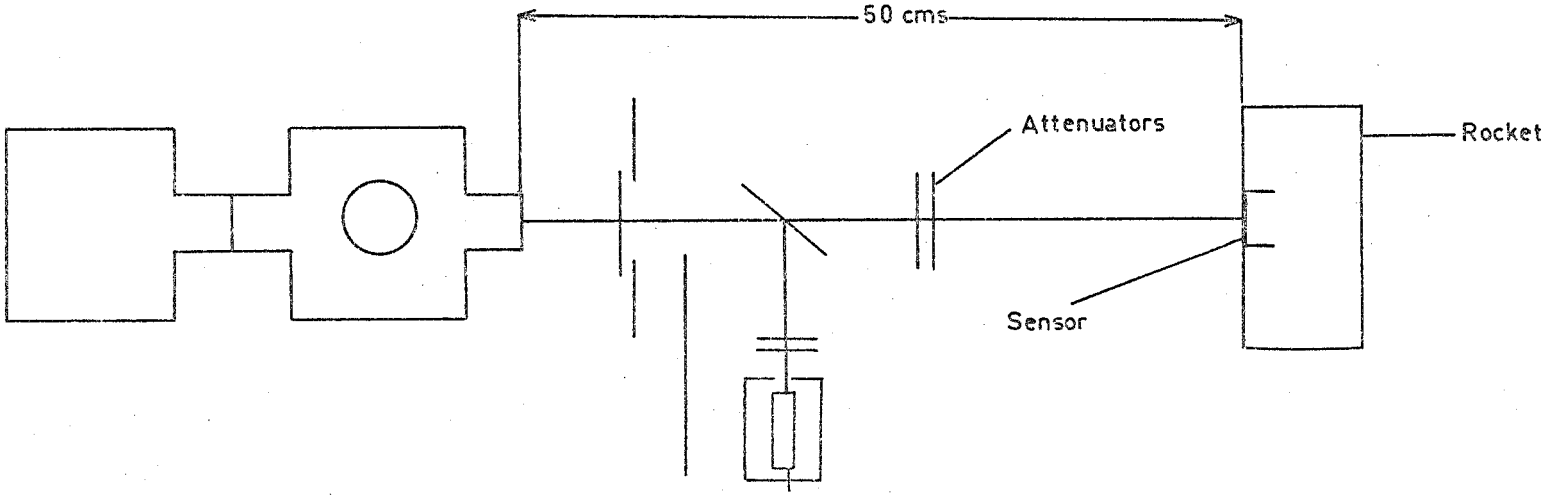

Figure 2 . 12 b Second stage of calibration procedure for C 104 .

2.12a and 2.12b was used for the calibration of C104. The lamp source and monochromator were the same as before, but the attenuators used were neutral density filters made in our laboratory. These consisted of 2" diam. Spectrosil plates coated with thin nichrome films. The transmission characteristics of these attenuators were measured on the Perkin Elmer spectrophotometer; a graph of log absorbance against wavelength for several of these filters is shown in Figure 2.13. To minimize the effects of draughts on the thermopile, the thermopile was mounted in a metal box, painted black on both inside and outside, containing a series of baffles, also painted black, to minimize air movement within the box. This system also had the advantage that it was much more compact than the old system and required a minimum of movement on the part of the observer.

The first stage of the calibration procedure consisted of calibrating the photomultiplier (E.M.I. Type 9734QB) by means of the thermopile. Once this tube was calibrated the thermopile was replaced by the rocket-mounted sensor, suitable attenuators were placed between the beam splitter and the sensor and the sensor was calibrated using the previously calibrated tube as a beam monitor. The response of the detector was calculated in the same way as for HAD 313. The curves obtained for C104 are shown in Figure 2.14. The sensitivities of the detectors flown in C104 are listed below. An error of 20 per cent was applied to these values.

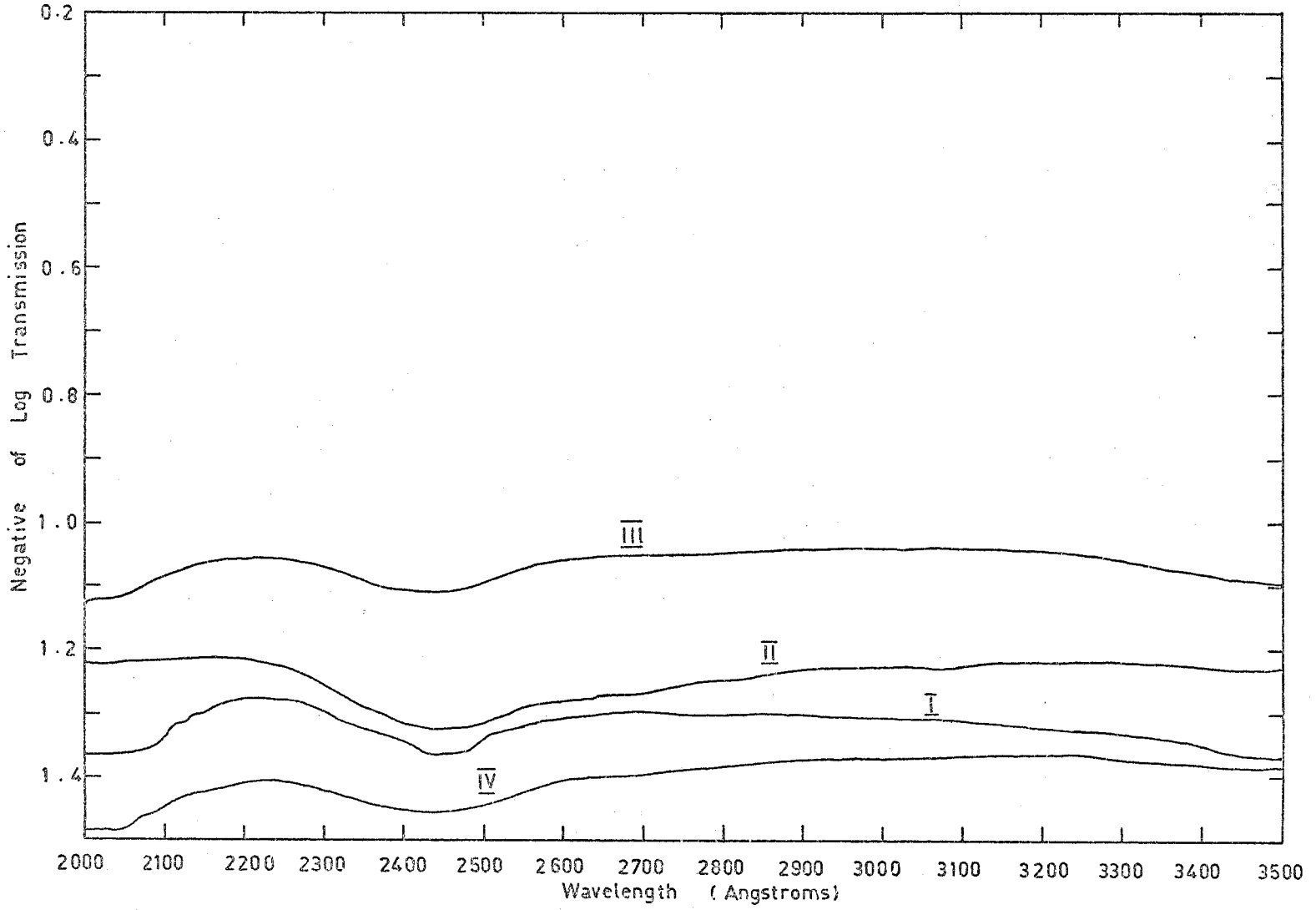

Figure 2.13 Transmission of neutral density filters used in calibrating C104. Attenuator zero for I and II was 1.4 and for III and IV was 2.0. The value of the curve shown should be added to the value of the appropriate attenuator zero.

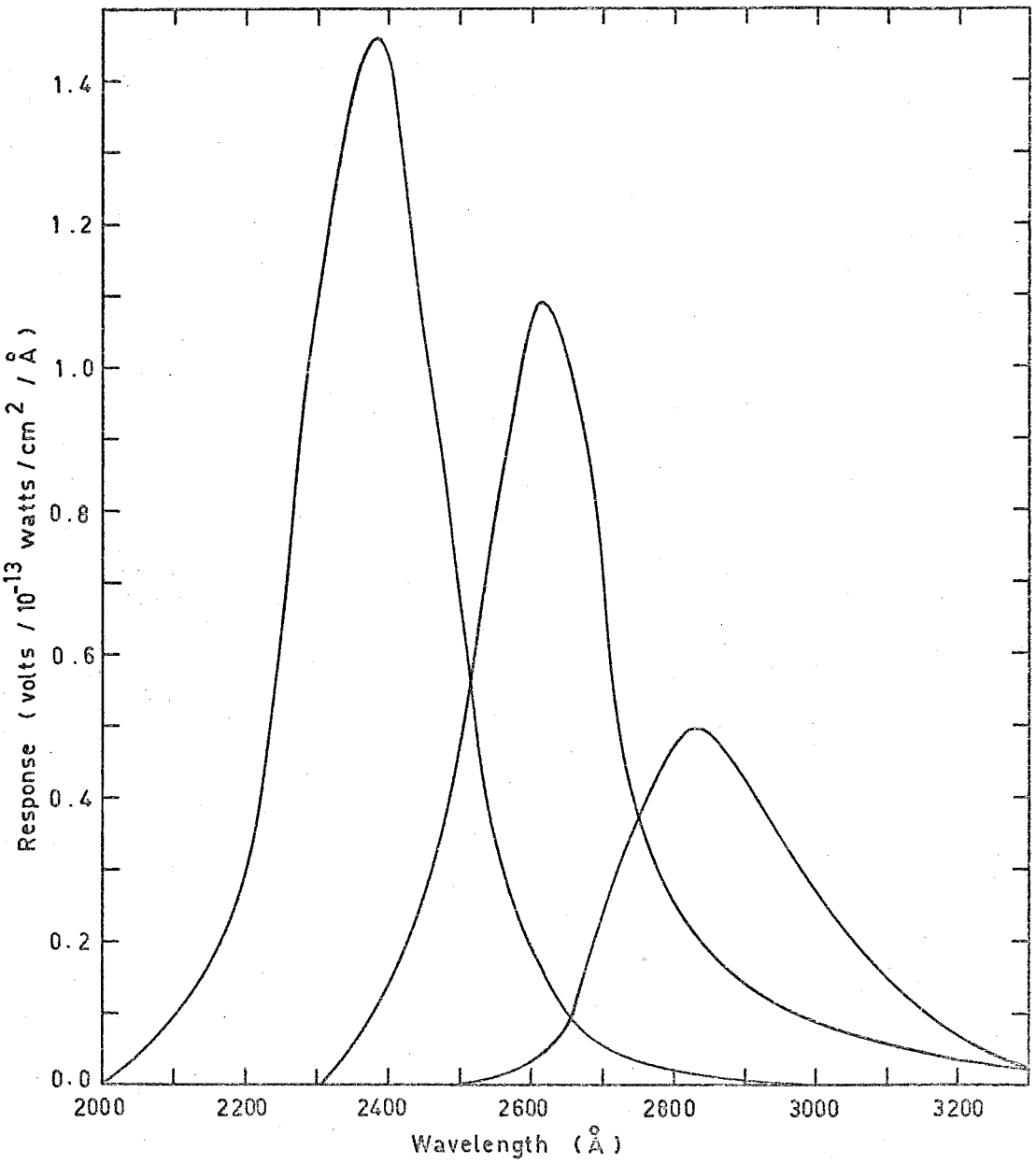

Figure 2.14 Spectral responses of detectors flown in C104.

Wavelength at Centre	Sensitivity of First Stage
2380	1.58 volts/10^{-6} ergs/cm^2/sec/Å
2620	1.43 volts/10^{-6} ergs/cm^2/sec/Å
2835	.54 volts/10^{-6} ergs/cm^2/sec/Å

2.5.3 Calibration of C105

The calibration system used for C105 was the same as that used for C104. The neutral density filters were all rechecked in case their transmissions had changed in the five months between the two rounds. In most cases a slight increase in transmission was observed. The spectral responses for the detectors flown in C105 are shown in Figure 2.15.

The sensitivities of the detectors flown in C105 are listed below. Again an error of 20 per cent was applied.

Wavelength at Centre	Sensitivity of First Stage
2410	.153 volts/10^{-6} ergs/cm^2/sec/Å
2620	.852 volts/10^{-6} ergs/cm^2/sec/Å

2.5.4 Calibration of C1014

The system used was the same as for C104 and C105 - the neutral density filters were again checked (see Figure 2.16). The data reduction in this case was a little more difficult because of the log amplifiers used but was carried out as follows:- the voltage output of each amplifier was equal to the logarithm of the output current from the corresponding photomultiplier, i.e.

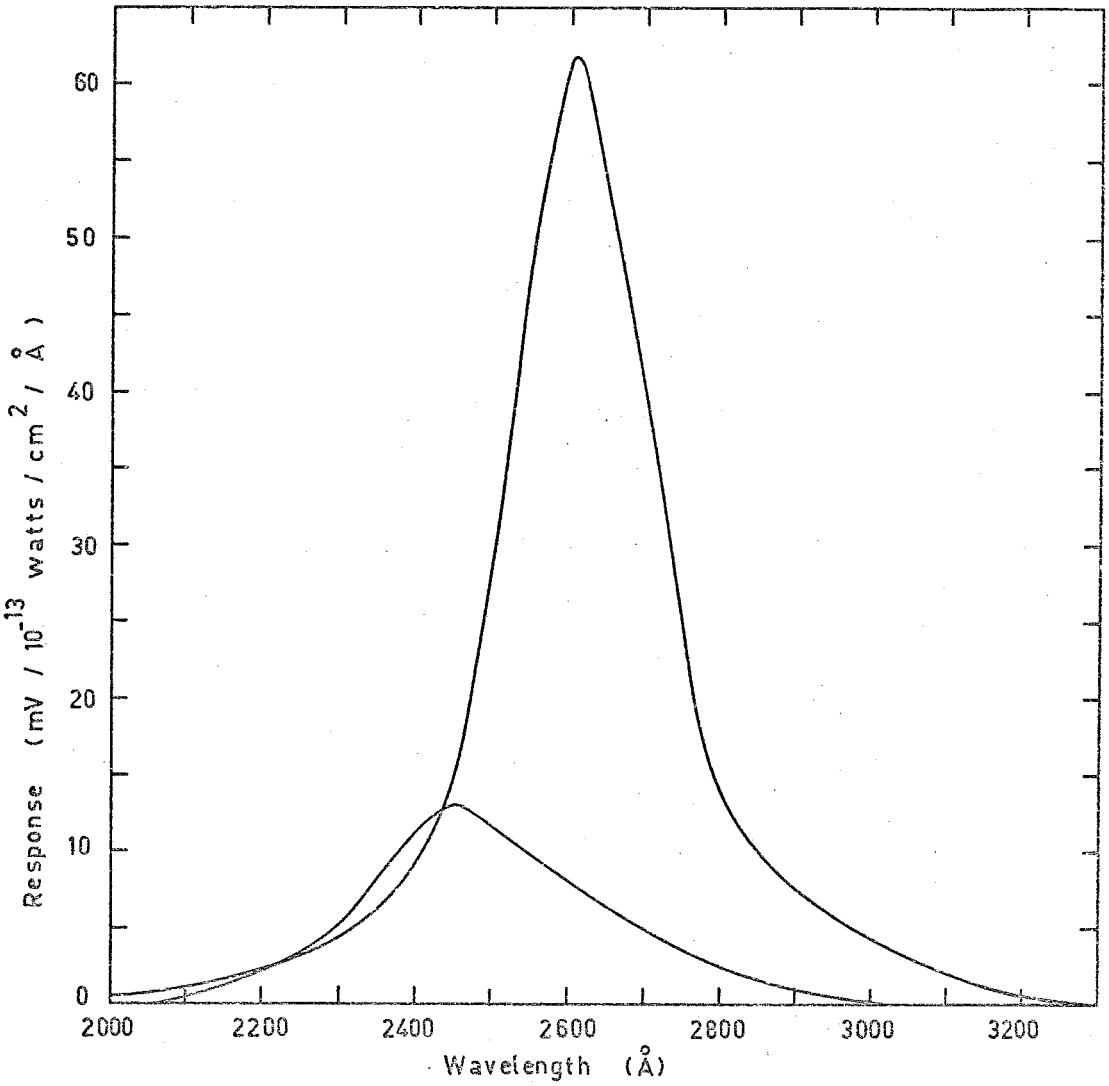

Figure 2.15 Spectral responses of detectors flown in C105.

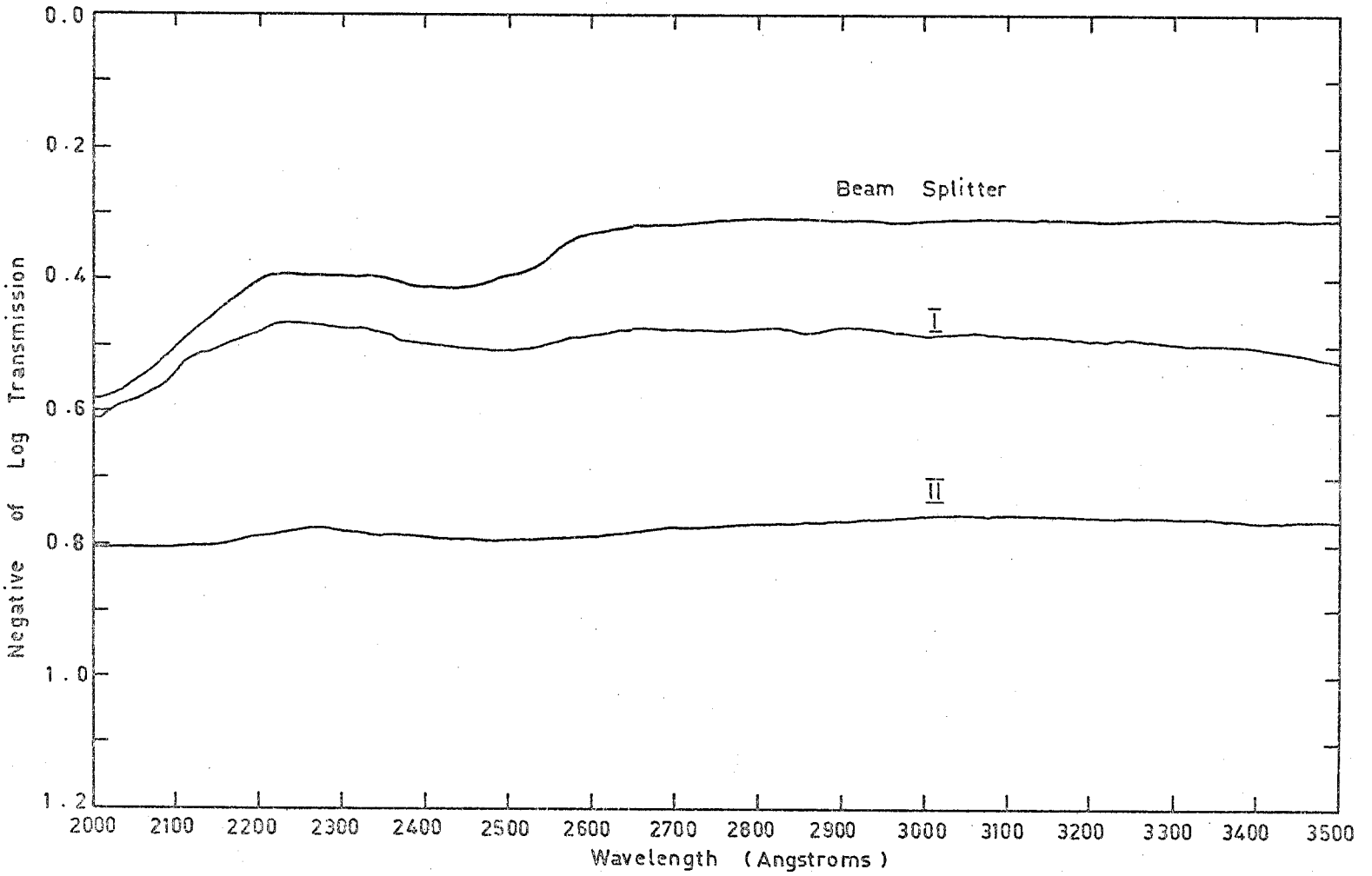

Figure 2.16 Transmission of neutral density filters used in calibrating C1014. Attenuator zero for I was 2.0 and for II was 1.4. The value of the curve shown should be added to the appropriate attenuator zero.

$$V = \log i \qquad \ldots (2.1)$$

If V_B is the output voltage with the shutter (see Figure 2.12b) closed and V_S is the voltage with the shutter open, then it can be shown that the signal current corresponding to a radiation flux F is given by

$$i = 10^{V_S} - 10^{V_B} \qquad \ldots (2.2)$$

The response curves for the detectors were plotted by dividing the output current given in (2.2) by the incident flux. The resulting response curves are shown in Figure 2.17. The total sensitivities were then found by evaluating the total area under each curve and dividing by the full width half maximum of the corresponding response curve. The total sensitivities are shown below:-

Wavelength at Centre	Sensitivity
2410	1.25×10^{-6} amps/10^{-13} watts/cm^2/Å
2590	0.39×10^{-6} amps/10^{-13} watts/sm^2/Å

An error of 20 per cent was also applied to these values.

2.6 Aspect Correction

As the angle between the normal to the sensor and the sensor-source line was expected to vary during the flight the angular response of each sensor was determined. For all four rounds this was done by mounting the instrumentation package,

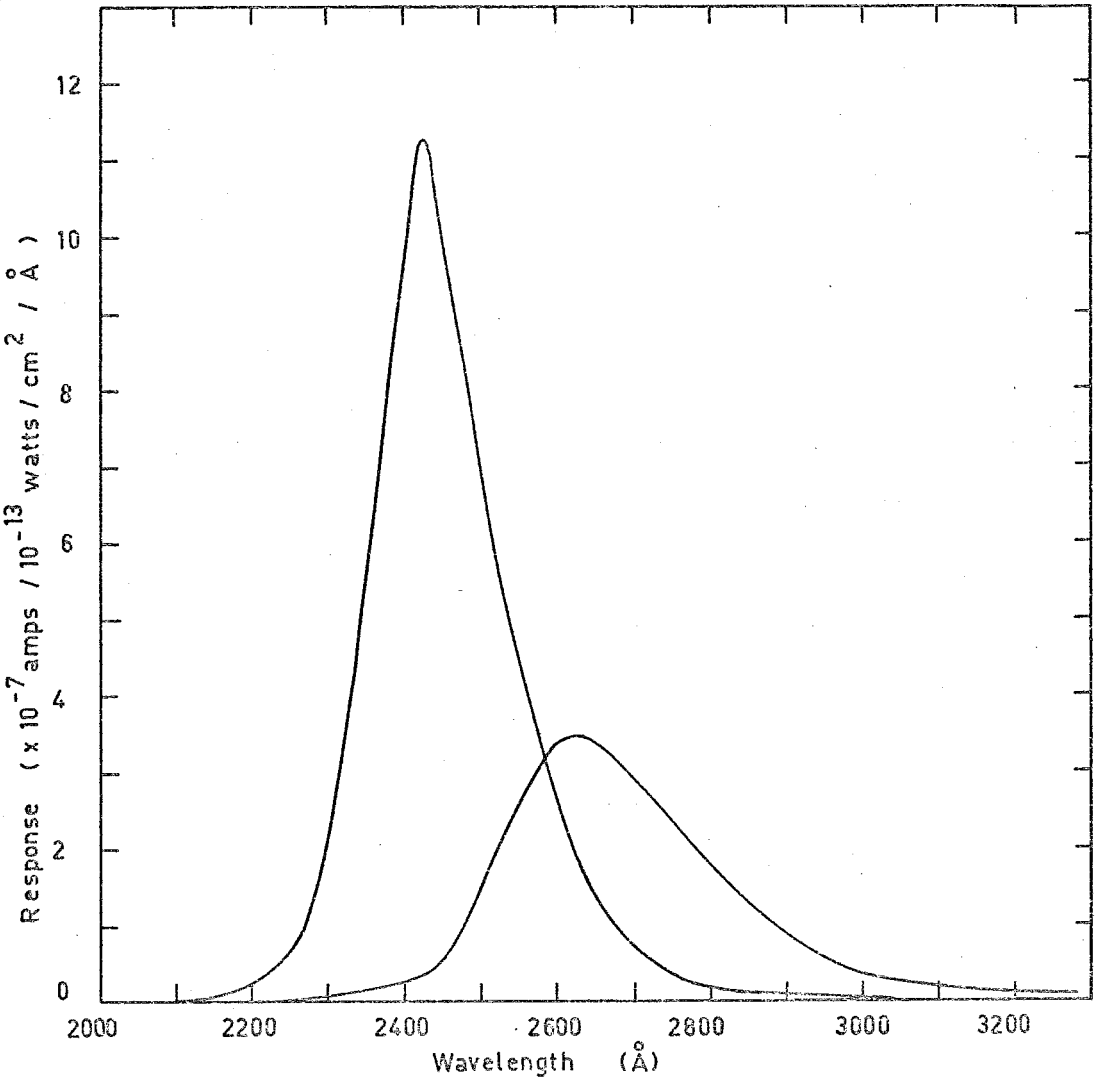

Figure 2.17 Spectral responses of detectors flown in C1014.

with its axis horizontal, on a table which was free to rotate in a horizontal plane, in such a way that the front of the detector was directly above the axis of the table (see Figure 2.18). The sensor was illuminated by a Bausch and Lomb Xenon lamp and the zero position was found by reflecting the incident light from the surface of the interference filter and adjusting the position of the instrumentation package until the reflected beam fell squarely on the exit aperture of the lamp. As the intensity of the radiation was too high it was reduced by using a suitable attenuator; in the case of HAD 313 this consisted of several Perkin Elmer attenuators arranged as described in Section 2.5.1, while for C104, C105 and C1014 it consisted of several neutral density filters of the type described in Section 2.5.2.

The output of each detector was recorded as a function of angle in the horizontal plane; while the table was rotating the shutter was opened and closed with a frequency of about 1 Hz to check that the background radiation did not change appreciably with angle. The results of these measurements are plotted out in Figs. 2.19, a,b,c,d,e,f,g,h,i.

2.7 Design and Calibration of Aspect Sensors

The variation of sensor response with aspect angle required that this angle be measured in flight. The aspect sensor used in HAD 313 is shown in Figure 2.20. To improve

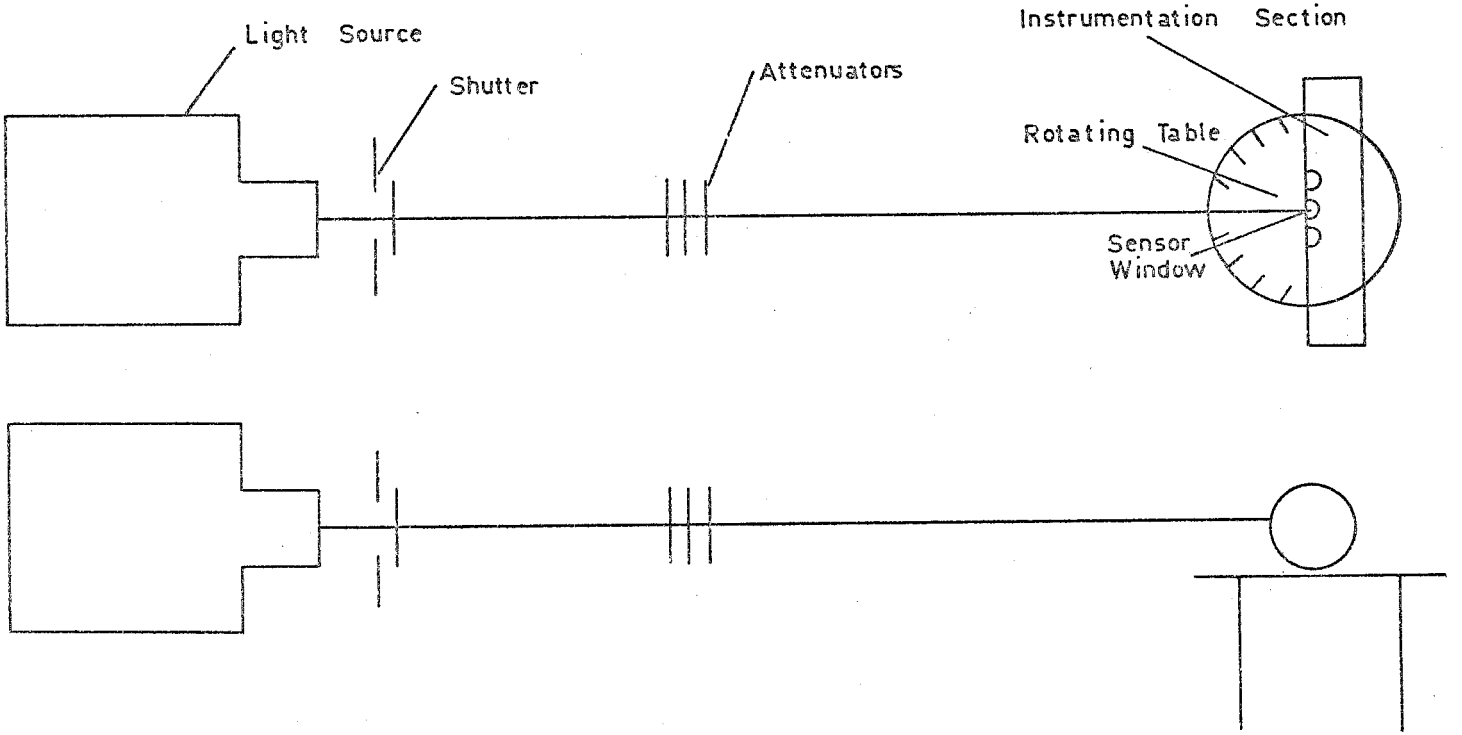

Figure 2.18 Diagram of method of measurement of angular response of detectors.

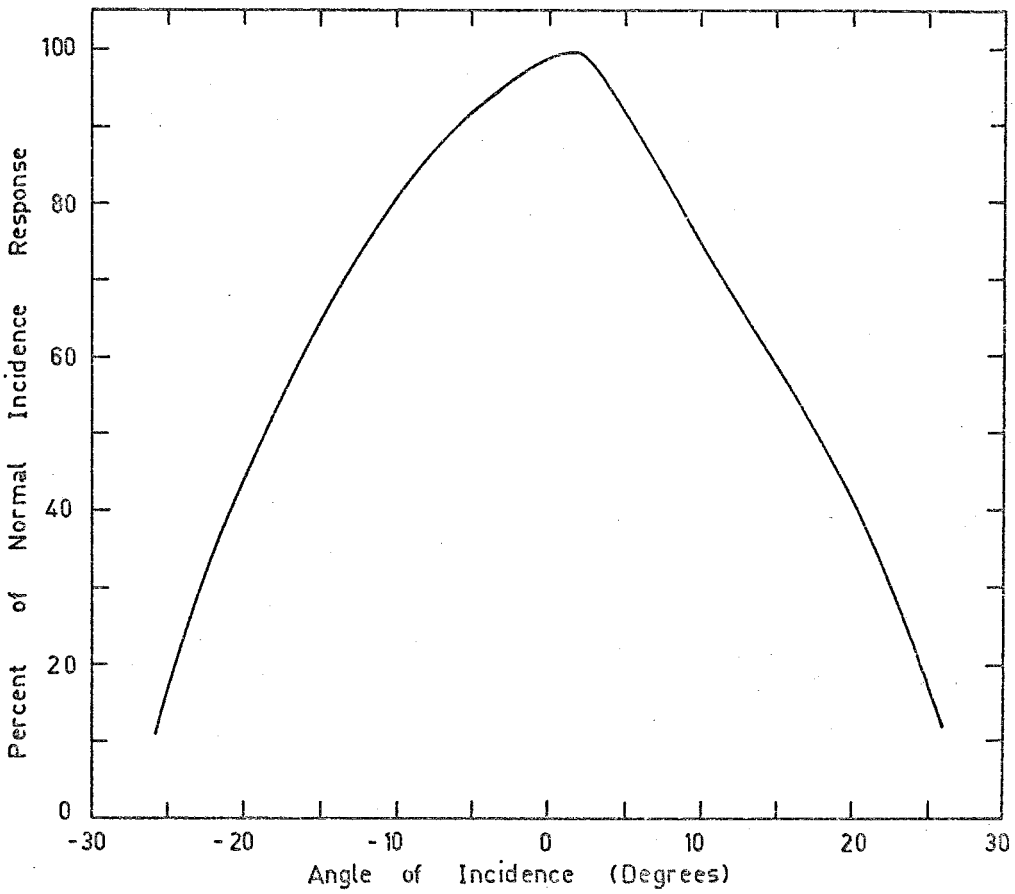

Figure 2 . 19 a Angular response of 2500 Å sensor in HAD313.

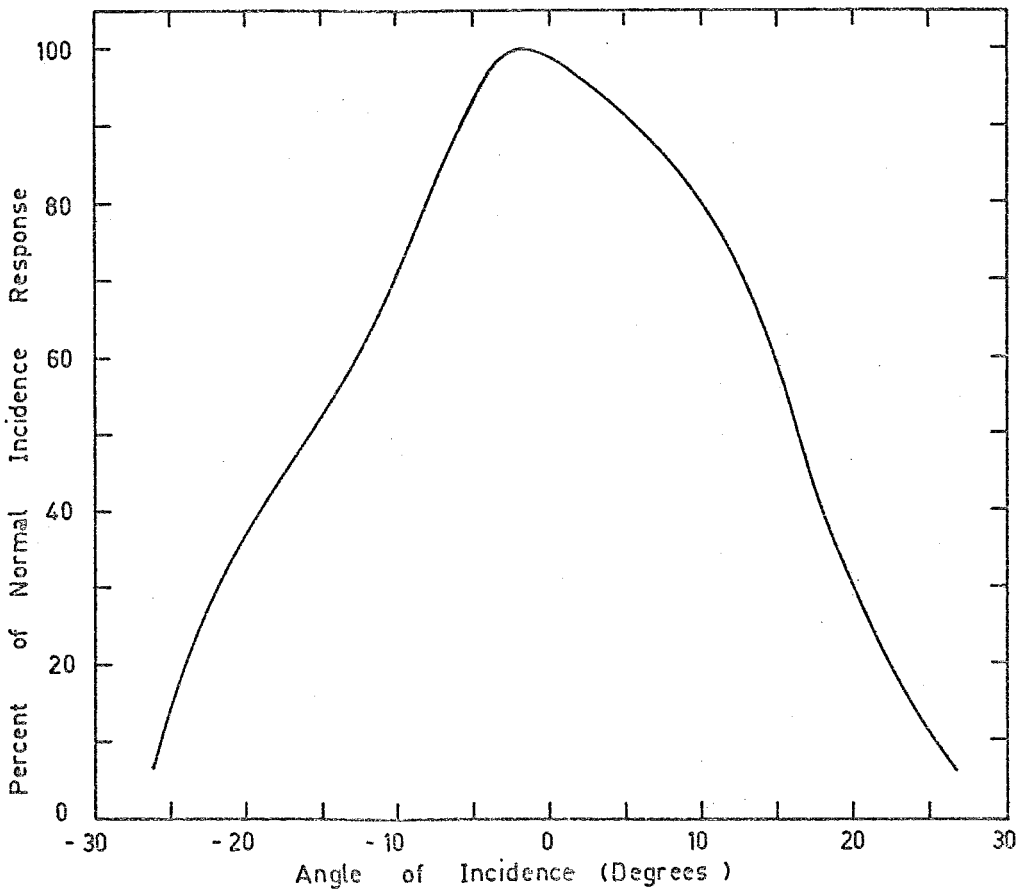

Figure 2 . 19b Angular response of 2900Å sensor in HAD313.

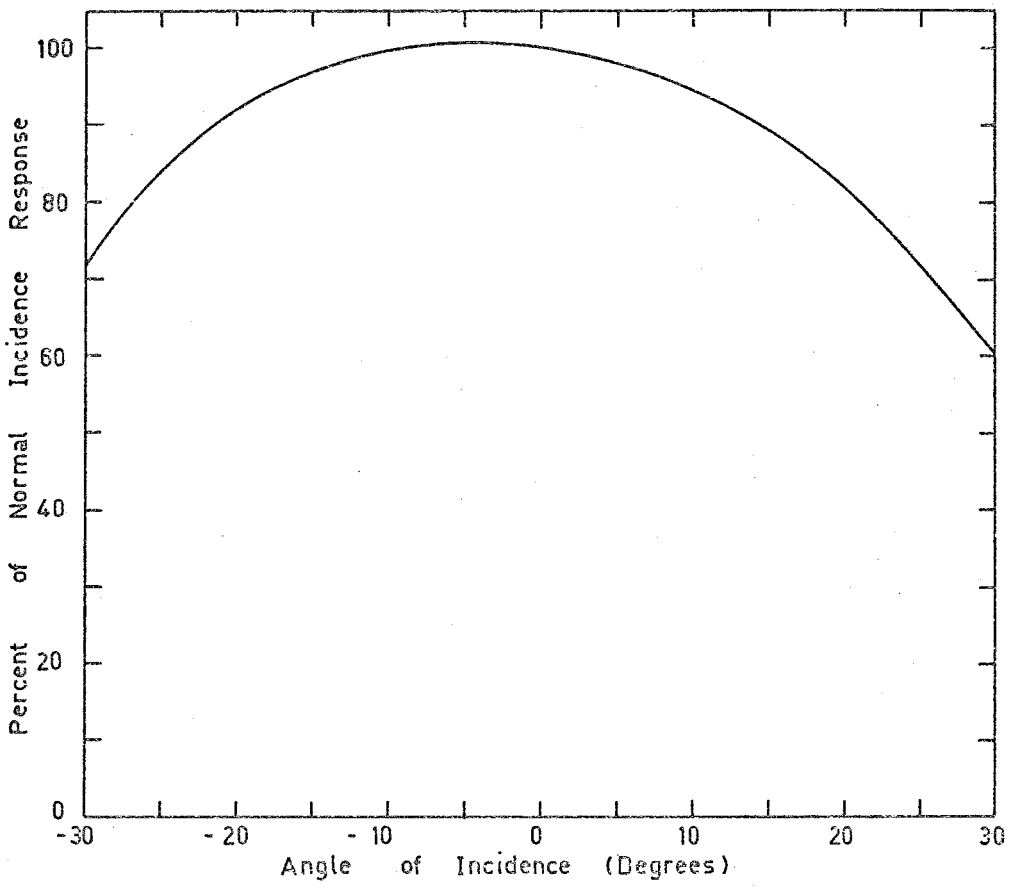

Figure 2 . 19 c Angular response of 2500Å sensor in C104 .

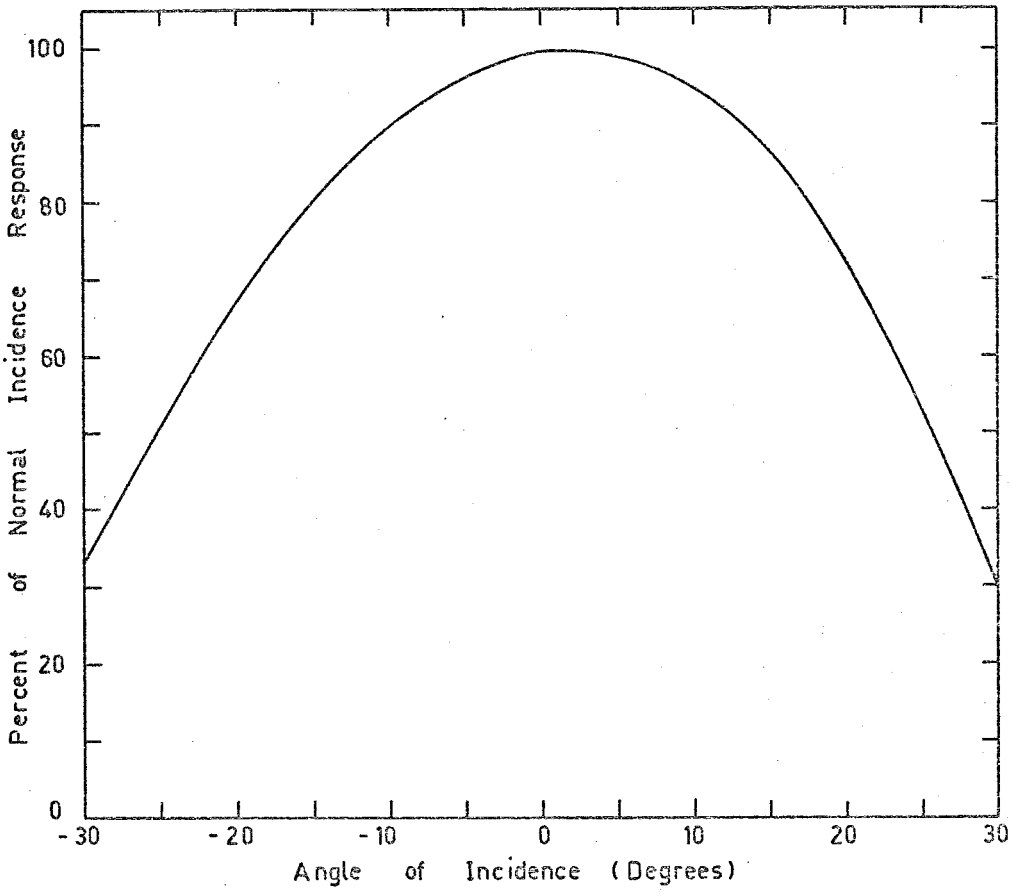

Figure 2 . 19 d Angular response of 2700 Å sensor in C104.

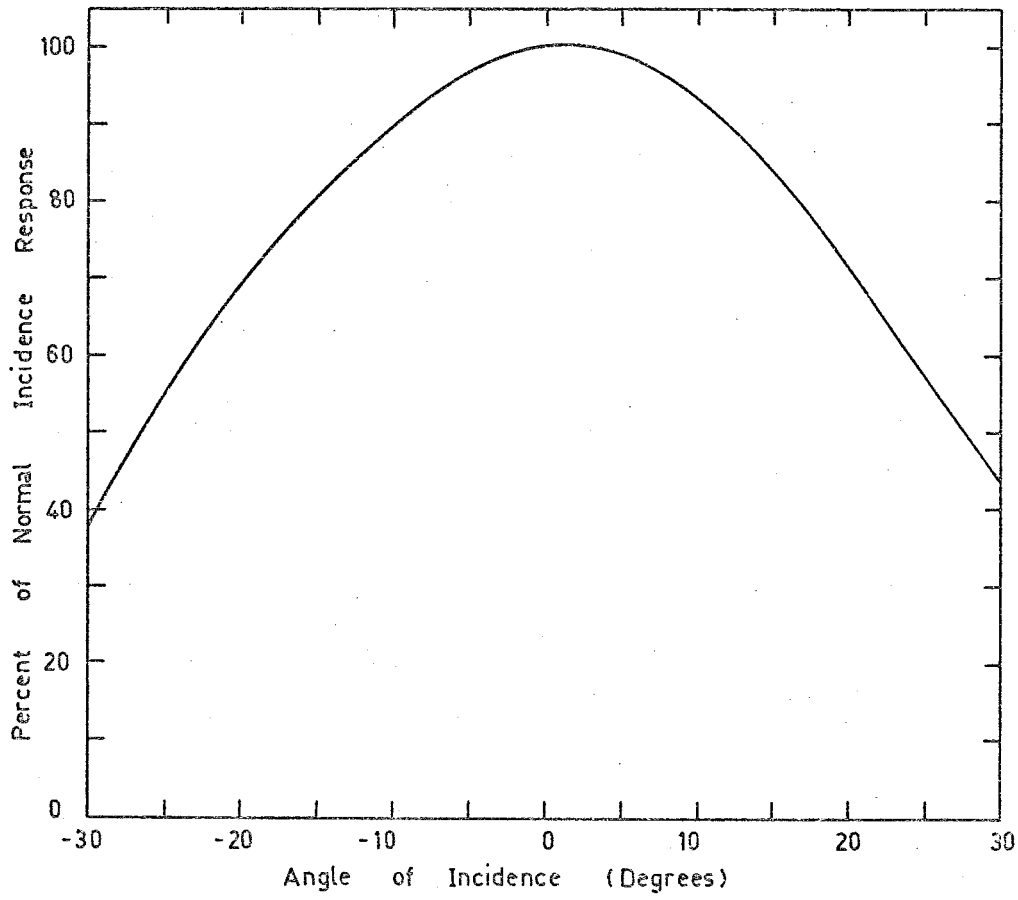

Figure 2 . 19 e Angular response of 2900 Å sensor in C104.

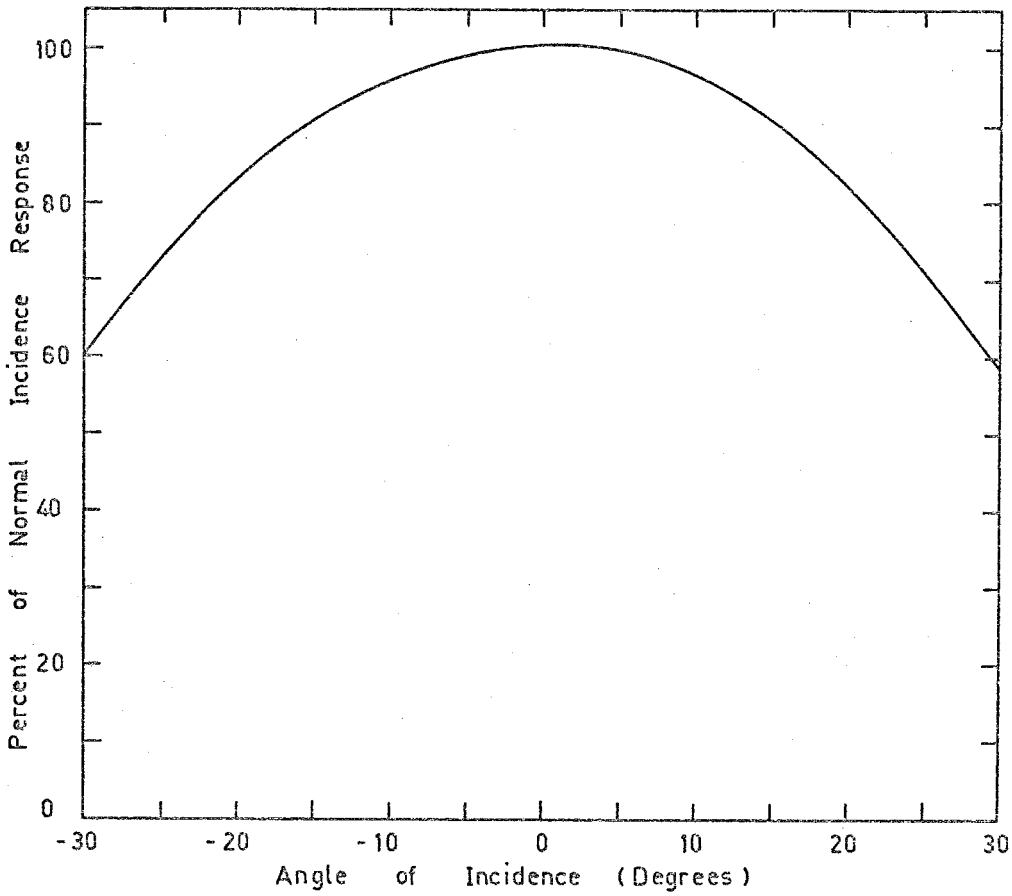

Figure 2.19f Angular response of 2500Å sensor in C105.

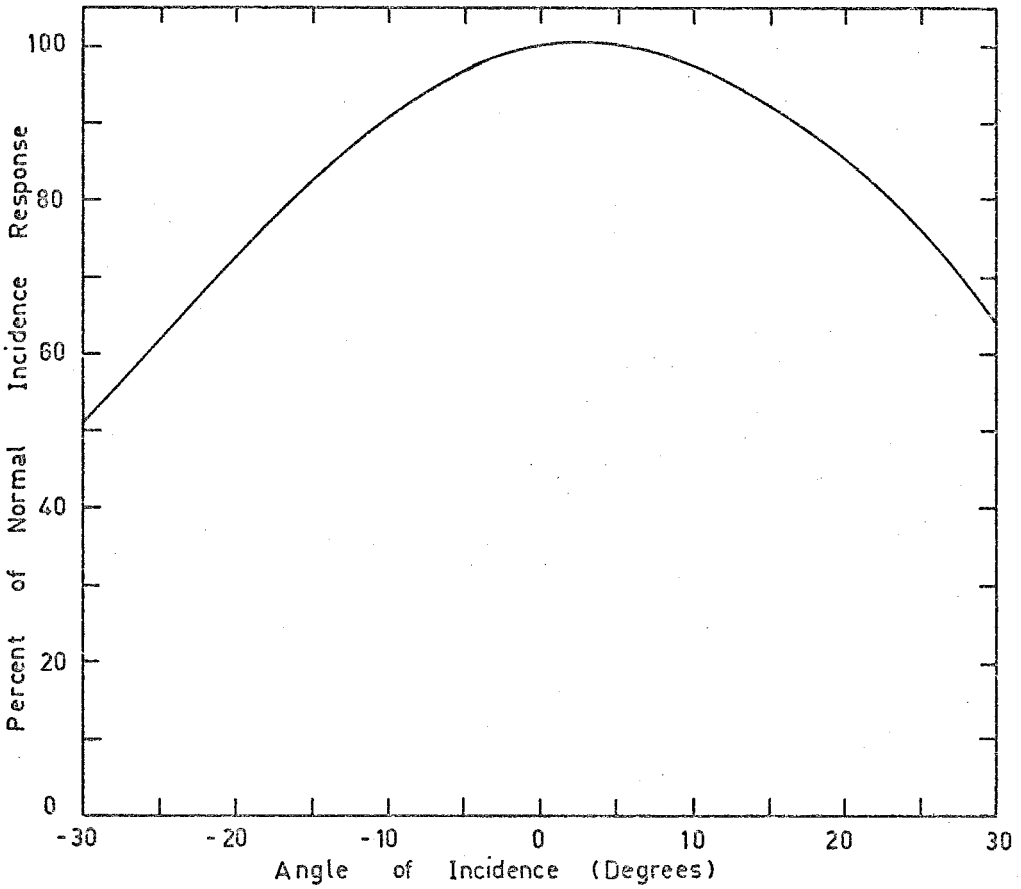

Figure 2.19g Angular response of 2700 Å sensor in C105.

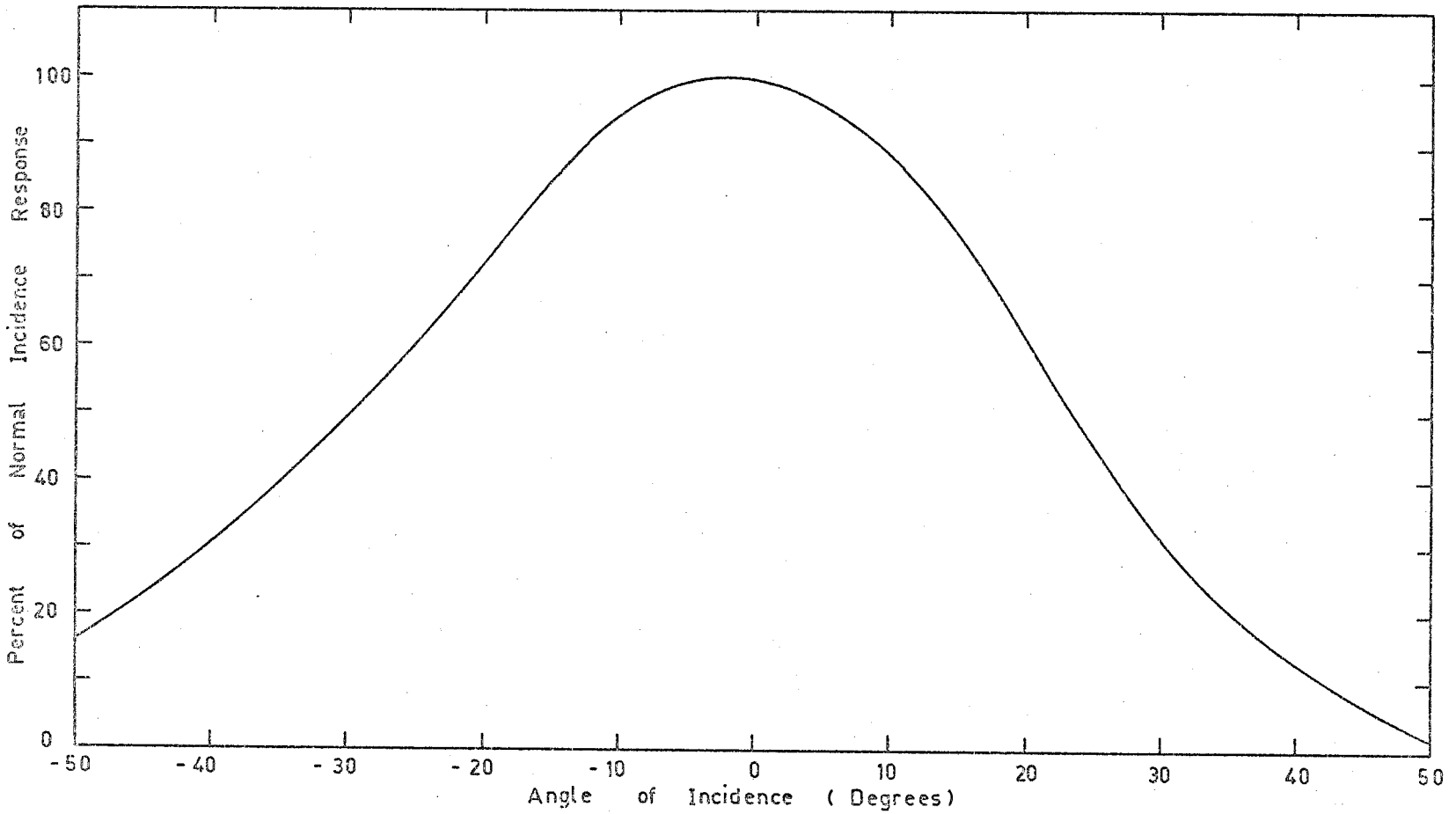

Figure 2 . 19h Angular response of 2500 Å sensor in C1014 .

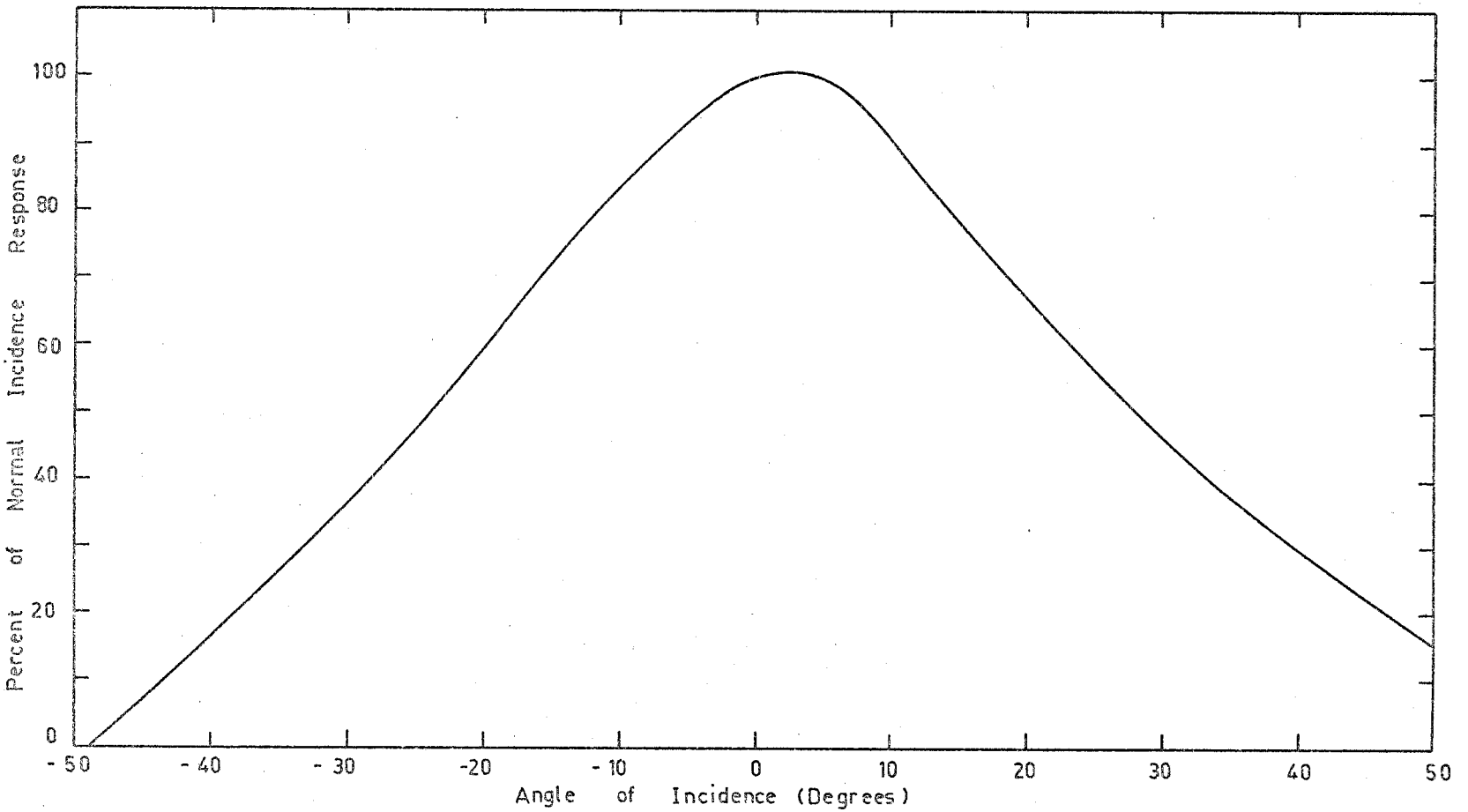

Figure 2 . 19i Angular response of 2700 Å sensor in C1014.

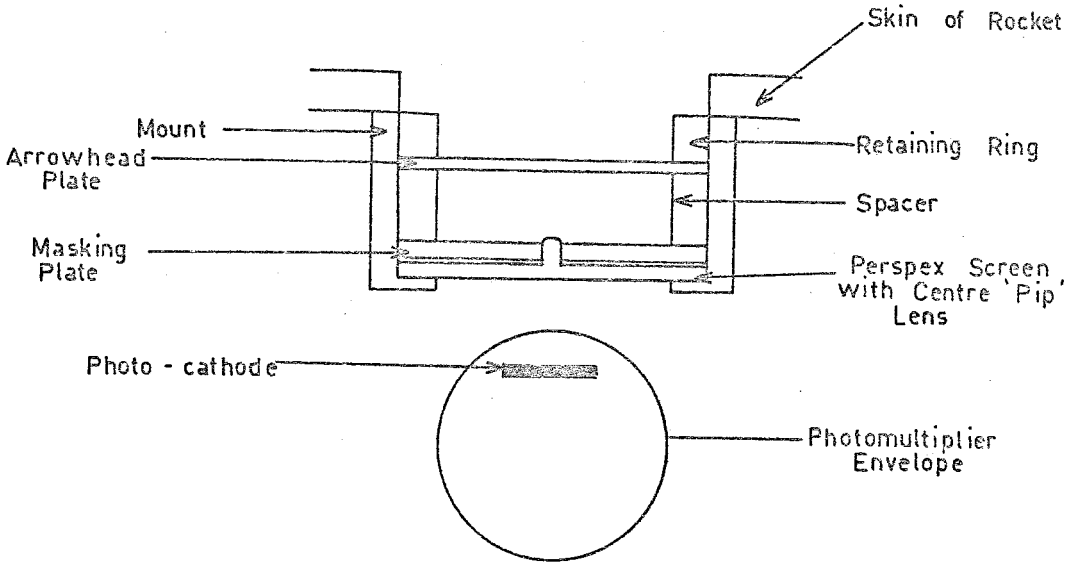

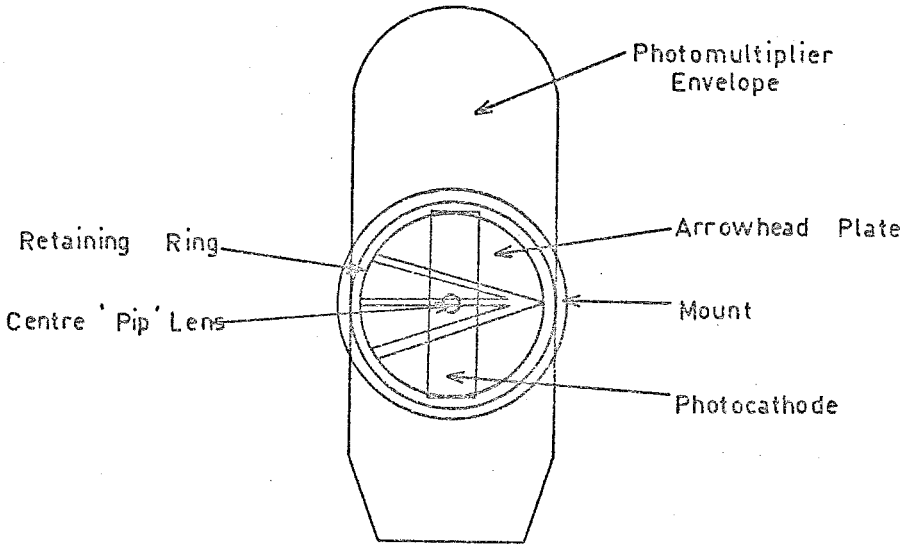

Figure 2.20 Design of the aspect sensor flown in HAD313.

the resolution this system was modified by the use of a double arrowhead plate in C104 and C105. The arrangement used is shown in Figure 2.21. It was found from C104 and C105 that the photometers were sensitive out to angles of 50°, compared with about 30° for HAD 313. The aspect sensor used in all three rounds could only measure angles out to ± 30° because of shadowing effects produced by the arrowhead plate being set back inside the outer skin of the rocket. To take advantage of the wider angular response curve of the photometers a cylindrical type of arrowhead plate which put the slits as close as possible to the outside of the skin was devised for C1014. The "plate" consisted of a nichrome film deposited on a quartz glass cylindrical lens: the lens was placed in a jig, across which fine wires had been stretched in the appropriate arrowhead pattern, and the nichrome film deposited on the lens under vacuum. The back of the lens was painted matt-black with a small clear spot at the centre to replace the perspex pip used in earlier aspect sensors. The arrangement of this sensor is also shown in Figure 2.21. A chamfer was also cut in the outer skin to reduce shadowing effects. The circuits for the amplifiers used with the aspect sensors are shown in Appendix 2.

The assumptions made in the measurement of aspect angle with this system were that the roll rate of the vehicle is only slowly varying, and that the roll rate of the vehicle is much

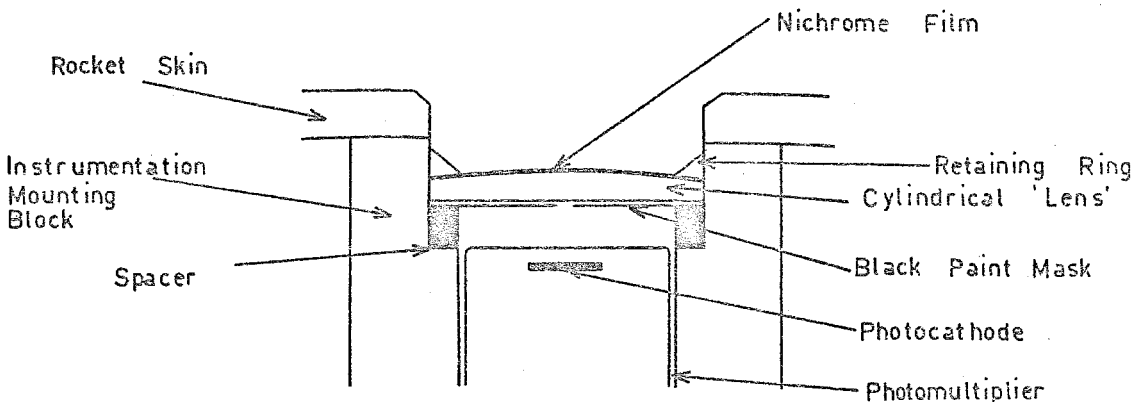

Arrangement used in C1014

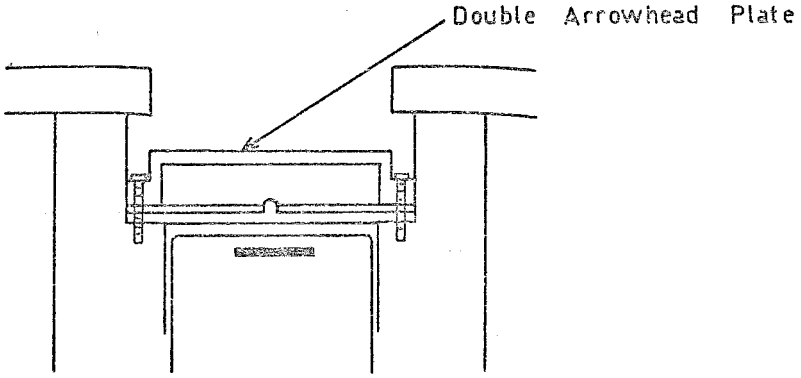

Arrangement used in C104 and C105

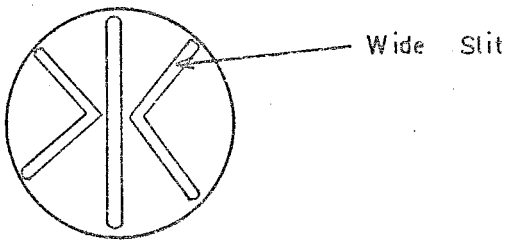

Double arrowhead design - one outer slit wider than the others to remove any ambiguity due to the symmetry of this double arrowhead arrangement.

Figure 2.21 Modifications made to the original aspect sensor design.

greater than the precession rate of the longitudinal axis of the vehicle. As the vehicle rolled, the source would illuminate the centre lens through each of the slits of the arrowhead array. The output of the sensor would be recorded as a function of time by the telemetry. If the period between the two outer pulses is t_o and the period between the centre pulses of two successive groups is t_1, then the angle through which the vehicle has rotated in order that the source illuminate the centre lens through the outer slits can be determined from the relation:

$$2\phi = 360 \times \frac{2t_o}{t_1} \text{ degrees} \qquad \ldots (2.3)$$

Referring to Figure 2.22 we see that

$$\theta = B - \arcsin\left(\frac{s \tan\phi}{(H^2+s^2)^{\frac{1}{2}} \tan\alpha}\right) \qquad \ldots (2.4)$$

By measuring ϕ at normal incidence (θ=0) we can determine B. Hence a theoretical curve of θ against ϕ can be calculated since the parameters in (2.4) are just the physical dimensions of the sensor.

The expression for the double arrowhead plate is similar to (2.4) but is symmetric about θ=0 because of the symmetry of the slit pattern.

It was found that the measured values of θ versus ϕ correspond reasonably well to the theoretical curves derived

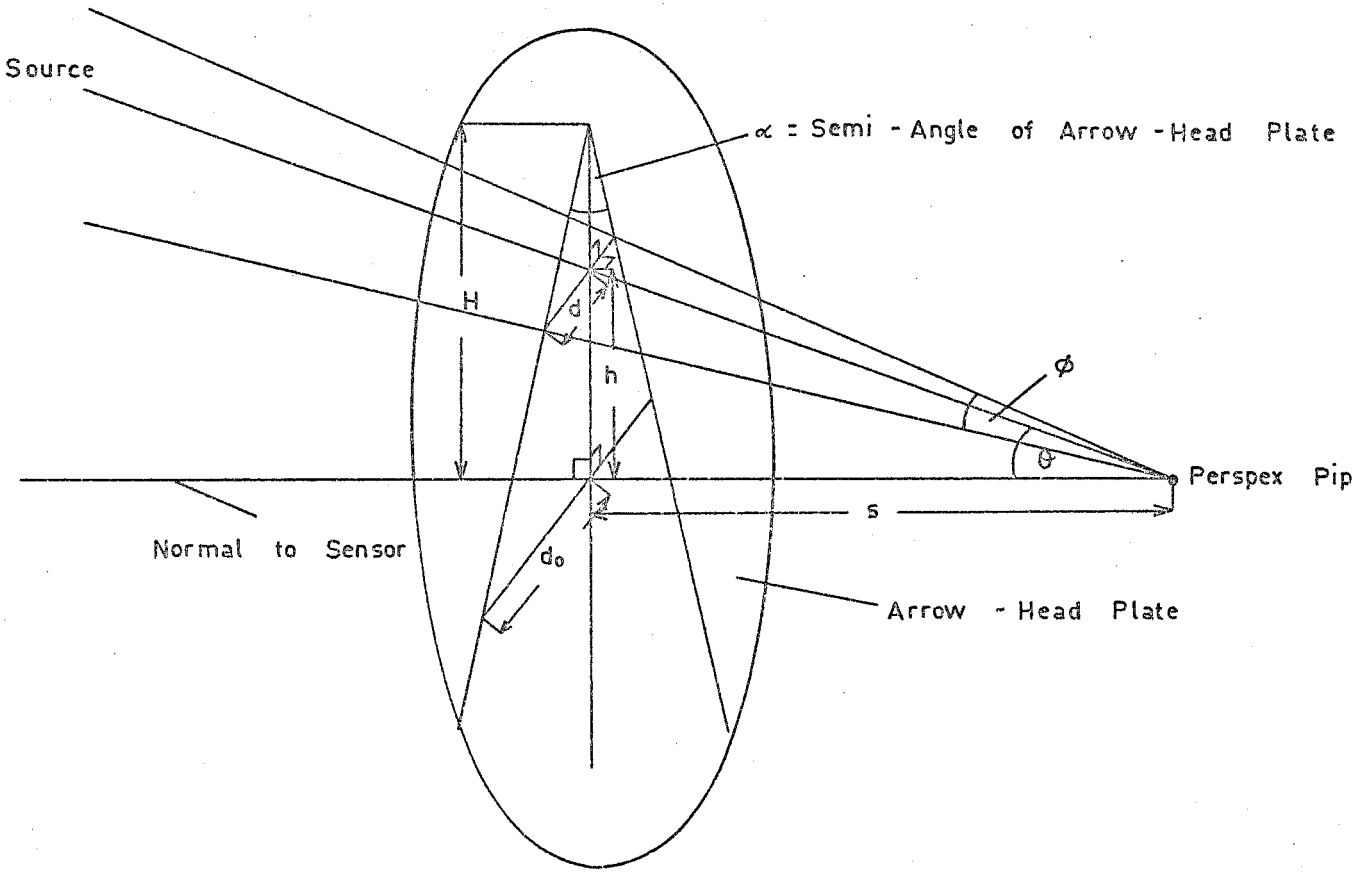

Figure 2 . 22 Schematic representation of the arrowhead aspect sensor.

from (2.4). The differences could be attributed to the finite size of the slits and of the perspex pip used as a lens to pass the light to the photomultiplier.

The arrangement of the apparatus used to calibrate the aspect sensors is shown in Figure 2.23. The lamp was housed in a metal box with a small hole cut in it to approximate the angular size of the moon (half a degree). The output of the aspect sensor amplifier was plotted as a function of angle as the table was rotated; this enabled the angular separation of the two outer peaks to be measured and also gave a record of the pulse shapes as a function of θ.

Results of the calibration of the aspect sensors for the four rounds are shown in Figs. 2.24.a,b,c,d.

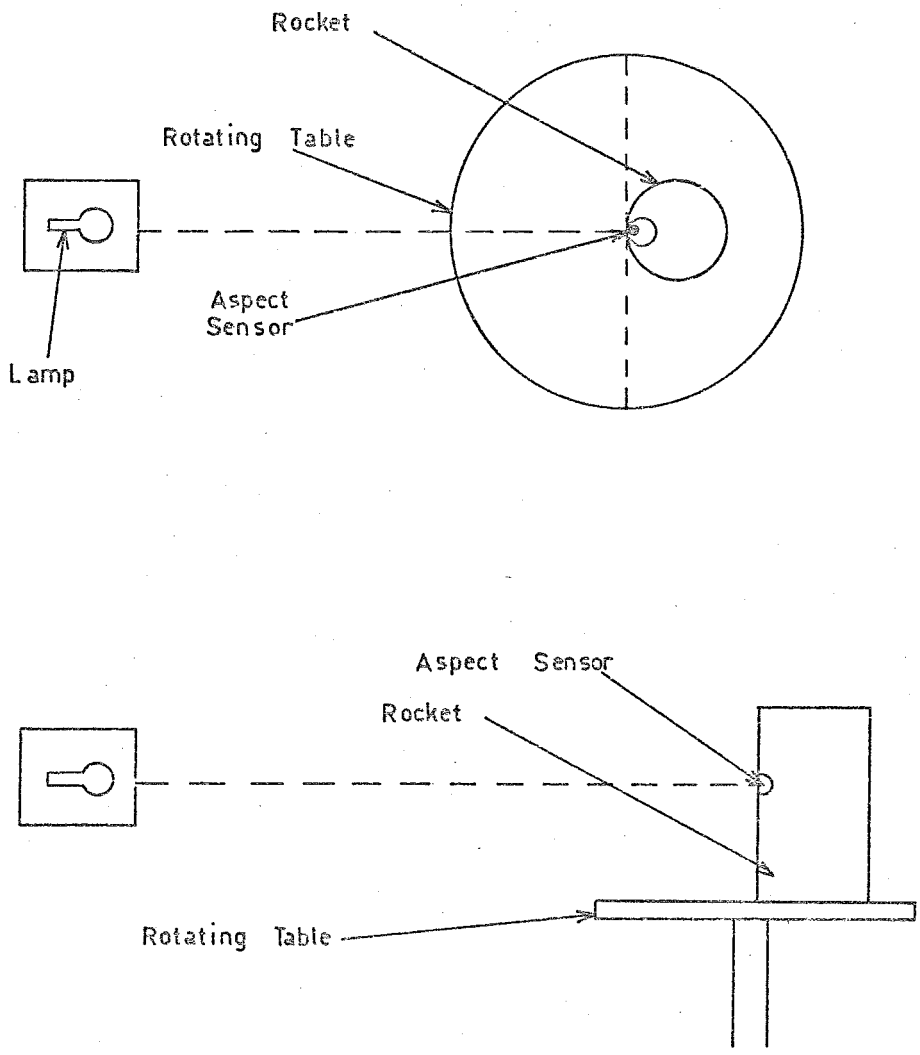

Figure 2.23 System used for calibrating the aspect sensors.

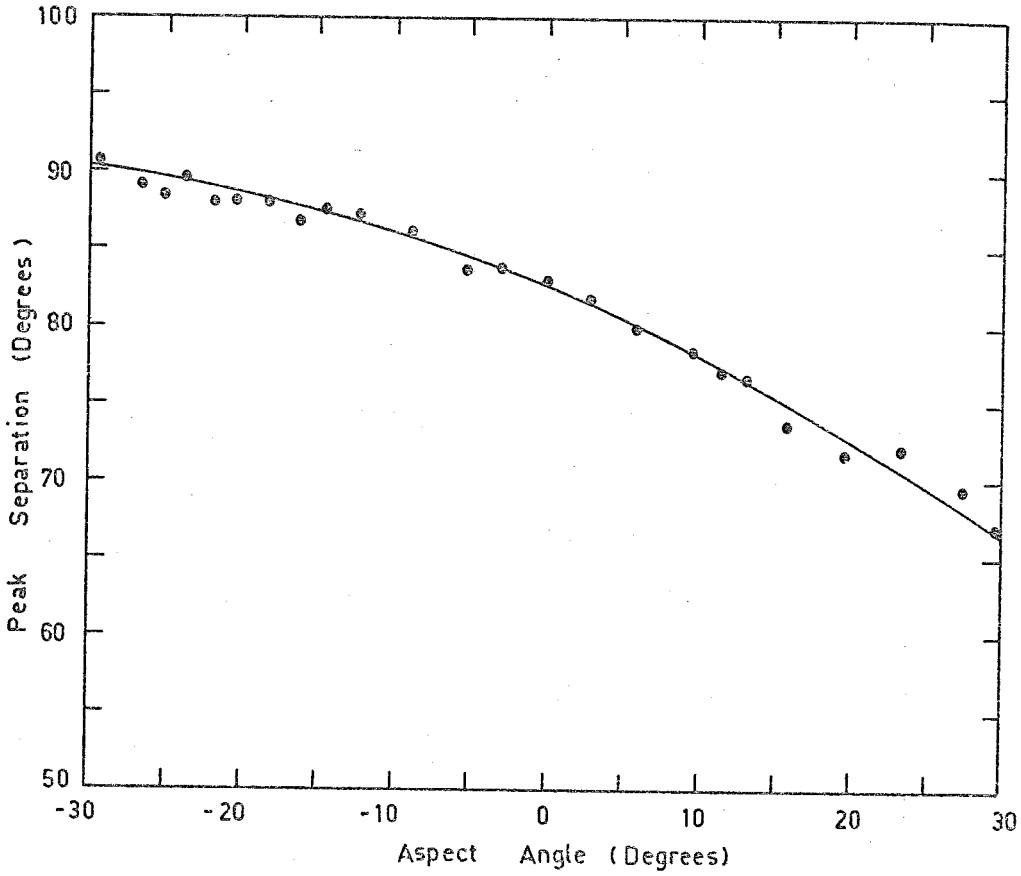

Figure 2 . 24 a Results of aspect calibration for HAD313.

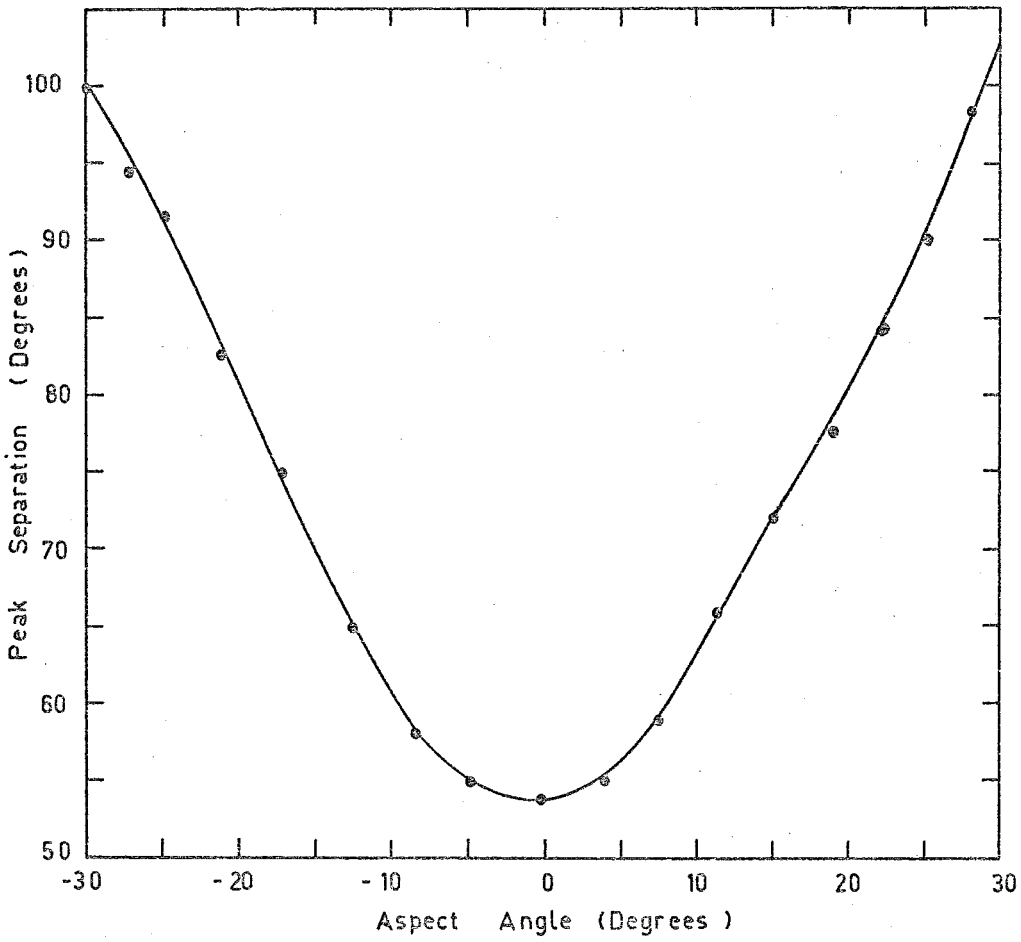

Figure 2.24b Results of aspect calibration for C104.

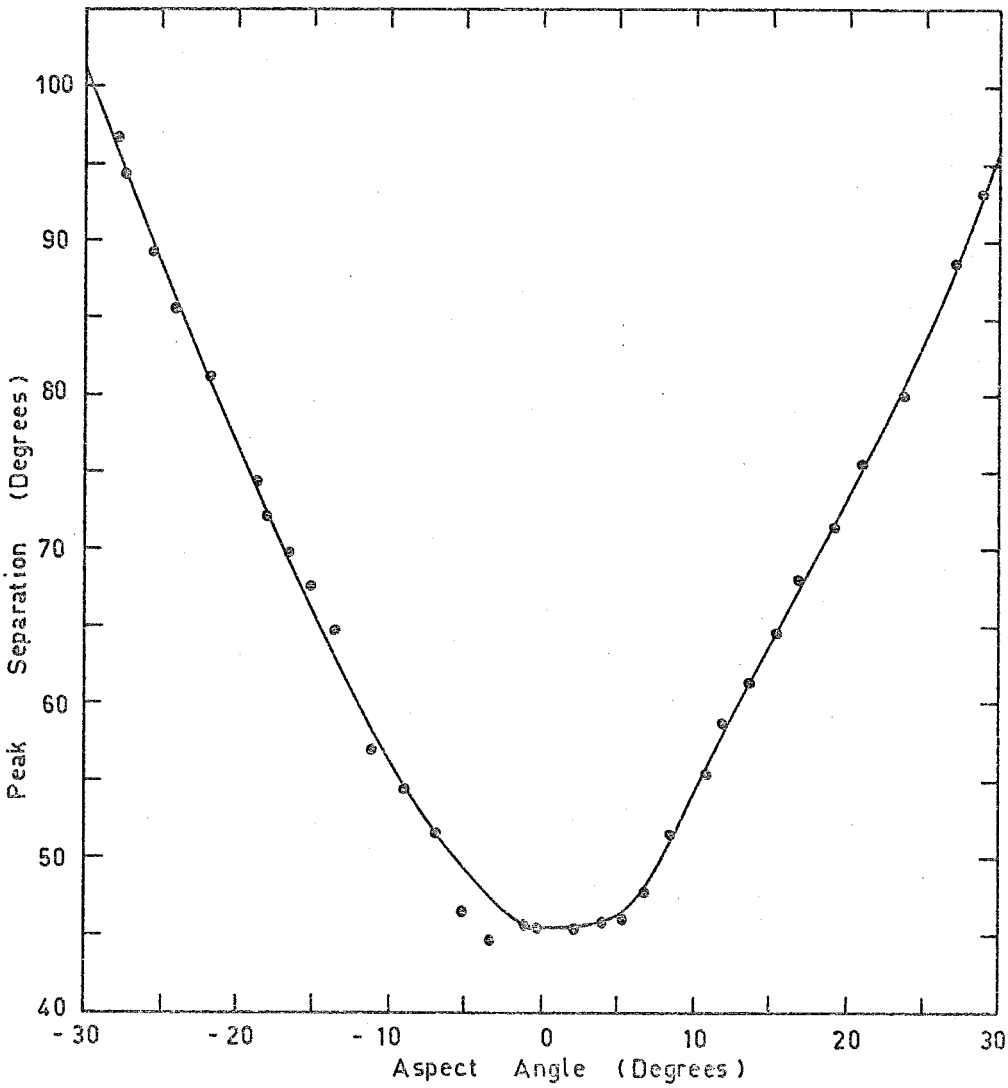

Figure 2 . 24 c Results of aspect calibration for C105.

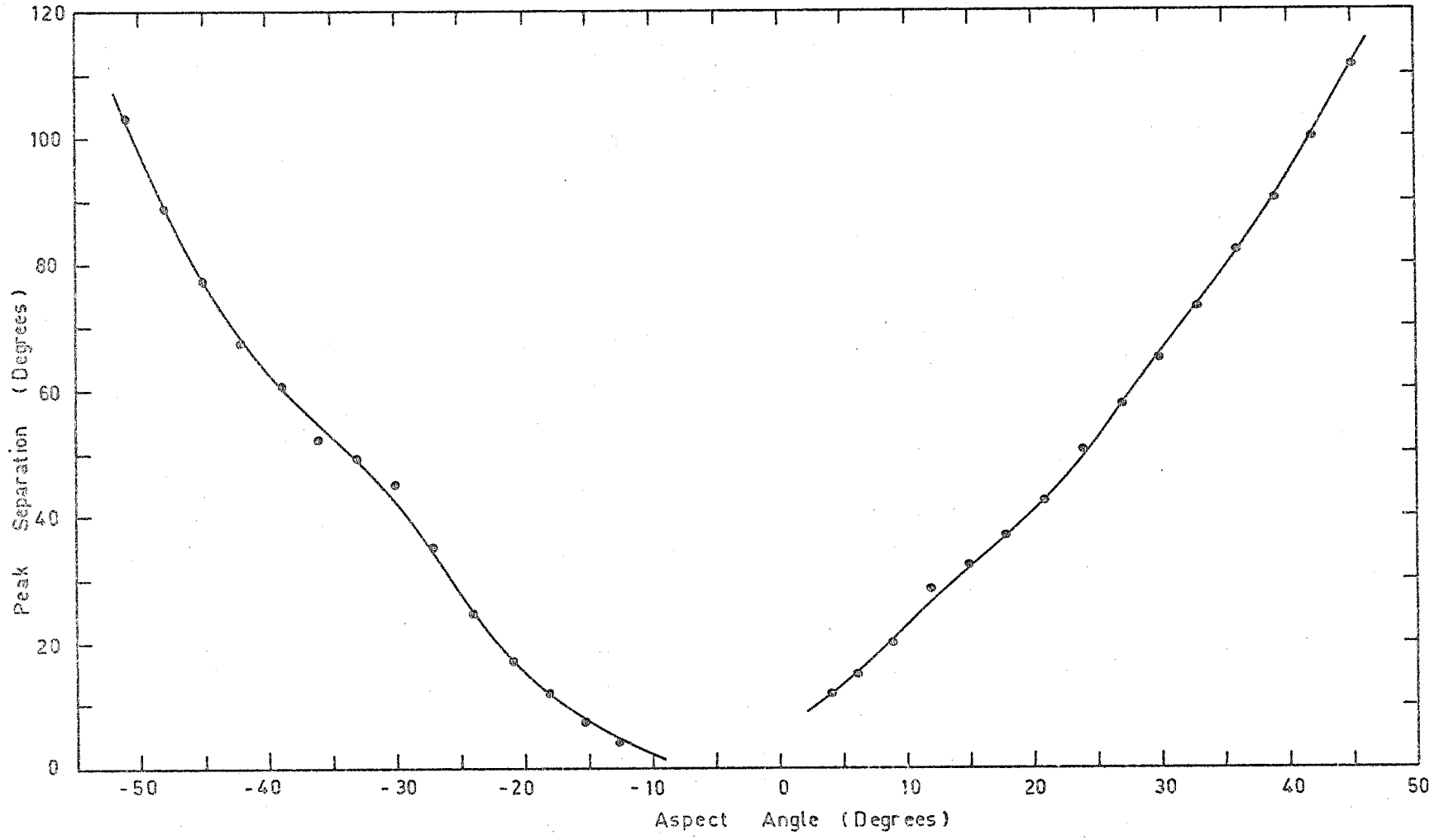

Figure 2.24d Results of aspect calibration for C1014.

CHAPTER 3

OZONE DENSITIES DEDUCED FROM ROCKET FLIGHTS

3.1 Details of Location and Times of Rocket Flights

In the course of the experiments performed, four vehicles were launched from the Woomera Rocket Range of the Weapons Ressearch Establishment of the Australian Department of Supply. The range head is situated at 30°35' South latitude and 136°31' East longitude.

The first vehicle, HAD 313, was fired at 1900 hours Australian Central Standard Time on August 7th, 1968, but, due to a malfunction in the first stage of the rocket vehicle the flight was abortive.

The second vehicle, Cockatoo 104, was fired at 1945 hours on May 21st, 1970, at which time the moon was at a zenith angle of 62°34' and at a phase angle (see Figure 3.1) of 5.3° from full moon.

The third vehicle, Cockatoo 105, was fired at 2030 hours on November 12th, 1970, at which time the moon was at a zenith angle of 63°55' and at a phase angle of 14.1° from full moon.

The fourth vehicle, Cockatoo 1014, was fired at 2004 hours on May 29th, 1972, at which time the moon was at a zenith angle of 63°15' and at a phase angle of 15.2° from full moon.

The firing times were chosen such that the aspect angle was as close as possible to zero while the lunar zenith angle was

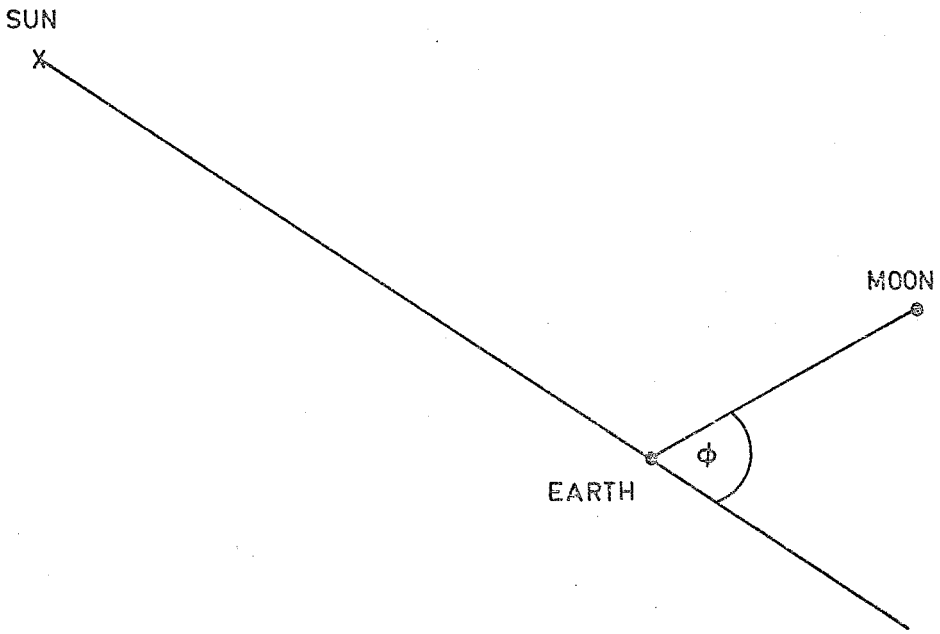

Figure 3.1 Showing how the lunar phase angle ϕ is defined with respect to the earth - sun line and the earth - moon line. ϕ is taken as positive after full moon, negative before full moon.

less than 65° so that the simplifying assumptions of Section 1.4.4 could be used.

3.2 Reduction of Data

3.2.1 Tracking Records Available

Since the range centre line extends to the North-west of the launching site the flight path of the vehicles was in this direction. All vehicles were skin tracked by on-range radar facilities. Magnetic tape records of the radar tracking data were processed by the Weapons Research Establishment and the resulting outputs were presented in the form of $X, Y, Z, \dot{X}, \dot{Y}, \dot{Z}$ and Height as a function of time from launch, where $\dot{X}$ measures the horizontal distance along the range centre line. Y the horizontal distance normal to X, and Z the vertical distance above the launch site. Height was the Z coordinate corrected for height above sea-level and the curvature of the earth. The time interval between listings was 0.5 seconds.

3.2.2 Form of the Telemetered Data Received

The telemetered values of the voltages appearing at the outputs of the various amplifiers were recorded on magnetic tape, processed by the Weapons Research Establishment and presented in two forms. One was a film record which gave a plot of voltage against time for each sensor for the duration of the flight. Figure 3.2 is an example of the record for C105 showing the outputs of the aspect sensor and the two ultraviolet photometers.

Figure 3.2 A segment of the telemetry record from Cockatoo 105. The time from launch is at the bottom. The top two traces show the output from the 2700Å sensor, the next two traces show the output of the 2500Å sensor, while the bottom trace shows the output of the aspect sensor

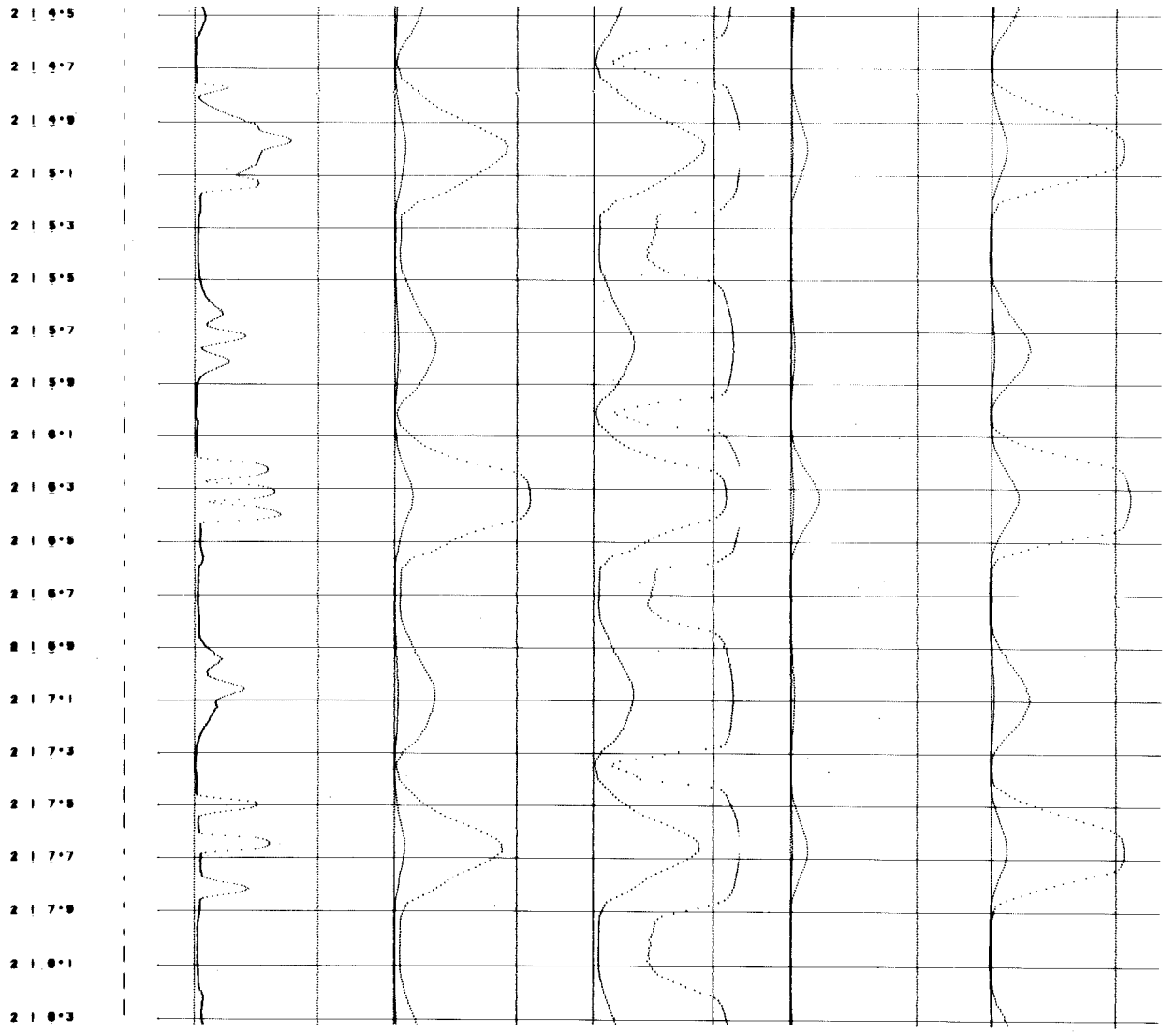
2 1 4·5
2 1 4·7
2 1 4·9
2 1 5·1
2 1 5·3
2 1 5·5
2 1 5·7
2 1 5·9
2 1 6·1
2 1 6·3
2 1 6·5
2 1 6·7
2 1 6·9
2 1 7·1
2 1 7·3
2 1 7·5
2 1 7·7
2 1 7·9
2 1 8·1
2 1 8·3

3.2.3 Determination of the Height versus Time Relation

The direction of flight of all vehicles was determined initially by the altitude at launch, while the velocity attained was determined by the magnitude of the two 3-second impulses imparted to the vehicles by the burning of the first and second stage motors. After second stage burnout the trajectories should have been ballistic to a first approximation. However, all trajectories were modified by the effects of air drag, but since the attitude of the vehicles was not known the drag coefficient of the surface of the rocket could not be determined and no quantitative measurements of air density could be made.

Plots of the variation of altitude as a function of time from launch for C104, C105 and C1014 are shown in Figures 3.3, 3.4 and 3.5 respectively.

The modification of the trajectories by the effect of air drag was illustrated in the following manner. Since the gravitational acceleration varies with height the rocket obeys an equation of motion of the form (neglecting air drag)

$$\frac{d^2Z}{dt^2} = - g(Z) = - (979.3244-0.30866Z+7.259\times10^{-5}Z^2)\times10^{-5}$$

where Z is the height in kilometres and the values of the coefficients of successive powers of Z on the right hand side are taken from C.I.R.A. (1965).

This equation of motion was solved numerically, for the downward leg of each flight, using a Runge-Kutta process

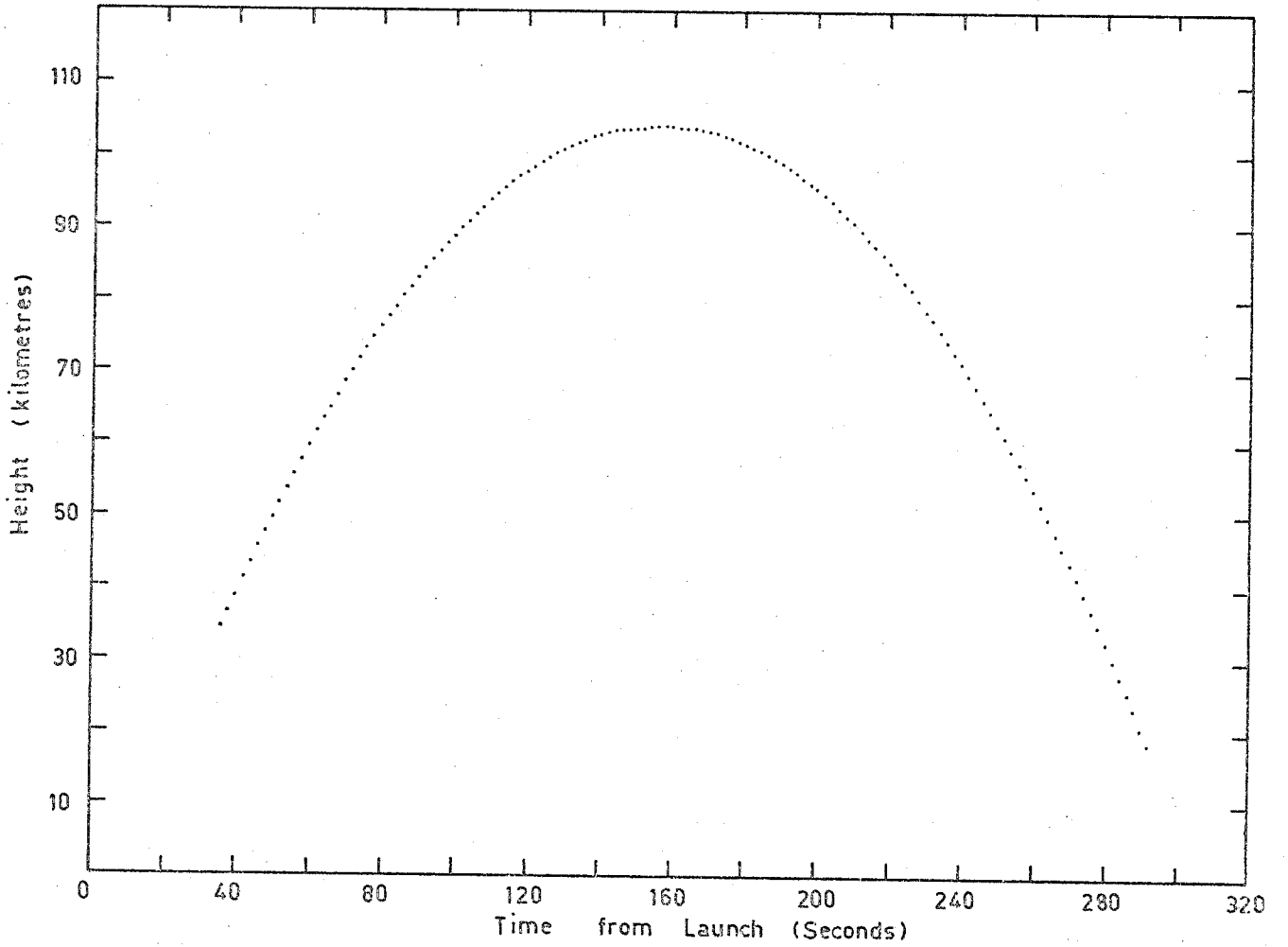

Figure 3.3 Variation of height with time for C104.

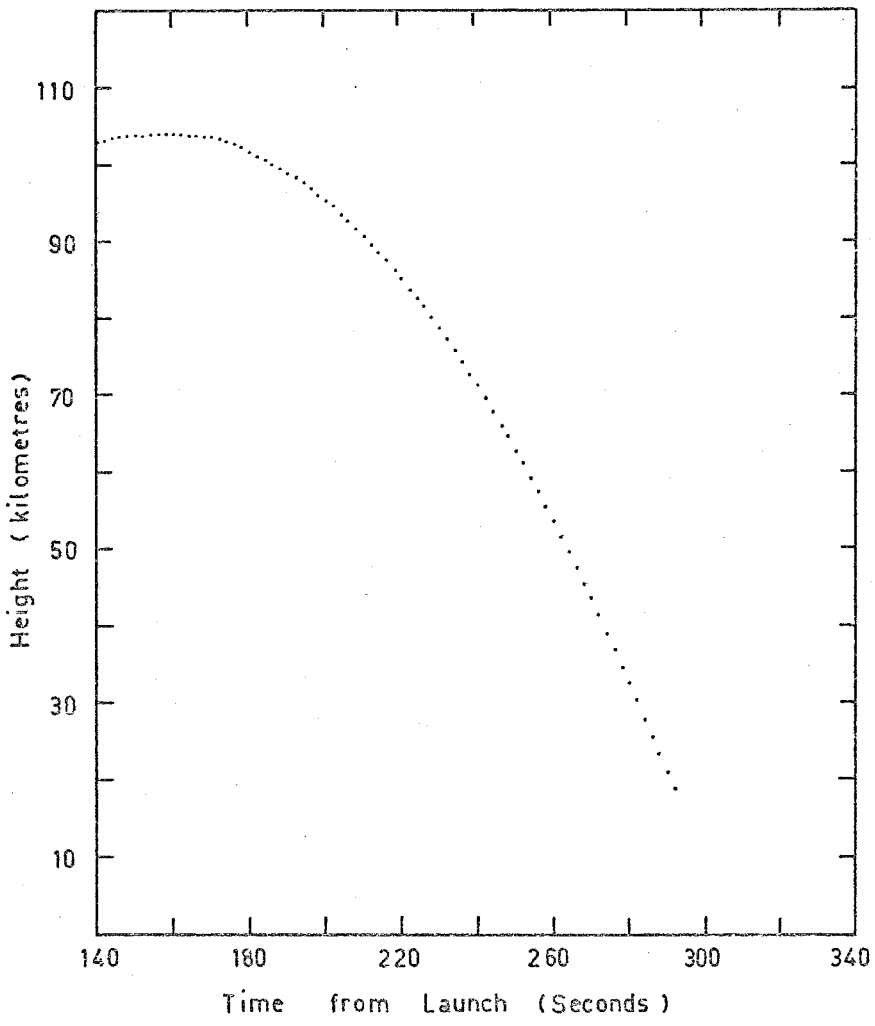

Figure 3 . 4 Variation of height with time for C105.

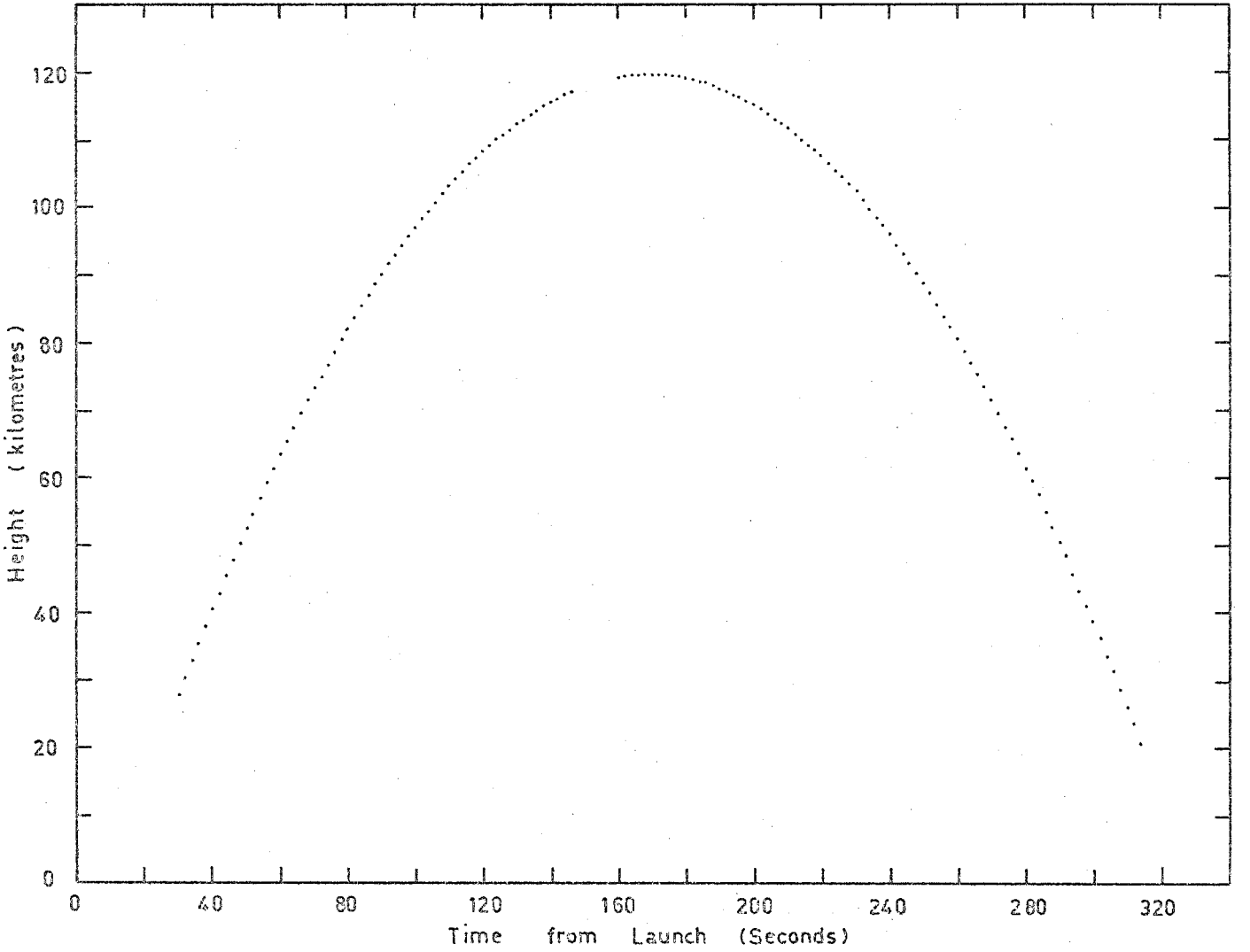

Figure 3.5 Variation of height with time for C1014.

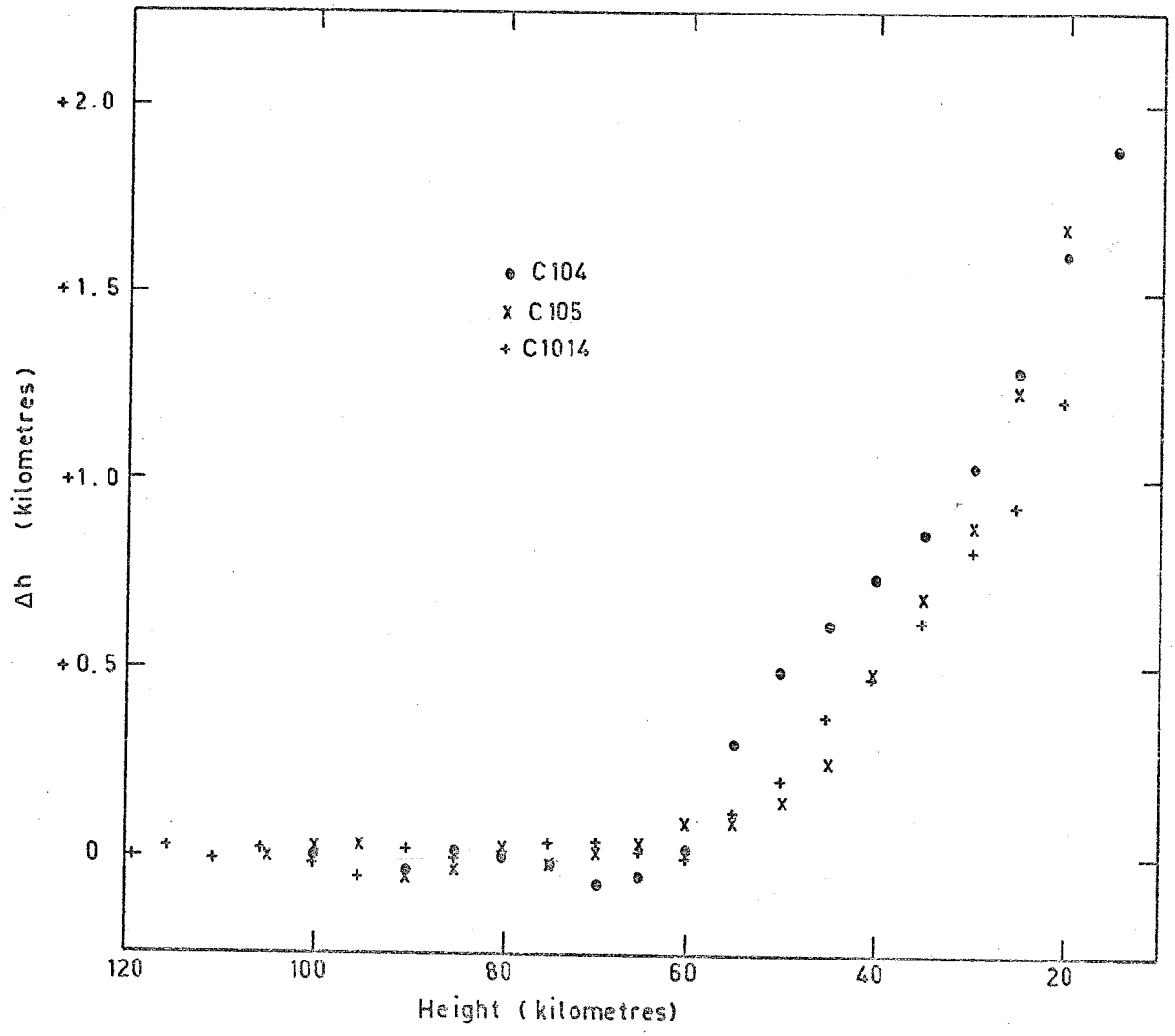

Figure 3.6 Height difference between the observed trajectory and a trajectory computed by neglecting the effects of air drag.

(Carnahan et al., 1969). The computed values of Z were then subtracted from the radar-determined values and the height difference was plotted as a function of height. The results are shown in Figure 3.6. The height difference is negligible for heights above 60 kilometres. However below 60 kilometres the height difference becomes appreciable as the air drag begins to take effect.

3.2.4 Variation of Aspect Angles During Flight

By using data from the aspect sensors carried in each round, as described in Section 2.7, the angle between the normal to the sensor and the source position vector was determined at the instant of closest approach for each reducible scan. The aspect angle for each scan is plotted out for C104 and C105 in Figures 3.7 and 3.8 respectively. For C104 the variation of aspect angle with time is shown in Figure 3.9 as a continuous line because the data points were too close together to be conveniently plotted on the scale used. For C104 useful data was obtained for both upward and downward legs of the flight, but for C105 the cover plate over the sensors came off later than intended, which meant that useful data was obtained only for the downward leg of the flight. For C104 the aspect angles were too large, during the last half of the downward leg, for the data to be of use.

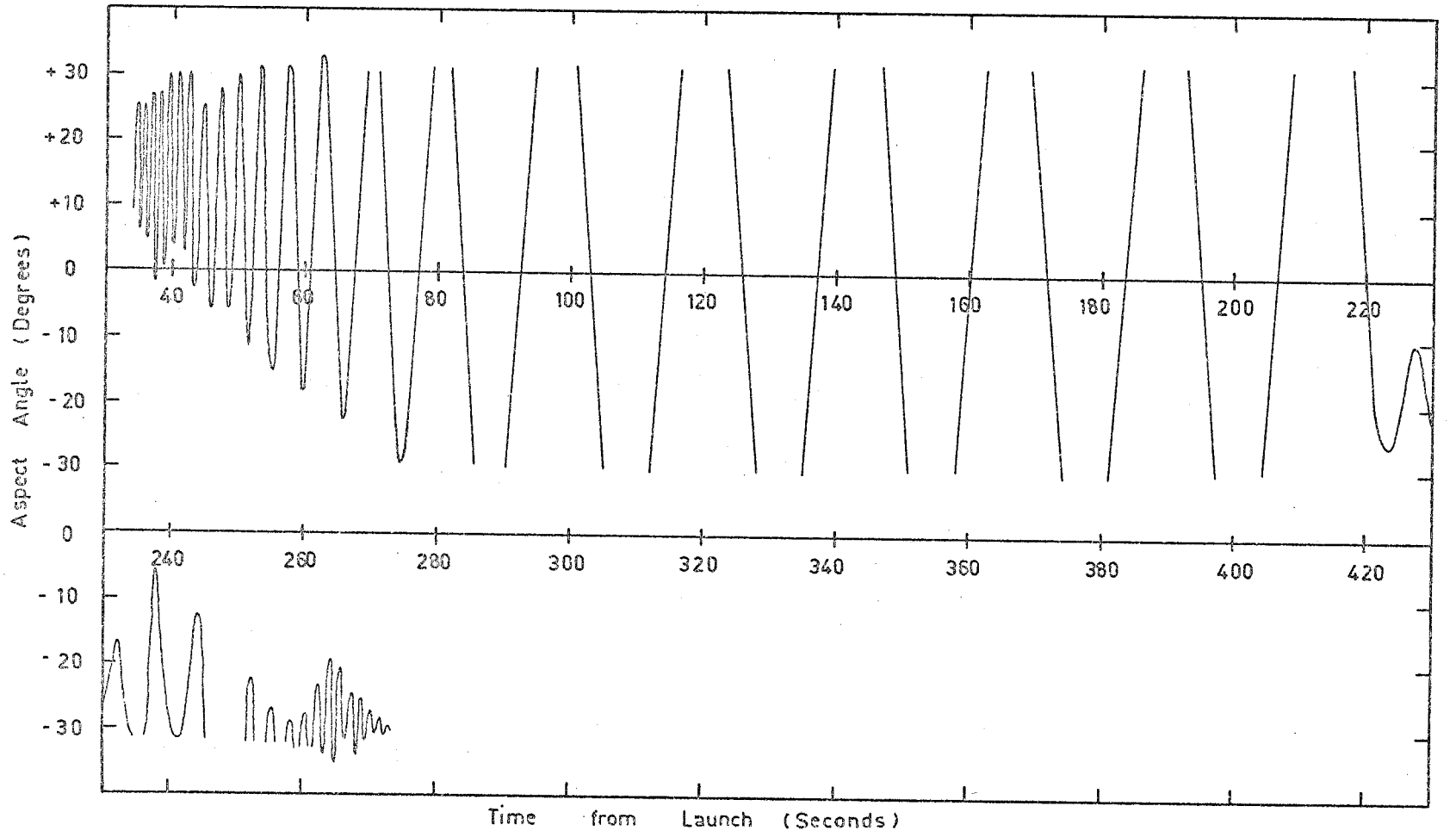

Figure 3 · 7 Variation of aspect angle with time for C104.

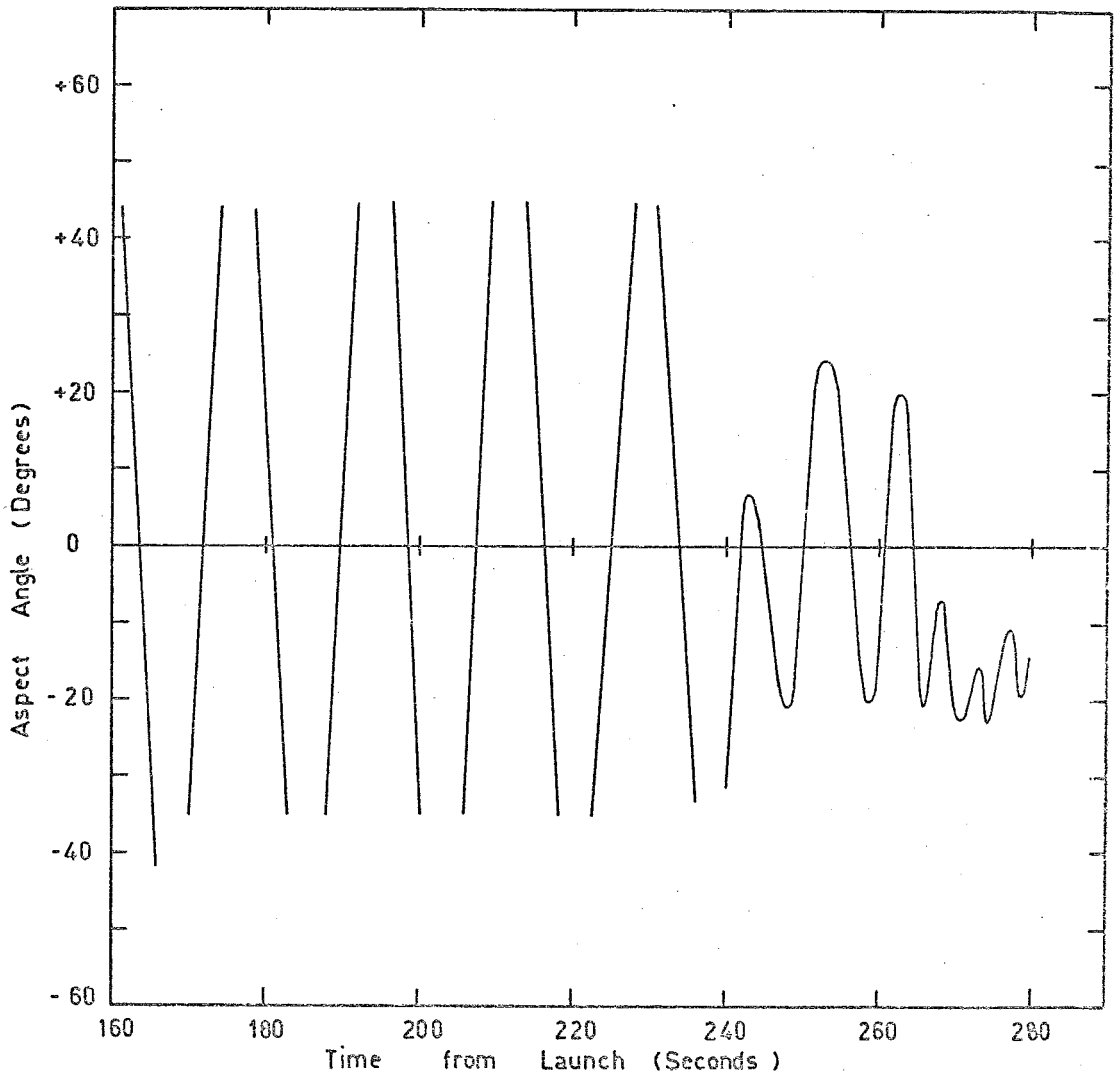

Figure 3.8 Variation of aspect angle with time for C105.

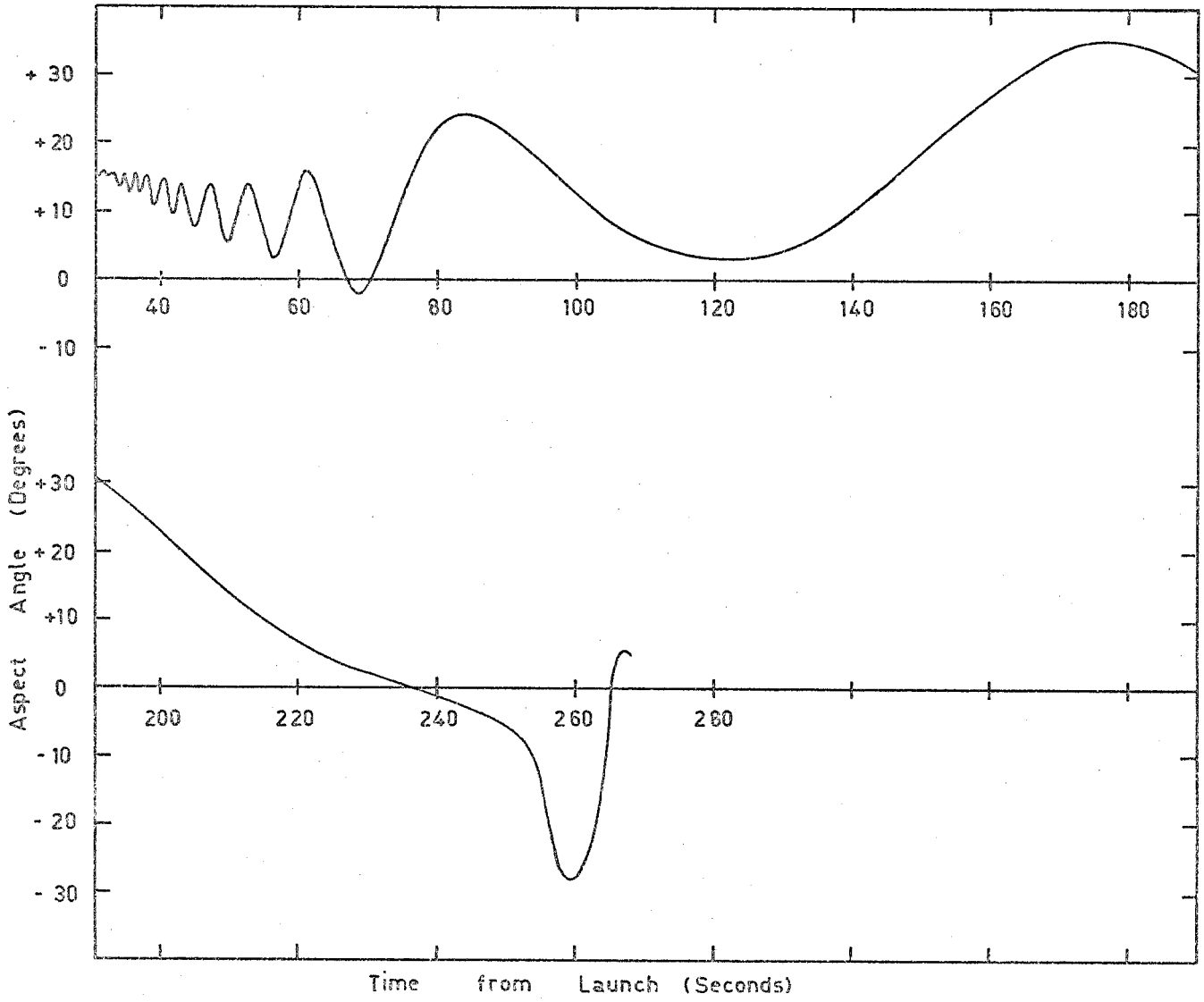

Figure 3.9 Variation of aspect angle with time for C 1014.

3.2.5 Reduction of Data to Give Curves of Incident Flux versus Height

The telemetry records were obtained from the Weapons Research Establishment in the form of film strips and also in the form of a computer printout, as mentioned in Section 3.2.2. The voltage outputs for each sensor were then calculated from these records with the aid of appropriate scaling factors. These scaling factors were needed because both the film records and computer program used different ranges which could be scaled (both by multiplication and axis shifts) to suit the needs of the user. The aspect angle correction for each sensor was then applied by means of Figures 2.19(a-i) to give the equivalent output for normal incidence.

The low altitude scans were made below the expected position of the ozone maximum, so that the value of these early signals was treated as background; this background is thought to consist of photomultiplier noise, radio-frequency interference from the telemetry transmitter in the rocket, noise picked up by the ground receiver, and visible light transmitted by the interference filters in the photometers. This background was subtracted from each subsequent reading. The voltage readings thus obtained were then converted to a value of incident flux via the calibration value for each sensor. The time of each scan was read from the records and was converted to height by means of the height versus time curves in Figures 3.3, 3.4 and 3.5. Values of the incident flux were then plotted out as a function

of height for each sensor. A smooth curve was then drawn through the results for each sensor and the degree of scatter in the data was determined. The plotted results, together with the applied curves, with error bars showing the scatter are shown in Figures 3.10, 3.11 and 3.12.

3.3 Methods of Calculating the Nocturnal Ozone Distributions

3.3.1 The Effective Cross-Section Method

Having calculated the curves of intensity versus height, as described in the previous section, the distribution of ozone as a function of height can now be calculated. In this case this was done using the well known result

$$I(h) = I(\infty)\exp\left[-\bar{\sigma}\sec\theta\int_h^\infty n(x)dx\right] \qquad \ldots (3.1)$$

where $I(h)$ = incident flux at height h

$I(\infty)$ = incident flux outside the atmosphere

θ = zenith angle of source

$\bar{\sigma}$ = effective cross-section for absorption over the band pass of the sensor

$\int_h^\infty n(x)dx$ = total ozone above height h in a vertical column with a cross-sectional area of 1 cm^2.

From (3.1) it can be shown by straightforward manipulation that

$$\frac{I(h+\Delta h)}{I(h-\Delta h)} = \exp\left[\bar{\sigma}\sec\theta\int_{h-\Delta h}^{h+\Delta h} n(x)dx\right] \qquad \ldots (3.2)$$

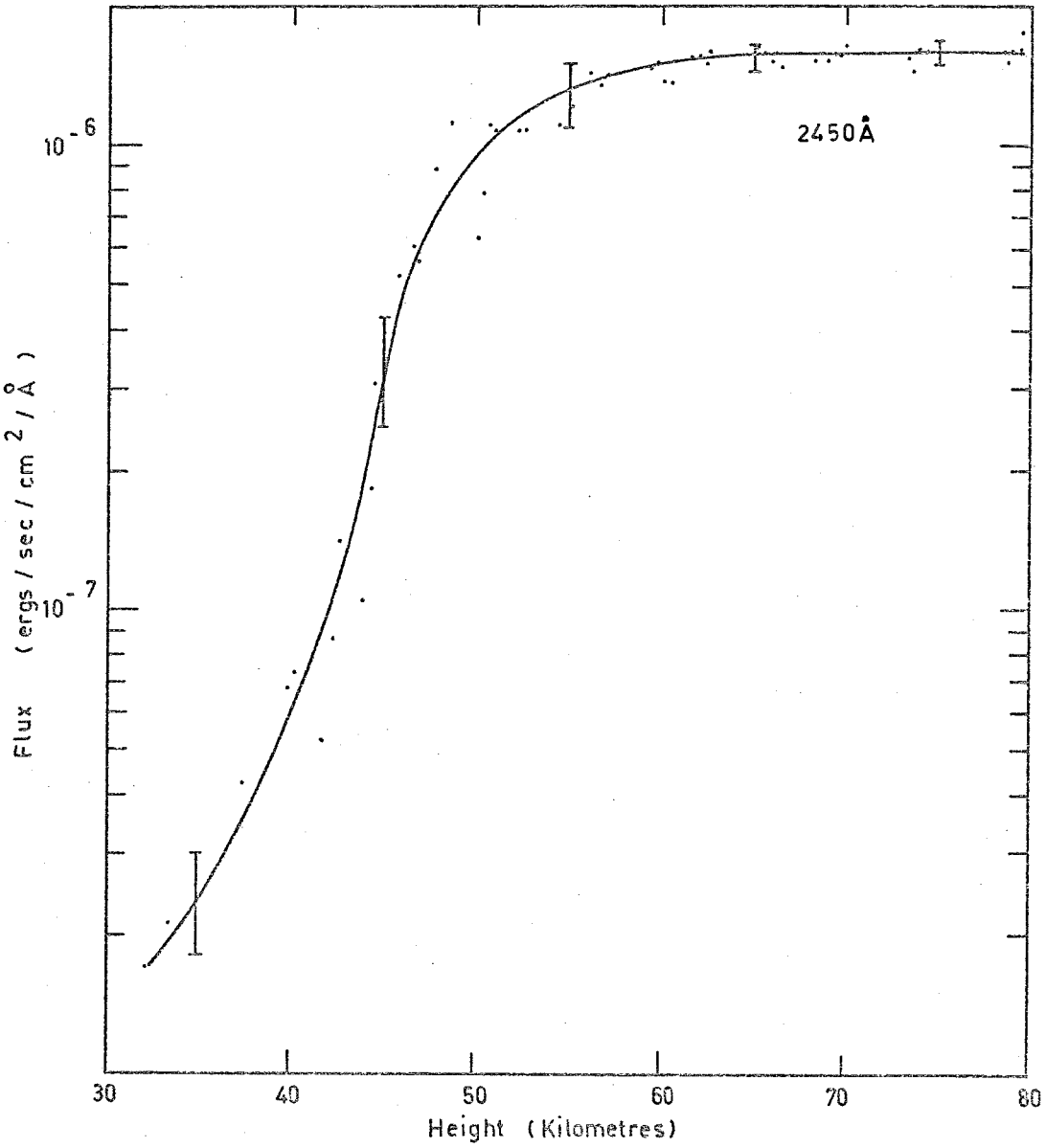

Figure 3.10 Variation of ultraviolet lunar flux with height as measured from C104.

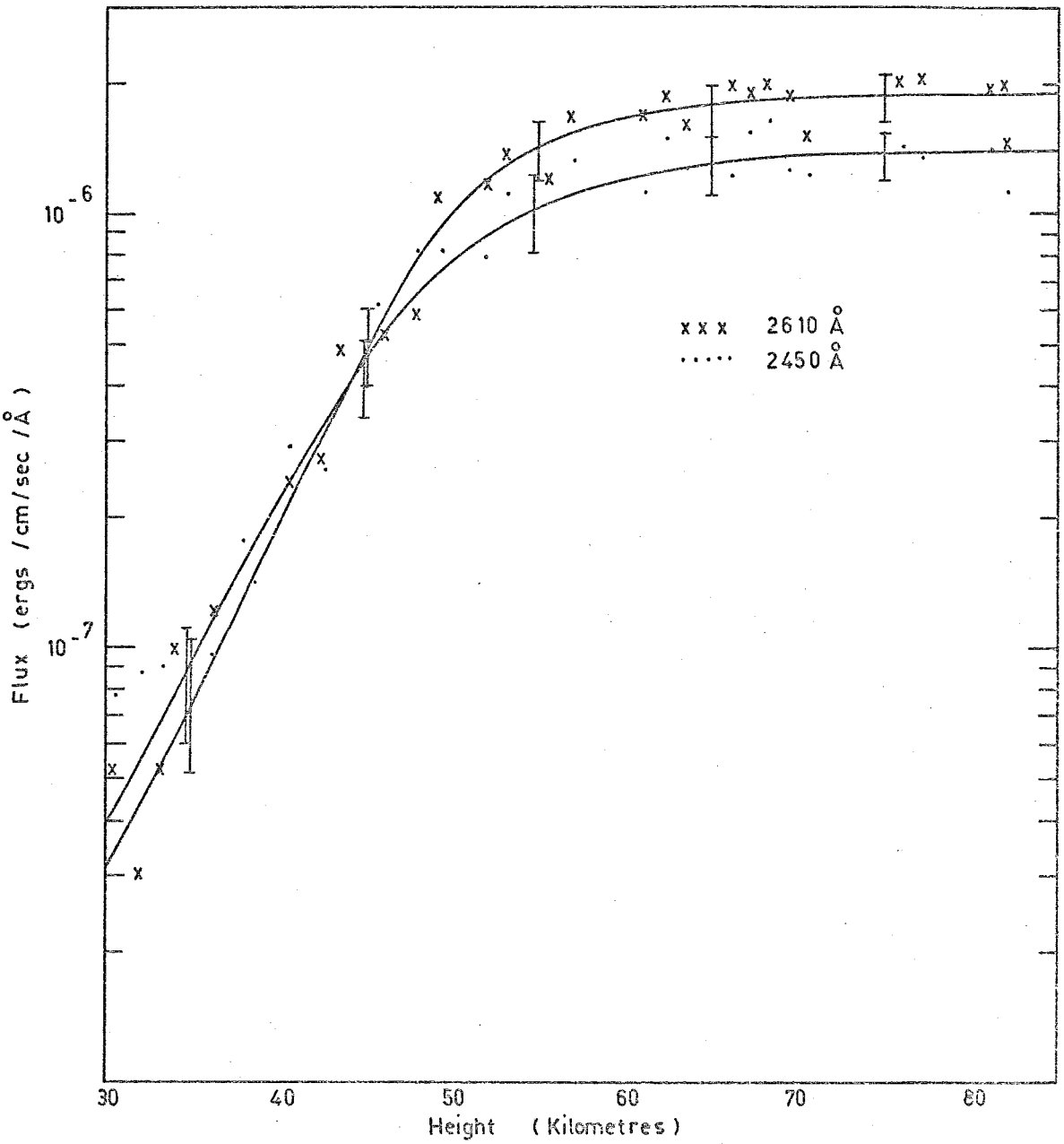

Figure 3.11 Variation of ultraviolet flux with height as measured from C105.

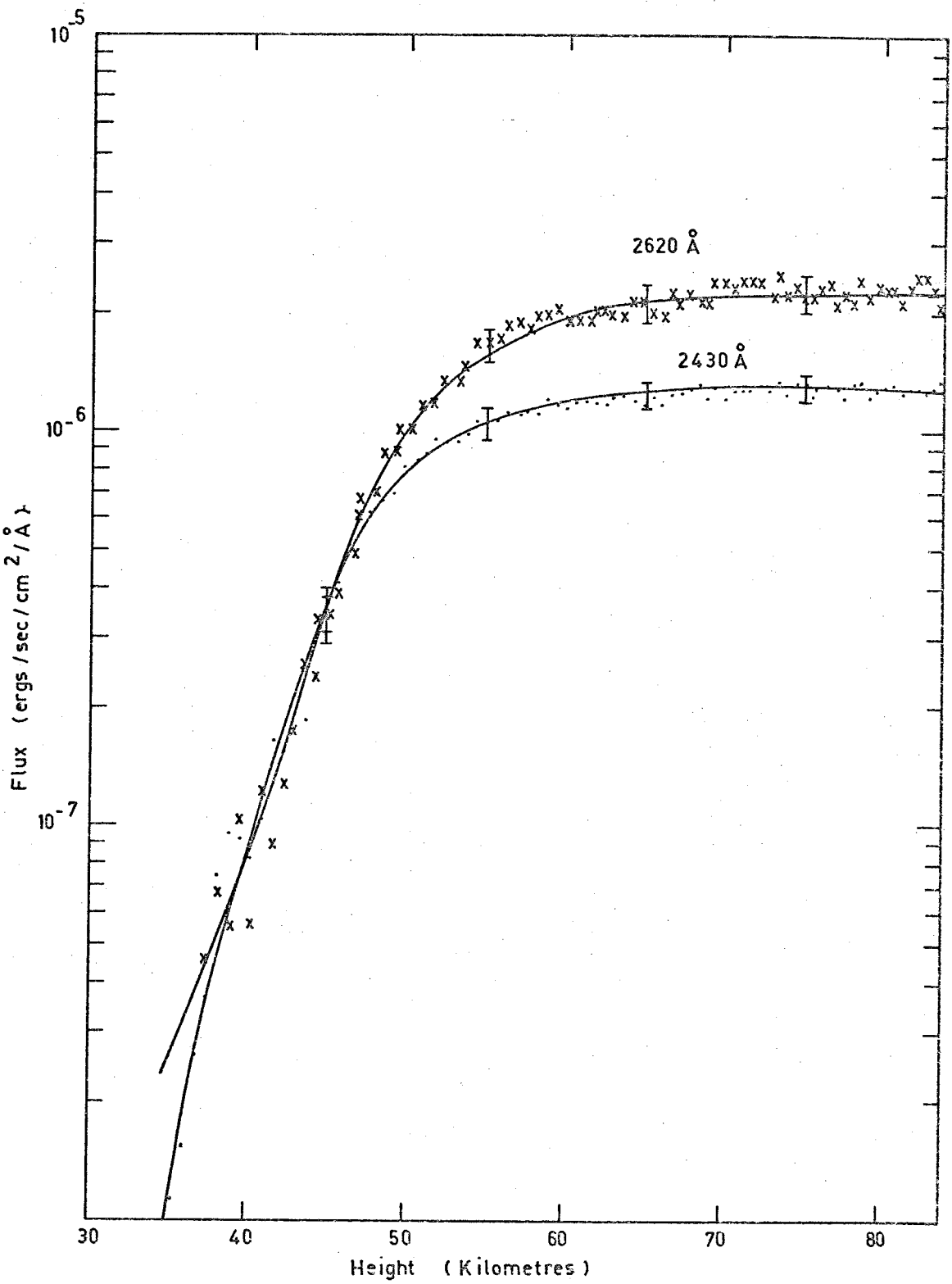

Figure 3.12 Variation of ultraviolet flux from the moon with height as measured from C1014.

$$\text{or} \quad n(h) = \frac{1}{2\Delta h \bar{\sigma} \sec\theta} \ln\left[\frac{I(h+\Delta h)}{I(h-\Delta h)}\right] \qquad \ldots (3.3)$$

where $n(h)2\Delta h$ is the number of absorbing molecules in a 1 cm^2 vertical column between heights $h-\Delta h$ and $h+\Delta h$.

A Table was made of intensity as a function of height at 1 kilometre intervals for each sensor. The ratios $\frac{I(h+\Delta h)}{I(h-\Delta h)}$ were then tabulated against the altitude mid-way between $h-\Delta h$ and $h+\Delta h$. The next step was to calculate the effective cross-section for each sensor. This was done using the formula

$$\bar{\sigma} = \frac{1}{L_n} \cdot \frac{\int_{\Delta\lambda} a(\lambda)S(\lambda)F(\lambda)d\lambda}{\int_{\Delta\lambda} S(\lambda)F(\lambda)d\lambda} \qquad \ldots (3.4)$$

where L_n = Loschmidt's Number = 2.689×10^{19} particles/cm^3 at N.T.P.

$a(\lambda)$ = absorption coefficient (in cm^{-1}) at wavelength λ.

$S(\lambda)$ = relative spectral sensitivity of the sensor

$F(\lambda)$ = the estimated lunar spectral intensity

The values for $a(\lambda)$ were taken from Inn and Tanaka (1959). A table was drawn up at 10Å intervals for each sensor and the effective cross-sections were calculated using (3.4). The results are shown in Table 3.1 below.

These values were then inserted into (3.3) and the ozone profiles for each sensor was then calculated. The value of Δh was 1 kilometre and the values of $n(h)$ were plotted at 1 kilometre intervals. The results of these calculations are

Vehicle	Centre Wavelength (Å)	$\bar{\sigma}(cm^2)$
C104	2375	7.78×10^{-18}
C105	2450	5.35×10^{-18}
	2610	4.35×10^{-18}
C1014	2430	8.34×10^{-18}
	2620	4.21×10^{-18}

Table 3.1 Effective Cross-sections for each detector, calculated from Equation (3.4)

shown in Figure 3.13. The spread in the number density curves for different detectors was substantially larger than the scatter in the curves of intensity versus height for the different detectors.

3.3.2 The Selective Absorption Method

In defining the effective cross-section for each sensor by means of equation (3.4) it was implicitly assumed that the variation of $F(\lambda)$ with height was approximately the same for all wavelengths so that $\bar{\sigma}$ remains constant with height. However, this is not strictly true; it would be more precise to define $\bar{\sigma}$ by means of a relation which allows for the fact that the variation of flux with height is not the same at all wavelengths. A still more satisfactory approach is not to use the idea of an effective cross-section at all but to proceed as follows:

If $\overline{F(h)}$ is the mean flux reaching the detector at height h then $\overline{F(h)}$ can be defined by

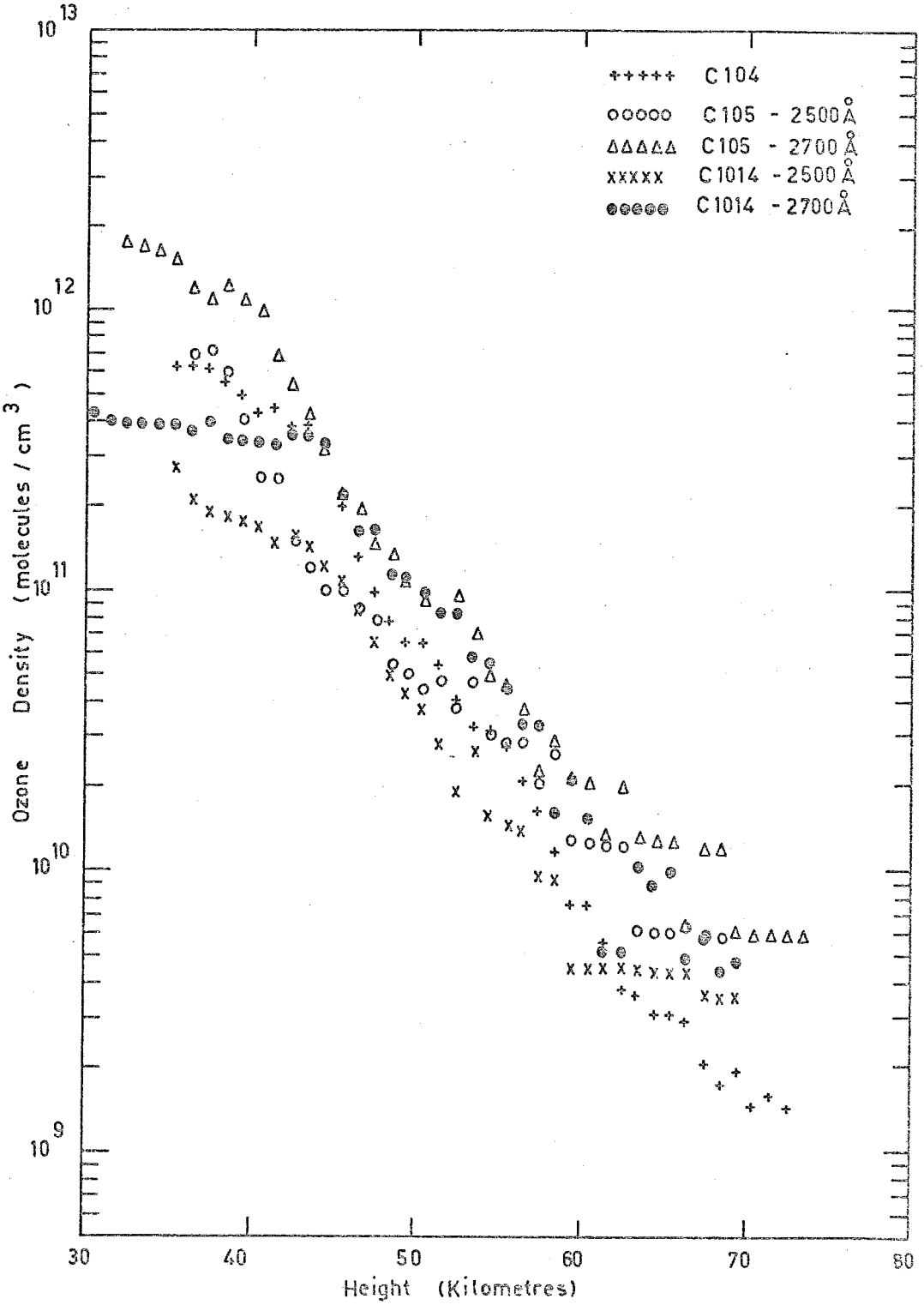

Figure 3.13 Number densities obtained by using the effective cross-section approximation described in section 3.3.1.

$$\overline{F(h)} = \frac{\int F(h,\lambda)S(\lambda)d\lambda}{\int S(\lambda)d\lambda} \qquad \ldots (3.5)$$

where $F(h,\lambda)$ = flux per unit wavelength at wavelength λ at height h

$S(\lambda)$ = relative spectral sensitivity of the sensor

$F(h,\lambda)$ is given by the familiar exponential law, viz,

$$F(h,\lambda) = F_{\infty}(\lambda)\exp\left[-\frac{a(\lambda)N(h)\sec\theta}{L_n}\right] \qquad \ldots (3.6)$$

where $F_{\infty}(\lambda)$ = flux at wavelength λ at the top of the atmosphere

$a(\lambda)$, L_n are as defined for equation (3.4)

and $N(h) = \int_h^{\infty} n(x)dx = \overline{n(h)}\ \Delta h$

where $\overline{n(h)}$ is the integrated number density above height h in a vertical column of cross-sectional area one square centimetre.

If one assumes a value, say n_1, for $\overline{n(h)}$ and calculates the flux $\overline{F(h,n_1)}$ which should reach the detector at height h, then this calculated flux can be compared with the measured flux $F_M(h)$ and a more accurate value for $\overline{n(h)}$ can be found as follows:

Suppose Δn_1 is the amount by which n_1 has to be increased to make the computed flux value agree with the measured value; then by putting

$$F_M(h) = \overline{F(h,n_1+\Delta n_1)} = \overline{F(h,n_1)} + \Delta n_1 \left[\frac{\partial}{\partial n}\left(\overline{F(h,n)}\right)\right]_{n=n_1} \ldots (3.7)$$

where $\frac{\partial}{\partial n}\left(\overline{F(h,n)}\right)$ is the rate of change of $\overline{F(h,n)}$ with respect to changes in n, the value of Δn_1 can be calculated. The form of $\frac{\partial}{\partial n}\left(\overline{F(h,n)}\right)$ can be derived from equations (3.5) and (3.6) and is given by

$$\frac{\partial}{\partial n}\left(\overline{F(h,n)}\right) = \frac{-\Delta h \sec\theta \int F(h,\lambda)S(\lambda)a(\lambda)d\lambda}{L_n \int S(\lambda)d\lambda} \quad \ldots (3.8)$$

A FORTRAN computer program was written to carry out these calculations. The values of $F(h,\lambda)$ at the top of the atmosphere were taken from Lebedinsky et al. (1967), and normalized to the value of $F_M(h)$ at the maximum value of h by using (3.5), and the starting values for $\overline{n(h)}$ were those derived using the method described in Section 3.3.1. The values of $\overline{n(h)}$ were changed until the calculated flux differed from the measured flux by no more than an amount ε, where ε was defined by

$$\varepsilon(h) = \frac{F_M(h+\tfrac{1}{2}\Delta h) - F_M(h-\tfrac{1}{2}\Delta h)}{100} \quad \ldots (3.9)$$

The results of these calculations are shown in Figure 3.14. As a check on the accuracy of the calculations two other starting number density profiles were fed into the program such that the values of n_1 were first increased by 50 per cent and then decreased by 50 per cent. It was found that even with this drastic variation the final answers obtained for the three calculations varied by less than 0.5 per cent over the entire height range.

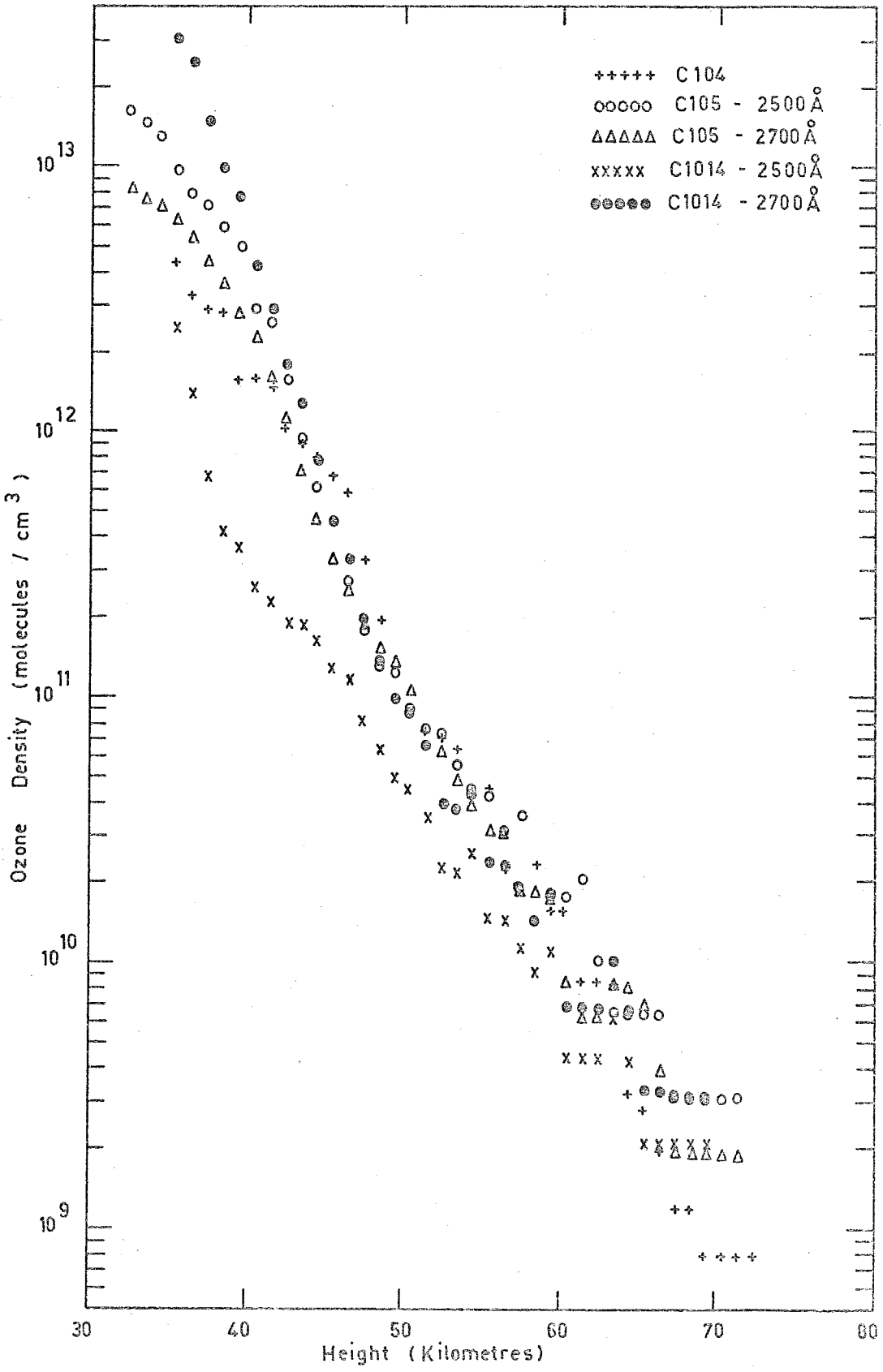

Figure 3.14 Number densities obtained by using the selective absorption method described in section 3.3.2.

3.3.3 Comparison of Results Obtained by the Effective Cross-Section and Selective Absorption Methods

Figure 3.15 shows the average ozone densities obtained from the methods described in the two previous sections. The curves shown were obtained by averaging the results for each detector. This simple averaging process can be used because the detectors are all working in wavelength regions where the ozone absorption coefficient is large, so that all detectors will be sensitive over approximately the same range of number densities. This means that the results from each sensor can be given equal weighting in the averaging process.

It can be seen from Figure 3.15 that the effective cross-section approximation is only good above about 60 kilometres. In this region the approximation

$$\frac{\Delta h \overline{n(h)} a(\lambda) \sec\theta}{L_n} = x << 1 \qquad \ldots (3.10)$$

becomes valid and under these conditions it can be shown that equations (3.1) and (3.5) reduce to the same result, namely

$$\overline{F(h)} \simeq \overline{F(h_{max})} \left(1 - \frac{\Delta h \overline{n(h)} a(\lambda) \sec\theta}{L_n}\right) \qquad \ldots (3.11)$$

The value of the quantity x, defined by (3.10), is shown in Table 3.2 at heights of 70, 60, 50 and 40 kilometres and at wavelengths of 2400, 2500, 2600, 2700 Angstroms.

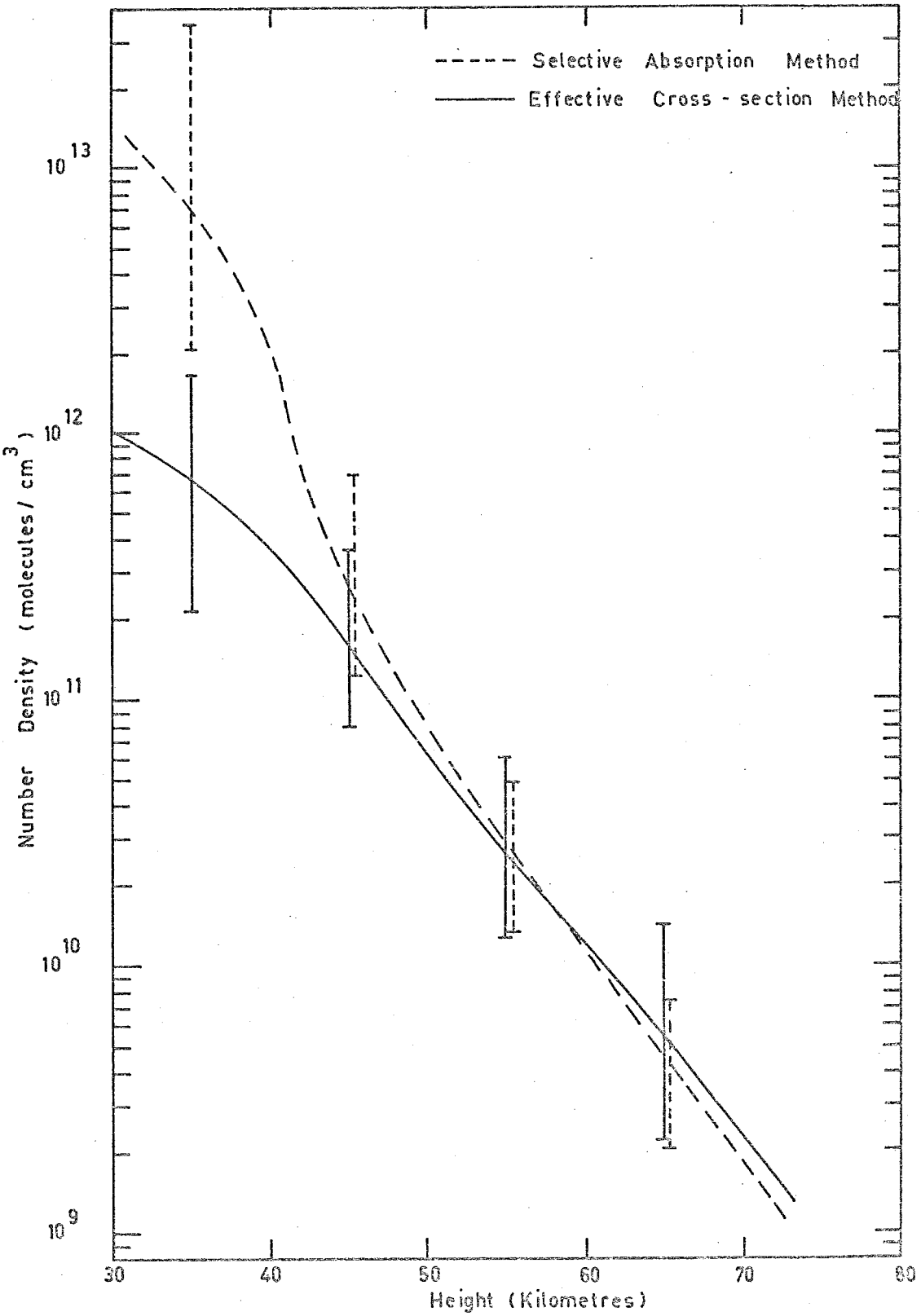

Figure 3 - 15 Average number densities obtained by using the effective cross - section method and selective absorption method.

	Height (Kms)			
λ(Å)	40	50	60	70
2400	4.441	1.421	.0213	.0036
2500	6.197	1.983	.0297	.0050
2600	5.928	1.897	.0285	.0047
2700	4.234	1.355	.0203	.0039

Table 3.2

Table 3.2 clearly shows that the effective cross-section method becomes more and more inaccurate at lower altitudes.

The effect of a varying absorption coefficient on the flux at different altitudes is shown in Figure 3.16. The values used in the calculation of $F(h,\lambda)/F(h_{max},\lambda)$ were those for the C1014 2500Å detector.

It should be noted that equations (3.5) and (3.6) can be used to obtain the result

$$\frac{1}{\overline{F(h)}}\frac{d\overline{F(h)}}{dh} = -\frac{\int F_\infty(\lambda)a(\lambda)\sec\theta\frac{dN(h)}{dh}\exp\left[-\frac{a(\lambda)}{L_n}N(h)\sec\theta\right]S(\lambda)d\lambda}{L_n\int F_\infty(\lambda)\exp\left[-\frac{a(\lambda)}{L_n}N(h)\sec\theta\right]S(\lambda)d\lambda}$$

If a narrow band detector is used to ensure that $a(\lambda)$ does not vary, or if the absorption measurements are carried out in a region of the spectrum where $a(\lambda)$ is constant or varies very slowly, the above expression reduces to the simple form

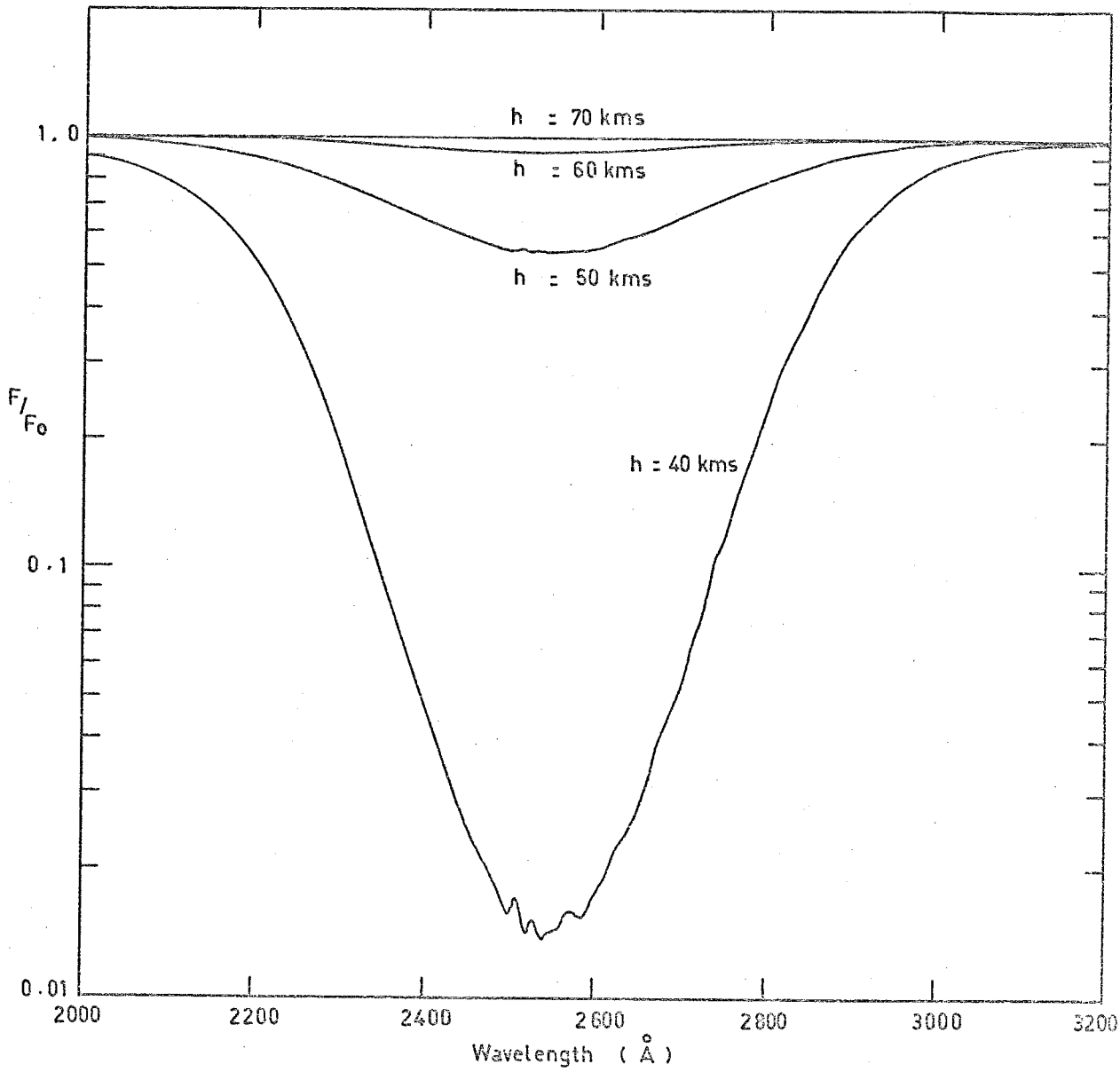

Figure 3.16 Plots of the ratio $\frac{F(h,\lambda)}{F(h_{max},\lambda)}$ as a function of altitude.

$$\frac{1}{\overline{F(h)}} \frac{d\overline{F(h)}}{dh} = - \frac{a(\lambda)\sec\theta}{L_n} \frac{dN(h)}{dh}$$

and this equation is identical in form with the equation obtained by forming $\frac{1}{I(h)} \frac{dI(h)}{dh}$ from equation (3.1), except that $\frac{a(\lambda)}{L_n}$ appears in place of $\overline{\sigma}$.

The conclusion to be drawn from this analysis is that the effective cross-section method will be a reasonable approximation if $a(\lambda)$ is constant or slowly varying across the pass-band of the photometer, or if the condition (3.10) is true. As it is very difficult to satisfy both these conditions using broad band photometers it is essential to have accurate information about the spectral distribution of lunar flux to enable the selective absorption calculations to be carried out accurately.

3.4 Comparison with Results of Other Measurements of Atmospheric Ozone

Figure 3.17 shows a comparison of the present results with the results of nocturnal measurements made by other workers. The results selected for comparison were chosen because they have been obtained by a wide variety of techniques. Randhawa (1966) and Hilsenrath (1971) have used rocket-borne chemiluminescent sondes. Horton (1968) and Weeks and Smith (1968b) used the absorption method, while Reed and Scolnik (1964) obtained their results from photometric measurements of airglow intensities. All these results have been reduced to units of mole-

Figure 3.17 Comparison of nocturnal ozone measurements in the 25-80 kilometre height range

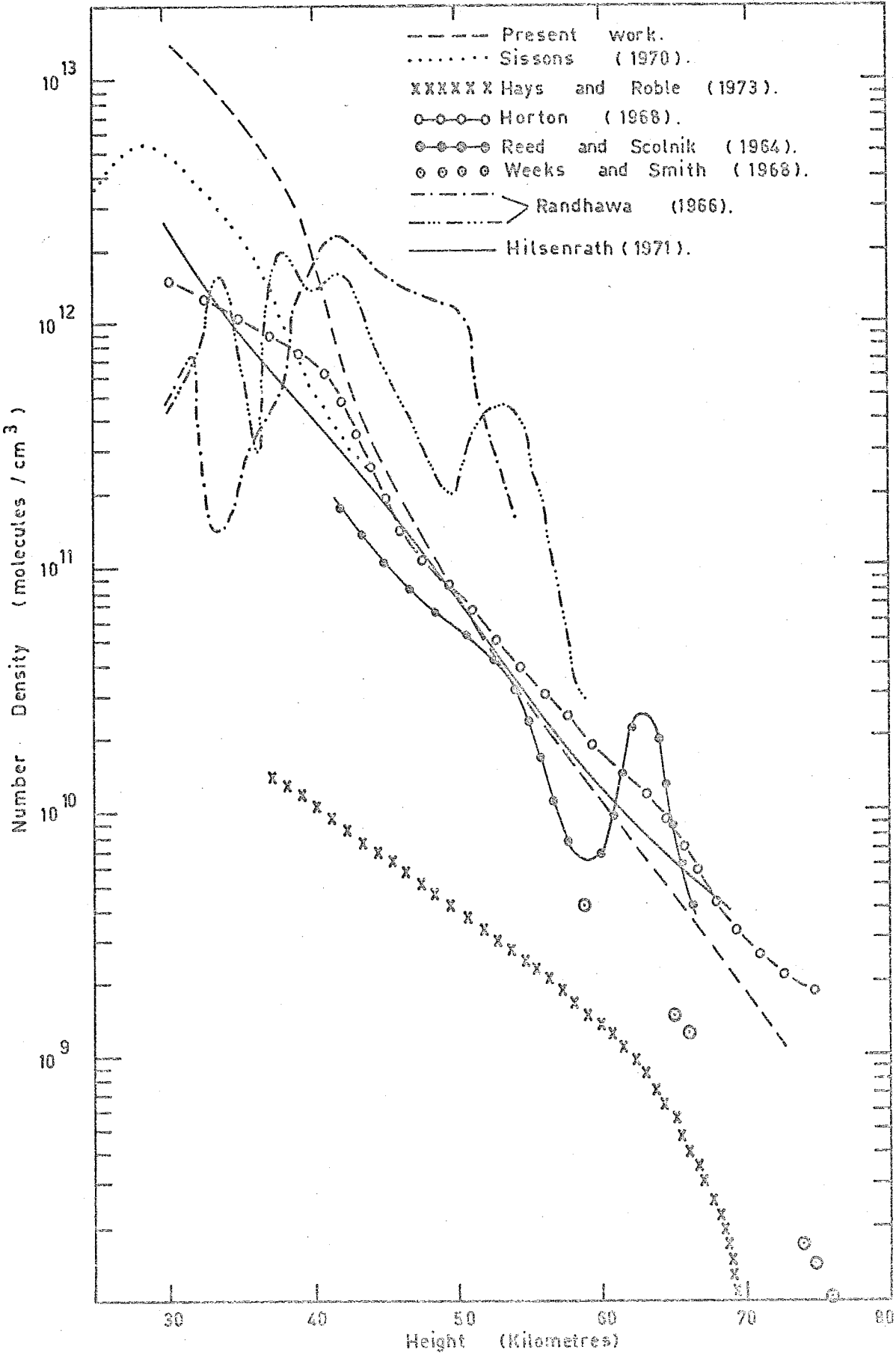
Present work.
Sissons (1970).
Hays and Roble (1973).
Horton (1968).
Reed and Scolnik (1964).
Weeks and Smith (1968).
Randhawa (1966).
Hilsenrath (1971).
Number Density (molecules / cm 3)
10 13
10 12
10 11
10 10
10 9
30
40
50
60
70
80
Height (Kilometres)

cules per cubic centimetre. The results of Randhawa (1966) have been extracted from his graphical representation and may not be a fair representation of the figures he obtained, particularly at high altitudes; the reason for this is the linear form of the plots, making errors in reading the values above 45 kilometres comparable with the values themselves.

The results of Poloskov et al. (1967) and Venkateswaran et al. (1961) which were based on absorption measurements in the Chappuis bands of the ozone absorption spectrum, have not been shown, but they deviate markedly from the results shown, particularly at higher altitudes.

Hays and Roble (1973) have made stellar occultation measurements of ozone concentration using the OAO-2 satellite. The average number densities resulting from these measurements are also shown in Figure 3.17. Since these occultation measurements involve path lengths of some thousands of kilometres in the earth's atmosphere and the ozone concentration is known to vary with longitude and latitude (Kulkarni and Garnham, 1970) the accuracy of these measurements is in some doubt.

The low altitude results of daylight measurements by Sissons (1970) are also included for comparison, since there should be very little change in number density from day to night at lower altitudes. This problem was discussed in Chapter 1, where it was suggested that the ozone at lower altitudes is shielded from the effects of solar ultraviolet radiation because of absorption by ozone at higher altitudes.

Figure 3.18 A segment of the telemetry record from Cockatoo 105 showing the lunar signals and the secondary signals discussed in Section 3.5

It can be seen from these results that there is a need to extend the ozone number density measurements to higher altitudes. As the attenuation of incident ultraviolet radiation is very small at altitudes above 60 kilometres these measurements will have to be made at high zenith angles to ensure that the path length traversed by the radiation in passing through the atmosphere is as long as possible.

3.5 Effects of Rayleigh Scattering on the Aspect Sensors

The signals obtained during the flight of Cockatoo 105 showed two features which were peculiar to this one flight. One of these features is shown clearly on the section of the film record shown in Figure 3.18. The lunar signal is easily recognized from the sharp peaks in the aspect sensor output and the peaks in the sensor outputs. However, between the lunar signals the aspect sensor produced an output which was quite distinct from that which would be produced by a point source. This series of peaks is designated on Figure 3.19 by (a). The outputs from the ultraviolet sensors also increased simultaneously with the aspect sensor output.

From the description of the aspect sensor in Chapter 2 we can see that a point source could not produce an aspect sensor output of the type shown. In fact a point source should produce peaks in which the signal changes very rapidly as the source moves across the edges of the slits in the arrowhead plate. One way of producing the signals shown would be a

source in the shape of a broad band (there are several other possibilities as well) with its direction making a fairly small angle with the direction of the centre slit of the arrowhead plate. (If the band was at approximately ninety degrees to the centre slit the aspect sensor output would only show a single broad peak).

The first step is to locate an approximate position for this "secondary" source; this can be done as follows. If the rocket axis was vertical the emitting band would also have to be approximately vertical; similarly, if the rocket axis was horizontal the emitting band would have to be approximately horizontal. Looking at the time spacing between the lunar peaks and the secondary peaks shows that the time separation between the various peaks is as shown in Figure 3.19. Since the rocket makes one complete revolution in time $t_1 + t_2$ this means that

$$t_1 + t_2 \equiv 360^\circ \simeq 1.36 \text{ secs} \qquad \ldots (3.12)$$

If Z is the lunar zenith angle at the launching point then the situation is as shown in Figure 3.20. ϕ is the zenith angle of the secondary source. From Figure 3.20 it can be seen that if ω is the angular velocity of rotation of the rocket about its axis

$$t_1 \equiv \frac{\phi + Z}{\omega} \simeq .76 \text{ secs} \qquad \ldots (3.13)$$

or

$$t_2 \equiv \frac{\phi + Z}{\omega} \simeq .60 \text{ secs}$$

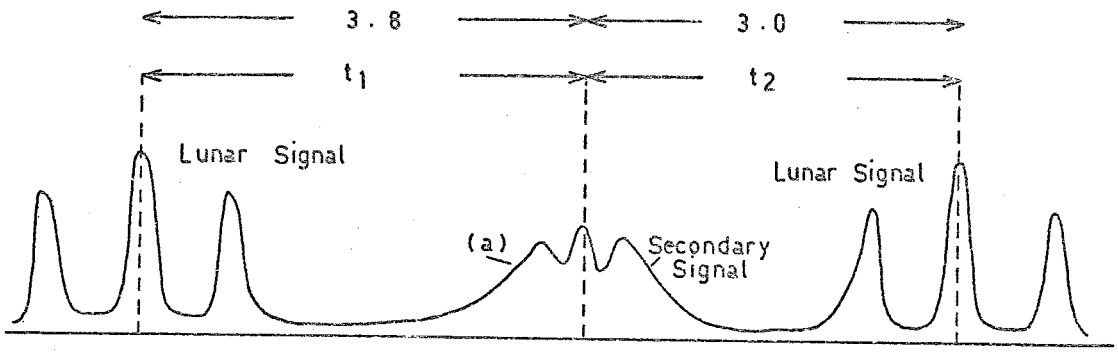

Figure 3.19 Time spacing between the two types of aspect signal.

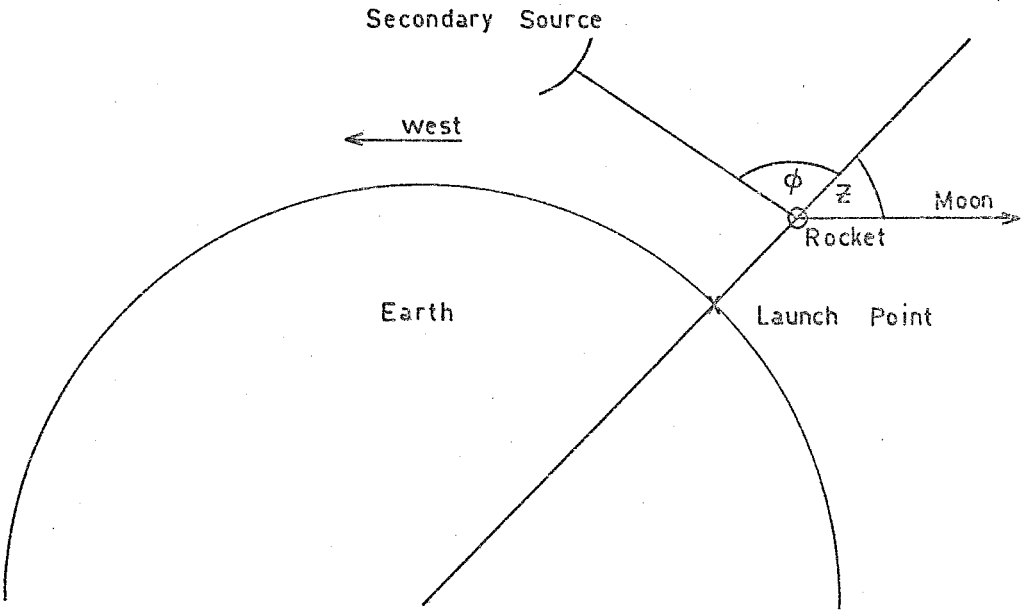

Figure 3.20 The relationship between the earth, moon and the secondary source.

For C105, Z was approximately 64° so combining this and equations (3.12) and (3.13) gives

$$\phi \simeq 95° \quad \text{or} \quad 137°$$

The value $\phi = 137°$ suggests a ground-based source. Since there are no large cities or towns within 1,000 miles to the west of the launch site a ground-based source is highly unlikely. The value $\phi = 95°$ suggests a source on the western horizon; the obvious possibility is radiation from the sun being scattered into the atmosphere at high altitudes.

To examine this possibility more closely consider the situation shown in Figure 3.21. The rocket is at P and BP is the line of sight. DX is the direction of incident radiation. x is the minimum height of the line DX above the earth's surface, z is the minimum height of the line BP, and θ is the solar depression angle. The problem is to calculate y, the height of the point of intersection of the line of sight with the direction of the incident radiation.

The geometry of Figure 3.21 shows that

$$(R+x) = (R+h)\cos\theta \qquad \ldots (3.14)$$

$$\therefore \quad h = \frac{R+x}{\cos\theta} - R \qquad \ldots (3.15)$$

$$\text{Also} \quad \frac{R+z}{R+l} = \sin(\pi-\phi) = \sin\phi \qquad \ldots (3.16)$$

$$\text{and} \quad \frac{R+z}{R+y} = \cos\alpha \qquad \ldots (3.17)$$

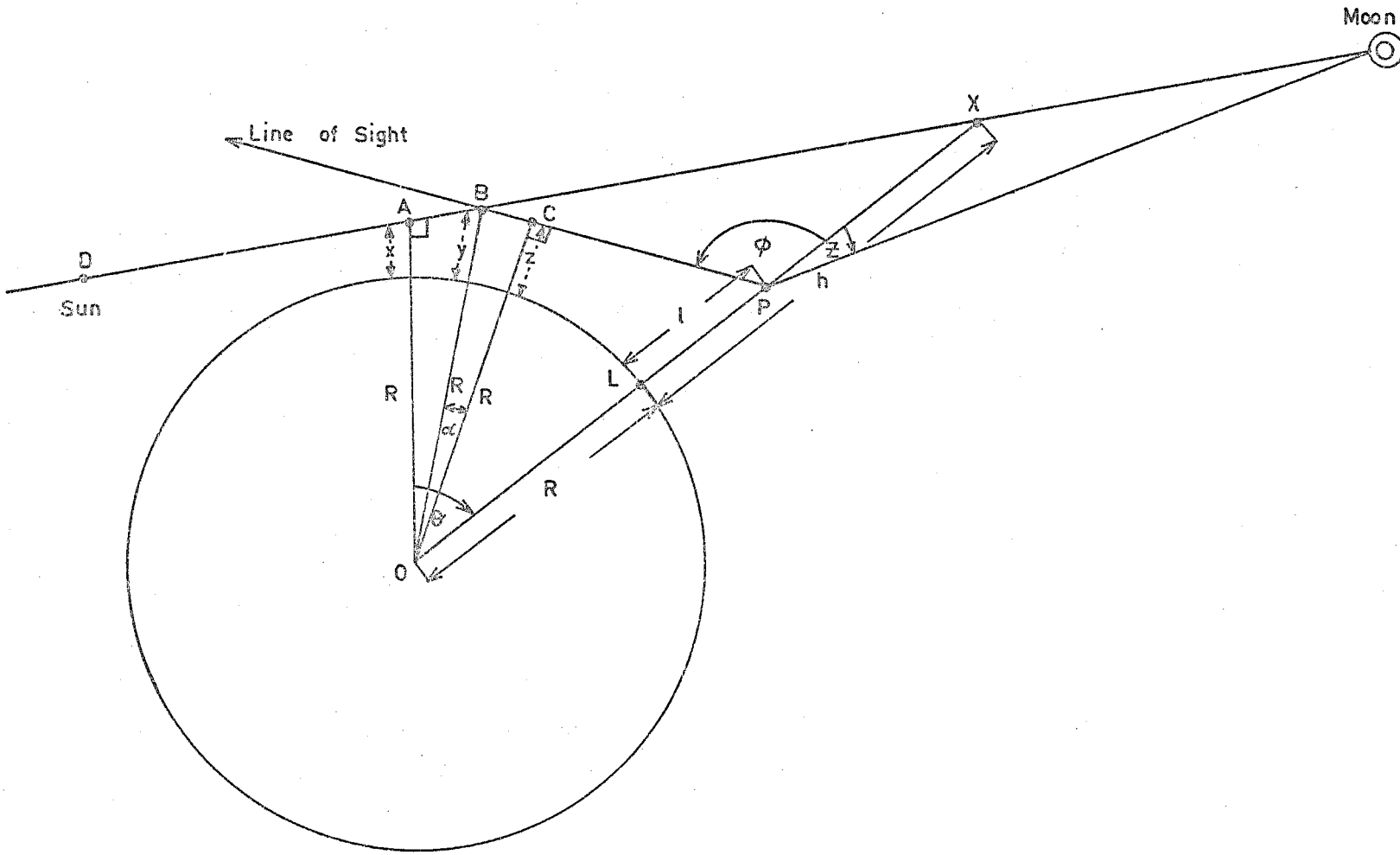

Figure 3.21 Geometry of horizon glow measurements. Angle θ is shown greatly exaggerated for clarity.

Applying the Sine Rule to triangles BPX and BPO gives

$$\frac{BP}{\sin(\frac{\pi}{2} - \theta)} = \frac{h-1}{\sin(\frac{\pi}{2} + \theta - \phi)} \qquad \ldots (3.18)$$

$$\frac{BP}{\sin(\alpha+\phi - \frac{\pi}{2})} = \frac{R+y}{\sin(\pi-\phi)} \qquad \ldots (3.19)$$

Eliminating BP from (3.18) and (3.19) leads to

$$\frac{(h-1)\cos\theta}{\cos(\phi-\theta)} = \frac{-(R+y)\cos(\alpha+\phi)}{\sin\phi} \qquad \ldots (3.20)$$

Eliminating α and h from (3.20) by means of (3.17) and (3.15) respectively gives

$$\frac{R+x-(R+1)\cos\theta}{\cos(\phi-\theta)} = \frac{-(R+y)\left[\left(\frac{R+z}{R+y}\right)\cos\phi - \left(1-\left(\frac{R+z}{R+y}\right)^2\right)^{\frac{1}{2}}\sin\phi\right]}{\sin\phi}$$

$$= \frac{\left[(R+y)^2 - (R+z)^2\right]^{\frac{1}{2}}\sin\phi - (R+z)\cos\phi}{\sin\phi} \qquad \ldots (3.21)$$

Solving for y and eliminating z by means of (3.16) gives

$$y = \left[\left[\frac{(R+x) - (R+1)\cos\theta)}{\cos(\phi-\theta)} + (R+1)\cos\phi\right]^2 + (R+1)^2\sin^2\phi\right]^{\frac{1}{2}} - R \qquad \ldots (3.22)$$

Since C105 was launched 90 minutes after local sunset the value

of θ was 22½ degrees. The value of 1 was set at 90 kilometres, R was made equal to 6320 kilometres and values of y were calculated using x and φ as parameters. The results are shown in Table 3.3.

x \ φ	70°	80°	90°	92.5°	95°	97.5°
0	315	259	174	145	111	74
10	321	264	178	149	115	78
20	327	270	182	153	119	83
30	333	275	187	157	124	87
40	340	281	191	162	128	92
50	346	286	196	166	133	98
60	352	291	201	171	138	103

Table 3.3 Values of y (in equation 3.22), calculated as a function of x (vertical axis) and φ (horizontal axis). (Refer to Figure 3.21 for nomenclature)

Stergis (1966) has calculated the scattered intensity produced by Rayleigh scattering as a function of altitude for different wavelengths and different angles of incidence. Although he has confined himself to radiation which has been scattered through an angle of 45 degrees, the intensity of the scattered light would be higher in the problem under consideration here because the scattering angle is smaller and the intensity distribution for Rayleigh scattering is a maximum for forward or back-scattering. The intensities computed by Stergis show that the intensity of the radiation scattered at

height of 50-150 kilometres would indeed be sufficient to register on the aspect sensor. In fact the intensity produced by scattering at an altitude of 100 kilometres would be of the order of 50 Rayleighs/steradian/100 Angstroms so that the integrated intensity over the wavelength region 4000Å-6000Å would be approximately 1000 Rayleighs/steradian. For a mean wavelength of 5000Å this corresponds to an energy flux of 1×10^{-7} ergs/ster/cm^2/sec/Å. Considering that this (following Stergis) is for radiation scattered at just one altitude shows that the effect of integrating the scattered intensity along the line of sight would be to greatly increase the intensity of the scattered radiation. Comparing these numbers with the ultraviolet fluxes obtained in Section 3.2.5 shows that the aspect sensor would certainly respond to the scattered light produced in this way.

These secondary signals were not seen on the records from C104 and C1014, but as these two rounds were fired 120 and 180 minutes after sunset respectively the scattered intensities would be much lower. Using equation (3.22) the values of y were calculated for C104 and C1014 with x = 0 and 1 = 90 kilometres. These values are shown in Table 3.4.

Stergis' results show that the scattered intensity decreases by at least three orders of magnitude as the point of scattering changes from 75 to 150 kilometres, so it is quite reasonable that the effects of Rayleigh scattering would only be important for C105.

ϕ	(C105)	(C104)	(C1014)
70°	315	499	1003
80°	259	402	801
90°	174	272	570
92.5°	145	232	507
95°	111	189	441
97.5°	74	142	373

Table 3.4 Values of y (in kilometres) for C105, C104 and C1014 as a function of ϕ. (Refer to Figure 3.21 for nomenclature)

3.6 Effects of Airglow on the Ultraviolet Sensors

The second effect peculiar to the results of C105 was a systematic variation of the aspect-corrected photometer outputs with aspect angle. During the high altitude part of the flight the signals obtained with positive aspect angles were much higher than those obtained with negative aspect angles. The uncorrected signal, aspect angle, detector zenith and aspect-corrected signal are shown as a function of height for the 2500Å photometer in Table 3.5.

The marked change in the detector zenith between 42.6 and 43.5 kilometres was due to the rocket tipping over because of the effect of air drag on the rocket fins. The data in Table 3.5 refers to the downward leg of the flight so that at high altitudes the nose of the rocket was pointing upwards.

The scatter in the values in the final column was very

Height (Kilometres)	Signal (Millivolts)	Aspect (Degrees)	Detector Zenith (Degrees)	Corrected Signal (Millivolts)
33.2	335	- 18.2	82.12	390
34.8	388	- 12.8	76.72	415
36.2	413	- 11.6	75.52	437
37.9	352	- 21.3	85.22	438
38.6	357	- 20.4	84.32	434
40.6	453	- 16.9	80.82	513
42.6	464	- 17.8	81.72	536
43.5	562	- 19.7	44.22	673
45.8	769	- 9.2	54.72	796
48.0	611	+ 22.2	86.12	796
49.3	1050	- 6.3	57.62	1069
52.0	1040	+ 13.8	77.72	1127
53.1	1200	- 9.6	54.32	1246
55.7	1060	+ 16.2	80.12	1194
57.0	1450	0.0	63.92	1450
61.1	1350	+ 11.6	75.52	1424
62.4	1520	- 5.6	58.32	1543
63.7	1170	+ 18.4	82.32	1376
66.2	1070	+ 20.5	84.42	1329
67.1	1610	0.0	63.92	1610
68.3	1600	- 5.7	58.22	1620
69.5	1550	0.0	63.92	1550
70.6	1120	+ 21.1	85.02	1411
76.0	1600	+ 7.5	71.42	1636
77.1	1040	- 26.6	37.32	1516
81.1	1280	- 19.2	44.72	1517
82.0	1630	0.0	63.92	1630
82.8	960	- 25.9	38.02	1360
86.6	1000	- 24.4	39.52	1351
87.3	1730	+ 5.1	69.02	1747
88.1	980	- 28.1	35.82	1503

Height	Signal	Aspect	Detector Zenith	Corrected Signal
(Kilometres)	(Millivolts)	(Degrees)	(Degrees)	(Millivolts)
91.1	1000	- 27.5	36.42	1497
91.8	1720	0.0	63.92	1720
92.3	1120	- 25.3	38.62	1556
95.3	920	- 27.6	36.32	1383
95.7	1730	0.0	63.92	1730
96.2	1170	- 23.6	40.32	1550
98.9	1650	+ 7.7	71.62	1689
99.3	1300	- 17.9	46.02	1537
100.9	784	- 30.0	33.92	1275
101.2	1700	+ 6.5	70.42	1728
101.6	1350	+ 21.7	85.62	1731
102.9	1580	+ 11.2	75.12	1656
103.0	1410	- 14.3	49.62	1538
103.9	1580	+ 10.0	73.92	1639
104.0	1480	+ 17.8	81.72	1721

Table 3.5

much greater than that obtained for any of the photometers in C104 or C1014. The systematic variation of the lunar signal with aspect angle (i.e. with the detector zenith angle) suggests the presence of an emitting layer in the atmosphere. This can be seen from Figure 3.22, which shows that the path length l increases as the zenith angle ψ increases. It is a well known feature of airglow emission that the observed intensity increases as the zenith angle increases - this behaviour was observed in the signals from both the 2500Å and 2700Å detectors in C105.

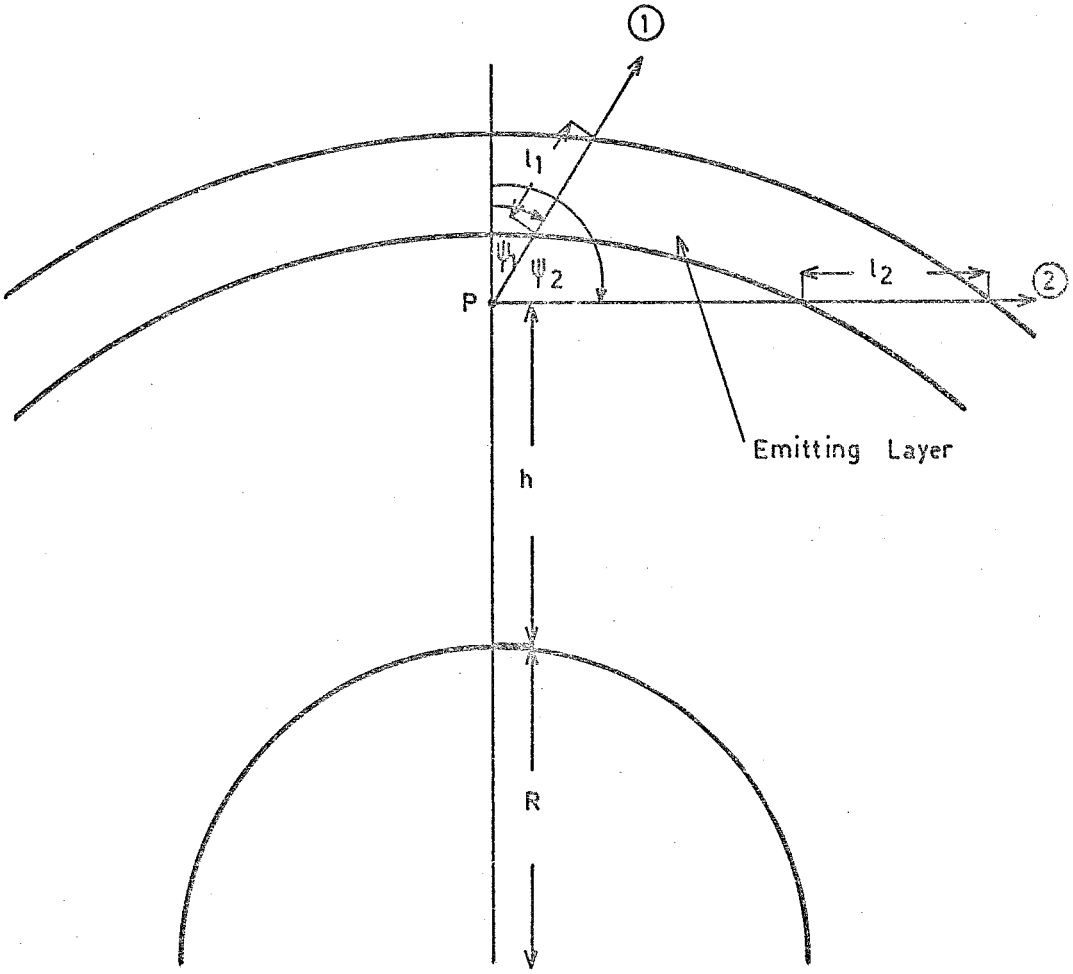

Figure 3 . 22 Effect of zenith angle on the path length through an emitting layer in the atmosphere.

The presence of such an emitting layer was suggested by the results of Tousey (1958), Stecher (1965), Krasnopolsky et al. (1966), Hennes (1966) and several other authors. Spectrophotoscopic studies of the airglow have been reviewed by Hunten (1967).

Another possible explanation of the C105 results is Rayleigh scattering of radiation which has already been scattered into the shadowed region of the atmosphere. The segment of film record in Figure 3.18 shows that both the visible (aspect) and ultraviolet signals in the anti-moon direction were of the same order of magnitude as the lunar signals. The lunar ultraviolet flux at 2500Å is of the order of 1 Rayleigh/Angstrom, so the flux measured in the anti-moon direction is of this order. Assuming that this flux is produced by Rayleigh scattering, the ratio of scattered flux to incident solar flux (Brinkmann, Green and Barth, 1966) is approximately 10^{-6}. The results of Stergis (1966) suggest that if the radiation which has been scattered into the shadowed region of the atmosphere is then backscattered towards the detector the intensity of this backscattered radiation would be negligible by comparison with the lunar flux.

3.7 Theoretical Computations of Airglow Intensities

In computing the absorption and emission of radiation in the atmosphere it is usual to start from the equation of radiative transfer. The solution of this equation for the particular

problem being considered here can be written (referring to Figure 3.23) as

$$I(s,\underline{s}) = I(o,\underline{s})e^{-\tau(o,s)} + \int_o^s J(s',\underline{s})e^{-\tau(s',s)}ds' \qquad \ldots (3.23)$$

where $I(o,\underline{s})$ is the intensity of radiation, outside the atmosphere, in the direction of the vector $\underline{s}$

$I(s,\underline{s})$ is the intensity of radiation at s in the direction of the vector $\underline{s}$

$J(s',\underline{s})$ is the intensity per unit length emitted at the point s' in the direction of the vector $\underline{s}$

$\tau(s',s)$ is the optical thickness of the absorbing material between the points s' and s

$$\text{i.e. } \tau(s',s) = \int_{s'}^{s} n(x)\sigma dx \qquad \ldots (3.24)$$

where $n(x)$ is the number of absorbing particles per unit volume at x', and

σ is the absorption cross-section for a single particle

It should be noted that the form of (3.23) is only valid for a single absorbing species - in the problem under consideration this assumption is certainly reasonable.

Equation (3.23) can be physically interpreted in the following way. The first term on the right hand side represents the intensity coming in from outside the atmosphere,

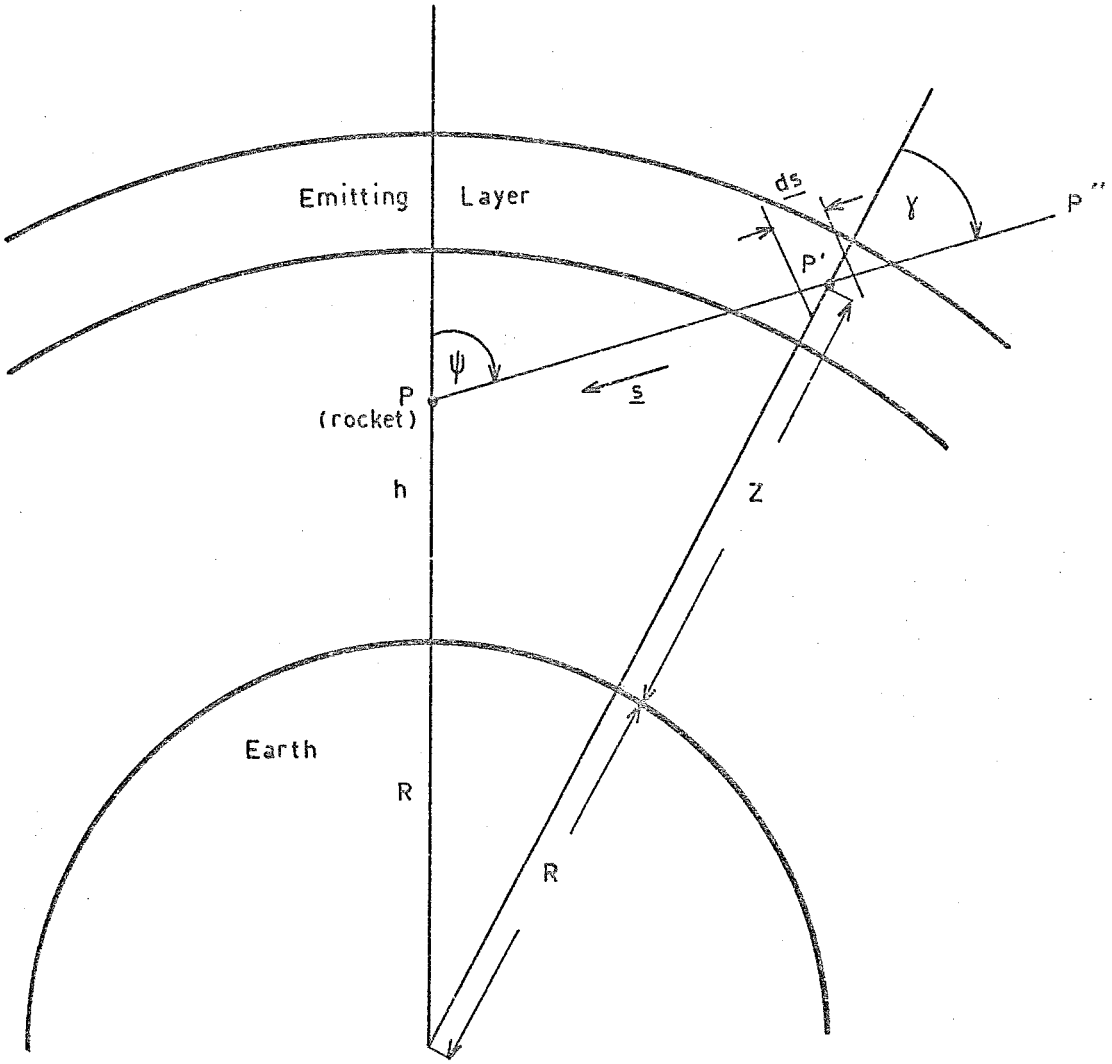

Figure 3 . 23 Showing the relation between the earth, the rocket and the emitting layer.

multiplied by the attenuation factor corresponding to absorption in the atmosphere, while the second term represents the integrated emission along the line of sight, the contribution at each point being attenuated by the absorbing material between the point of emission and the detector. A formal derivation of (3.23) can be found in most text-books on radiative transfer, e.g. Chandrasekhar (1950).

From Figure 3.23 it can be seen that

$$ds = - \sec\gamma \, dz \qquad \ldots (3.25)$$

where $\gamma = \gamma(z)$ is the zenith angle along the line of sight at P'.

Applying the Sine Rule to triangle OPP' gives

$$\frac{R+h}{\sin\gamma} = \frac{R+z}{\sin\psi} \qquad \ldots (3.26)$$

where R is the radius of the earth

h is the height of the rocket

z is the height of point P'

ψ is the zenith angle along the line of sight at the rocket

Solving (3.26) for $\sec\gamma$ and substituting in (3.25) gives

$$ds = - \mu(z,\psi)dz \qquad \ldots (3.27)$$

where

$$\mu(z,\psi) = \frac{1}{\left(1 - \left(\frac{R+h}{R+z}\right)^2 \sin^2\psi\right)^{\frac{1}{2}}} \qquad \ldots (3.28)$$

Noting that the points s = o, s = s', s = s correspond to z = ∞, z = z and z = h respectively, and substituting (3.27) into (3.23) and (3.24) gives

$$I(h,\underline{s}) = I(\underline{s})e^{-\tau(h,\infty)} + \int_h^\infty J(z,\underline{s})e^{-\tau(h,z)}\mu(z,\psi)dz \qquad \ldots (3.29)$$

where

$$\tau(h,z) = \int_h^z n(z)\sigma\mu(z,\psi)dz \qquad \ldots (3.30)$$

For this particular problem where there is only one external source, the moon, and an emitting layer which has cylindrical symmetry about the direction $\psi = 0$ so that equation (3.29) becomes

$$I(h,\psi) = I_M e^{-\tau(h,\infty)} + \int_h^\infty J(z,\psi)e^{-\tau(h,z)}\mu(z,\psi)dz \qquad \ldots (3.31)$$

where I_M is the lunar intensity and is zero in all directions except that of the moon.

The next problem is to convert from a frame of reference with respect to the earth to a frame of reference with respect to the detector. The first step is to find a relation between coordinates in the detector frame and the rocket frame and then between coordinates in the rocket frame and the earth frame. The first relation is found as follows: the rocket frame is denoted by axes OX, OY and OZ where OZ coincides with the

rocket axis and OY with the detector axis. (α,β) are the zenith and azimuth angles relative to OZ while (θ,ϕ) are the angles relative to OY as shown in Figure 3.24.

$$\text{Now} \quad X = r\sin\alpha\cos\beta = r\sin\theta\sin\phi$$
$$Y = r\sin\alpha\sin\beta = r\cos\theta \qquad \ldots (3.32)$$
$$Z = r\cos\alpha \quad = r\sin\theta\cos\phi$$

$$\cos\alpha = \sin\theta\cos\phi \qquad \ldots (3.33)$$

and

$$\tan\beta = \cot\theta\,\mathrm{cosec}\,\phi \qquad \ldots (3.34)$$

In considering the relation between the rocket frame and the earth frame there are two effects to consider:

(i) the tilting of the rocket axis relative to the zenith in the plane containing the moon and the zenith

(ii) an additional tilting of the rocket about the detector axis

The second effect will be neglected since a study of the aspect records showed that it was small. The earth and rocket frames are related as shown in Figure 3.25. The moon is assumed to be in the zOy (ZOY) plane.

Figure 3.25 shows that, if the zenith and azimuth angles in the earth frame are (ψ,χ) and if the rocket axis has tilted through an angle η in the xOy plane then

$$x = r\sin\psi\cos\chi = X$$
$$y = r\sin\psi\sin\chi = Y\cos\eta + Z\sin\eta \qquad \ldots (3.35)$$
$$z = r\cos\psi \quad = Z\cos\eta - Y\sin\eta$$

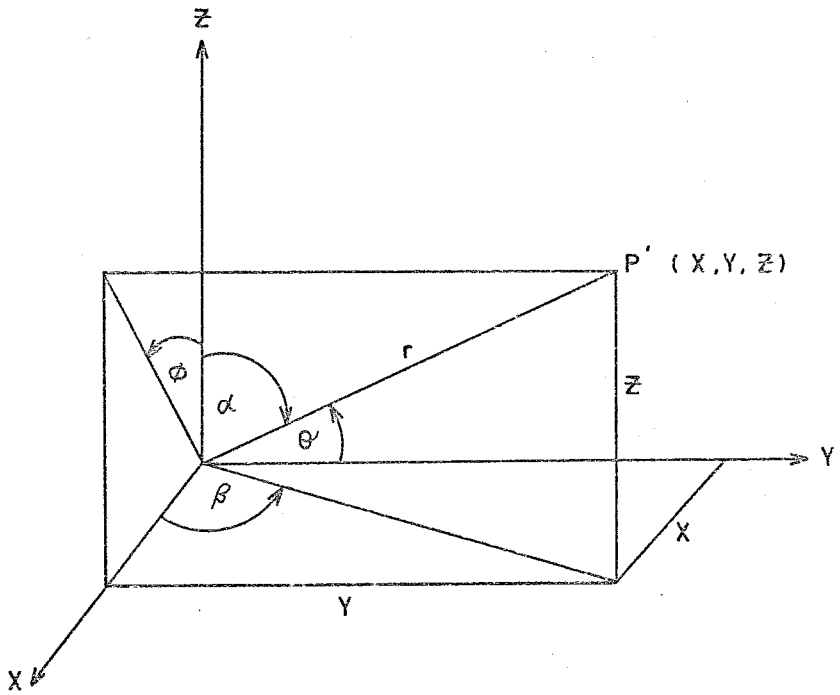

Figure 3 · 24 Geometry of the rocket and detector reference frames.

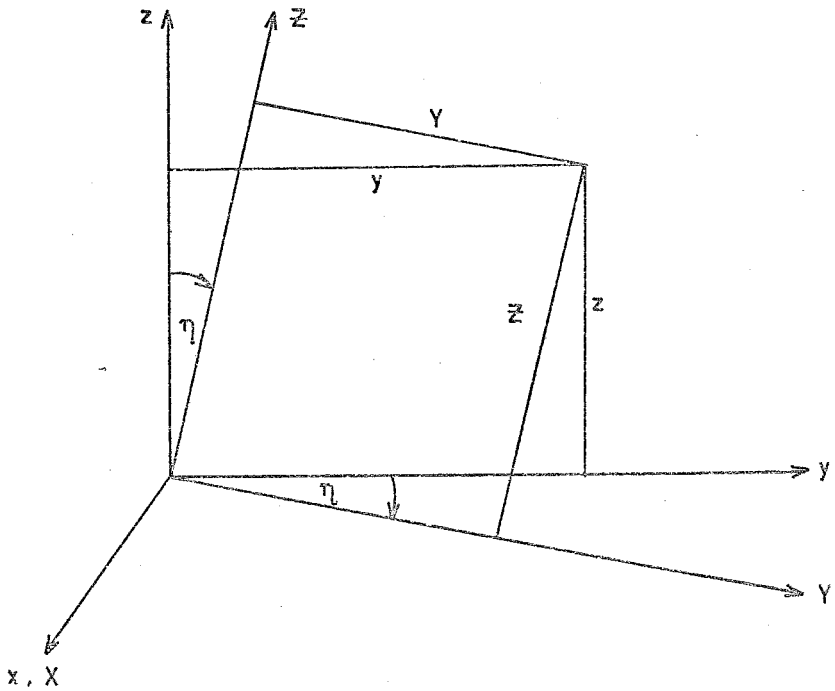

Figure 3 · 25 The relation between the earth frame (x,y,z) and the rocket frame (X , Y , Z) .

Substituting for Y and Z from (3.35) gives

$$\cos\psi = \cos\eta \sin\theta \cos\phi - \sin\eta \cos\theta \qquad \ldots (3.36)$$

If Z is the zenith angle of the detector axis then

$$Z = \frac{\pi}{2} + \eta \qquad \ldots (3.37)$$

Also, since the moon is in the ZOY plane and the lunar zenith angle is Z_M, then

$$Z = Z_M + A \qquad \ldots (3.38)$$

where A is the lunar aspect angle, i.e. the angle between the detector axis and the direction of the moon.

$$\therefore \quad \cos\psi = \sin(Z_M+A) \sin\theta \cos\phi + \cos(Z_M+A) \cos\theta \qquad \ldots (3.39)$$

Inserting this result in (3.31) gives the intensity of radiation reaching the detector at height h along a direction characterized by the angles (ψ,χ) relative to the earth frame.

If the angular response of the detector is $R(\theta,\phi)$ then the total signal given out by the detector is given by

$$S(h) = \int_{\Omega} R(\theta,\phi) I(h,\theta,\phi) d\Omega \qquad \ldots (3.40)$$

where Ω is the solid angle of the detector and $I(h,\theta,\phi)$ is given by (3.31). Since the element of solid angle is given by

$$d\Omega = \sin\theta \, d\theta d\phi \qquad \ldots (3.41)$$

the signal is given by

$$S(h) = I_M R(A,0) e^{-\tau(h,\infty,Z_M,0)} + \int_0^{2\pi}\int_0^{\pi}\int_h^{\infty} R(\theta,\phi) J(z,\theta,\phi) \mu(z,\theta,\phi) e^{-\tau(h,z,\theta,\phi)} \sin\theta \, dz d\theta d\phi \qquad \ldots (3.42)$$

where $\mu(z,\theta,\phi)$ is defined by (3.28), $\tau(h,Z,\theta,\phi)$ is defined by (3.30) and ψ is defined by (3.39) and (3.26).

A computer program was written to evaluate (3.42). The integration process was replaced by summation, with the atmosphere being divided up into layers one kilometre thick. The intensity reaching the bottom of each layer was computed by means of an iterative formula similar to (3.31), viz,

$$I(h_i,\psi) = I(h_{i+1},\psi) e^{-\tau(h_i,h_{i+1},\psi)} + \int_{h_i}^{h_{i+1}} J(z,\psi) e^{-\tau(h_i,z,\psi)} \mu(z,\psi) dz \qquad \ldots (3.43)$$

where

$$\tau(h_i,z,\psi) = \int_{h_i}^{z} \frac{\sigma n_i dz}{\left(1 - \left(\frac{R+h}{R+z}\right)^2 \sin^2\psi\right)^{\frac{1}{2}}} \qquad \ldots (3.44)$$

The value of n_i was taken to be constant over each interval. Values of n_i were taken from a profile derived by taking a smooth curve through the aspect corrected data for the appro-

priate detector and using the values taken from this smooth curve in equation (3.3) to derive $n(h_i)$. Since n_i is constant over the height interval h_i to h_{i+1} the integral in (3.34) can be readily evaluated to give

$$\tau(h_i,z,\psi) = \sigma n_i\left[s(z) - s(h_i)\right] \qquad \ldots (3.45)$$

where

$$s(z) = \left((R+z)^2 - (R+h)^2\sin^2\psi\right)^{\frac{1}{2}} \qquad \ldots (3.46)$$

The value of $J(z,\psi)$ was taken to be constant in each height interval and the emission was assumed to be isotropic so that J did not depend on ψ. If $J(h_i)$ is the emission per unit length in the height interval h_i to h_{i+1} then (3.43) can be evaluated to give

$$I(h_i,\psi) = I(h_{i+1},\psi)e^{-\sigma n_i[s(h_{i+1})-s(h_i)]} + \frac{J(h_i)}{\sigma n_i}\left[1 - e^{-\sigma n_i(s(h_{i+1})-s(h_i))}\right] \qquad \ldots (3.47)$$

Values of $I(h,\psi)$ computed by means of (3.47) were then fed into (3.40). The angular response of the detector was assumed to be cylindrically symmetric about the detector axis, i.e. no dependence on ϕ.

The emission profile used was a Gaussian function of the form

$$J(z) = J_a e^{-\left(\frac{z-a}{b}\right)^2} \qquad \ldots (3.48)$$

where the values of a and b could be changed until the best fit was obtained. Physically a represents the mid-point of the emitting layer and b is a measure of the thickness of the layer. This form was chosen after examining the results of Reed and Scolnik (1964), and Hennes and Dunkelman (1966).

The value of the cross-section was taken to be the same as that used in equation (3.3). Although not strictly valid this approximation was used because insufficient data was available to enable the cross-section to be calculated in terms of the airglow intensities.

The results of these computations for the C105 2500Å detector are shown in Figures 3.26, 3.27, 3.28, 3.29, 3.30 and 3.31. It was found that the model only worked satisfactorily up to a height of about 65 kilometres. One of the main reasons for this was the size of the solid angle increments used in evaluating s(h) in equation (3.42). Values of θ increased in steps of five degrees and values of ϕ in steps of ten degrees. This was not very important when the rocket was some distance below the emitting layer but became much more critical when the rocket was actually in, or very close to, the emitting layer. However, the results obtained for the increments used are encouraging - the best results are obtained for values of J_a, a and b equal to 1×10^{-13} (ergs/cm^2/secÅ)/cm.ster, 95 kilometres, and 6 kilometres respectively. In this case nearly all the corrected values of detector signal (in the region 30 to 65 kilometres) lie on a smooth curve. The zenith intensity at

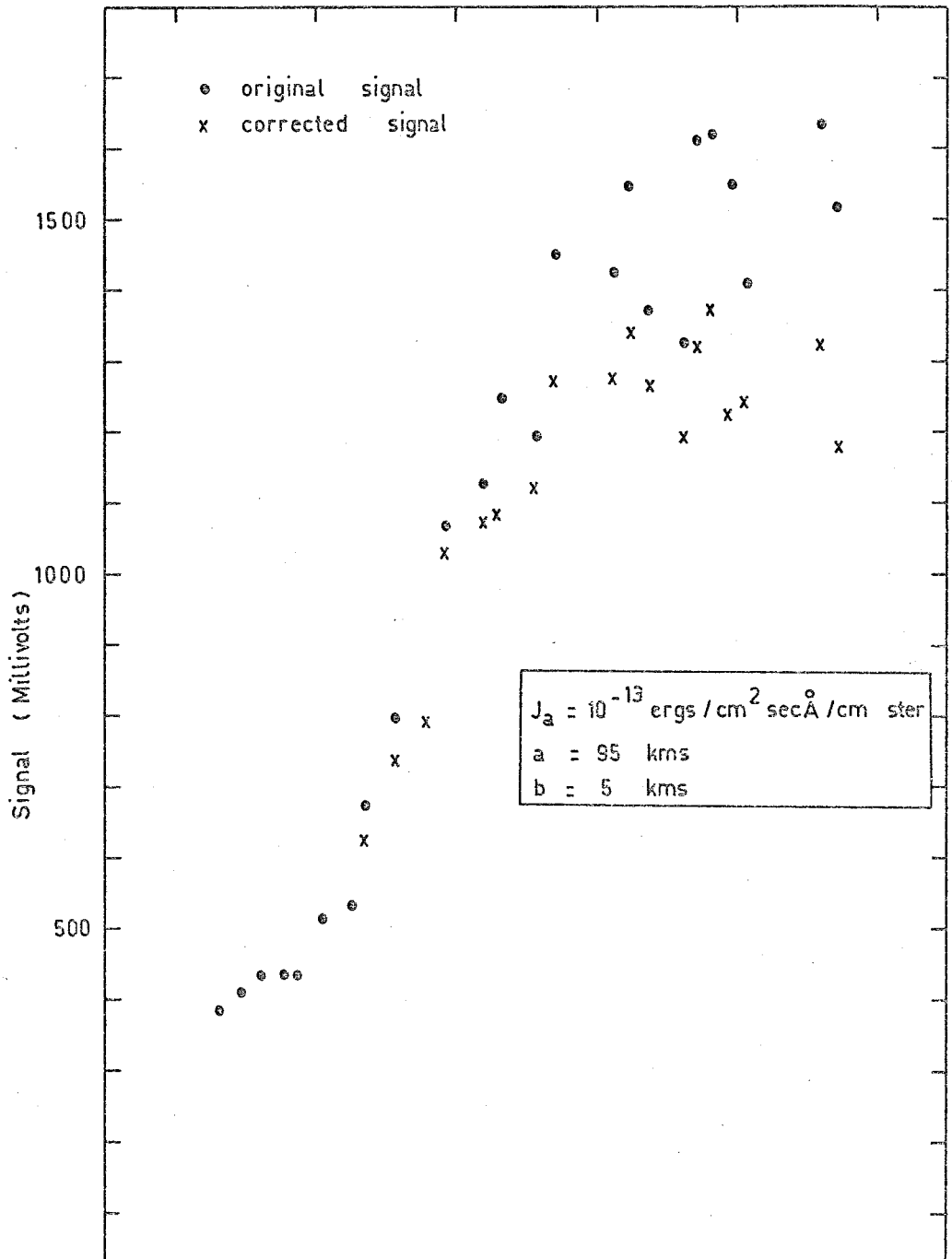

Figure 3 . 26 Effects of airglow on lunar signals.

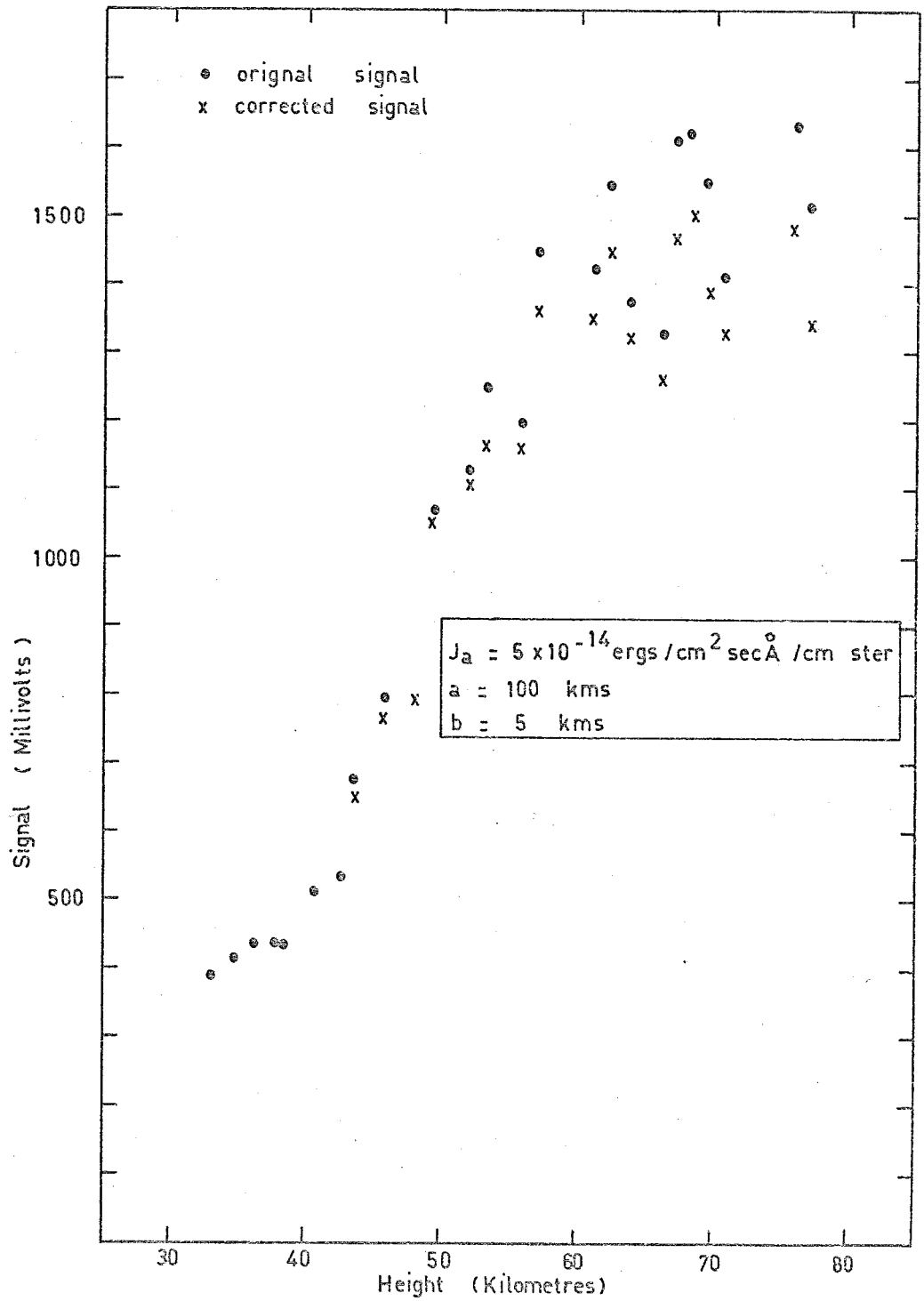

Figure 3 . 27 Effects of airglow on lunar signals.

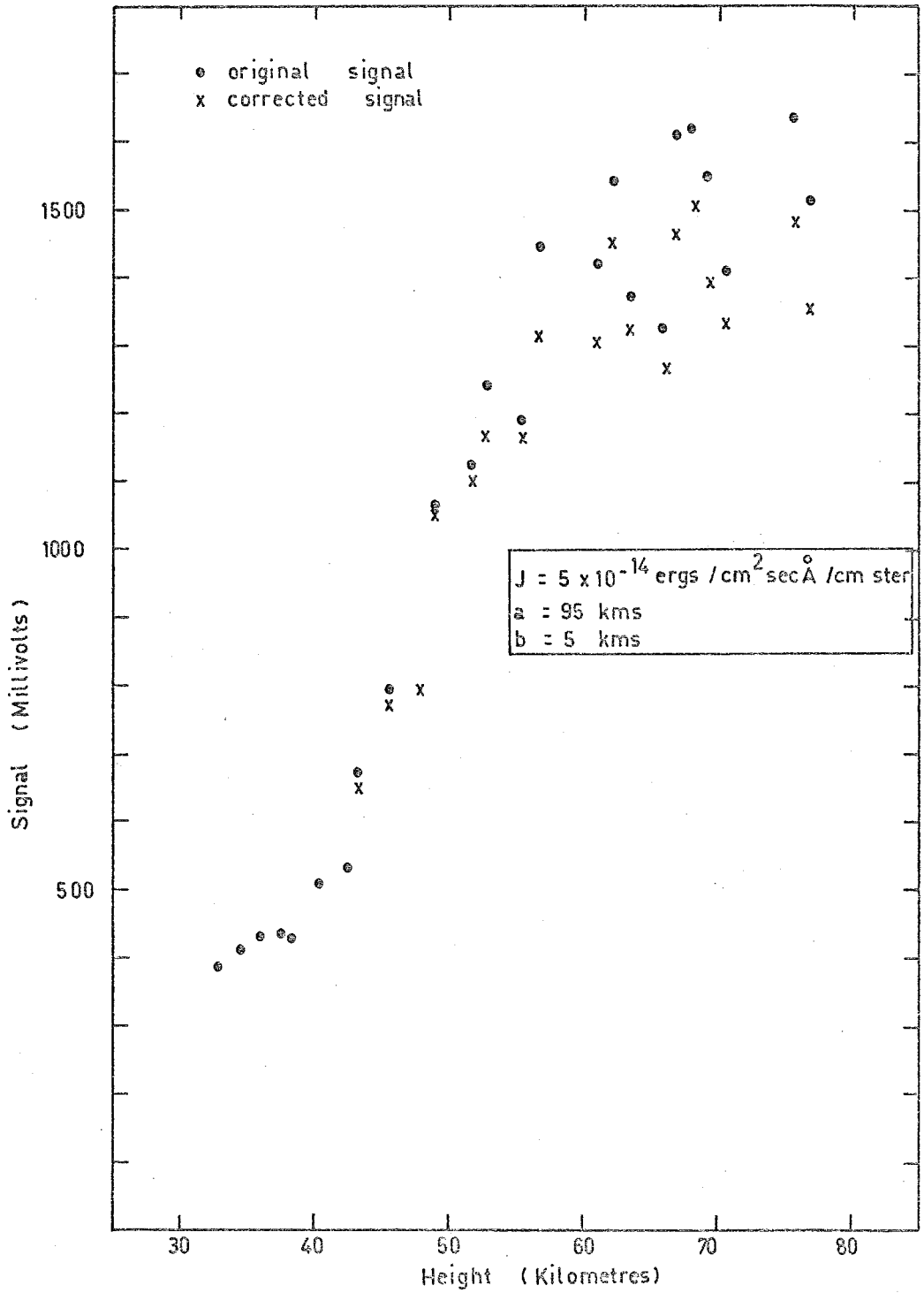

Figure 3.28 Effects of airglow on lunar signals.

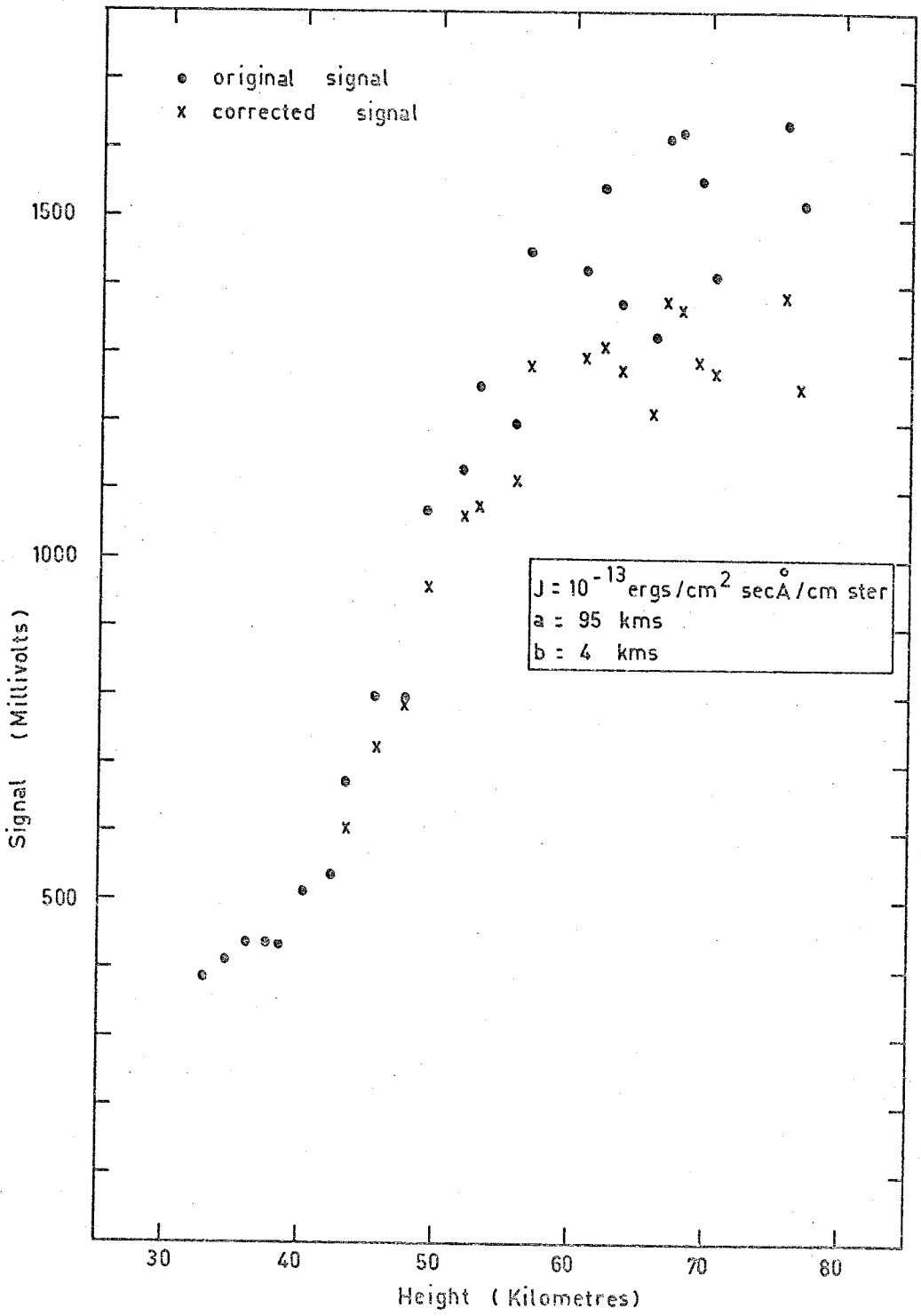

Figure 3 . 29 Effects of airglow on lunar signals.

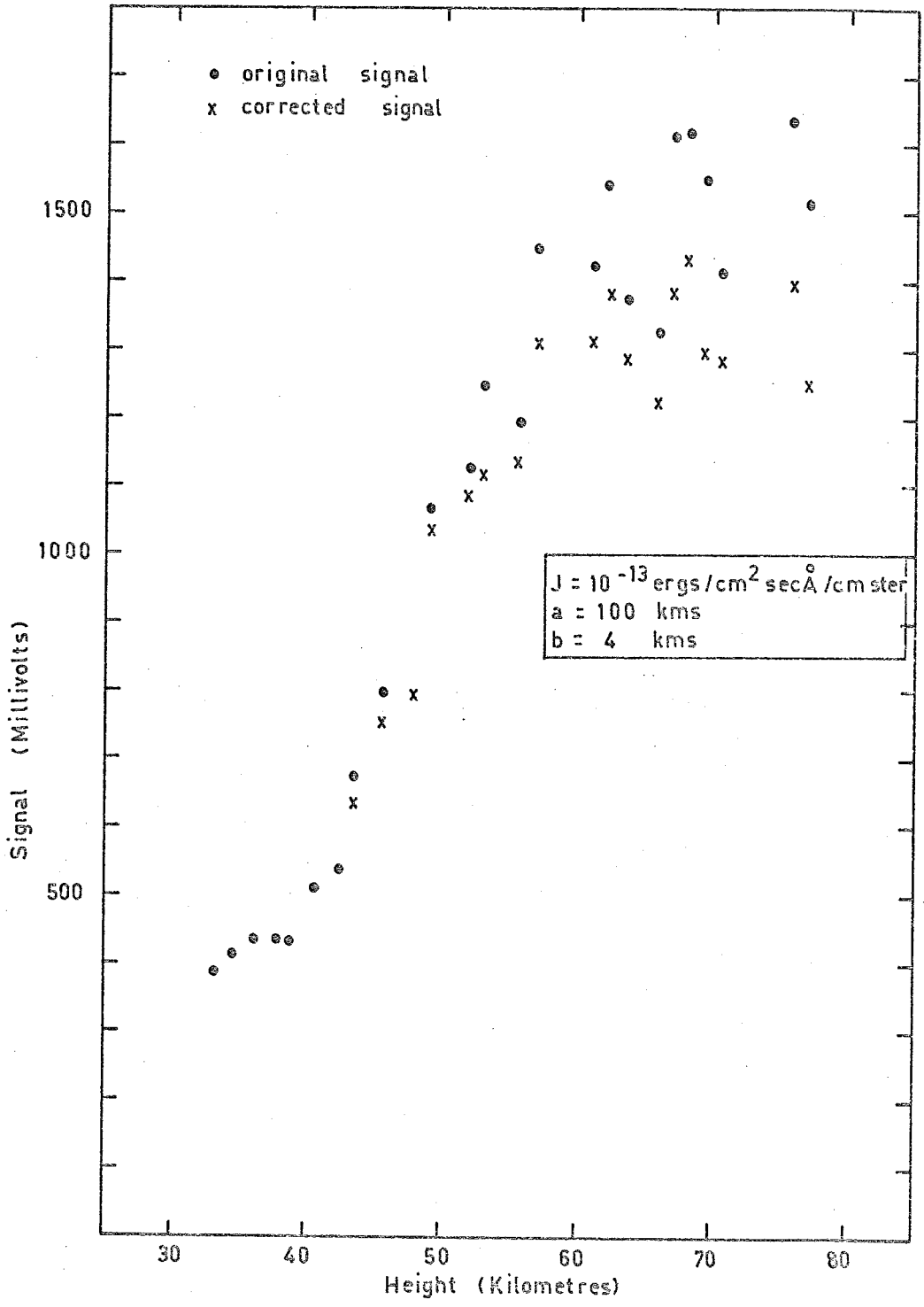

Figure 3 . 30 Effects of airglow on lunar signals.

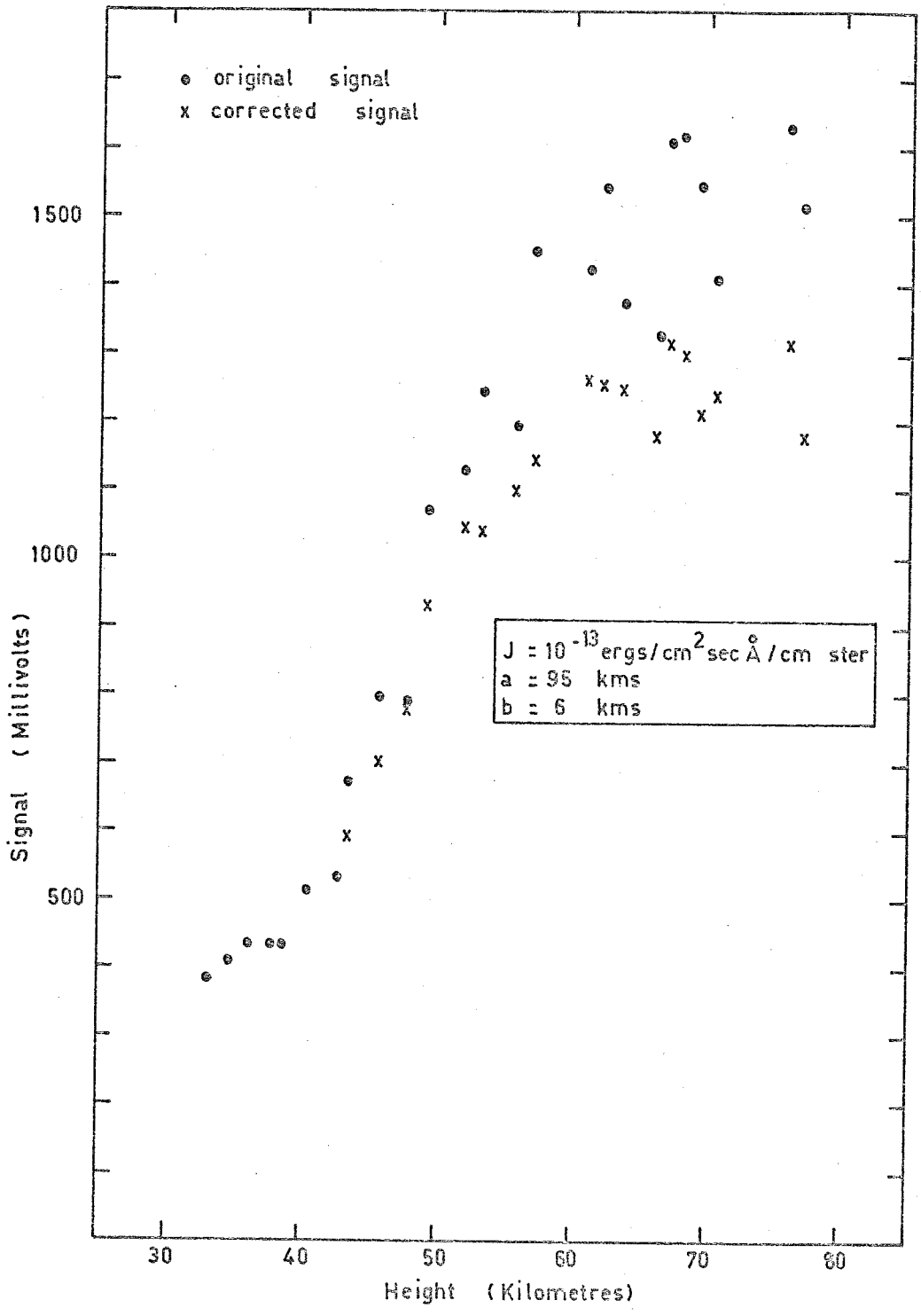

Figure 3.31 Effects of airglow on lunar signals.

65 kilometres in this case was calculated to be approximately 0.1 R/Å.

While these results are not conclusive they at least suggest that ultraviolet airglow emission may have a significant effect on measurements of lunar ultraviolet flux, at least up until approximately two hours after ground sunset.

3.8 Possible Sources of Ultraviolet Post-Twilight Airglow

The exact mechanism producing the ultraviolet airglow mentioned in the previous two sections is not well known. One possibility is the NO bands between 2000 and 3000Å (Barth, 1966) which occur in the dayglow and are emitted strongly in the region between 80-140 kilometres. The zenith intensity of these bands is approximately one kilo-Rayleigh at 80 kilometres. However, if this radiation is present in the nightglow with an intensity similar to the dayglow intensity, then it should easily have been detected by the photometers flown in C104, C105 and C1014.

Another possibility is emission by hydroxyl radicals. Bates and Nicolet (1950) suggest that this emission may be enhanced at twilight but would be of very low intensity. This would certainly not contradict the results calculated in the previous section.

CHAPTER 4

THE ULTRAVIOLET REFLECTIVITY OF THE LUNAR SURFACE

4.1 Introduction

Until the advent of rockets and satellites, with their ability to make observations from outside the earth's atmosphere, observations of the light reflected and emitted from the lunar surface were confined to the visible and some infra-red regions of the spectrum.

The optical properties of the lunar surface have been summarized by Hapke (1965,1971); the more important properties may be listed as follows:-

(i) the lunar albedo is low, ranging from 5% to 20%

(ii) the spectral albedo increases monotonically with wavelength from 0.3 - 3 microns with only minor variations in spectrum from place to place

(iii) the brightness of every area on the lunar sphere peaks strongly at full moon when the sun is directly behind the observer

(iv) the average polarization of moonlight near quadrature is about 8%, with maximum variation from place to place of only 3.5:1. The polarization changes with phase angle in a distinctive manner

(v) these laws are true for every known area on the moon, regardless of location on the lunar sphere, surface tilt, or type of terrain

Hapke (1963) has developed a theoretical photometric function for the lunar surface which reproduces (iii) with reasonable accuracy. He postulated that the lunar surface layer must consist of very fine, loose dust particles. This postulate has subsequently been confirmed by the American and Russian lunar probes, which have found that a large part of the surface is covered by fine dust. Photographs of imprints formed by spacecraft landing on the moon and of the Apollo astronauts' footprints have confirmed that the dust layer is loosely compacted as predicted by Hapke.

The colour differences on the lunar surface have been studied in detail by McCord (1969) and McCord et al. (1972), who found that the colour differences could be correlated with the lunar morphology.

Infra-red measurements have also been made by numerous workers. These measurements provide information about temperature conditions on the lunar surface.

Radar and radio-wave measurements have also been made. Because of the wide range of wavelengths used (decimetre to centimetre) and the dielectric properties of the lunar surface, which allow transmission to a depth of several wavelengths, these studies make it possible to observe the surface layer to some depth. In particular, a combination of these measurements and infra-red studies allow the gradient of the thermal conductivity to be determined. This in turn provides information about the variation of conditions with depth in the surface layer.

4.2 Measured Values of Ultraviolet Radiation from the Moon

The aim of the present series of measurements was to extend the measurements made by Carver et al. (1967) in the region 2000Å-3000Å. As this is the wavelength range covered by the Hartley absorption bands of ozone the photometers discussed in Chapters 2 and 3 were used for these measurements.

Figures 3.10, 3.11 and 3.12 show that the values of the flux incident on the sensors became almost constant at the top of each flight - certainly within the range of calibration of the sensors the value of the absolute flux could be assumed constant. Furthermore, by determining a value of scale height for each detector from Figures 3.13 and 3.14 the amount of ozone along the line of sight to the top of the atmosphere was estimated, and the correction to the flux due to absorption by this residual ozone was calculated. In all cases this correction was found to be negligible by comparison with the calibration error. This meant that the values of flux could be read off from Figures 3.10, 3.11 and 3.12. Having obtained these values two corrections were applied, viz.

(i) a correction for the phase angle of the moon - this was needed to bring the value of flux up to the full moon value

(ii) a correction for the earth-moon distance - this was needed because the earth-moon distance varies with time and the flux values cannot be meaningfully compared unless referred to some mean distance

The phase correction was applied by assuming that the phase law in the ultraviolet was the same as in the visible. The lunar phase angle was calculated from Ephemeris data which gave the position of the sun and moon relative to the earth. The lunar brightness relative to full moon was calculated from Rougier's Phase Law, which is shown in Figure 4.1.

To correct for the earth-moon distance the semi-diameter of the moon was read from the Ephemeris tables as a function of Universal Time and the value of the semi-diameter at the time of launch was calculated by interpolation. To obtain the correction factor the value of the semi-diameter was divided into the mean value of the semi-diameter (taken to be 15' 32.58" of arc) and the resulting ratio squared. This factor was then multiplied by the value of full-moon flux to give the value of flux at the mean earth-moon distance.

Table 4.1 shows the time of firing of each flight, the time of the nearest full-moon and the semi-diameter of the moon at time of launch.

The flights designated C104, C105 and C1014 were described in Chapters 2 and 3. Those designated HAD 305 and HAD 312 were described by Horton (1968) and have been included because they were not previously corrected for variations in the earth-moon distance.

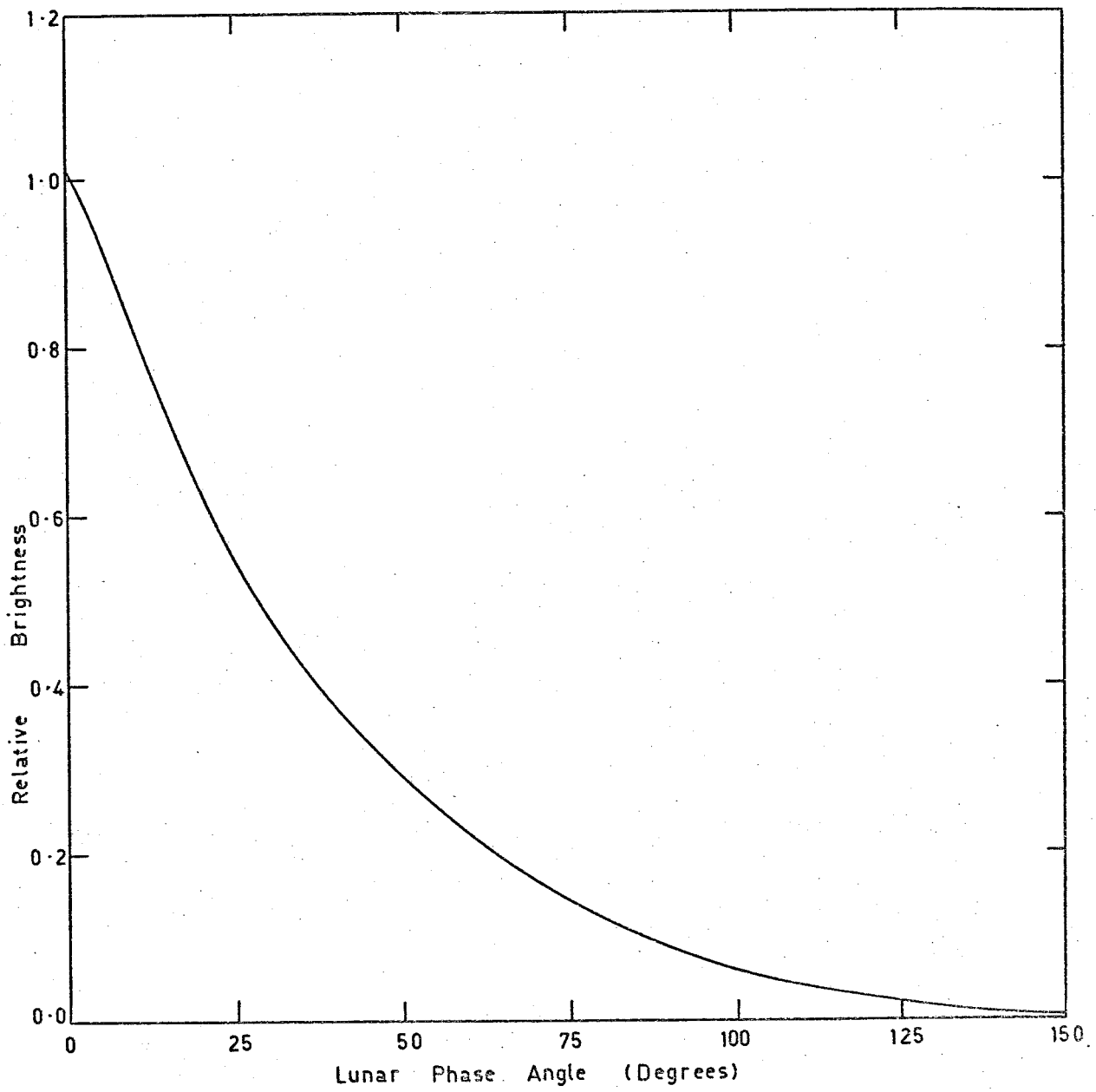

Figure 4 . 1 Variation of lunar brightness with phase angle (Allen, 1962)

Flight	Launch Time	Nearest Full Moon	Lunar Semi-Diameter
C104	19.45 hr 21/5/70	13.08 hr 21/5/70	15' 55.69"
C105	20.30 hr 12/11/70	16.58 hr 13/11/70	16' 06.95"
C1014	20.04 hr 29/5/72	13.58 hr 28/5/72	14' 53.80"
HAD 305	22.35 hr 9/12/65	02.52 hr 9/12/65	16' 18.67"
HAD 312	19.35 hr 30/8/66	09.44 hr 31/8/66	14' 43.89"

TABLE 4.1: Summary of launch times, nearest full moon times, and lunar semi-diameter at time of launch

4.3 The Lunar Ultraviolet Albedo

If L_M is the flux near the earth from the full moon and $L_\odot$ is the solar flux then the lunar spherical albedo A is given by (Kopal, 1969)

$$A = 0.585 \frac{L_M}{L_\odot} \left(\frac{r}{a}\right)^2 \qquad \ldots (4.1)$$

where r is the mean earth-moon distance (3.84×10^5 kms), a is the radius of the Moon and the factor 0.585 comes from a numerical integration of Rougier's phase law which is shown in Figure 4.1. As already mentioned this assumes that the visible phase law can be applied at ultraviolet wavelengths.

The solar flux (in units of ergs/cm^2/sec/Å) was calculated for each detector using the solar ultraviolet fluxes of Detwiler et al. (1961) as tabulated by Brinkman et al. (1966). The measured values of L_M and calculated values of $L_\odot$ were then used in (4.1) to calculate the lunar albedo.

The values of lunar albedo obtained from these calculations are tabulated in Table 4.3 and shown in Figure 4.2.

Flight	Effective Wave-length	Full Moon Flux	Solar Flux	Albedo
	Å	ergs/cm^2/sec/Å	ergs/cm^2/sec/Å	
HAD 305	2400	2.0×10^{-6}	7.6	$7.6\pm2.3\times10^{-3}$
	2740	6.5	22.2	8.5±2.5
	2910	13.6	55.5	7.1±2.1
HAD 312	2400	1.4	7.6	5.5±1.5
	2490	2.3	9.6	6.5±2.0
	2740	15.0	22.2	20.0±6.0
	2910	30.0	55.4	15.5±5.0
C104	2375	1.7	6.5	7.6±2.3
C105	2450	1.6	9.4	4.8±1.6
	2610	2.1	18.5	3.2±1.0
C1014	2430	2.0	6.8	8.5±2.5
	2620	3.4	18.9	5.2±1.6

TABLE 4.3 A summary of the lunar flux values and albedo values obtained for the different detectors

4.4 Comparison with Other Measurements of Lunar Albedo

The visible albedo of the lunar surface varies from 5% to 20% (see Section 4.1). Measurements have been extended into the near ultraviolet region of the spectrum by Stair and Johnston (1953), using a ground-based system. Heddle (1963) has made a single measurement at 2200Å, while Lebedinsky et al. (1967a,1967b)

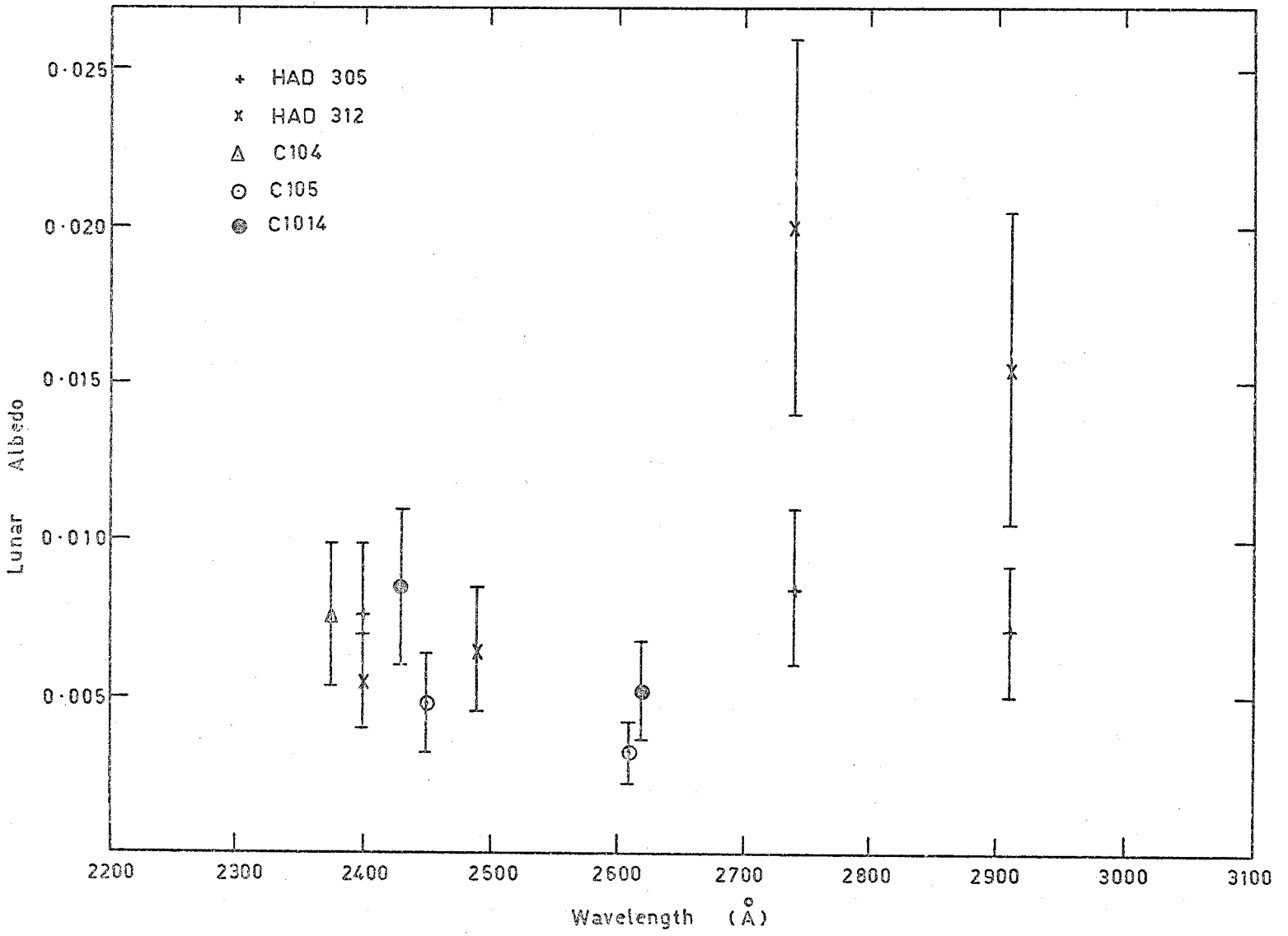

Figure 4.2 Values of lunar albedo as a function of wavelength.

have reported measurements made from the Zond-3 space probe in the wavelength range 1900Å to 3550Å. Ahmad and Deutschman (1972) have reported measurements in the ranges 1050Å to 2150Å and 1350Å to 2150Å, while O'Connor (1973) has made a single measurement at Lyman-alpha (1215Å).

The results of all these measurements, together with the results of the present work, are shown in Figure 4.3. The results of Ahmad and Deutschman, being referred to the N.R.L. solar data, have been multiplied by a factor of 0.585 to make them comparable with the results of the present work (see Section 4.3), while the results of Lebedinsky have been divided by π.

It can be seen from Figure 4.3 that the results of the present work are consistent with those of other workers. However, further studies of lunar ultraviolet flux between 1000Å and 3000Å will be needed to improve the accuracy of the present results. The fact that the results of Lebedinsky et al. apply only to a continental area of the moon, whereas the results of the present work apply to the entire lunar disc, suggests that the continental areas of the moon have a higher reflecting power in the ultraviolet than do the maria which constitute the major portion of the lunar surface. This would be consistent with variations in the lunar albedo, between maria and continental regions, at visible wavelengths.

Lucke et al. (1973) have measured the albedo of Apollo 11,

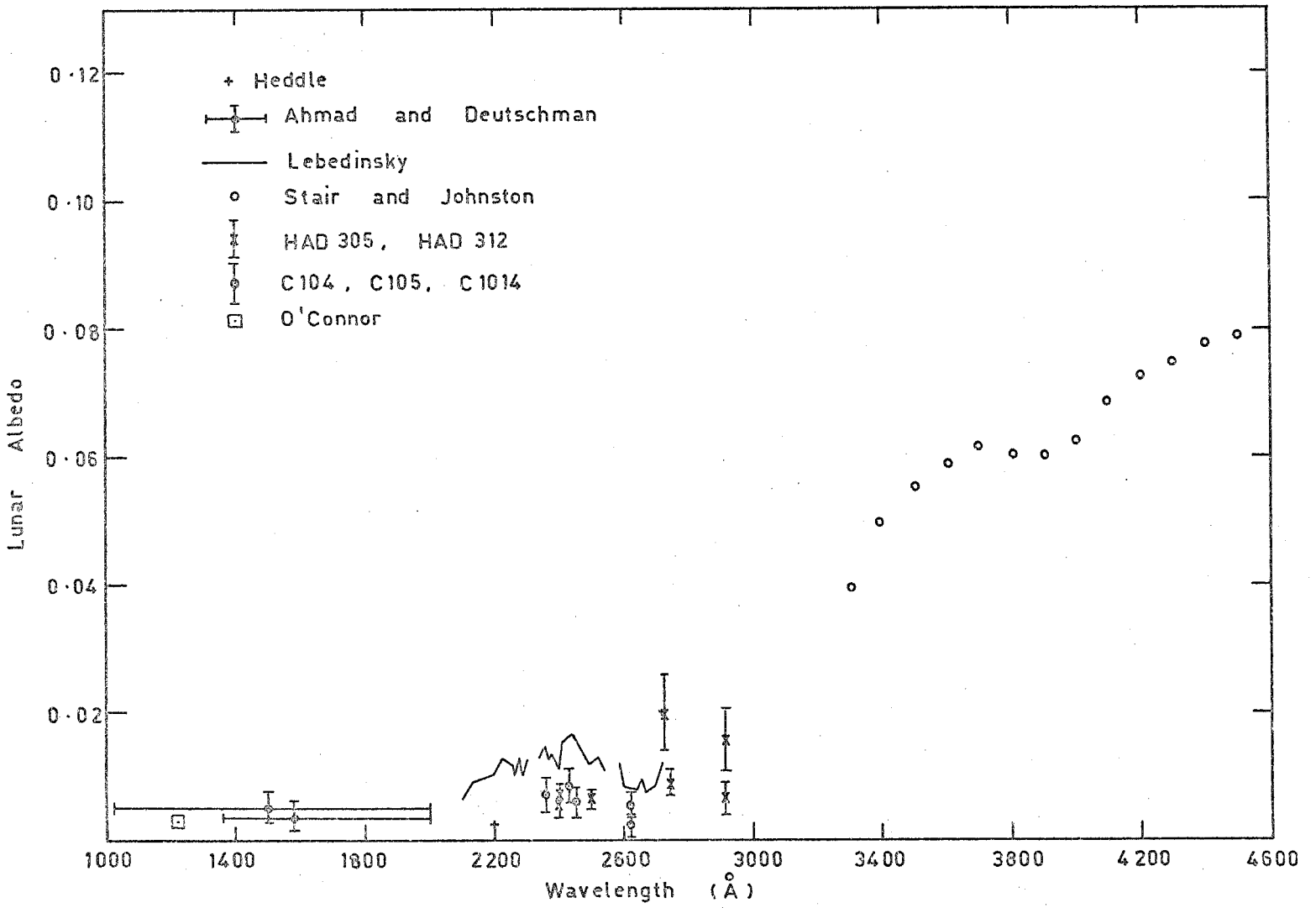

Figure 4.3 A comparison of the present results with other measurements of lunar albedo.

12 and 14 dust samples in the laboratory. Their results indicated values of albedo a factor of two higher than those shown in Figure 4.3 in the range 2000Å to 3500Å.

4.5 Wavelength Dependence of Lunar Albedo

The most striking feature of the lunar albedo values shown in Figure 4.3 is the sharp decrease between 3600Å and 2600Å. This corresponds to a marked colour variation in moonlight between visible and middle ultraviolet wavelengths. The results shown in Figure 4.3 indicate that this sharp decrease in reflectivity with decreasing wavelength does not continue to far ultraviolet wavelengths.

The comparison between the lunar albedo and the measured reflectivities of terrestrial rocks will be discussed in detail in Chapter 6.

CHAPTER 5

DESIGN OF AN EXPERIMENT TO MEASURE THE ULTRAVIOLET REFLECTIVITY OF SOME TERRESTRIAL MATERIALS

5.1 Introduction

A great deal of experimental and theoretical work has been done in an attempt to explain the unusual optical properties of the lunar surface. On the experimental side the reflectance spectra of some common terrestrial materials have been measured in the laboratory. Greenman et al. (1967) have measured the reflectance of granitic, gabbroic and serpentinite rocks in the range 2000-3000 Angstroms, while Korolev et al. (1971) have used synchrotron radiation to study the reflection spectra of various solids between 500Å and 2700Å. Fielder (1967) and Fielder et al. (1967) have studied simulated lunar surfaces with a view to determining the composition of the lunar surface layer. Hapke (1967) has shown that the optical properties of the lunar surface layer can be reproduced by a mixture of commercial cement powder and suitable colouring agents.

Sandercock (1967) has measured the reflectivity of some common terrestrial substances in the wavelength region 500-3000Å. These measurements were carried out for both polished and unpolished specimens. The results are shown in Figures 5.1 and 5.2. It can be seen that they show no significant features which may be correlated with the lunar albedo values shown in Figure 4.3.

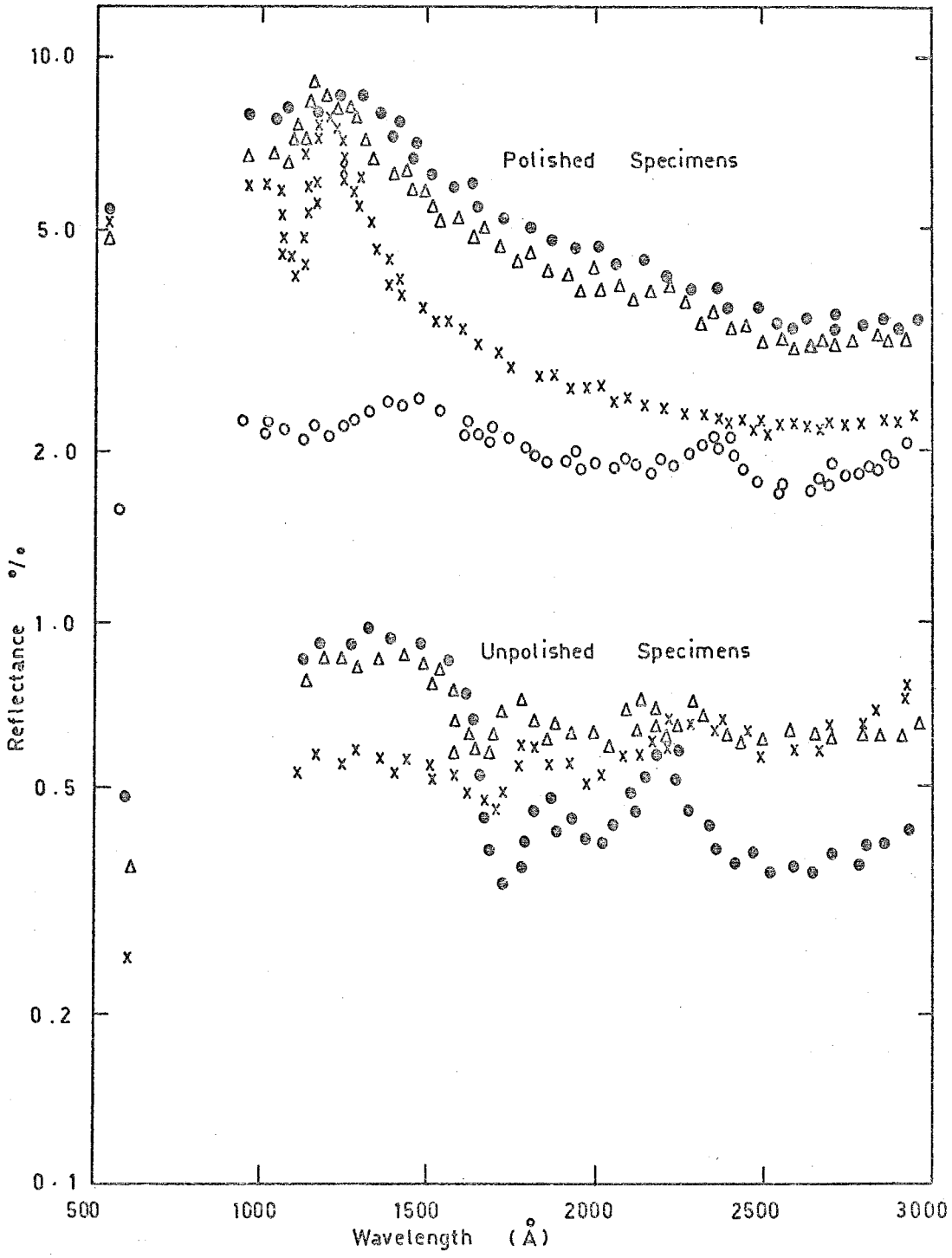

Figure 5 . 1 Reflectances of some terrestrial materials (Sandercock).

● ● ● - obsidian
Δ Δ Δ - aplite
x x x - sandstone
o o o - chondrite (meteoritic)

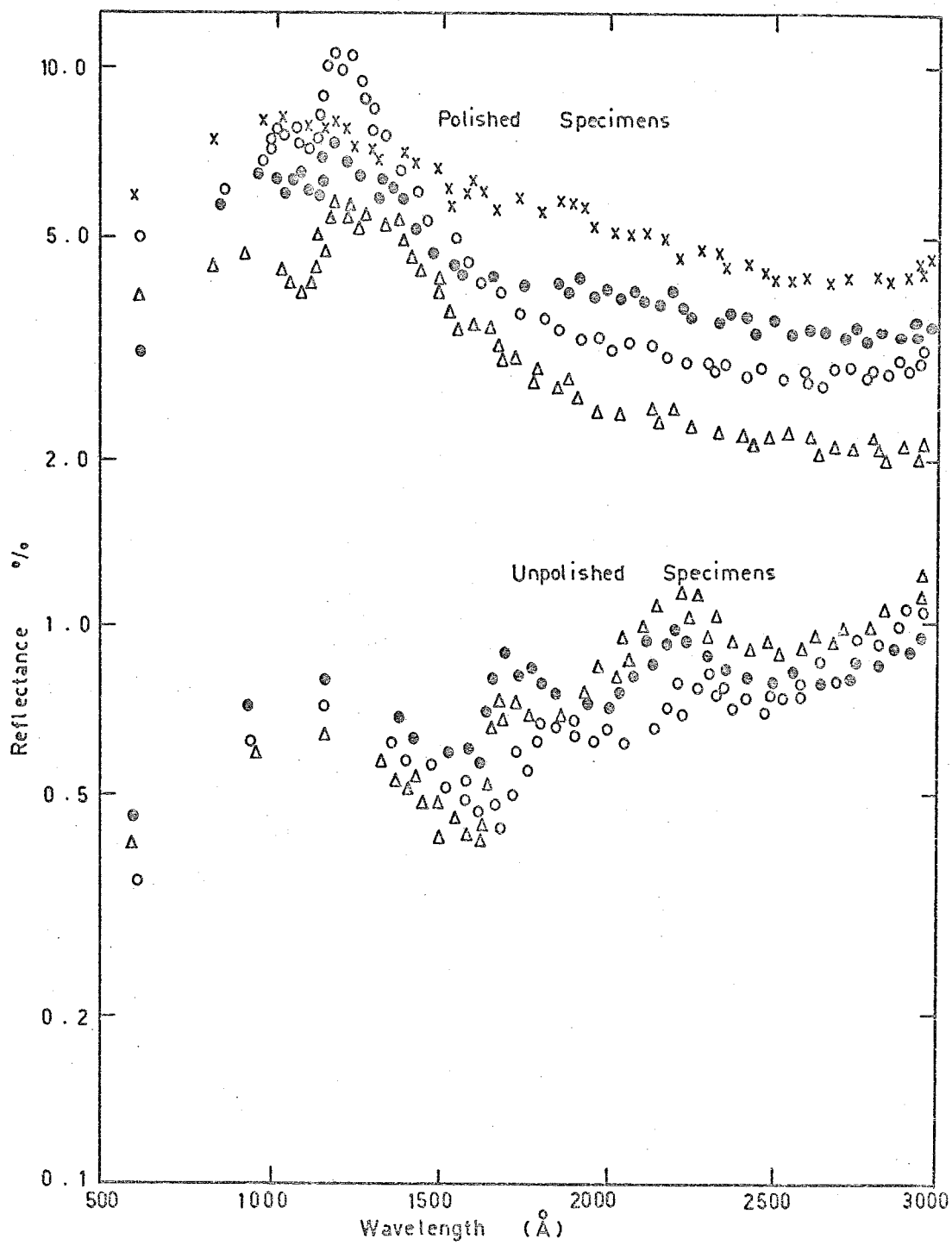

Figure 5.2 Reflectances of some terrestrial materials (Sandercock).

●●● - granodiorite
ΔΔΔ - sandstone
xxx - olivine
ooo - trachyte

5.2 The Reflection Chamber

5.2.1 The Original Reflection Chamber

The reflection chamber used for the present measurements was the same as that used by Sandercock (1967), but was modified to allow measurements of diffuse reflectance to be made. The original system consisted of a vacuum chamber containing holders for a specimen and a detector. These two holders were mounted on shafts which were connected by a 2:1 ratio gear system such that when the specimen was rotated through an angle θ relative to the incident beam the detector was rotated through an angle 2θ.

The chamber was arranged so that it could be mounted at the exit slit of a monochromator and since it was known that the radiation from the monochromator was partially polarized the chamber was built so that it could be rotated through 90 degrees about the axis of the light beam. In addition the shaft attached to the specimen holder had sliding vacuum seals mounted on it so that the specimen could be moved out of the path of the incident beam.

The entrance pipe to the chamber incorporated a beam splitter - this was used to monitor the intensity of the radiation incident on the specimen. Approximately 10% of the radiation fell onto a set of parallel horizontal wires, coated with sodium salycilate phosphor, and was reradiated as fluorescent radiation in the wavelength region 3900Å to 4300Å. A fraction of this radiation was collected by a perspex light pipe and trans-

mitted up the pipe to the photocathode of an EMI 9514S photomultiplier. This photomultiplier was used to monitor the incident radiation falling on the specimen. Approximately 90% of the radiation incident on the beam splitter was transmitted to the specimen.

The reflection chamber was physically supported by means of a vacuum pumping table on which were mounted a mechanical pump and an oil diffusion pump. These pumps were used to maintain the pressure in the reflection chamber at somewhat less than 10^{-5} torr during reflectance measurements.

5.2.2 Modifications to the Reflection Chamber

Since it was intended in the presented series of measurements to measure the angular distribution of the reflected radiation as well as the specular reflection, the reflection chamber had to be modified so that the specimen and detector could be rotated independently when desired. This was done by replacing the shaft controlling the movements of the specimen and detector by two concentric shafts arranged so that one controlled the movement of the detector and the other controlled the movement of the specimen. These two shafts could be operated from outside the chamber, either independently or as one shaft by locking them together with a locking nut mounted on the inner shaft. The arrangement is shown in Figure 5.3.

Figure 5.3 Exploded view of the reflection chamber

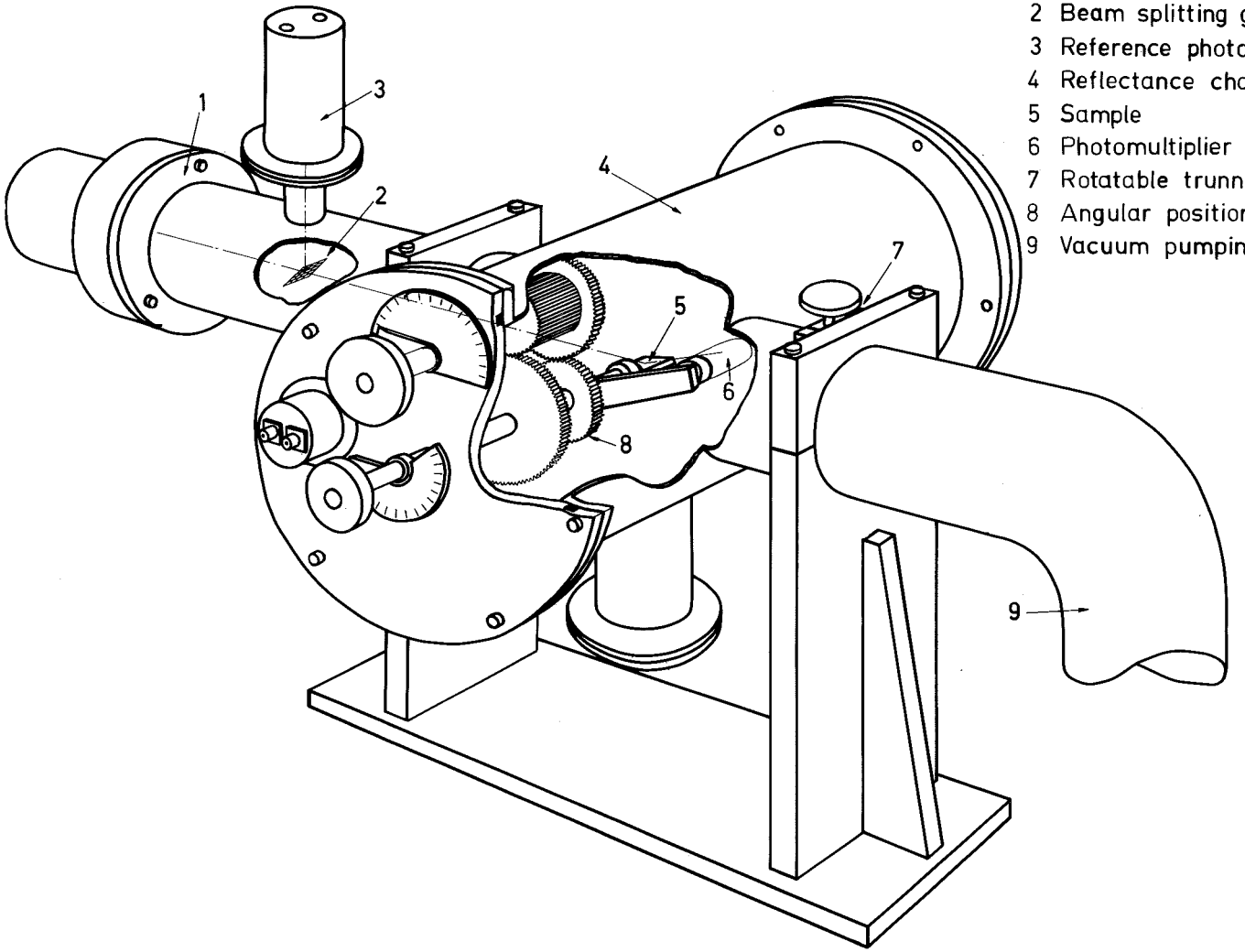

1 Monochromator exit slit
2 Beam splitting grid
3 Reference photomultiplier
4 Reflectance chamber
5 Sample
6 Photomultiplier
7 Rotatable trunnions
8 Angular positioning gear train
9 Vacuum pumping line

5.3 The Electronic Dividing Unit

Some preliminary reflectivity measurements were made using a potentiometric method of recording data similar to that described by Sandercock (1967). However, it was found that when measurements were repeated at the same wavelength the scatter in the data was large enough to render the results almost meaningless. It was found in fact that the 1P28 photomultiplier tube used as a detector had a dark current of approximately 5×10^{-9} amperes, while the reflected signal (including the dark current) was approximately 6×10^{-9} amperes. At these very low current levels the large statistical fluctuations (up to 50%) in the dark current level were such as to make reading of the chart records extremely difficult.

To overcome this problem some means of averaging the signal and compensating for the dark current was needed. This was done electronically by integrating the input signal over a time interval much longer than the period of the dark current fluctuations. The integrated signal was then fed into a logarithmic amplifier. This was done for both detector and monitor and the result signals were subtracted and the difference was recorded on a Bausch and Lomb Model VOM5 Chart Recorder or on a Hewlett Packard Model H23562A Digital Recorder which was driven by a Dynamco Model DM2006 Digital Voltmeter.

A block diagram of the dividing unit is shown in Figure 5.4. Detailed circuit diagrams, together with a description of the operation of the circuits, will be found in Appendix 3.

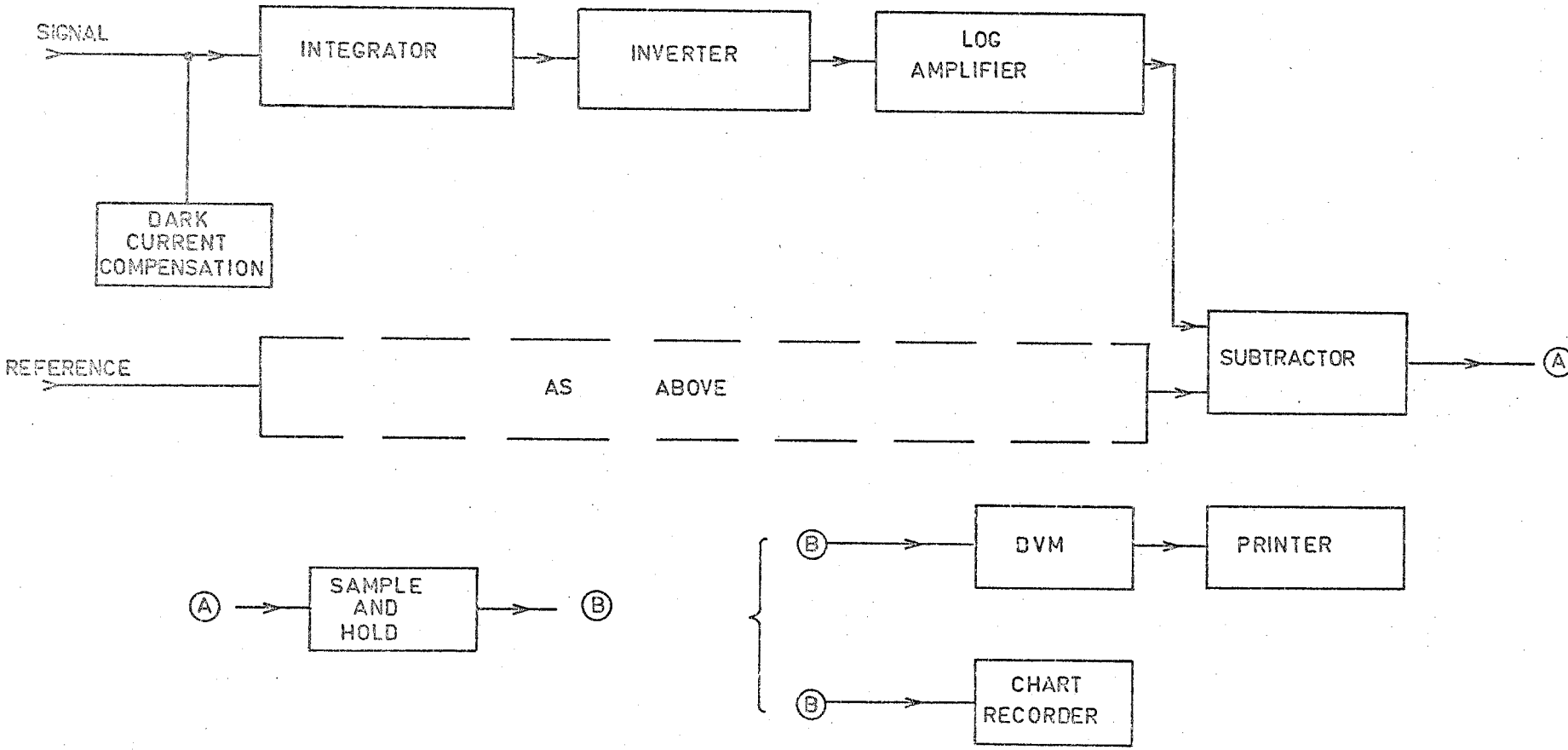

Figure 5.4 Block diagram of the electronic dividing unit.

The relays for the reset switches for the integrators and the sampling switch of the sample and hold circuit were controlled by a series of conventional pulse circuits. The pulse circuitry also provide the command pulse for the Digital Voltmeter-Printer combination when in use.

A block diagram of the pulse circuitry is shown in Figure 5.5. The pulse sequence for the different outputs is shown in Figure 5.6. Detailed circuit diagrams for the pulse circuitry are shown in Appendix 3. The pulse circuitry was originally designed to be free-running, but it was found necessary to add a push-button-controlled manual starter capable of over-riding the normal integrating cycle. This was needed so that the integrating cycle could be synchronized with the monochromator scanning drive, so that successive scans could be started at the same wavelength.

5.4 Experimental Procedure

An experimental procedure for measuring reflectivity using the reflection chamber and logarithmic dividing unit described in sections 5.2 and 5.3 respectively, can be set up in the following way.

Consider the situation shown in Figure 5.7a. The intensity of the light beam entering the reflection chamber is I_o. If a fraction f_S is transmitted straight through and a fraction F_M is reflected towards the monitor the signal produced by the logarithmic dividing unit will be

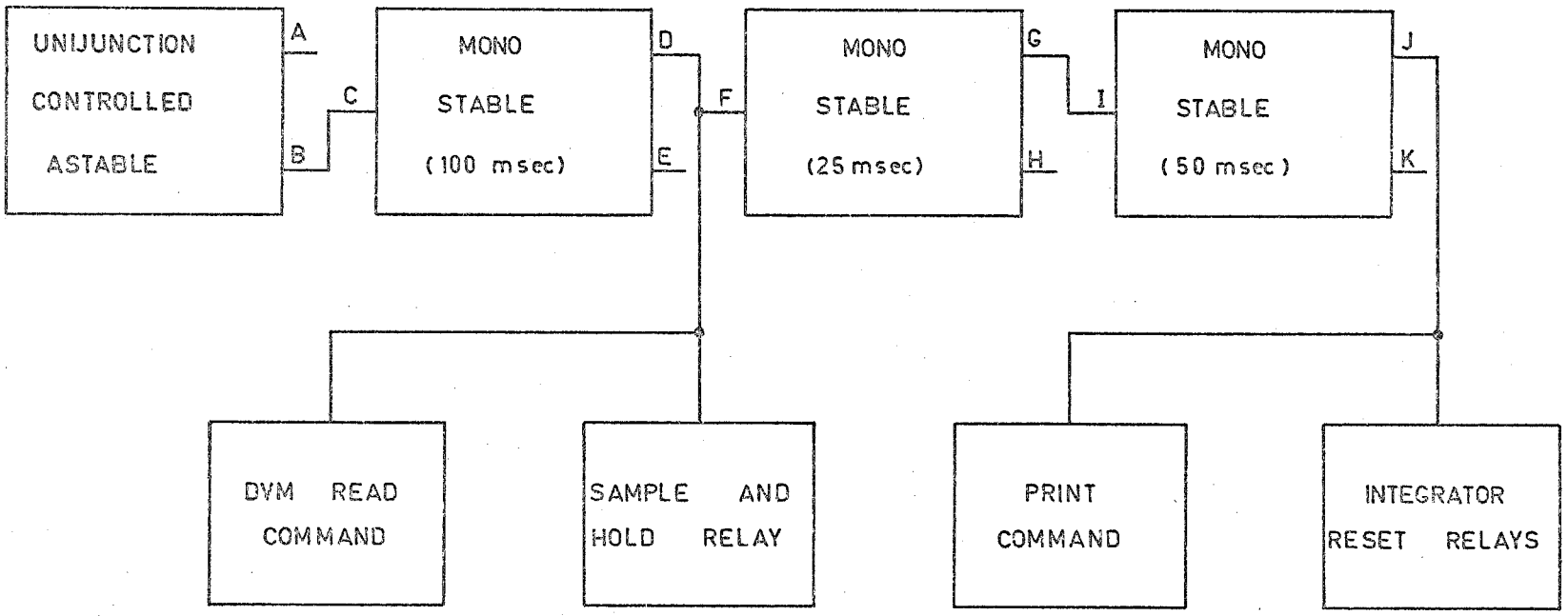

Figure 5.5 Block diagram of the pulse circuitry used to control the integrating time and sampling circuits.

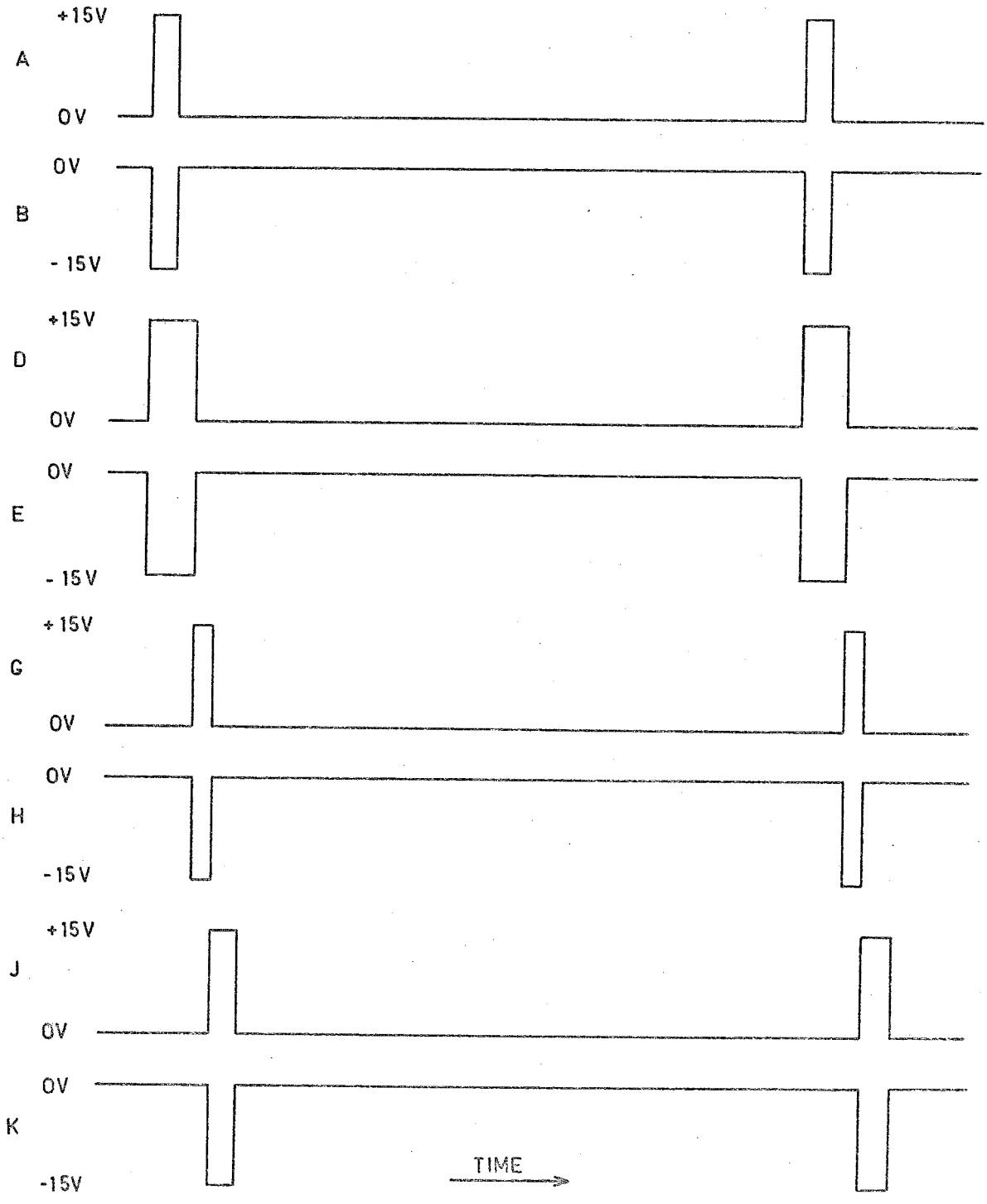

Figure 5.6 Sequence of control pulses for the logarithmic dividing unit. The letters A, B, C, etc. correspond to those in figure 7.5.

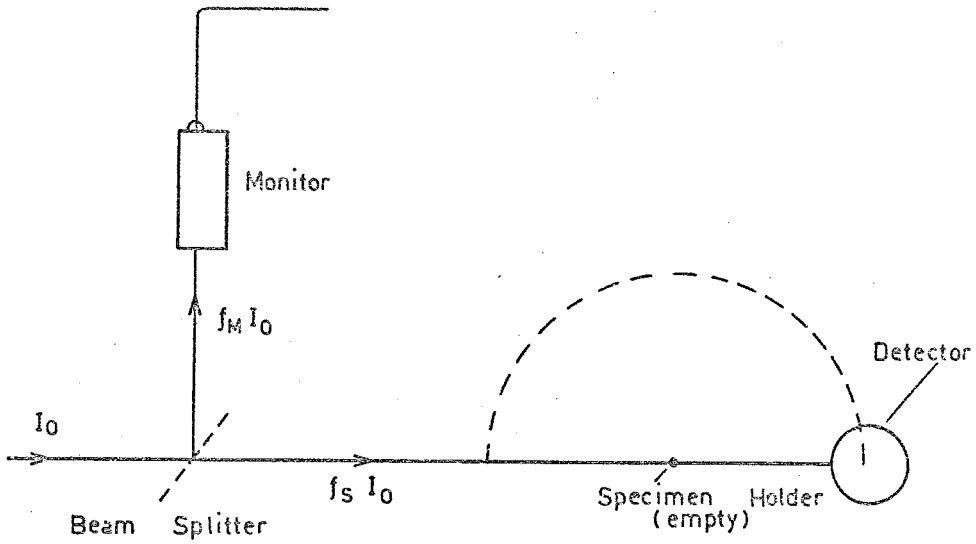

Figure 5.7a Orientation of detector for measuring the intensity of radiation reaching the specimen.

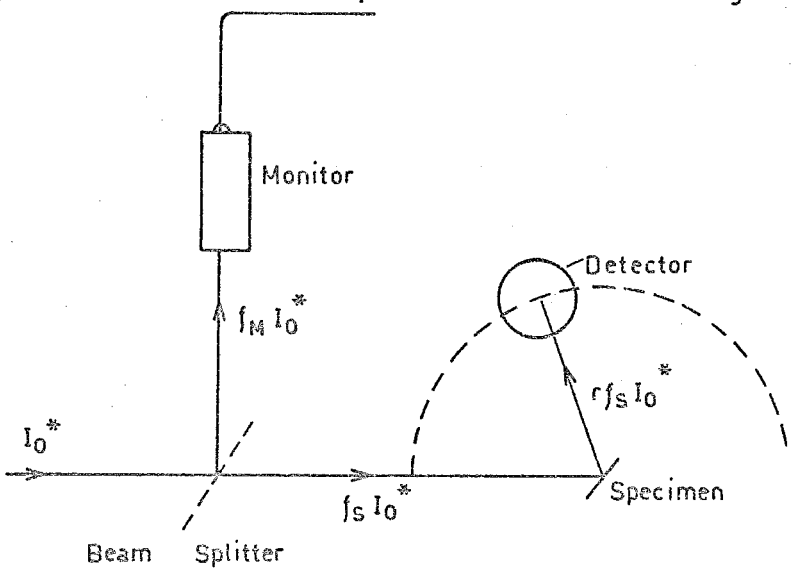

Figure 5.7b Orientation of detector for measuring the intensity of radiation reflected from the specimen.

$$V_1 = \log \frac{f_S \, I_o}{F_M \, I_o} = \log \frac{f_S}{f_M} \qquad \ldots (5.1)$$

Suppose that the specimen is now put into the path of the beam as shown in Figure 5.7b. In this case the signal produced by the logarithmic dividing unit will be

$$V_2 = \log \frac{rf_S \, I_o^*}{f_M \, I_o^*} = \log \frac{rf_S}{f_M} \qquad \ldots (5.2)$$

Subtracting (5.1) from (5.2) gives

$$V_2 - V_1 = \log r \qquad \ldots (5.3)$$

and this last equation can be inverted to obtain r, the reflectivity of the specimen.

The derivation of (5.3) assumes that f_S and f_M remain constant, not only with time but also with changes in the intensity of the light. The second of these assumptions was tested by using a hydrogen discharge lamp as a light source and varying the intensity of the light produced, both by varying the voltage across the discharge tube and by varying the gas pressure in the tube. It was found that the ratio f_S/f_M remained constant to within one percent. The first assumption was not easy to test directly; however, the salycilate coating on the beam splitting grid was renewed periodically while the experiment was in progress to counter aging effects.

The other fundamental assumption made in deriving (5.3) is that the background signal (dark current) is zero. This was

the main reason for including a dark current compensation circuit in the design of the logarithmic dividing unit (see Section 5.3). It was found that this assumption was good to within five percent over most of the spectral region used in the measurements. However, to ensure that errors due to both short- and long-term variations in photomultiplier dark currents were kept to a minimum, the spectral scans were repeated several times with the dark current compensation being adjusted at the beginning of each scan. The results of the different scans could then be averaged.

CHAPTER 6

RESULTS OF LABORATORY SPECTRAL REFLECTIVITY MEASUREMENTS

6.1 Introduction

The reflectivities of some terrestrial materials were measured between 800Å and 3900Å, using the apparatus described in the previous chapter. The aim of these measurements was to see if a way could be found to identify the rocks from their spectral reflectivity, and also to see if the sharp rise in the lunar reflectivity curve (discussed in Section 4.3) could be explained in terms of the chemical composition of the lunar surface material or in terms of the surface roughness.

The light source used was a hydrogen discharge lamp, mounted at the entrance slit of a Seya-Namioka ½-metre monochromator. The reflection chamber, containing the sample and a photomultiplier tube, was mounted at the exit slit of the monochromator. The two monochromator slits were set to give a resolution of approximately 5 Angstroms. The interior of the reflection chamber was maintained at a pressure of 10^{-5} torr by means of an oil diffusion pump in series with a rotary backing pump, while the pressure inside the monochromator was kept at 5×10^{-4} torr by means of a second set of vacuum pumps. A diagram of the system is shown in Figure 6.1.

To allow for the polarization of the light beam from the monochromator, measurements of the incident and reflected light

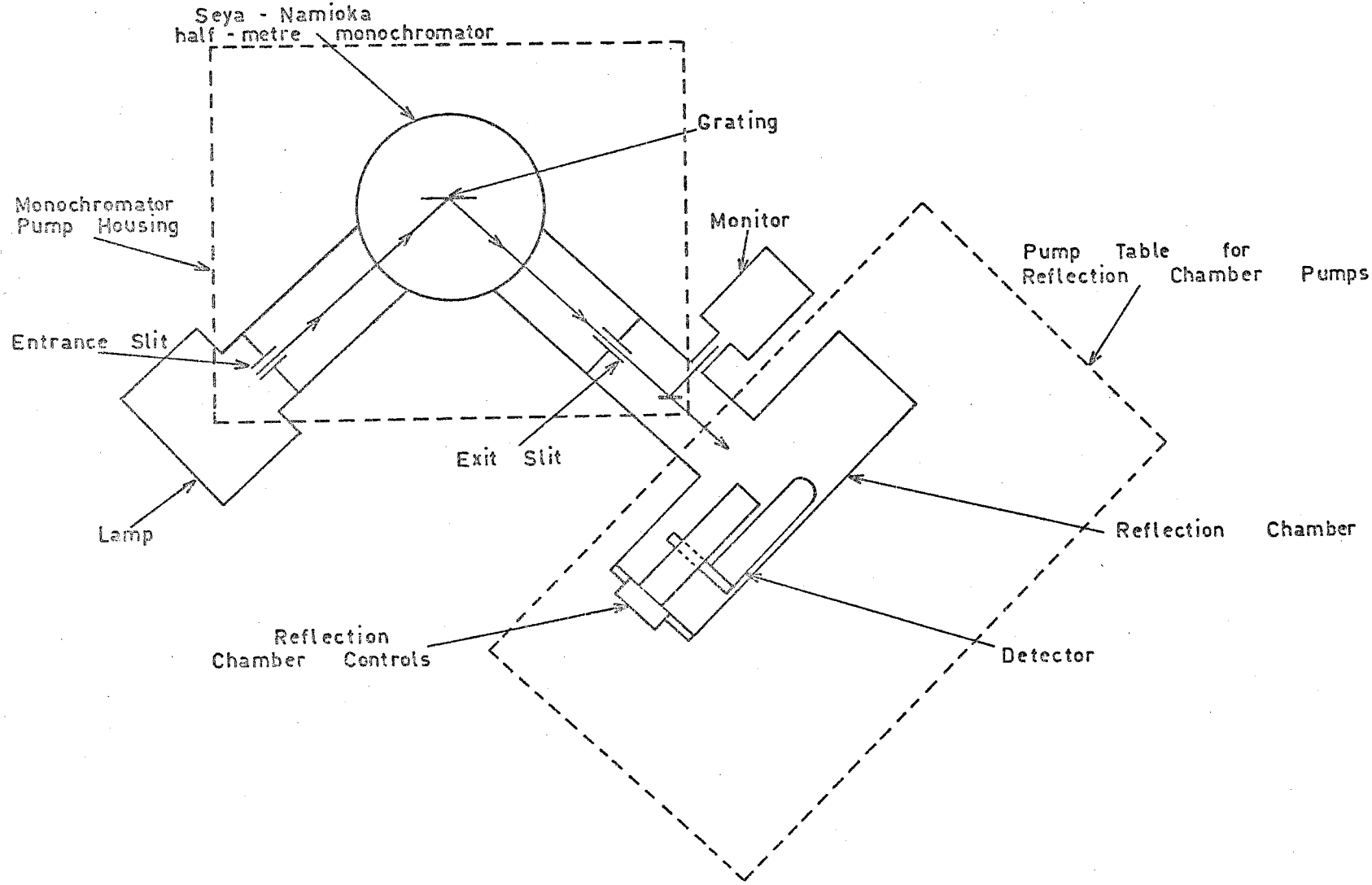

Figure 6 . 1 Layout of the apparatus used for the laboratory reflectivity measurements.

were taken with the reflection chamber in both the horizontal and vertical positions (see Section 5.2.1). The results of these two sets of measurements were analysed separately and the two values of reflectivity were then averaged to give the final value of reflectivity.

The angular distribution of reflected radiation was also measured for several of the specimens. These measurements were carried out at 1215Å (Lyman-alpha) and 1597Å, as these wavelengths corresponded to strong wavelengths in the lamp spectrum, making the relative errors in the measurements at these wavelengths much smaller than at wavelengths where the intensity of light from the lamp was appreciably lower. These measurements were also taken for both orientations of the reflection chamber.

Samples of Lithium Fluoride, Sapphire and Silica glass (Spectrosil) were also included. The Lithium Fluoride and Sapphire were included to serve as a check on the accuracy of the apparatus, as the transmission of these materials is well known. These samples were in the form of ion-chamber windows, one millimetre thick. The Sapphire sample also gave a useful indication of the possible effects of a high aluminium oxide content in the rock specimens.

The reflectivity and transmissivity of Silica were measured to see if the results could be correlated with the results from the rock sample measurements. The Silica sample

was also in the form of an ion-chamber window, one millimetre thick.

The reflectivity measurements were extended to 7000Å, using a Perkin-Elmer Model 137 UV Spectrophotometer, with resolution ranging from 10Å at 2000Å to 250Å at 7000Å.

The rock sample reflectivities between 2000Å and 7000Å were measured for several values of surface roughness to see if the rise in the lunar reflectivity curve could be explained in terms of the surface roughness.

6.2 Selection and Description of the Samples

The success of the Apollo space program from 1965-1972 has provided considerable knowledge of the composition of the lunar surface over limited regions surrounding the different landing points.

Chung et al (1970) have measured the dielectric properties of Apollo 11 lunar samples, while Jackson et al (1968) have concluded, on the basis of alpha-scattering experiments, that surface material on parts of the lunar mare is similar in chemical composition to terrestrial flood basalts while a sample of highland material appears to be similar to a terrestrial basalt with a high alumina content.

Wood (1970) has shown that soil samples from Apollo 11 consist of mostly basaltic and anorthositic type materials, while O'Leary et al (1970) have shown that the lunar powder

samples from Apollo 11 are similar in their optical properties to those measured for an area of several square kilometres surrounding the point where the samples were collected. Both Ringwood (1970) and O'Keefe (1970) have put forward theories for the origin of the moon based on the analysis of Apollo 11 samples. Wood et al (1971) have also examined samples from Apollo 12. These authors agree that the lunar surface material appears to have undergone recrystallization at some point in its history, but the exact mechanism for this process is uncertain.

Klein (1972) has discussed the results of studies on the samples obtained by the Apollo 11, 12, 14 and 15 missions and the automated Luna 16 mission. These results showed that most of the samples were basalts or basaltic origin. The chemistry of the lunar basalts showed a depletion in the more volatile elements (e.g. alkalis) with respect to terrestrial basalts, while some refractory elements (e.g. titanium and rare earths) showed a considerably higher concentration in lunar basalts than in their terrestrial counterparts.

The samples chosen for the laboratory measurements were chosen with these considerations in mind. A list of the samples used in the detailed measurements made with the system described in Chapter 5 is shown in Table 6.1, together with the place of origin and mode of formation (where known) of each sample.

As can be seen from Table 6.1 these rock specimens showed two distinct modes of origin. The basalts fell into both classes, i.e. those which cooled quickly and those which cooled slowly. The samples showed considerable variation in structure; for example, sample 2 was an extremely fine-grained rock with a porous surface, whereas sample 6 showed quite large crystals, some light and some dark in colour, with no surface porosity.

The chemical compositions of typical samples of basalt, anorthosite, gabbro and dolerite are shown in Table 6.2. This table shows that the composition of the rock samples ranged from a high concentration of ferro-magnesian minerals (basaltic) to a high concentration of alkali minerals (anorthositic).

An additional series of measurements was made, using the Perkin-Elmer Spectrophotometer, on a different set of rock samples to see if any of these samples exhibited spectral behaviour similar to that of the lunar surface (see Section 4.3). The samples used in these measurements, together with their locality and mode of origin are shown in Table 6.3.

Sample No.	Nature	Locality	Mode of Formation
1	Basalt	Toowoomba, Queensland	-
2	Basalt	Mount Schanck, South Australia	Flow basalt, quickly cooled
3	Anorthosite (coarse-grained)	Mount Davies, South Australia	Very slowly cooled, deep seated
4	Gabbro (feldspar-rich)	Mount Davies	Very slowly cooled
5	Basalt	Liawenee, Central Tasmania	-
6	Dolerite	Mount Wellington Tasmania	Cooled at depth over a period of 100-1000 years

TABLE 6.1 Specimens used in the work described in Sections 6.4, 6.6 and 6.7

Sample	Main Minerals	
	Name	Chemical Formula
Basalt	Olivine	$(Mg,Fe)_2SiO_4$
	Feldspar (Plagioclase)	$NaAlSi_3O_8$ to $CaAl_2Si_2O_8$
	Pyroxene (Augite)	$(Ca,Mg,Fe,Al)_2(Al,Si)_2O_6$
Dolerite	Similar to basalt	
Gabbro	Pyroxene (Augite) Feldspar (Plagioclase)	
Anorthosite	Feldspar (Plagioclase) (> 90% of rock)	

TABLE 6.2 Typical composition of the rock-types used in the reflectivity measurements described in Sections 6.4, 6.6 and 6.7 (after Read and Watson, 1963)

Sample No.	Nature	Locality	Mode of Formation
7	Basalt	Geelong, Victoria	-
8	Basalt	Mount Gambier, South Australia	Flow basalt, quickly cooled
9	Basalt	Grosser Nichus, Hesse Province, Germany	-
10	Basalt	Great Oelberg, Siebengebirge, Germany	-
11	Basalt	Merleo, Victoria	-
12	Anorthosite (fine-grained)	Mount Davies, South Australia	Very slowly cooled
13	Gabbro (feldspar-rich)	Mount Davies	Very slowly cooled
14	Basalt	Burnie Tasmania	-
15	Basalt (glassy)	-	Very quickly cooled
16	Dolerite	Mount Wellington, Tasmania	Cooled at depth over a period of 100-1000 years
17	Anorthosite (brecciated)	Cripple Creek Colorado, U.S.A.	Slowly cooled
18	Gabbro	Black Hill South Australia	-
19	Anorthosite	Ekersund, Norway	Slowly cooled
20	Dolerite	Guthega, New South Wales	Quickly cooled

Cont....

Sample No.	Nature	Locality	Mode of Formation
21	Gabbro (> 60% plagioclase)	Rockhampton, Queensland	Slowly cooled
22	Gabbro	Kiandra, New South Wales	Quickly cooled (may be 1000 yrs)
23	Gabbro (Eucrite, rich in plagioclase)	Ardnamurchan, Scotland	Slowly cooled
24	Andesite Tuff	Mount Egment, New Zealand	Volcanic ash (consolidated)

TABLE 6.3 Specimens used in the work described in Section 6.8

6.3 Preparation of the Specimens

For the main series of measurements the specimens were prepared by polishing with 180 grade carborundum grinding powder until the surface roughness appeared uniform (under a reading microscope). The samples were then cleaned in an ultrasonic bath to remove any traces of grinding powder or other loose material, and then cleaned with acetone to remove any traces of grease, etc., and were then baked in an oven for several days at a temperature of about 80 degrees Centigrade, to remove any traces of moisture from the surface.

The samples used in the measurements made to study the effects of roughness on reflectivity were prepared for the additional series of measurements by polishing with several different grades of carborundum grinding powders. The remaining preparation was carried out using the procedure in the previous paragraph.

To examine the effect of the grinding process on the surfaces of the samples the root mean square roughness and correlation length of several of the samples were measured using a Taylor-Hobson Talysurf 4 surface measuring instrument. This device amplifies the vertical displacement of a diamond-tipped stylus by means of an inductance bridge, and produces a chart recording of the displacement as the stylus is drawn across the surface being measured.

The results of these measurements are shown in Table 6.4. The correlation length was obtained by assuming a Gaussian correlation function of the form

$$\rho(\tau) = e^{-\frac{\tau^2}{T^2}}$$

where τ is the horizontal displacement between two points on the surface. The range of values for the r.m.s. roughness and correlation length indicate the variation in these parameters over the different samples measured.

Size of grinding powder (microns)	r.m.s. roughness (microns)	Correlation length (microns)
60	40 ± 5	50 ± 5
12	9 ± 2	15 ± 2
3	0.8 ± 0.3	10 ± 2

TABLE 6.4 The results of measurements of r.m.s. roughness and correlation length for ground surfaces

6.4 Analysis of Experimental Data

For the main series of measurements four sets of results were taken for each specimen. These comprised measurements of the incident and reflected light for both horizontal and vertical components of the reflection chamber. The measurements of incident light were repeated four times for each orientation of the chamber for each specimen and the measurements of reflected light were repeated eight times. Each set of data was then averaged to give a mean value and a standard deviation. These values were then used to give a value of reflectivity and a

variance for both orientations of the reflection chamber.

The reflectivity for each orientation was calculated from the formula

$$R^* = 10^{V_S - V_B} = \exp\left[2.3026(V_S - V_B)\right] \quad \ldots (6.1)$$

where V_S = signal due to the reflected light

V_B = signal due to the incident light

while the variance σ^* was calculated from the formula (Bevington, 1969)

$$\sigma^* = \tfrac{1}{2}R^*(\sigma_S^2 + \sigma_B^2)^{\frac{1}{2}} \quad \ldots (6.2)$$

where σ_S = variance in V_S

σ_B = variance in V_B .

The final reflectivity and variance were then calculated using

$$R = \tfrac{1}{2}(R_H^* + R_V^*) \quad \ldots (6.3)$$

$$\sigma_R = \tfrac{1}{2}((\sigma_H^*)^2 + (\sigma_V^*)^2)^{\frac{1}{2}} \quad \ldots (6.4)$$

where R_H^* = reflectivity measured using the horizontal orientation

R_V^* = reflectivity measured using the vertical orientation

σ_H^* = variance in R_H^*

σ_V^* = variance in R_V^* .

This procedure was used for both the spectral reflectivity measurements described in Sections 6.5 and 6.7, and the angular distribution measurements described in Section 6.6.

6.5 Reflectivities and Transmissivities of Lithium Fluoride, Sapphire and Silica

The results of the transmissivity and reflectivity measurements for the Lithium Fluoride, Sapphire and Silica samples are shown in Figures 6.2, 6.3 and 6.4.

The Lithium Fluoride cut-off wavelength appeared from these results to be approximately 1030 - 1040Å. This agreed with results published by Dunkelmann et al (1963) and Carver and Mitchell (1964). The reflectivity curve for Lithium Fluoride showed no structure except for a small peak at 1000Å.

The Sapphire cut-off was approximately 1400 - 1420Å. This result also agreed with the data of Carver and Mitchell. The reflectivity curve for Sapphire showed a small peak at 1350 - 1360 Angstroms.

The results for the Silica specimen showed that the cut-off wavelength was approximately 1550Å. The reflectivity curve for the Silica showed an interesting feature at approximately 1200Å. This feature has also been reported by Samson (1967) and Sandercock (1967).

The agreement between these results and those of other authors provided a useful check on the accuracy of the experimental apparatus.

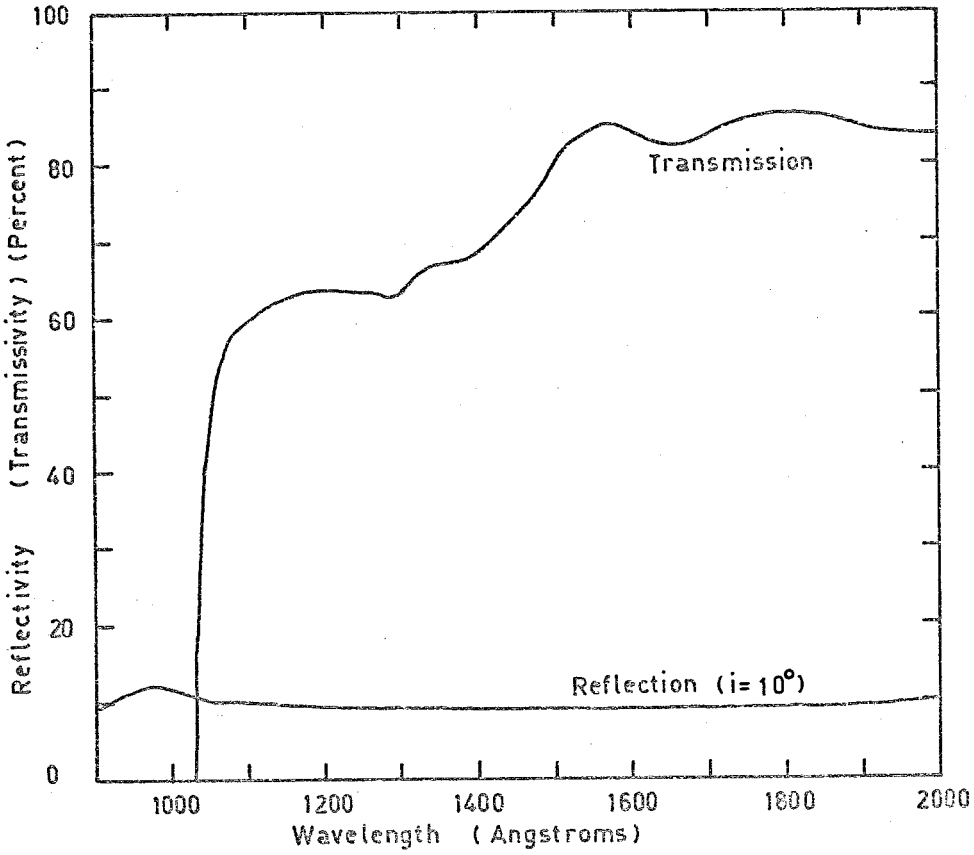

Figure 6.2 Reflectivity and transmissivity of lithium fluoride.

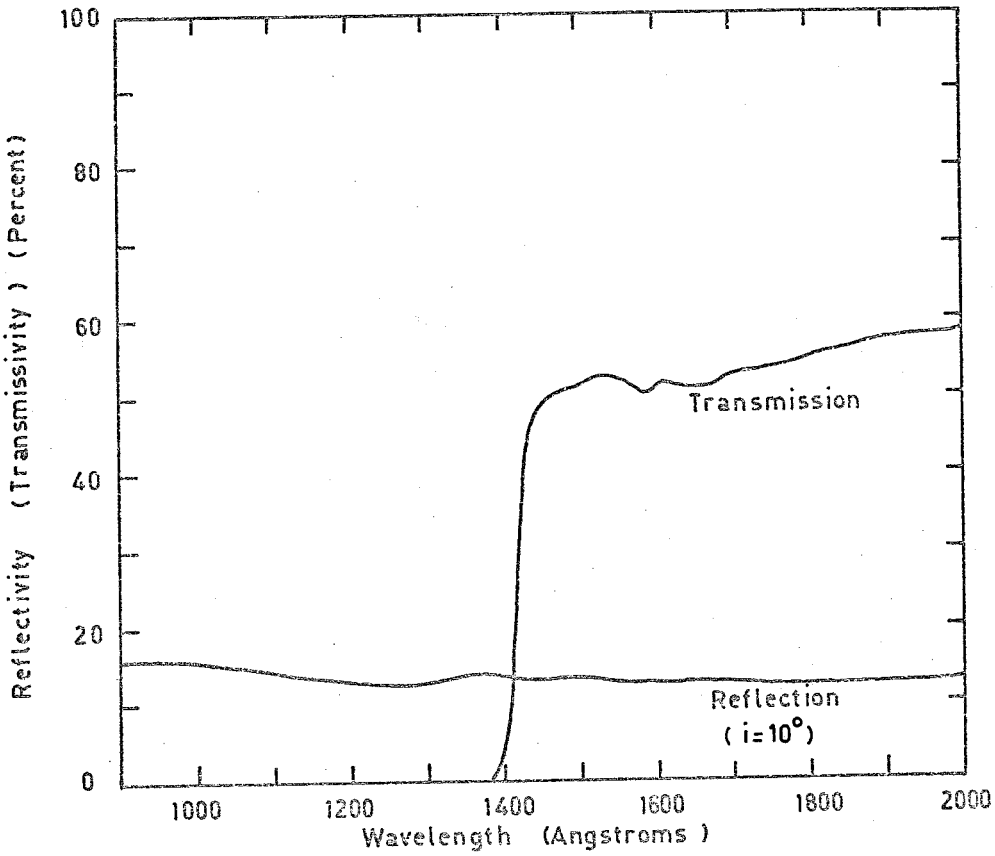

Figure 6.3 Reflectivity and transmissivity of sapphire.

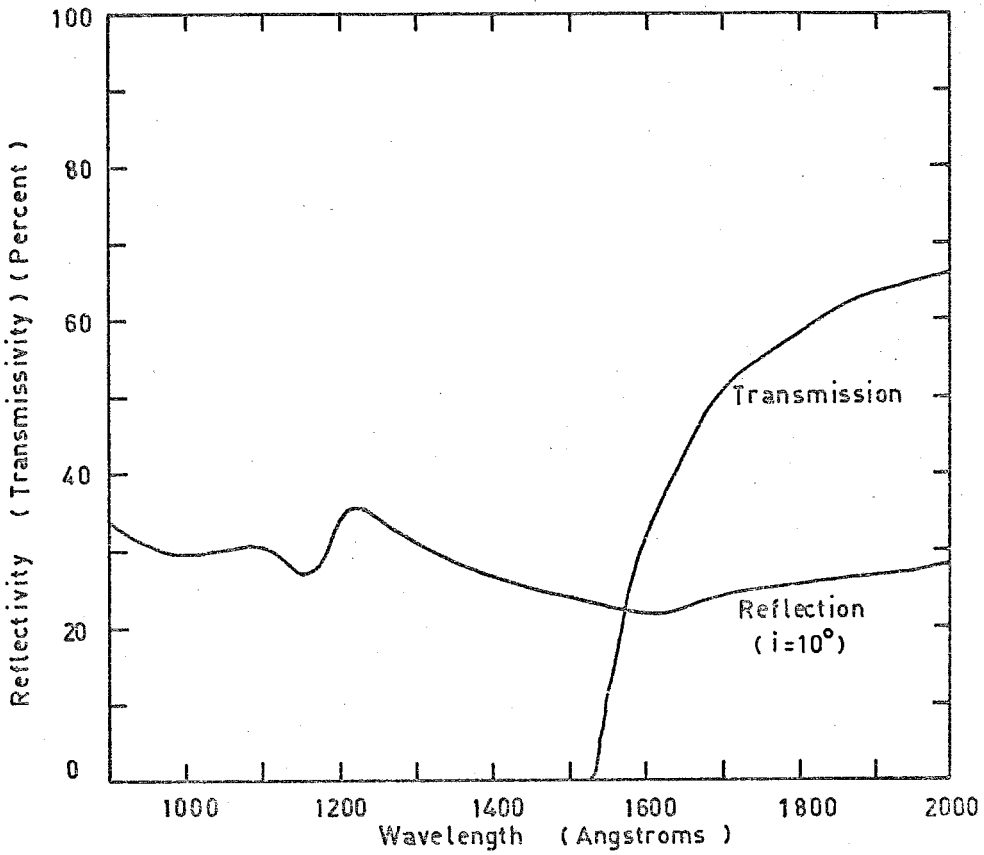

Figure 6.4 Reflectivity and Transmissivity of silica (spectrosil).

6.6 Results of Measurements of the Angular Distribution of Reflected Radiation

The results of the measurements of the angular distribution of reflected radiation for samples 1 and 4 are shown in Figures 6.5 (a to d) together with the variance in the reflectivity at the specular angle. The results for the other samples measured were similar to those shown.

It can be seen from these results that the reflected radiation is concentrated in a broad peak centred on the specular direction. These results show that the behaviour of rough surfaces at ultraviolet wavelengths is similar to their behaviour in the visible part of the spectrum.

6.7 Results of Measurements of the Spectral Reflectivity of some Terrestrial Materials

The results of the measurements of the spectral reflectivity of some naturally occurring rock samples are shown in Figures 6.6 and 6.7. The values of reflectivity are shown, together with error bars indicating the variances calculated by means of the analysis outlined in Section 6.4.

The data points were originally plotted at 10-Angstrom intervals together with a variance for each data point. However, the results showed no fine-scale structure (of the order of 10 Angstroms or less) and the calculated values of variance did not show any rapid fluctuations with wavelength, so the results have been plotted as smooth curves and the value of

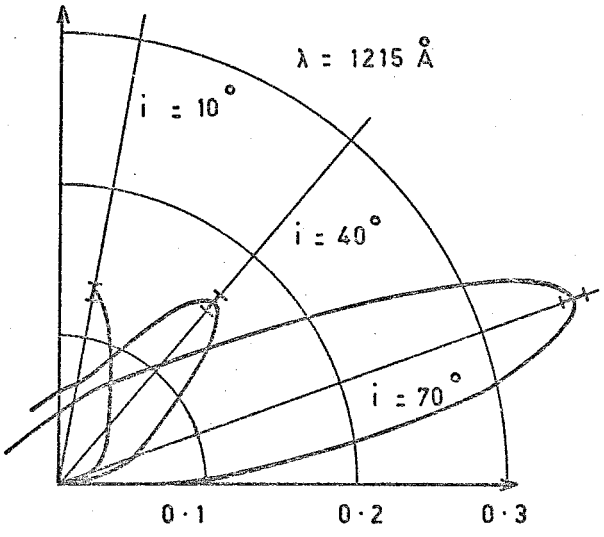

Reflectivity (%)

Figure 6 · 5a

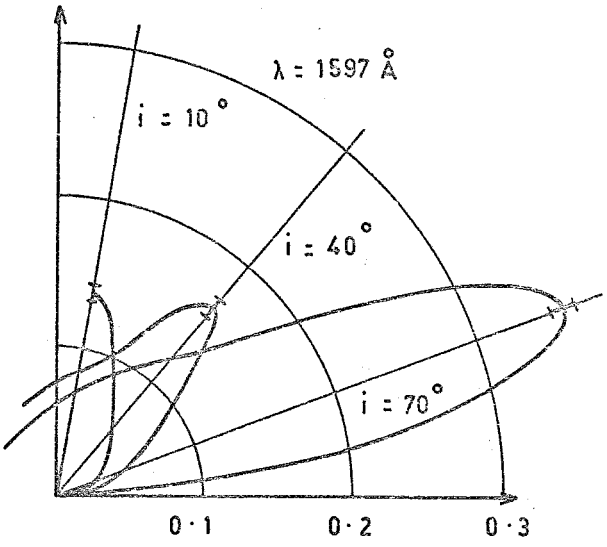

Reflectivity (%)

Figure 6 · 5b

Angular distribution of reflected radiation from sample 1. (errors are shown by I).

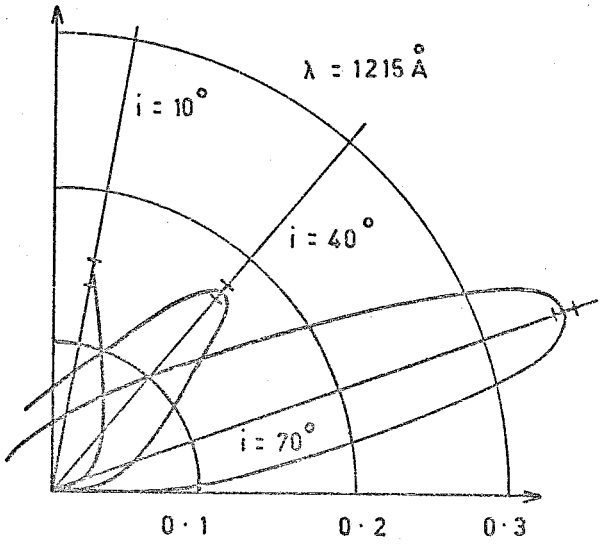

Reflectivity (%)

Figure 6 · 5c

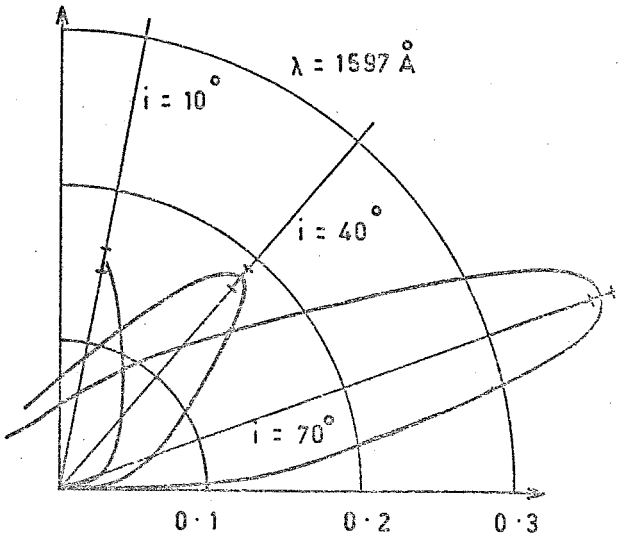

Reflectivity (%)

Figure 6 · 5d

Angular distribution of reflected radiation from sample 4. (errors are shown by I).

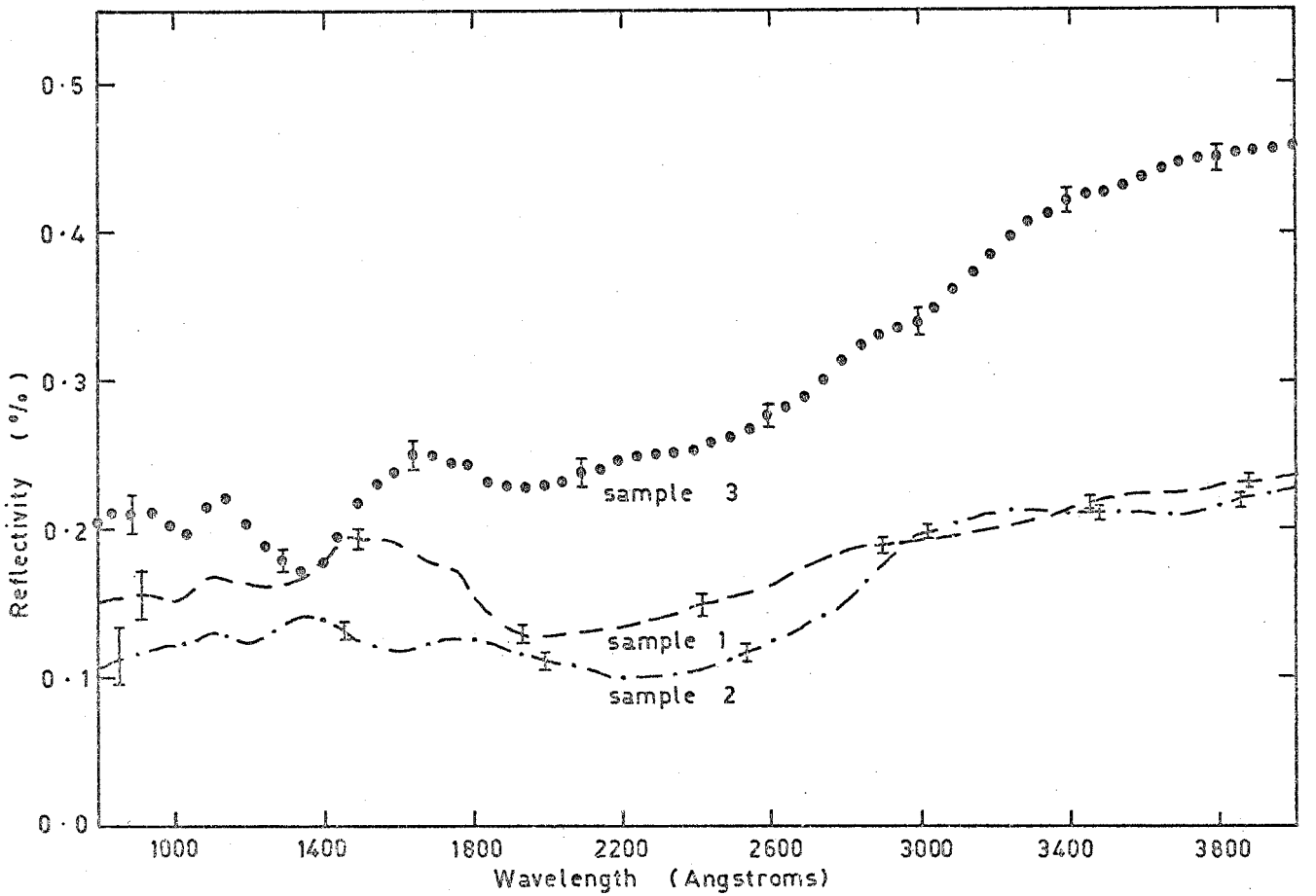

Figure 6·6 Spectral reflectivities of some naturally occuring materials.

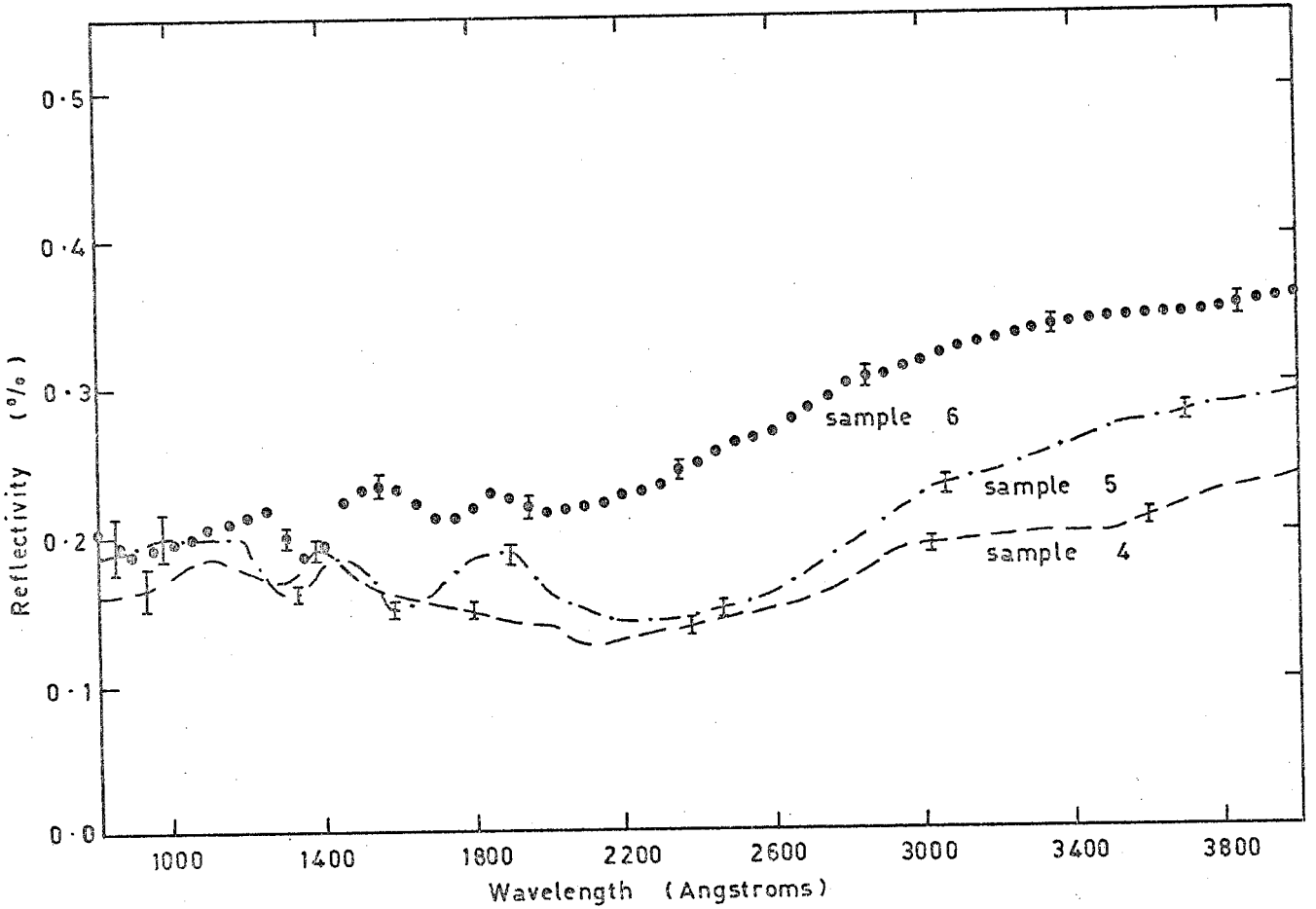

Figure 6·7 Spectral reflectivities of some naturally occurring materials.

the variance has only been shown at intervals of approximately 400 Angstroms, except where the reflectivity is changing relatively quickly with wavelength. The values of reflectivity agree reasonably well with those of Sandercock (see Figures 5.1 and 5.2).

These results certainly show that the structure indicated in the reflected curves is significantly larger than the statistical fluctuations (as indicated by the variance) in the reflectivity values for the different scans.

It can be seen that all the curves show some evidence of structure in the region 1000 - 1800Å but over the range 1800 - 3900Å there is very little evidence of any significant structure.

The structure from 1000 - 1400Å cannot be positively associated with the presence of Silicon compounds in the rock samples. However, it should be remembered that these samples would only contain impure Silica whereas the curve shown in Figure 6.4 was obtained for a very pure, highly refined form of Silica. In addition different varieties of Silica have their short wavelength cut-off at different values of wavelength (mostly higher than that of Spectrosil), so it is possible that the structure in the reflectivity curves from 1000 - 1400Å is due to the presence of Silica or Silicon compounds in the rock samples. Further work with a variety of samples with accurately known chemical compositions will be needed to clarify this point.

There does not seem to be any strong correlation between the reflectivity curves and the mode of formation of the rock. However, the results suggest that the rise in reflectivity between 2000Å and 4000Å is more pronounced for those samples with the more porous surfaces or with more prominent granular structure.

These reflectivity measurements were extended from 4000Å to 7000Å using the Perkin-Elmer spectrophotometer. In all cases the reflectivity remained constant or decreased slightly with increasing wavelength.

6.8 Further Measurements of Spectral Reflectivity

A second series of measurements was made, using the Perkin-Elmer Spectrophotometer, to see if any particular type of rock samples exhibited behaviour similar to that of the lunar surface. The additional specimens used in these measurements are listed in Table 6.3.

To check the accuracy of the spectrophotometer three tests were made. The reference mirrors used were calibrated independently, the reflectivity of a freshly prepared magnesium oxide surface was measured, and the samples used in the measurements described in Section 6.7 were then measured with the spectrophotometer. It was found that the results obtained by using the spectrophotometer agreed with those obtained from the reflection chamber measurements to within fifteen per cent,

with the Perkin-Elmer instrument giving consistently higher values of reflectivity than the reflection chamber measurements.

To compare the results of the measurements on the rock samples with the lunar albedo it was necessary to calculate the Bond albedo of the rock samples. The Bond albedo of a surface is defined by Allen (1964, p.144) as the ratio of the total light reflected from a surface to the total light incident on the surface. Thus, if the angular reflectivity of a flat surface at angle θ (assuming normal incidence) is $R(\theta)$ and the solid angle of the detector is Ω_D, so that $R(\theta)/\Omega_D$ is the fraction of incident light reflected into unit solid angle, then the Bond albedo is given by (following Lucke et al., 1973)

$$A = \frac{2\pi}{\Omega_D} \int_o^{\pi/2} R(\theta) \sin\theta \, d\theta \qquad \ldots (6.5)$$

If we define a normalized angular reflectivity $\varepsilon(\theta)$ by

$$\varepsilon(\theta) = \frac{R(\theta)}{R(O)} \qquad \ldots (6.6)$$

then

$$A = \frac{2\pi}{\Omega_D} R(O) \int_o^{\pi/2} \varepsilon(\theta) \sin\theta \, d\theta \qquad \ldots (6.7)$$

where $R(O)$ is the reflectivity for $\theta = 0$.

This expression is analogous in form to equation (4.1). The integral involving the normalized phase law $\varepsilon(\theta)$ was calculated from the results of the angular reflectivity measurements described in Section 6.6. The results of these calculations gave

$$\int_0^{\pi/2} \varepsilon(\theta) \sin\theta \, d\theta = 0.25 \pm 0.025 \qquad \ldots (6.8)$$

while the value of Ω_D, calculated from the dimensions of the reflection chamber, was $\frac{1}{16}$. Using these values in (6.7) leads to the result

$$A = 8\pi R(0) \qquad \ldots (6.9)$$

The results of the measurements with the Perkin-Elmer spectrophotometer are shown in Figures 6.8, 6.9, 6.10, 6.11, 6.12 and 6.13. The value of the albedo was calculated using the measured values of R(0) and equation (6.9). In all cases these results are for samples which were prepared (see Section 6.3) by grinding with 180 grade Carborundum powder.

6.9 The Effect of Surface Roughness on Spectral Reflectivity

The results of the previous section give no indication of the effect of surface roughness on reflectivity. To examine this effect the samples were treated with grinding powders of different sizes, and their reflectivities were then measured with the Perkin-Elmer spectrophotometer. The grinding powder sizes used were 60μ, 25μ, 12μ, 5μ and 3μ.

It was found in all cases that the reflectivity after grinding with 25μ powder was higher than after grinding with 60μ powder, but that grinding with powders less than 25μ in size did not produce any measurable change in reflectivity. There are two possible explanations for this - either the increase in specular reflection as the sample surfaces became

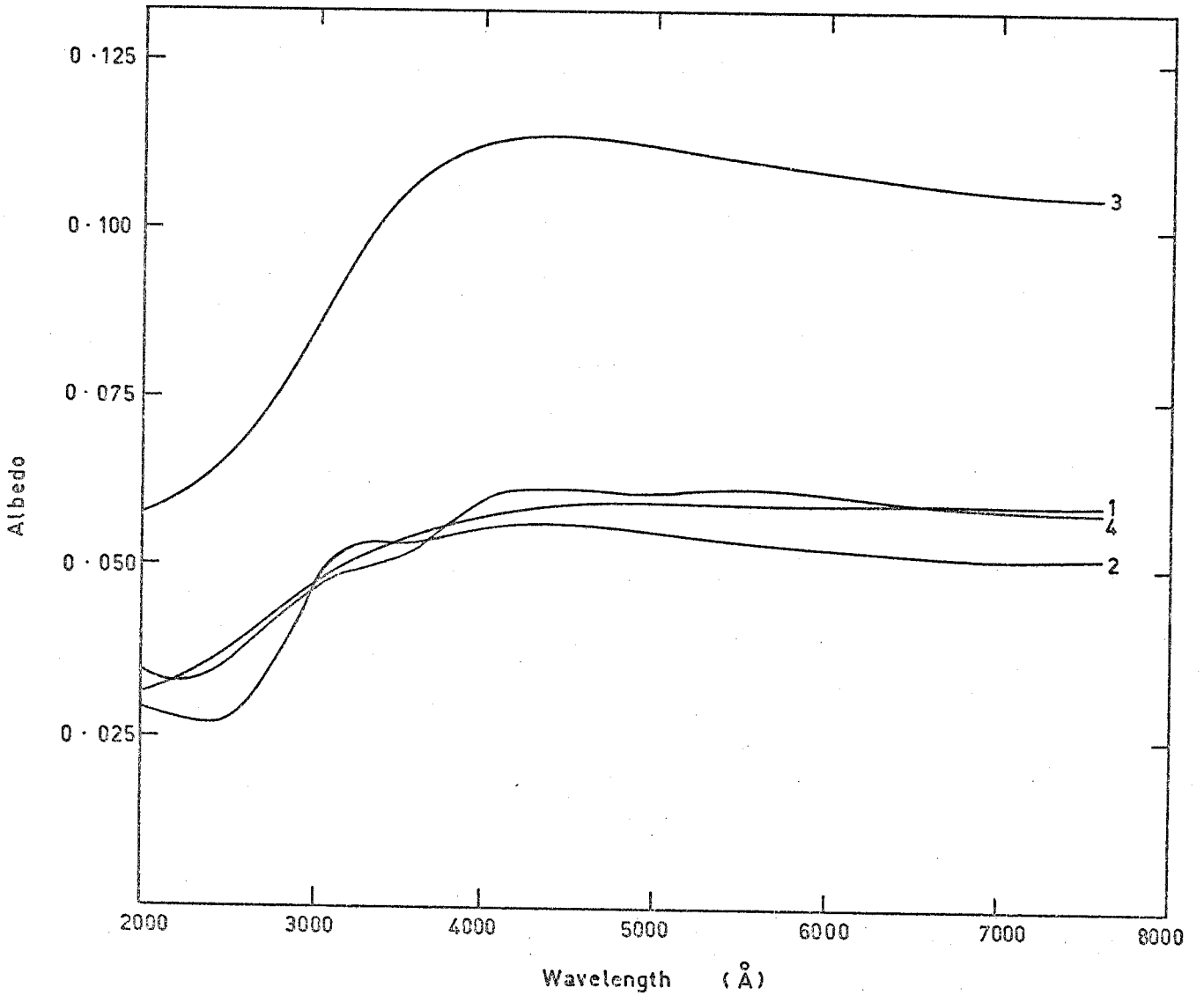

Figure 6 · 8 Albedos of some terrestrial rocks.

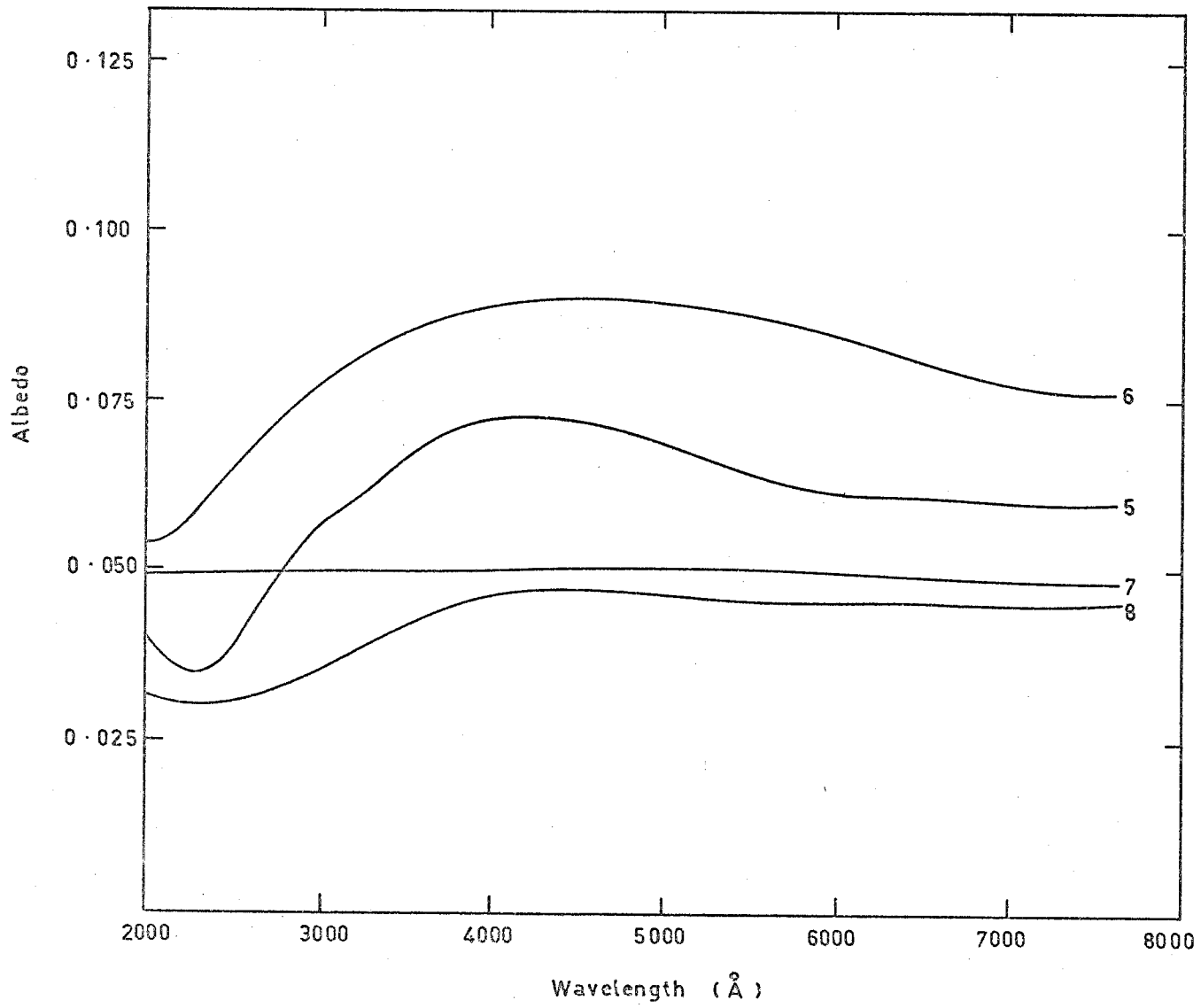

Figure. 6·9 Albedos of some terrestrial rocks.

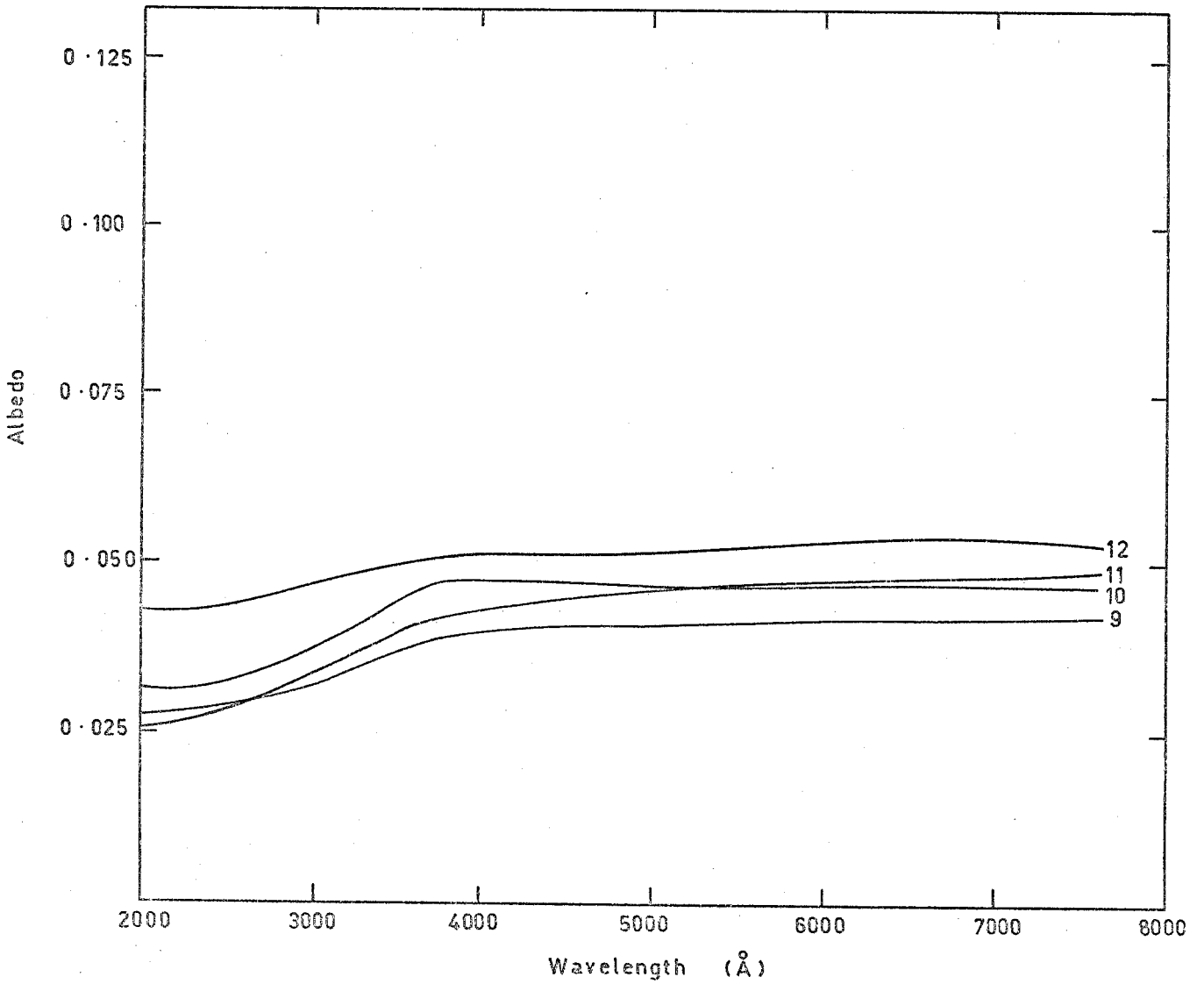

Figure 6 · 10 Albedos of some terrestrial rocks.

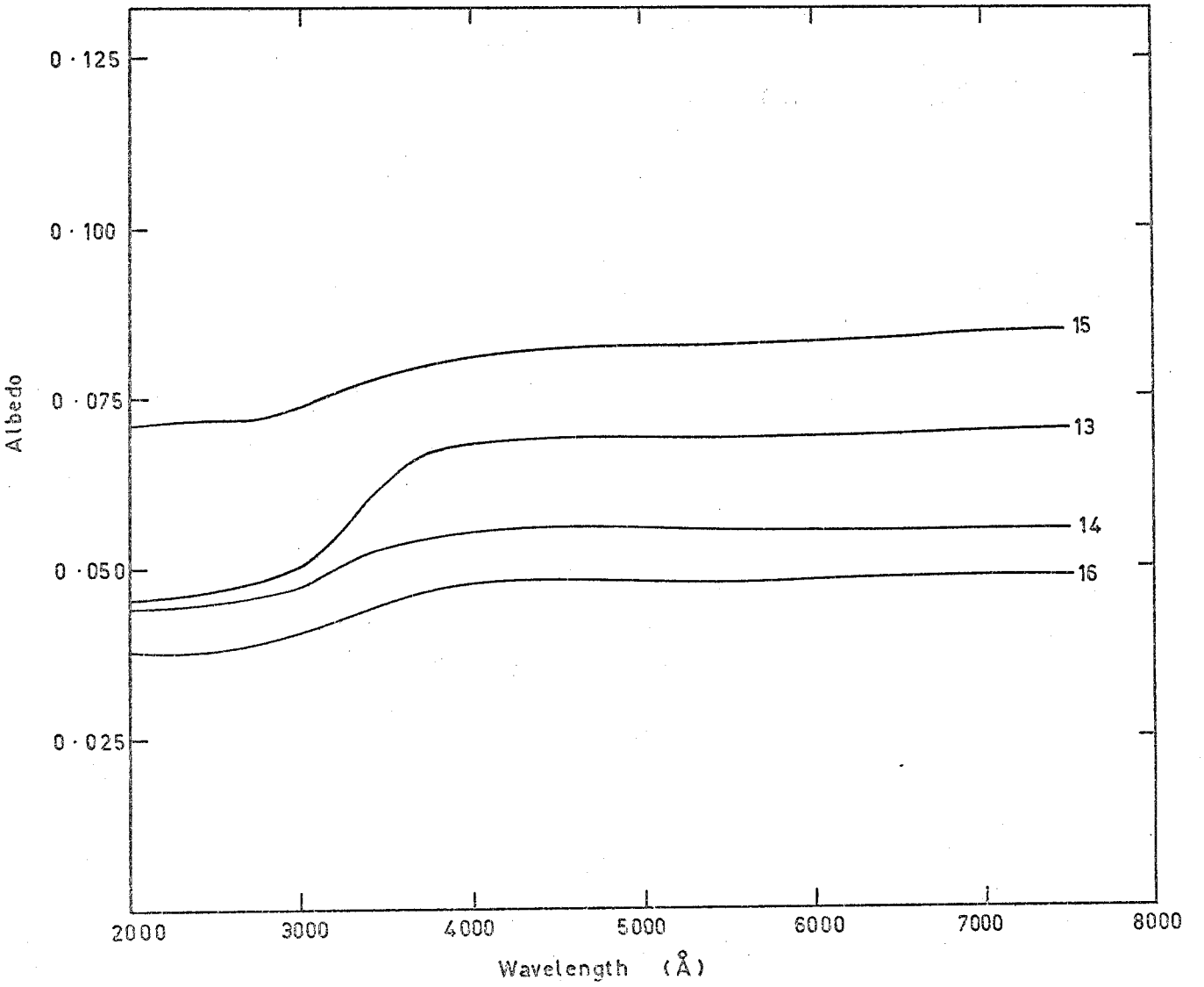

Figure 6 · 11 Albedos of some terrestrial rocks.

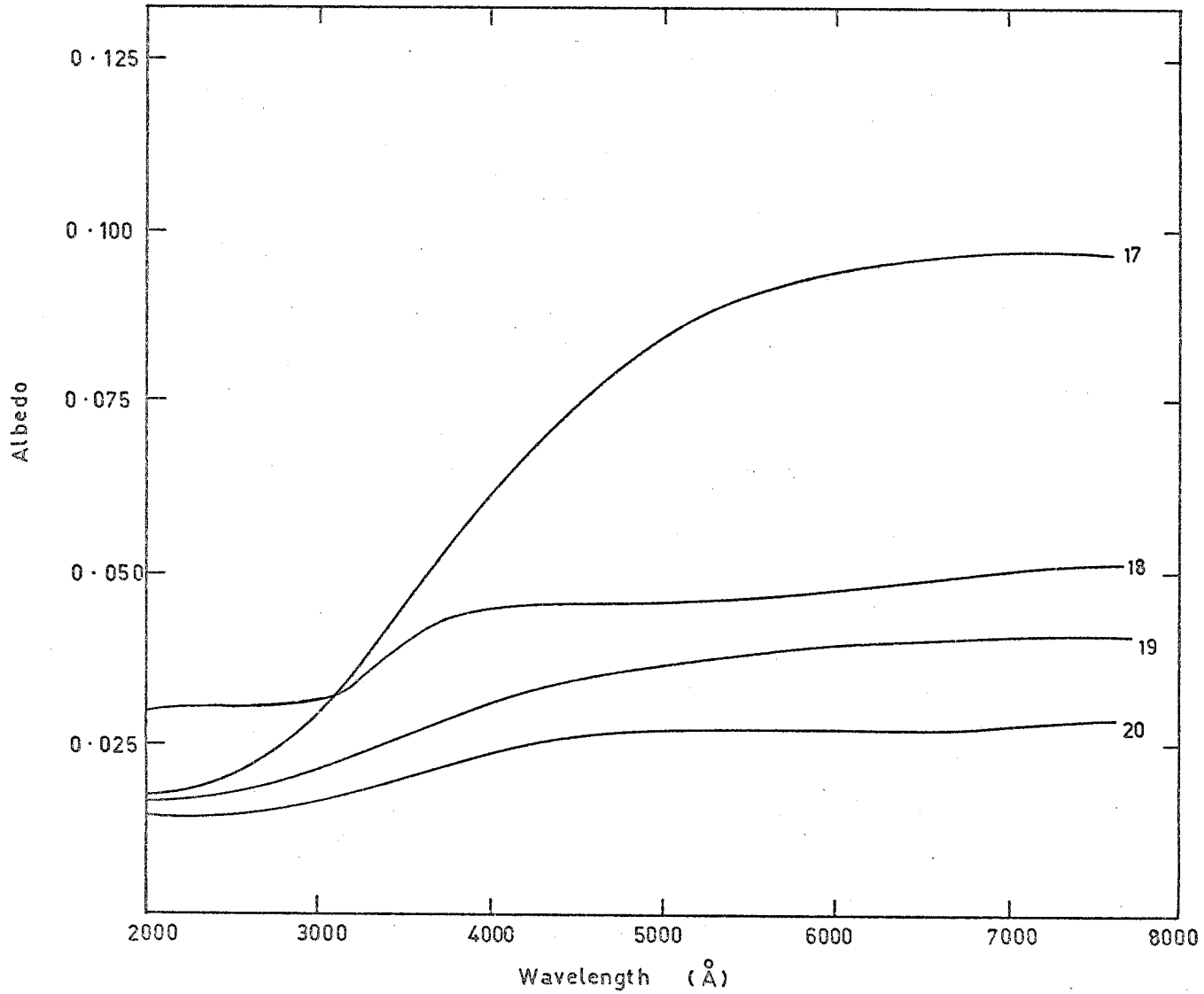

Figure 6 · 12 Albedos of some terrestrial rocks.

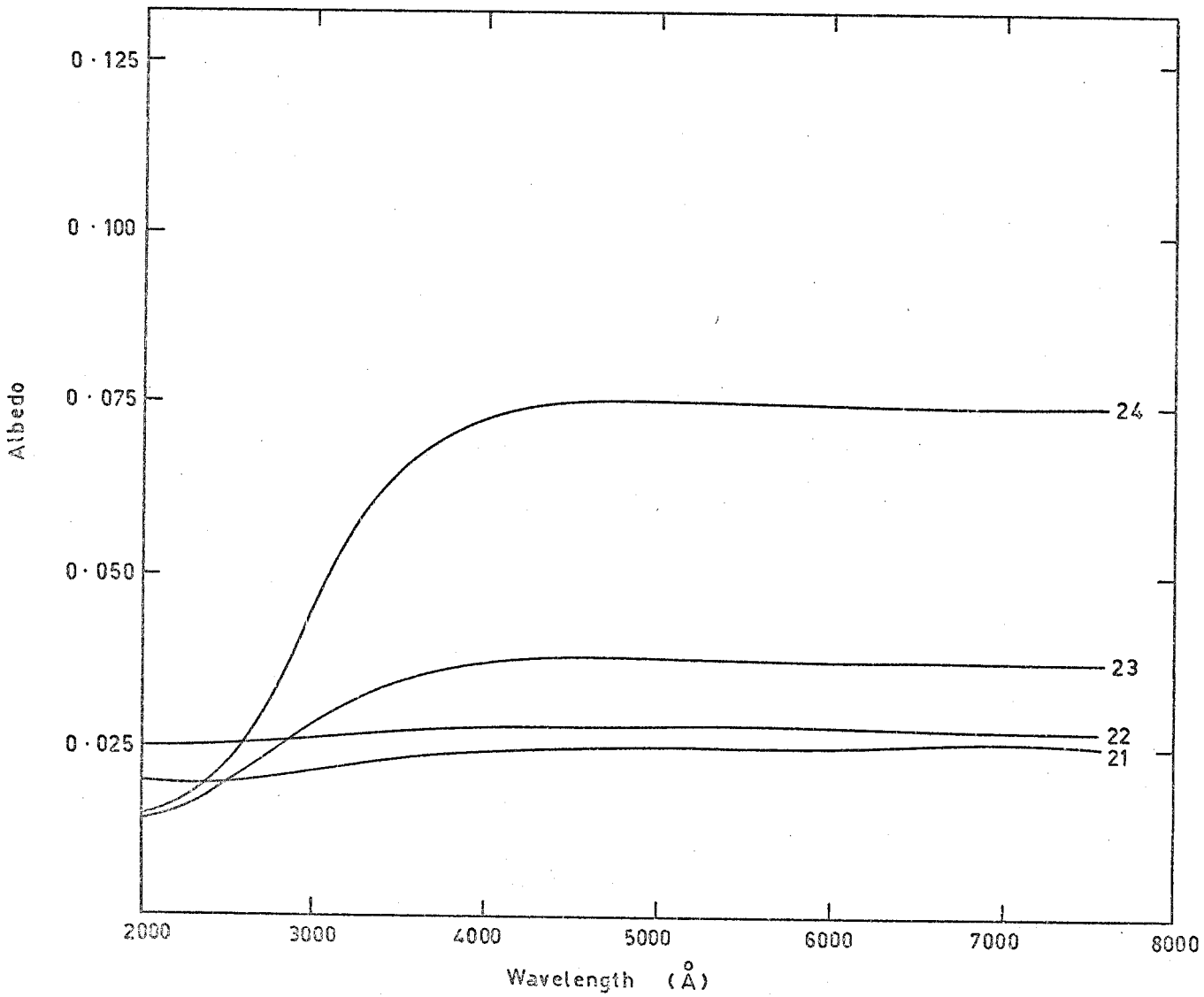

Figure 6 · 13 Albedos of some terrestrial rocks.

smoother was balanced by the decrease in the amount of diffuse reflection, or, alternatively, for the surfaces prepared with grinding powders of less than approximately 30μ in size there was very little multiple scattering while the surfaces prepared with 60μ grinding powder there was appreciable multiple scattering from the surface irregularities. The effect of multiple scattering would be to reduce the measured reflectivity unless the absorption coefficient of the surface was so small that radiation which underwent multiple reflections was not significantly attenuated relative to radiation which was only reflected once before reaching the detector.

The results for a typical specimen are shown in Figure 6.14.

6.10 Comparison of Rock Measurements with the Lunar Albedo

The albedos of some of the rock samples, calculated using (6.9) are compared in Figure 6.15 with the values of lunar albedo taken from Figure 4.3, and also with the values of lunar albedo given by Lane and Irvine (1973). The curves shown are for the samples which showed a large change in albedo between 2000Å and 4000Å. The remainder of the samples tested gave results which showed little resemblance to the lunar spectral albedo.

It can be seen that samples 17 and 24 (see Table 6.3) gave results very similar to the lunar albedo curve from 2000Å to 6000Å. Most of the other samples were much brighter than

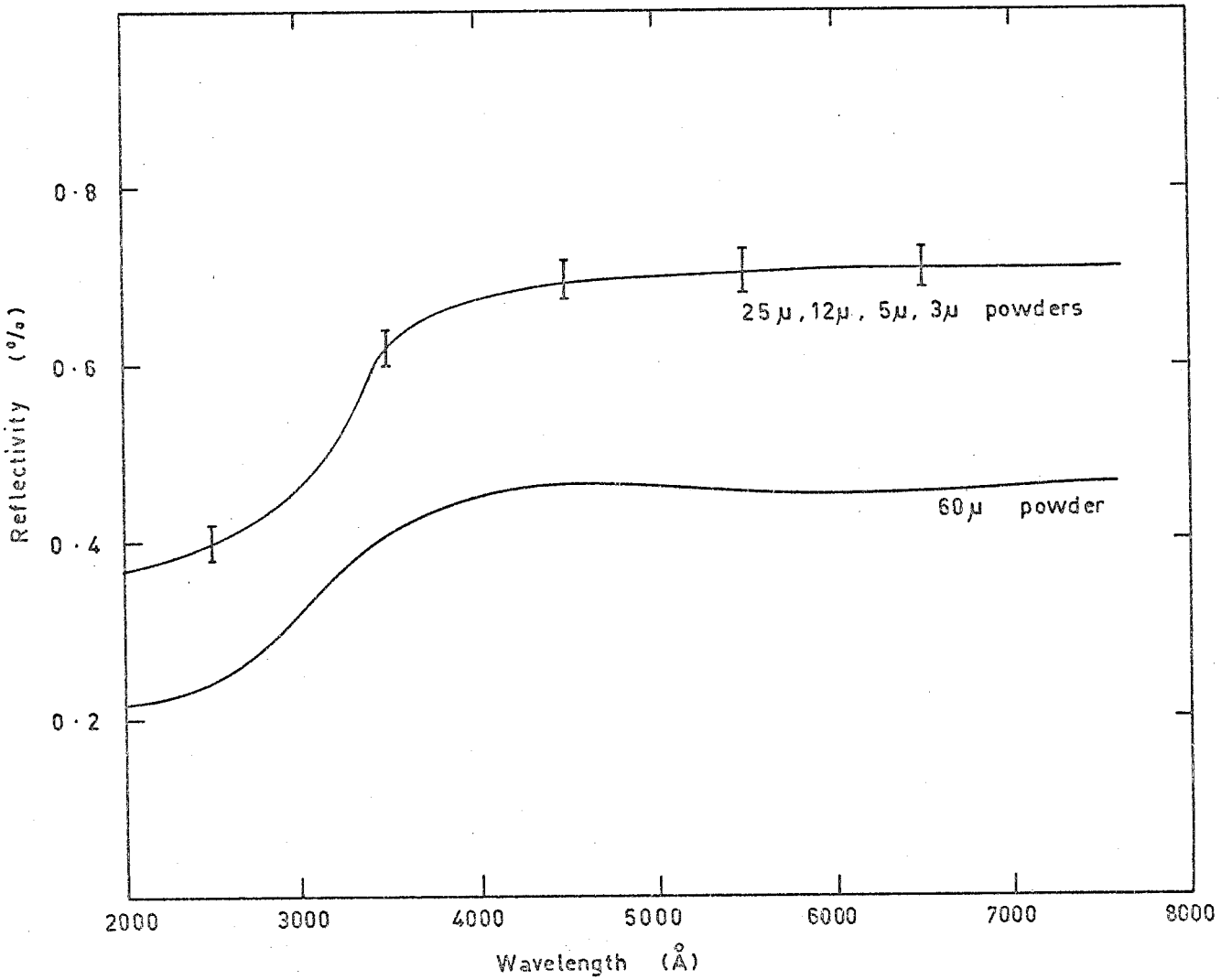

Figure 6 · 14 Effects of different grinding powders on the reflectivity of a typical rock sample. The error bars indicate the variation in reflectivity after grinding with 25 μ, 12 μ, 5 μ and 3 μ powders.

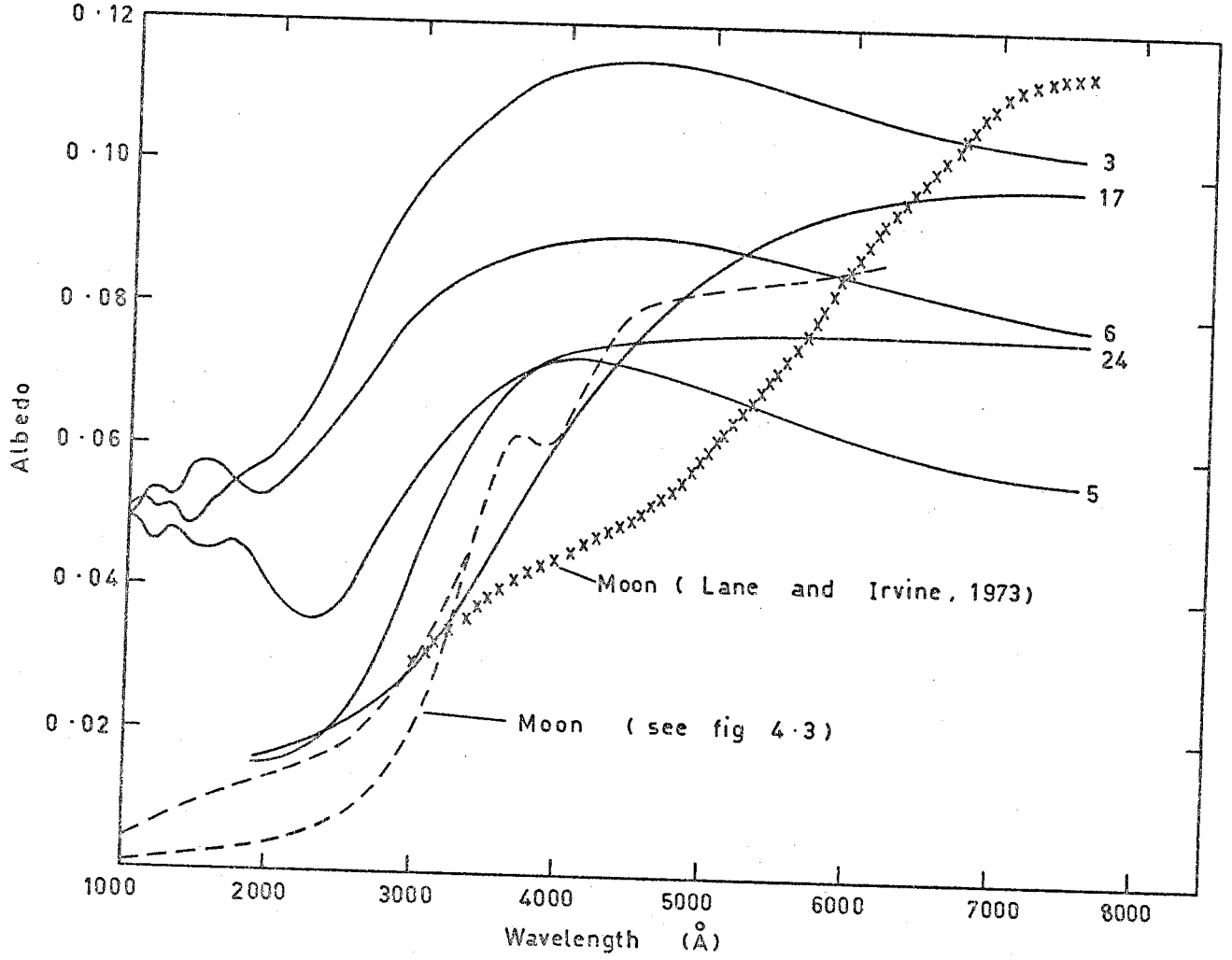

Figure 6 · 15 Comparison of the lunar albedo with the albedo of some terrestrial rocks (the relative error in the rock albedos is of the order of 15 %).

the moon below about 3000Å but darker than the moon above 3000Å.

The curves shown in Figure 6.15 were normalized to 1 at 6000Å and the relative spectral albedos were then plotted. These relative spectral albedos are shown in Figure 6.16.

The similarity between the albedo for sample 17 (an anorthosite rock) and the lunar albedo, together with the sharp rise in reflectivity between 2000Å and 4000Å for sample 3 (another anorthosite), suggests that anorthosite type rocks may have considerable influence on the lunar spectral reflectivity. This is consistent with the results of Wilshire et al (1973), who reported that most of the rock samples collected around the Apollo 16 landing site on the moon were derived from anorthosite-norite type rocks. (Norite is a member of the gabro → anorthosite family of rocks (Read and Watson, 1962, p.414) and is usually rich in the minerals Hypersthene, $(Mg,Fe)SiO_3$, and Labradorite, one of the plagioclase feldspar group of minerals).

The other sample (No. 24) which showed a similar albedo to that of the moon was an andesite tuff. This sample, in contrast to sample 17 (which was a very coarse-grained rock) consisted of a very fine-grained groundmass of uniform colour, with some small crystals (up to 1 mm in diameter) embedded in this groundmass. The surface of this sample was extremely porous whereas that of sample 17 showed no evidence of porosity at all.

The similarity in composition between these two samples is summarized below:-

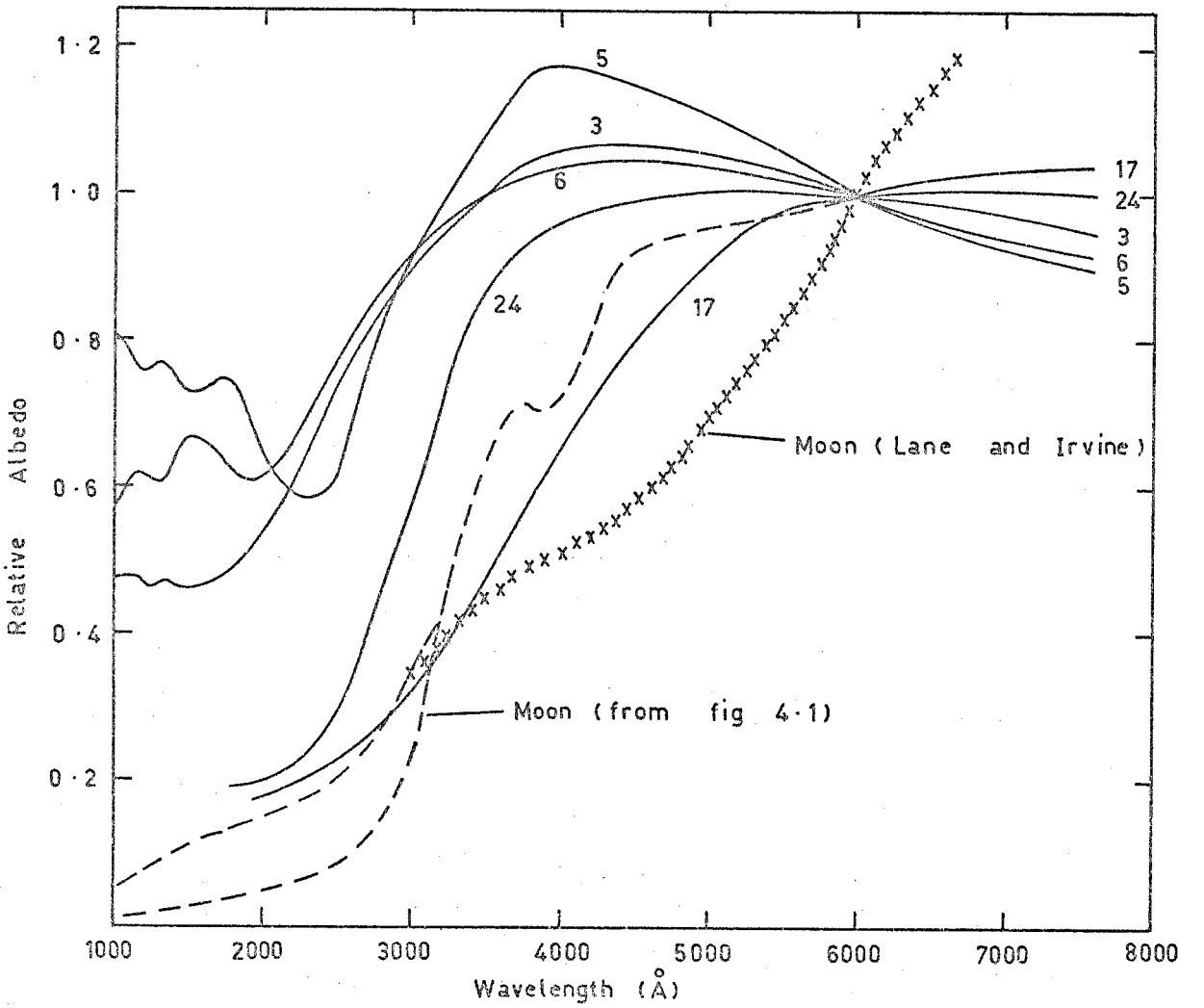

Figure 6 · 16 A comparison of the relative spectral albedos of the moon and some terrestrial rocks.

anorthosite - > 90% anorthite ($CaAl_2Si_2O_8$), plus < 10% albite ($NaAlSi_3O_8$)

andesite - 30-50% anorthite plus 70-50% albite.

The remaining three samples (3,5 and 6) which showed rises in albedo comparable with that of the moon in the region 2000Å to 4000Å were all medium- to coarse-grained samples with no surface prosity, and were generally darker in colour to the eye than samples 17 and 24.

The feature common to all these samples (3, 5, 6, 17 and 24) is that they are all rich in the plagioclase feldspar minerals and relatively deficient in the ferromagnesian minerals.

6.11 Conclusions

The identification of rock types and rock forming minerals from their ultraviolet reflectance spectra appears to be a difficult process, since the reflectance measurements indicate very little structure which can positively be identified with specific rock-forming minerals.

The sharp rise in the lunar spectral albedo between 3000Å and 4000Å appears to be partly due to the presence of surface materials rich in the plagioclase feldspar minerals and relatively deficient in the ferromagnesian minerals. This suggests the presence on the lunar surface of rocks similar in composition to terrestrial anorthosites, andesites and gabbros.

The rise in the lunar albedo appears to be predominantly due to either the chemical composition of the surface material or to the surface structure, but does not appear to depend on the mode of formation of the surface rocks.

CHAPTER 7

THEORY OF REFLECTION FROM A ROUGH SURFACE

7.1 Introduction

It has long been known that materials reflect light in a way which depends both on their optical properties and their surface structure. In Chapter 4 the unusual way in which the lunar surface reflects visible light was briefly discussed and some of the properties of the lunar surface layer, which have been deduced from its reflecting properties, were discussed.

This process is not confined to problems of this type - Maxwell's theory of electromagnetic waves enables us to deduce that for metals and dielectrics the reflection from a plane interface between two such media depends directly on the optical properties of the materials involved. In the case of a rough surface the problem is much more complicated because of the effect of the surface structure.

7.2 Reflection from Smooth Surfaces

If we consider a plane electromagnetic wave incident on a smooth surface the reflection coefficients for this surface can be found by solving Maxwell's equations for the electromagnetic fields, subject to the appropriate boundary conditions. It can be shown that the reflection coefficients depend on the properties of the two media involved, on the polarization of the incident wave, and on the angle of incidence.

For the two cases where the incident wave is polarized parallel and perpendicular to the plane of incidence the reflection coefficients for the electric component of the incident wave are given by

$$R_{\parallel} = \frac{\cos\theta_2 - n\cos\theta_1}{\cos\theta_2 + n\cos\theta_1}$$

$$R_{\perp} = \frac{\cos\theta_1 - n\cos\theta_2}{\cos\theta_1 + n\cos\theta_2} \qquad \ldots (7.1)$$

where n is the complex refractive index of medium 2 relative to that of medium 1

θ_1 is the angle of incidence (in medium 1)

θ_2 is the angle of refraction (in medium 2)

The coefficients $R_{\parallel}$ and $R_{\perp}$ are called the Fresnel Coefficients. For the magnetic component of the wave the reflection coefficients are given by the negatives of the corresponding coefficients for the electric component of the wave.

The angles θ_1 and θ_2 are related by Snell's Law, which states

$$\sin\theta_1 = n\sin\theta_2 \qquad \ldots (7.2)$$

7.3 Reflection from Rough Surfaces

The radiation reflected from a rough surface is usually regarded as consisting of two distinct parts. The first is the specular component which obeys the same laws as radiation

which is reflected from a smooth surface. This type of reflection is produced by the change in optical properties at the interface between two media. The second component of the reflected radiation is the non-specular, or diffuse, component. This is produced by the penetration of some of the incident radiation into the interior of the reflecting material; some of this radiation returns to the surface of the material after undergoing partial absorption and multiple scattering at the boundaries of the individual particles inside the material.

The experimental evidence for the existence of these two distinct components is summarized by Wendlandt and Hecht (1966).

The diffuse component of the reflected radiation is found experimentally to be unpolarized for many materials (with the exception of strongly coloured materials), regardless of the state of polarization of the incident radiation. This feature of diffuse reflection is discussed in detail by Wendlandt and Hecht and also by Hecht (1967).

7.3.1 Lambert's Law

It is found experimentally that many matt surfaces irradiated with radiation of constant intensity appear uniformly bright at all angles of observation. This is expressed in terms of Lambert's Law, viz.,

$$R(\theta_1,\theta_2) = \frac{R(0,0)}{\pi} \cos\theta_1 \cos\theta_2 \qquad \ldots (7.3)$$

where θ_1 is the angle of incidence

θ_2 is the angle of reflection

and $R(\theta_1,\theta_2)$ is the reflection coefficient for radiation incident at angle θ_1 and reflected at angle θ_2.

The Lambert Law is not derived from first principles, and has been found to be strictly valid only for small values of θ_1 and θ_2 (Wendlandt and Hecht (1966), Kortüm (1969)). Wendlandt and Hecht have also discussed several attempts to formulate the reflection problem in such a way as to describe both specular and diffuse reflection in a single formulation. This approach is suggested by the experimental observation that both types of reflection always occur, the relative proportion of each depending on the nature of the reflecting medium.

7.3.2 The Lommel-Seeliger Law

In some cases, e.g. Pikkarainen (1969), and Hapke (1963), the reflection coefficient is given to good accuracy by the Lommel-Seeliger scattering law, which may be expressed in the form (using the same notation as before)

$$R(\theta_1,\theta_2) = R(0,0)\,\frac{\cos\theta_1\,\cos\theta_2}{\cos\theta_1 + \cos\theta_2} \qquad \ldots (7.4)$$

Kortüm (1969) has shown that the Lommel-Seeliger Law is generally inferior to the Lambert Law, even for small values of θ_1 and θ_2. However the work of Pikkarainen and Hapke suggests that the Lommel-Seeliger Law may be preferable when dealing with highly porous surfaces or very rough surfaces.

7.3.3 Rough Surface Models

Several authors have developed models for rough surfaces in attempts to explain the observed reflecting and scattering properties of such surfaces. One rough surface which has been extensively studied is the lunar surface; its unusual optical properties have already been described in Chapter 4.

Several different models of the lunar surface have been developed. Hapke (1963) assumed a model surface consisting of a semi-infinite, porous layer of randomly placed obscuring objects suspended in depth in such a way that the interstices separating them were interconnected. Gehrels (1964) proposed that the lunar surface consisted of a smooth sub-surface layer covered by a very thin over-lying layer of ionized, accreted interplanetary particles. Pikkarainen (1969) used a model consisting of a surface covered with parabolic holes.

In discussing the theory of radar scatter from the lunar surface Fung (1964) used a model in which the height distribution of points on the surface was specified, while Marcus (1969) used a statistical model in which the distribution of the slopes of small areas on the surface was specified. Both these models gave quite good agreement with experimental observations for angles of incidence up to about 30 degrees.

7.4 Basic Theory and Notation

The theory developed in this and the following sections is based on the work of Beckmann and Spizzichino (1963), and Davies (1954).

The starting point for the theory is the Kirchhoff formula for the reflected field at a point P a distance R´ from the point of reflection, viz.,

$$E_P = \frac{1}{4\pi} \int_S \int \left(E_S \frac{\partial \psi}{\partial n} - \psi \left(\frac{\partial E}{\partial n} \right)_S \right) dS \qquad \ldots (7.5)$$

where E_P = the reflected field at P

E_S = the field on the surface S

$\left(\frac{\partial E}{\partial n}\right)_S$ = the normal derivative of the field on the surface

$\psi = \frac{e^{i\underline{k}_2 . \underline{R}'}}{R'}$ (an expanding spherical wave)

$\underline{k}_1$ = the incident wave-vector

$\underline{k}_2$ = the reflected wave-vector

$\underline{n}$ = the normal to the surface at the point of reflection

θ_1 = the zenith angle of incidence

θ_2, θ_3 = the zenith and azimuth angles of reflection

$\underline{R}'$ = a vector from the point of reflection to the point of observation

The field on the surface at the point of reflection is

$$E_S = (1+R) E_o e^{-i(\omega t - \underline{k}_1 . \underline{r}')} \qquad \ldots (7.6)$$

where E_o = the field at the source

R = the reflection coefficient of the surface

$\underline{r}'$ = a vector from the point of reflection to the source

Also $$\left(\frac{\partial E}{\partial n}\right)_S = -i(1-R)E_o e^{-i(\omega t - \underline{k}_1 . \underline{r}')} \underline{k}_1 . \underline{n} \qquad \ldots (7.7)$$

The relation between the surface and the directions of incidence and reflection is shown in Figure 7.1. It should be noted that we have assumed that the zenith angle of incidence is zero. This can always be done by rotating the set of reference axes (in Figure 7.1) so that the plane of incidence coincides with the xOz plane.

The relation between the surface and the vectors $\underline{n}$, $\underline{k}_1$, $\underline{k}_2$, $\underline{r}$ and $\underline{R}'$ is shown in Figure 7.2.

The assumptions made in deriving (7.5), (7.6) and (7.7) are briefly listed below -

(i) the incident wave is plane, infinite in extent, and linearly polarized - this enables the reflection coefficient R to be written in terms of the Fresnel coefficients $R_{\parallel}$ and $R_{\perp}$ which were discussed in Section 7.2

(ii) the reflection coefficient R is independent of the local angle of incidence. This means that R is constant over the entire surface

(iii) multiple scattering can be neglected

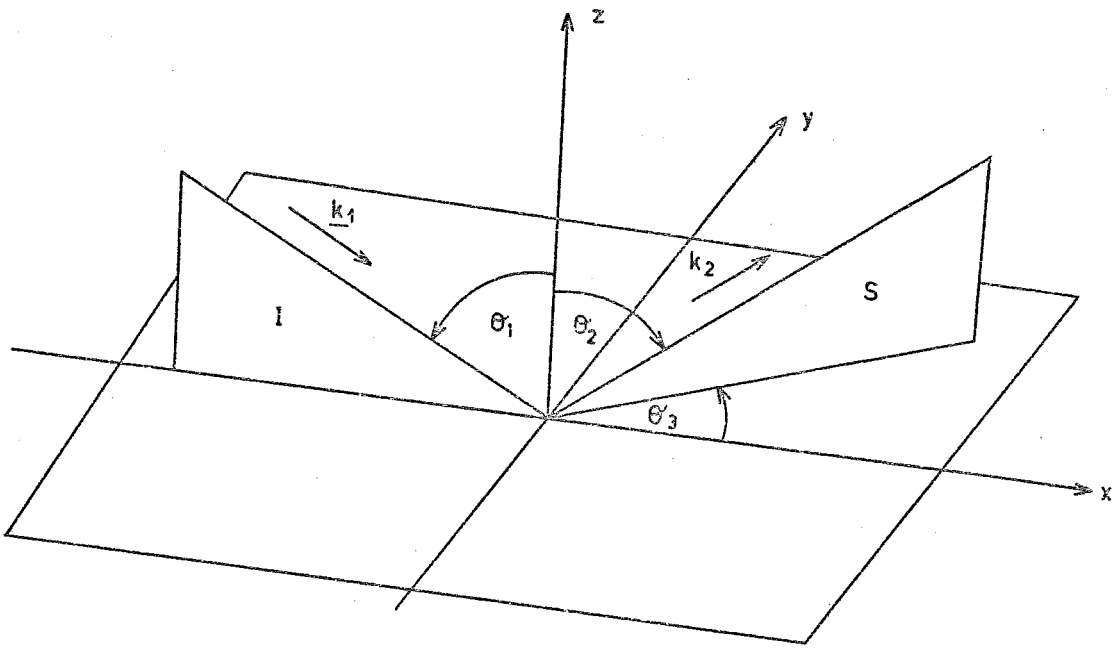

Figure 7 · 1 The relation between the reference axes, the plane of incidence (I), and the scattering plane (S).

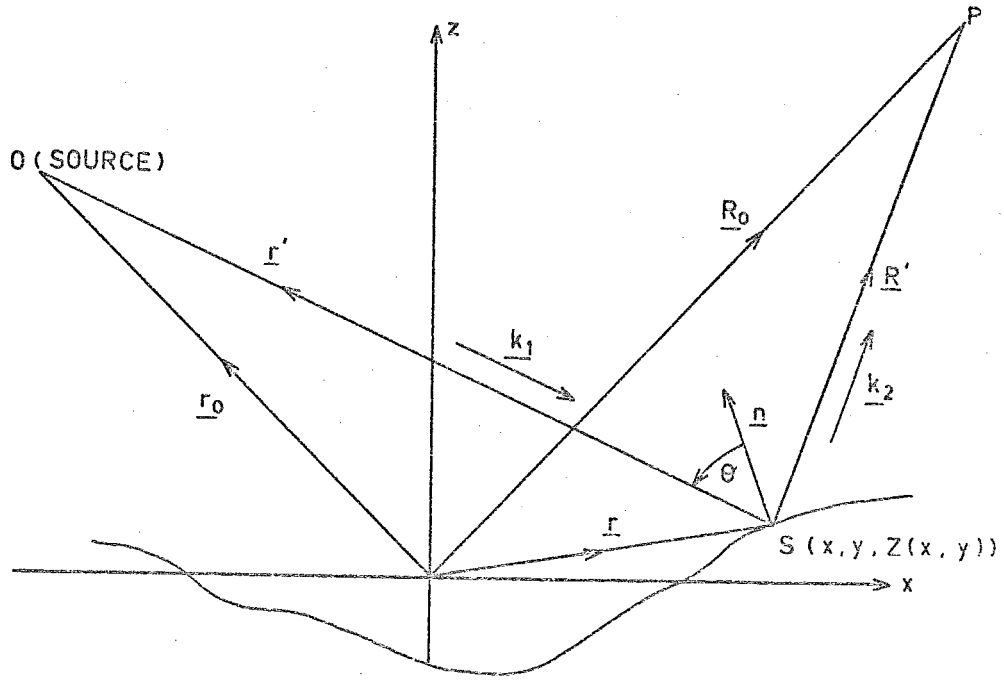

Figure 7 · 2 The relation between $\underline{k}_1$, $\underline{k}_2$, $\underline{R}'$ $\underline{R}$ and $\underline{n}$, the unit vector normal to the surface at S. (θ is the local angle of incidence at point S.)

(iv) the field and its normal derivative on the surface can be defined as in (7.6) and (7.7), i.e. E_S and $\left(\frac{\partial E}{\partial n}\right)_S$ can be approximated at any point on the surface by their values on the tangent plane at that point. This approximation is good if the radius of curvature of the surface irregularities are large compared with the wavelength but breaks down if the surface includes sharp edges or sharp points.

(v) writing E_S and $\left(\frac{\partial E}{\partial n}\right)_S$ in the form given by (7.6) and (7.7) assumes that the dimensions of the surface (in the xOy plane) are much greater than the wavelength.

If we define the vectors $\underline{r}$, $\underline{r}_o$ and $\underline{R}_o$ by means of Figure 7.2 and assume that both the source and the point of observation are removed to infinity (this enables the reflected field to be treated as a plane wave) then

$$\underline{r}_o = \underline{r}' + \underline{r} \qquad \ldots (7.8)$$

so that $\underline{k}_1 . \underline{r}' = \underline{k}_1 . \underline{r}_o - \underline{k}_1 . \underline{r}$ ... (7.9)

Similarly $\underline{k}_2 . \underline{R}' = -\underline{k}_1 . \underline{R}_o + \underline{k}_2 . \underline{r}$ ... (7.10)

and $$\psi = \frac{e^{-i(\omega t + \underline{k}_2 . \underline{R}_o - \underline{k}_2 . \underline{r})}}{R_o} \qquad \ldots (7.11)$$

and $$\frac{\partial \psi}{\partial n} = \frac{\partial R_o}{\partial n} \cdot \frac{\partial \psi}{\partial R_o} = +i\underline{k}_2 . \underline{n}\psi \qquad \ldots (7.12)$$

where a term involving $\frac{1}{R_o^2}$ has been neglected.

Substituting (7.6), (7.7), (7.11) and (7.12) into (7.5) leads to the following result (in which the time dependence $e^{-i\omega t}$ has been neglected).

$$E_P = \frac{iE_o}{4\pi R_o} e^{i(\underline{k}_1 . \underline{r}_o - \underline{k}_2 . R_o)}$$

$$. \int\int_S ((1+R)\underline{k}_2 + (1-R)\underline{k}_1) \; . \; \underline{n} e^{i(\underline{k}_2 - \underline{k}_1) . \underline{r}} \, dS \qquad \ldots (7.13)$$

The effect of shadowing of one part of the surface by another can be included by replacing dS by

$$dS = \Gamma_S(Z, Z_x, Z_y, \theta_1, \theta_2, \theta_3) dS_o \qquad \ldots (7.14)$$

where Γ_S represents the probability that the point S will contribute to the intensity of scattered radiation at P, given that the point S is illuminated, while dS_o is the area of the surface element being considered, and Z_x and Z_y denote the partial derivatives of Z(x,y) with respect to x and y respectively.

If we assume that

$$|\underline{k}_1| = |\underline{k}_2| = \frac{2\pi}{\lambda}$$

then it can be seen from Figures 7.1 and 7.2 that

$$\underline{k}_1 = k(\sin\theta_1 \; \underline{i}_1 - \cos\theta_1 \; \underline{i}_3) \qquad \ldots (7.15)$$

$$\underline{k}_2 = k(\sin\theta_2 \cos\theta_3 \; \underline{i}_1 + \sin\theta_2 \sin\theta_3 \; \underline{i}_2 + \cos\theta_2 \; \underline{i}_3) \qquad \ldots (7.16)$$

$$\underline{r} = x\underline{i}_1 + y\underline{i}_2 + Z(x,y)\underline{i}_3 \qquad \ldots (7.17)$$

where $\underline{i}_1, \underline{i}_2, \underline{i}_3$ denote the unit vectors parallel to the x, y and z axes respectively.

$$\therefore \quad (\underline{k}_2 - \underline{k}_1).\underline{r} = k(ax+by+cZ) \qquad \ldots (7.18)$$

where
$$a = \sin\theta_2 \cos\theta_3 - \sin\theta_1 \qquad \ldots (7.19)$$
$$b = \sin\theta_2 \sin\theta_3 \qquad \ldots (7.20)$$
$$c = \cos\theta_2 + \cos\theta_1 \qquad \ldots (7.21)$$

The unit normal to the surface at the point $(x,y,Z(x,y))$ is given by

$$\underline{n} = \frac{-Z_x\underline{i}_1 - Z_y\underline{i}_2 + \underline{i}_3}{(1 + Z_x^2 + Z_y^2)^{\frac{1}{2}}} \qquad \ldots (7.22)$$

where

$$Z_x = \frac{\partial Z}{\partial x}(x,y), \quad Z_y = \frac{\partial Z}{\partial y}(x,y) \qquad \ldots (7.23)$$

Therefore

$$((1+R)\underline{k}_2 + (1-R)\underline{k}_1) \cdot \underline{n} = k(w - uZ_x - vZ_y) \qquad \ldots (7.24)$$

where

$$u = (1+R)\sin\theta_2 \cos\theta_3 + (1-R)\sin\theta_1 \qquad \ldots (7.25)$$
$$v = (1+R)\sin\theta_2 \sin\theta_3 \qquad \ldots (7.26)$$
$$w = (1+R)\cos\theta_2 - (1-R)\cos\theta_1 \qquad \ldots (7.27)$$

Since the surface is not, in general, parallel to the x-y plane, the surface element dS_o is given by

$$dS_o = \frac{dxdy}{|\underline{n}.\underline{i}_3|} = (1+Z_x^2+Z_y^2)^{\frac{1}{2}}dxdy \qquad \ldots (7.28)$$

Substituting (7.14), (7.18), (7.24) and (7.28) into (7.13) gives

$$E_P = \frac{ikE_o}{4\pi R_o} e^{i(\underline{k}_1.\underline{r}_o - \underline{k}_2.\underline{R}_o)}$$

$$. \int_S\int e^{ik(ax+by+cZ)} (w-uZ_x-vZ_y)\Gamma_S dxdy \qquad \ldots (7.29)$$

where the shadowing function has been denoted by Γ_S for brevity.

In the experiments described in Chapters 5 and 6 the quantity measured was the energy (i.e. the total number of photons) reaching the detector. This quantity can be calculated from (7.29) in the following way.

The mean intensity of scattered radiation in the direction (θ_2,θ_3) is given by I_S where

$$I_S = \left\langle |E_P|^2 \right\rangle = \left\langle E_P E_P^* \right\rangle \qquad \ldots (7.30)$$

where $\left\langle F \right\rangle$ denotes the value of F, averaged over the surface, and E_P^* is the complex conjugate of E_P.

The total energy reaching the detector is then given by ε_S where

$$\varepsilon_S = \int_A\int I_S.dA \qquad \ldots (7.31)$$

where A denotes the sensitive area of the detector.

In terms of the angles θ_2 and θ_3 this last result can be written as

$$\varepsilon_S = R_o^2 \int_\Omega\int I_S d\Omega = R_o^2 \int_\Omega\int I_S \sin\theta_2 d\theta_2 d\theta_3 \qquad \ldots (7.32)$$

where Ω is the solid angle subtended by the detector at a point on the surface.

Substituting (7.29) into (7.30) gives the result

$$I_S = \left(\frac{kE_o}{4\pi R_o}\right)^2 \left\langle \iiiint e^{ik[a(x-x')+b(y-y')+c(Z-Z')]} \right.$$

$$\left. \cdot (w-uZ_x-vZ_y)(w-uZ'_x-vZ'_y)\Gamma_S\Gamma'_S dx dy dx' dy' \right\rangle \qquad \ldots (7.33)$$

where

$$Z' = Z(x',y'), \quad Z'_x = \frac{\partial Z}{\partial x}(x',y'), \text{ etc.} \qquad \ldots (7.34)$$

$$\Gamma'_S = \Gamma_S(\theta_1,\theta_2,\theta_3,Z',Z'_x,Z'_y) \qquad \ldots (7.35)$$

and (x,y,Z), (x',y',Z') are two points on the surface such that the projection of the distance between them onto the x-y plane is given by τ, where

$$\tau^2 = (x-x')^2 + (y-y')^2 \qquad \ldots (7.36)$$

If the surface is perfectly smooth, $Z = Z' = 0, T_S = T'_S = 1$ so that substitution of (7.33) into (7.32) leads to the result

$$\varepsilon_S = (\varepsilon_S)_o = \left(\frac{kE_o 1m}{\pi R_o}\right)^2 R_o^2 \int_\Omega \int w^2 \left[\frac{\sin(kla)}{kla} \cdot \frac{\sin(kmb)}{kmb}\right]^2 \sin\theta_2 d\theta_2 d\theta_3$$

... (7.37)

where 21 and 2m are the dimensions of the surface in the x and y directions respectively.

If the surface is perfectly reflecting (i.e. $|R| = 1$) it can be shown (see Appendix 4.1) that carrying out the integration in (7.37) leads to the result

$$(\varepsilon_S)_o = E_o^2 .41m \cos\theta_1 \qquad \ldots (7.38)$$

This result can also be derived intuitively in the following way. A perfect reflector will, by definition, reflect all the energy falling on its surface, regardless of the angle of incidence. If the surface is smooth the reflected energy will be concentrated in the direction of specular reflection. From Figure 7.3 it can be seen that if the incident wave is infinite, plane and of uniform intensity, the total amount of energy falling on the surface is $E_o^2 .41m.\cos\theta_1$, where E_o^2 is the intensity of the incident wave, θ_1 is the angle of incidence and $41m.\cos\theta_1$ is the area of the surface projected in the direction of the incident wave.

This argument shows that the Kirchhoff approximation leads to a result which is consistent with simple considerations for perfect reflectors, provided the results of the Kirchhoff approximation are correctly applied. It also shows that if we

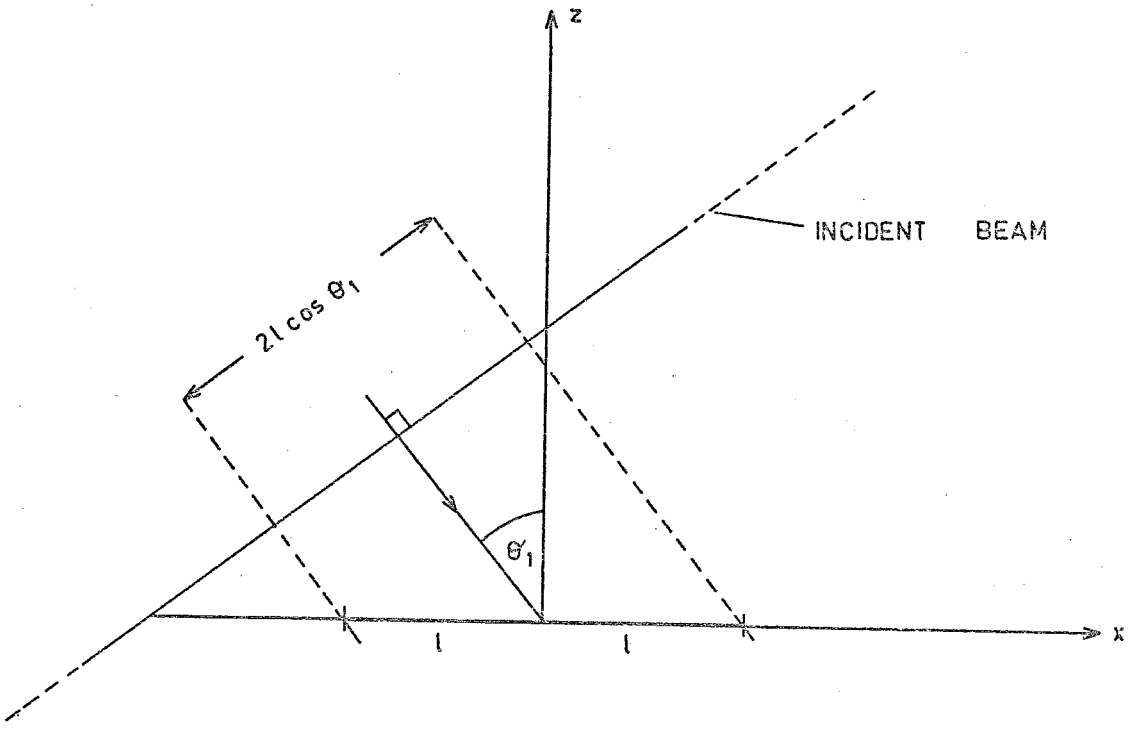

Figure 7.3 The effect of angle of incidence on the amount of energy reaching the reflecting surface. (The y - axis is vertically into the page, and the incoming wave is travelling parallel to the x - z plane).

consider an experimental situation such as that described in Chapters 5 and 6 where the reflecting surface intercepts all the incident energy (except, of course, at grazing incidence), then the total energy reaching the detector must be modified by a factor $\frac{1}{\cos\theta_1}$. Thus (7.32) has to be written as

$$\varepsilon_S = \frac{R_o^2}{\cos\theta_1} \int\int_{\Omega} I_S d\Omega \qquad \ldots (7.39)$$

where I_S is given by (7.33).

The argument used by Beckmann and Spizzichino (pp. 22 and 23 of their book) is equivalent to putting $\theta_1=\theta_2$, $Z=0$ in (7.29) and using the resulting expression in (7.30). This leads to

$$I_S = 4\left(\frac{kE_o}{4\pi R_o}\right)^2 \cos^2\theta_1$$

so that the total energy reaching a detector with a sensitive area A_D would be

$$\varepsilon_S = A_D\left(\frac{kE_o}{4\pi R_o}\right)^2 \cos^2\theta_1$$

The argument following equation (7.38) shows that this result is not consistent with intuitive considerations for a smooth perfectly reflecting surface.

An examination of the experimental results presented in Figure 6.5 shows that the energy reflected from the specimens

does show a $\frac{1}{\cos\theta_1}$ dependence to within ten percent, except at high angles of incidence, where the discrepancy is somewhat greater. This would certainly seem to justify the argument leading up to equation (7.39).

7.5 The Distribution Function

Suppose the function $P_2(Z,Z',\tau)$ describes the joint density distribution of surface heights, and $P(Z)$, $P(Z')$ describe the distribution of Z and Z' values respectively. Then

$$P(Z) = \int_{-\infty}^{\infty} P_2(Z,Z',\tau)dZ' \qquad \ldots (7.40)$$

$$P(Z') = \int_{-\infty}^{\infty} P_2(Z,Z',\tau)dZ \qquad \ldots (7.41)$$

and

$$I_S = \int_{-\infty}^{\infty}\int_{-\infty}^{\infty} |E_p|^2 P_2(Z,Z',\tau)dZdZ' \qquad \ldots (7.42)$$

If the function $P_2(Z,Z',\tau)$ is known, then (7.42) can be used directly to find the distribution of scattered radiation.

The function $P_2(Z,Z',\tau)$ has some important properties which should be noted - they are

(i) if the horizontal separation, τ, between the points (x,y,Z) and (x',y',Z') is large the values of Z and Z' are independent of each other.

i.e. $P_2(Z,Z',\tau) \to P(Z).P(Z')$ for large τ $\qquad \ldots (7.43)$

(ii) if the surface is smooth and Z=0 for all (x,y) then

$$P_2(Z,Z',\tau) = \delta(Z-Z').\delta(Z) \qquad \ldots (7.44)$$

and

$$P(Z) = \delta(Z), \quad P(Z') = \delta(Z') \qquad \ldots (7.45)$$

where $\delta(Z)$ is the Dirac delta function. If we combine these two results we see that, in the limiting case of a smooth surface

$$P_2(Z,Z',\tau) \rightarrow P(Z).P(Z') \qquad \ldots (7.46)$$

7.6 Specular and Diffuse Reflection

In Section (7.3) it was mentioned that experimental evidence suggests that radiation reflected from a rough surface consists of a specular component and a diffuse component. The object of any theory of reflection from rough surfaces is to explain the two different modes of reflection. In the present case, although a detailed mechanism for the two types of reflection cannot be described, the expression for the scattered radiation can be broken up into two parts which behave like the two components of the reflected radiation. This can be done by writing

$$I_S = \left\langle E_P E_P^* \right\rangle = \left\langle E_P \right\rangle \left\langle E_P^* \right\rangle + \left(\left\langle E_P E_P^* \right\rangle - \left\langle E_P \right\rangle \left\langle E_P^* \right\rangle \right) \qquad \ldots (7.47)$$

In terms of the distribution functions defined in Section 7.4 this last equation can be written as

$$I_S = \int_{-\infty}^{\infty}\int_{-\infty}^{\infty}\iiiint P(Z)P(Z')E_P E_P^* dx dy dx' dy' dZ dZ'$$

$$+ \int_{-\infty}^{\infty}\int_{-\infty}^{\infty}\iiiint (P_2(Z,Z',\tau)-P(Z)P(Z'))E_P E_P^* dx dy dx' dy' dZ dZ' \quad \ldots (7.48)$$

$$\text{i.e. } I_S = I_S(S) + I_S(D) \quad \ldots (7.49)$$

where the arguments S and D refer to the specular and diffuse components respectively.

This procedure can be partly justified by noting that for the limiting case of a smooth surface

$$I_S(S) \to (I_S)_o \ , \ I_S(D) \to 0 \quad (\text{as } Z \to Z' \to 0) \quad \ldots (7.50)$$

and this is in agreement with the experimentally observed fact that specular reflection is the dominating effect for smooth surfaces.

7.7 The Shadowing Function

The shadowing function T_S was defined in Section 7.4 as the probability that the point (x,y,Z) will contribute to the scattered intensity, given that S is illuminated. This means that we can write

$$T_S = S_1(Z,Z_x,Z_y,\theta_1) \ . \ S_2(Z,Z_x,Z_y,\theta_2,\theta_3) \quad \ldots (7.51)$$

where S_1 is the probability that the point (x,y,Z) will be illuminated, while S_2 is the probability that this point will contribute to the scattered intensity at P.

Several authors have tried to deduce the form of the shadowing function S. Beckmann (1965) found that for a Gaussian surface

$$S(\theta) = \exp\left(-\frac{1}{4}\tan\theta \ \mathrm{erfc}\left[\frac{\cot\theta}{\sigma(|\rho''(0)|)^{\frac{1}{2}}}\right]\right) \qquad \ldots (7.52)$$

where σ is the root-mean-square roughness of the surface, $\rho(\tau)$ is the auto-correlation function of the surface, and erfc(X) is the complementary error function.

Smith (1967) has developed a much more complicated expression, also for a Gaussian surface, involving the partial derivatives of Z.

Hapke (1963) developed a shadowing function for the lunar surface. Using the model described in Section 7.3, he showed that for such a surface the shadowing function is given by

$$T(Z,\theta_1,\theta_2) = \begin{cases} \frac{2}{\pi}\left[\arccos X - X(1-X^2)^{\frac{1}{2}}\right], & 0 \leqslant X \leqslant 1 \\ 0 \quad , \quad X < 0, \quad X > 1 \end{cases} \qquad \ldots (7.53)$$

where

$$X = \frac{Z\sec\theta_1 \tan(\theta_2+\theta_1)}{2p} \qquad \ldots (7.54)$$

and the quantities Z and p are as shown in Figure 7.4.

In the subsequent analysis it will be assumed, for simplicity, that the shadowing function can be taken outside the integral signs in equation (7.33).

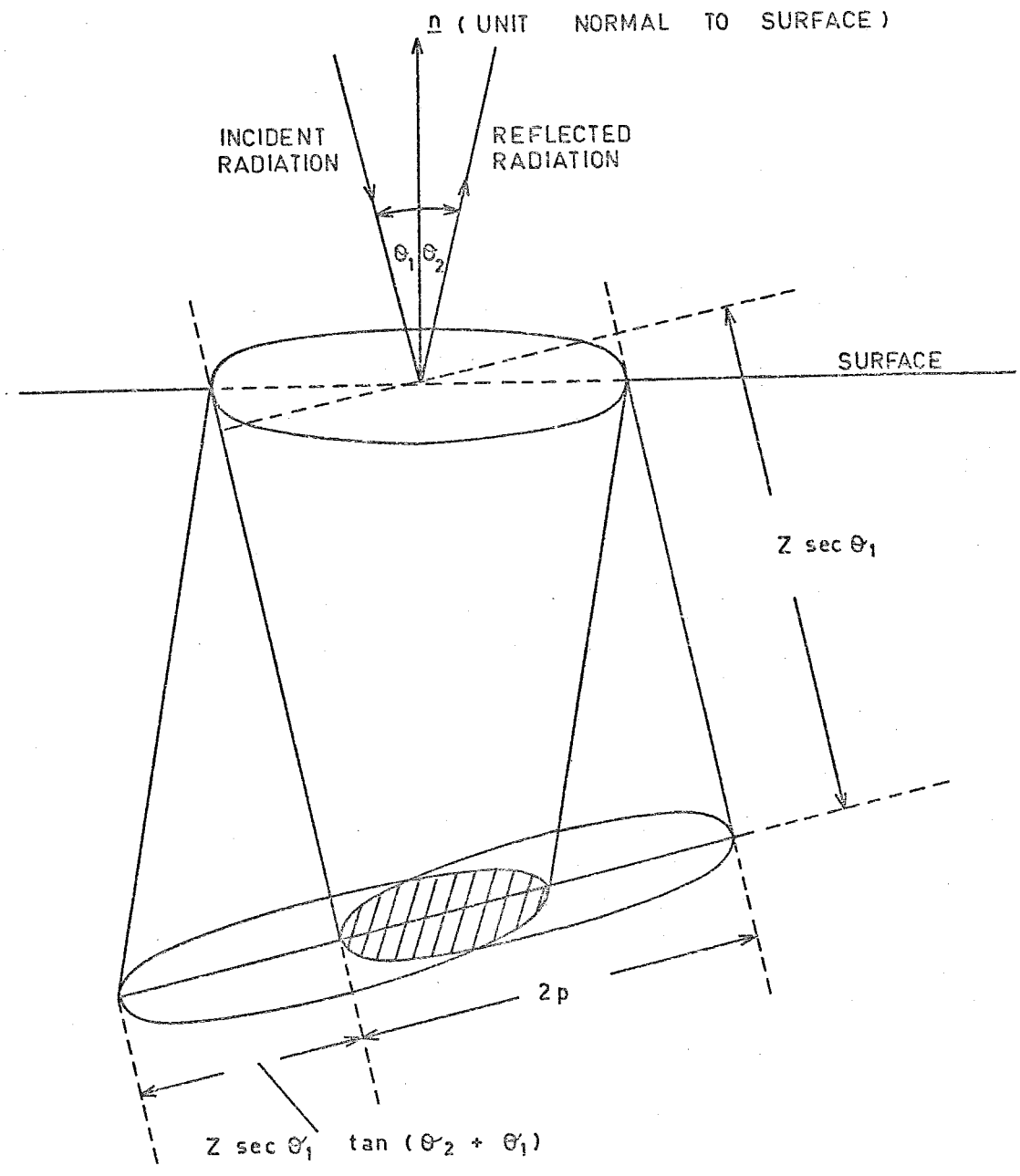

Figure 7 · 4 The geometry used by Hapke (1963) to derive a shadowing function for the lunar surface.

7.8 The Normally Distributed Surface

At this stage it is appropriate to consider a specific form for the distribution function $P_2(Z,Z',\tau)$. One of the simplest forms to handle is the normal distribution. In this case, if $Z(x,y)$ is considered to be a stationary process as well as Gaussian, the distribution function takes the form

$$P_2(Z,Z',\tau) = \frac{1}{2\pi\sigma^2(1-\rho^2)^{\frac{1}{2}}} \exp\left[-\frac{Z^2-2\rho ZZ'+Z'^2}{2\sigma^2(1-\rho^2)}\right] \quad \ldots (7.55)$$

where σ is the r.m.s. roughness of the surface and ρ is the auto-correlation function of the surface. In general ρ is a function of the parameter τ (defined by (7.36)) and the correlation length of the surface, which will be denoted by T.

The choice (7.55) does not imply a marked loss of generality, since the value of σ is a measure of the size of the surface irregularities while the value of T is a measure of the density of these irregularities.

Using the method outlined in Appendix 4.2, equation (7.48) can be evaluated to give

$$I_S(S) = (I_S)_o \, F(\theta_1,\theta_2,\rho''(0))e^{-k^2c^2\sigma^2} \quad \ldots (7.56)$$

and

$$I_S(D) = \left(\frac{kE_o}{4\pi R_o}\right)^2 F(\theta_1,\theta_2,\rho''(0)) \cdot \iiint e^{ik[a(x-x')+b(y-y')]} \cdot \left[e^{-k^2c^2\sigma^2(1-\rho)}\left[u^2\sigma^2\left(\frac{\partial^2\rho}{\partial x\partial x'} + k^2c^2\sigma^2 \frac{\partial\rho}{\partial x} \cdot \frac{\partial\rho}{\partial x'}\right.\right.\right.$$

$$+uv\sigma^2\left(\frac{\partial^2\rho}{\partial x\partial y'} + k^2c^2\sigma^2\,\frac{\partial\rho}{\partial x}\cdot\frac{\partial\rho}{\partial y'}+\frac{\partial^2\rho}{\partial x'\partial y}+k^2c^2\sigma^2\,\frac{\partial\rho}{\partial x'}\cdot\frac{\partial\rho}{\partial y'}\right)$$

$$+v^2\sigma^2\left(\frac{\partial^2\rho}{\partial y\partial y'} + k^2c^2\sigma^2\,\frac{\partial\rho}{\partial y}\cdot\frac{\partial\rho}{\partial y'}\right)+ iuwkc\sigma^2\left(\frac{\partial\rho}{\partial x} - \frac{\partial\rho}{\partial x'}\right)$$

$$+ivwkc\sigma^2\left(\frac{\partial\rho}{\partial y} - \frac{\partial\rho}{\partial y'}\right)+ w^2\Big] - w^2e^{-k^2c^2\sigma^2}\Big]dxdydx'dy' \qquad \ldots (7.57)$$

where $F(\theta_1,\theta_2,\rho''(0))= S(\theta_1)S(\theta_2)$ ... (7.58)

and $S(\theta)$ is the shadowing function defined by (7.52).

The evaluation of (7.57) is greatly simplified by transforming to polar coordinates (τ,α) defined by

$$x-x' = \tau\cos\alpha \quad , \quad y-y' = \tau\sin\alpha \qquad \ldots (7.59)$$

If we assume that the surface is isotropic so that the auto-correlation function does not depend on α, then

$$\frac{\partial\rho}{\partial x} = -\frac{\partial\rho}{\partial x'} = \cos\alpha\,\frac{d\rho}{dt} \qquad \ldots (7.60)$$

$$\frac{\partial\rho}{\partial y} = -\frac{\partial\rho}{\partial y'} = \sin\alpha\,\frac{d\rho}{d\tau} \qquad \ldots (7.61)$$

Substituting these transformations in (7.57) and integrating over x' and y' leads to the result

$$I_S(D) = \left(\frac{kE_o}{4\pi R_o}\right)^2 \cdot 4\mathrm{Im}F(\theta_1,\theta_2,\rho''(0))\int_o^\infty\int_o^{2\pi} e^{ik\tau(a\cos\alpha+b\sin\alpha)}$$

$$\cdot\left[e^{-k^2c^2\sigma^2(1-\rho)}\left[w^2-\sigma^2(u\cos\alpha+v\sin\alpha)^2\left(\frac{d^2\rho}{d\tau^2}+k^2c^2\sigma^2\left(\frac{d\rho}{d\tau}\right)^2\right)\right.\right.$$

$$\left.\left.+\,2iwkc\sigma^2(u\cos\alpha+v\sin\alpha)\frac{d\rho}{d\tau}\right]-w^2e^{-k^2c^2\sigma^2}\right]\tau d\tau d\alpha \qquad \ldots (7.62)$$

The limit of integration over τ has been taken to be infinite in this last expression since the integrand is only significant when $\tau \simeq 0$ (see Section 7.5).

Suppose we put

$$a\cos\alpha + b\sin\alpha = h\cos\psi \qquad \ldots (7.63)$$

$$u\cos\alpha + v\sin\alpha = f\cos(\psi+\delta) \qquad \ldots (7.64)$$

Then

$$h^2 = a^2 + b^2 \qquad \ldots (7.65)$$

$$f^2 = u^2 + v^2 \qquad \ldots (7.66)$$

$$\cos\delta = \frac{au+bv}{hf} \qquad \ldots (7.67)$$

Now,

$$\int_\theta^{2\pi+\theta} e^{it\cos\psi+in\psi}\,d\psi = 2\pi(i)^nJ_n(t) \qquad \ldots (7.68)$$

where $J_n(t)$ is the Bessel function of the first kind, of order n. (Beckmann and Spizzichino, p. 183).

Using these results it can be shown that the integration of (7.62) with respect to α leads to the following result.

$$I_S(D) = 4\pi 1m\left(\frac{kE_o}{4\pi R_o}\right)^2 F(\theta_1,\theta_2,\rho''(0))$$

$$\cdot \int_o^\infty \left[e^{-k^2c^2\sigma^2(1-\rho)}\left[2w^2J_o(hk\tau)\right.\right.$$

$$- \sigma^2 f^2(J_o(hk\tau)-J_2(hk\tau)\cos 2\delta)\left(\frac{d^2\rho}{d\tau^2} + k^2c^2\sigma^2\left(\frac{d\rho}{d\tau}\right)^2\right)$$

$$\left.\left. - 4wfkc\sigma^2 J_1(hk\tau)\frac{d\rho}{d\tau}\cos\delta\right] - 2w^2J_o(hk\tau)e^{-k^2c^2\sigma^2}\right]\tau d\tau$$

... (7.69)

To proceed any further the form of the auto-correlation function $\rho(\tau)$ must be specified. Since we have chosen $\langle Z \rangle = 0$ the auto-correlation function (defined in Appendix 4) is given by

$$\rho(\tau) = \frac{\langle Z(x,y)Z(x',y')\rangle}{\langle (Z(x,y))^2\rangle} \qquad \ldots (7.70)$$

Putting $\tau = 0$ gives $Z(x',y') = Z(x,y)$

$$\therefore \quad \rho(0) = 1 \qquad \ldots (7.71)$$

Further, since we have restricted the discussion to isotropic surfaces $\rho(\tau)$ must be an even function of τ.

One form which satisfies these requirements is

$$\rho(\tau) = e^{-\frac{\tau^2}{T^2}} \qquad \ldots (7.72)$$

where T is the auto-correlation length.

The integrals in (7.69) can be evaluated by using the result (Watson, 1922)

$$\int_0^\infty J_m(ax)e^{-p^2x^2}\, x^{n-1}dx = \sum_{s=0}^{\infty} \frac{(-1)^s(\frac{1}{2}a)^{m+2s}}{s!\Gamma(m+s+1)} \cdot \frac{\Gamma(\frac{1}{2}m+\frac{1}{2}n+s)}{2p^{m+n+2s}} \qquad \ldots (7.73)$$

(where $\Gamma(X)$ is the well-known Gamma Function), and by making the expansion (Beckmann and Spizzichino, p. 82)

$$e^{-k^2c^2\sigma^2(1-\rho)} = e^{-g} \sum_{n=0}^{\infty} \frac{g^n}{n!} e^{-\frac{n\tau^2}{T^2}} \qquad \ldots (7.74)$$

where

$$g = k^2c^2\sigma^2 \qquad \ldots (7.75)$$

Substituting (7.74) and (7.72) into (7.69) and using (7.73) leads to the result

$$I_S(D) = 4\pi 1m\left(\frac{kE_o}{4\pi R_o}\right)^2 F(\theta_1,\theta_2,\rho''(0))e^{-g} \cdot \sigma^2$$

$$\cdot \left[k^2T^2\left[(cw+hf\cos\delta)^2 \sum_{n=0}^{\infty} \frac{g^n}{(n+1)!(n+1)} e^{-\frac{h^2k^2T^2}{4(n+1)}}\right.\right.$$

$$\left. - \frac{1}{4}h^2f^2\cos 2\delta \sum_{n=0}^{\infty} \frac{g^n}{(n+1)!(n+1)} S\left(\frac{h^2k^2T^2}{4(n+1)}\right)\right]$$

$$\left. - f^2 \sum_{n=0}^{\infty} \frac{g^n}{(n+1)!} e^{-\frac{h^2k^2T^2}{4(n+1)}}\right] \qquad \ldots (7.76)$$

where $S(x) = \frac{1}{2}$, $x = 0$

$= \dfrac{1 - e^{-x}(1+x)}{x^2}$, $x \neq 0$ ... (7.77)

The expressions (7.56) and (7.76) are consistent with the earlier decision to call $I_S(S)$ and $I_S(D)$ the specular and diffuse components respectively, of the reflected radiation. We can see immediately from (7.56) and (7.76) that in the limiting case of a smooth surface ($\sigma \to 0$), $I_S(S) \to (I_S)_o$ and $I_S(D) \to 0$.

7.9 Range of Validity of the Theory

The principle assumptions made in deriving (7.56) and (7.76) have already been discussed in Section 7.4. It was also assumed that the scattered waves can be regarded as plane so that the angles θ_1, θ_2 and θ_3 are constant over the whole surface.

Assumption (iii) in Section 7.4 has one important consequence - since the radius of curvature of the surface irregularities must be large compared with the wavelength we must also have

$$T >> \lambda \qquad \ldots (7.78)$$

In addition, since the surface is rough, the correlation distance must be small compared with the dimensions of the surface.

i.e. $T << 1,m$ ... (7.79)

If this were not so the surface would consist of only one or two irregularities and could not be considered to be rough.

The derivation of the results of the previous section is strictly only valid if the reflection coefficient R at any point is independent of the local angle of incidence. This is true only for a perfect conductor. In all other cases it has been assumed that the value of R has been obtained by averaging the Fresnel coefficients (see Section 7.2) over the entire surface.

In terms of the function Z(x,y) it can be seen from Figure 7.2 that if θ is the local angle of incidence the value of $\cos\theta$ is given by

$$\cos\theta = - \frac{\underline{k}_1 . \underline{n}}{k} \qquad \ldots (7.80)$$

Using (7.15) and (7.22) this expression becomes

$$\cos\theta = \frac{-Z_x \sin\theta_1 - \cos\theta_1}{(1+Z_x^2+Z_y^2)^{\frac{1}{2}}} \qquad \ldots (7.81)$$

Substituting this result in equations (7.1) and (7.2) leads to extremely complicated expressions for the Fresnel Coefficients $R_{\parallel}$ and $R_{\perp}$. From this it can be seen that the mathematics is greatly simplified by the assumption that R is independent of θ.

7.10 Comparison with Other Theories

The form of the expression (7.56) for the specular component of the reflected radiation agrees (except for the

shadowing function) with the results of Davies (1954), Porteus (1963), and Beckmann and Spizzichino (1963). However equation (7.38), which gives the total energy reflected from a smooth surface illuminated by an infinite plane wave, has not been derived by any of these authors.

These authors all made approximations in deriving the expression for the diffuse component of the reflected radiation. In particular, Beckmann and Spizzichino obtained an expression identical to the first term of (7.76) - they obtained this result by integrating (7.29) by parts and neglecting all terms other than the first term of (7.76). The present treatment shows that this procedure was not justified in general.

7.11 Applications of the Solution

In applying the results of the foregoing theory there are several situations to consider. The case $g >> 1$, i.e. $\sigma^2 >> \lambda^2$ is most relevant to the results of the reflectivity measurements described in Chapter 6. The cases $g = 0$, $g << 1$, and $g \approx 1$ will only be briefly discussed.

7.11.1 Reflection from Smooth Surfaces

In this case $g = \sigma = 0$ and it has already been shown that under these conditions the diffuse component $I_S(D)$ vanishes while the specular component $I_S(S)$ peaks strongly in the direction of specular reflection ($\theta_3 = 0$, $\theta_1 = \theta_2$).

The case of a perfectly reflecting surface was discussed in Section 7.4. If the surface is not perfectly reflecting (i.e. $|R| < 1$) but we assume that R is constant over the entire surface then it can be shown, using (7.37), (7.39) and the results of Appendix 4.1, that

$$\varepsilon_S = 4\pi l m E_o^2 R^2 \qquad \ldots (7.82)$$

This result shows that measurements of radiation reflected from smooth surfaces can be used to obtain an estimate of the mean value of the reflection coefficient of the surface.

7.11.2 Reflection from Slightly Rough Surfaces

In this case $g << 1$, and equation (7.56) shows that the radiation is confined to a cone about the direction of specular reflection, while the diffuse component (given by (7.76)) makes a negligible contribution to the total reflected radiation.

7.11.3 Reflection from Moderately Rough Surfaces

In this case $g \approx 1$, and the infinite series in equation (7.76) converge slowly so that, in general, they cannot be computed easily. However for small values of θ_1 and θ_2 the specular and diffuse components can be written (using (7.56) and (7.76)) as

$$I_S(S) = (I_S)_o F(\theta_1, \theta_2, \rho''(0)) \, e^{-g} \qquad \ldots (7.82)$$

$$I_S(D) \simeq 4\pi l m \left(\frac{kE_o}{4\pi R_o}\right)^2 F(\theta_1, \theta_2, \rho''(0)) e^{-g}$$

$$\cdot \sigma^2 k^2 T^2 (cw + hf\cos\delta)^2 \sum_{n=0}^{\infty} \frac{g^n}{(n+1)!(n+1)} e^{-\frac{h^2 k^2 T^2}{4(n+1)}} \qquad \ldots (7.83)$$

where

$$(I_S)_o = \left(\frac{kE_o lm}{4\pi R_o}\right)^2 \omega^2 \left[\frac{\sin(kla)}{kla} \cdot \frac{\sin(kmb)}{kmb}\right]^2 \quad \ldots (7.84)$$

Substituting these expressions into (7.39) and using the procedure discussed in Appendix 4.1 it can be shown that if the detector is set at the specular angle ($\theta_D = \theta_1$) then the total energy reaching the detector is given by

$$\varepsilon_S = \varepsilon_S(S) + \varepsilon_S(D) \quad \ldots (7.85)$$

where

$$\varepsilon_S(S) \simeq 4lmE_o^2R^2F(\theta_1,\theta_1,\rho''(0))\, e^{-4k^2\sigma^2\cos^2\theta_1} \quad \ldots (7.86)$$

and

$$\varepsilon_S(D) \simeq 4lmE_o^2R^2F(\theta_1,\theta_1,\rho''(0))\, e^{-4k^2\sigma^2\cos^2\theta_1} \cdot \sum_{n=o}^{\infty} \frac{(4k^2\sigma^2\cos^2\theta_1)^{n+1}}{(n+1)!}\, \mathrm{erf}(BL\cos\theta_1)\, \mathrm{erf}(BM) \quad \ldots (7.87)$$

where

$$B^2 = \frac{k^2T^2}{4R_o^2(n+1)} \quad \ldots (7.88)$$

erf(x) is the error function

2L, 2M are the dimensions of the detector surface.

It is worth noting that if the dimensions of the detector are such that BL >> 1, BM >> 1, then

$$\varepsilon_S(D) \simeq 4lmE_o^2R^2F(\theta_1,\theta_1,\rho''(0))(1 - e^{-4k^2\sigma^2\cos^2\theta_1}) \quad \ldots (7.89)$$

and using (7.89) and (7.86) in (7.85) gives

$$\varepsilon_S = 4lmE_o^2R^2F(\theta_1,\theta_1,\rho''(0)) \quad \ldots (7.90)$$

which means that under these conditions ($g \approx 1$, BL >> 1,

BM >> 1) the reflectivity of the surface depends only on the reflection coefficient (R) and the shadowing function F (defined by (7.58) and (7.52).

7.11.4 Reflection from Very Rough Surfaces

In this case g >> 1, and (7.83) is difficult to evaluate because a large number of terms are needed to calculate the infinite series. However, we can go back to (7.42) and (7.33). Using the results of Appendix 4.2 and the transformations (7.59), (7.60) and (7.61), it can be shown that

$$I_S = 4\pi \mathrm{lm}\left(\frac{kE_o}{4\pi R_o}\right)^2 F(\theta_1,\theta_2,\rho''(0))$$

$$\cdot \int_o^\infty e^{-g(1-\rho)}\left[2\omega^2 J_o(hk\tau) - 4k\sigma^2 cwf J_1(hk\tau)\,\frac{d\rho}{d\tau}\cos\delta\right.$$

$$\left. - \sigma^2 f^2 (J_o(hk\tau) - J_2(hk\tau)\cos 2\delta)\left(\frac{d^2\rho}{d\tau^2} + g\left(\frac{d\rho}{d\tau}\right)^2\right)\right]\tau d\tau \quad \ldots (7.91)$$

It can be shown that for g >> 1 the integrand in (7.91) has significant values only for $\tau \simeq 0$.

If we approximate the auto-correlation function by

$$\rho(\tau) \simeq 1 - \frac{\tau^2}{T^2} \quad \ldots (7.92)$$

then it can be shown that

$$I_S = 4\pi \mathrm{lm}\left(\frac{E_o}{4\pi R_o}\right)^2 F(\theta_1,\theta_2,\rho''(0))$$

$$\cdot \left[\frac{T^2}{c^4\sigma^2}\left[(cw + hf\cos\delta)^2\, e^{-\frac{h^2T^2}{4c^2\sigma^2}}\right.\right.$$

$$\left.\left. - \tfrac{1}{4}h^2 f^2 \cos 2\delta\; S\left(\frac{h^2T^2}{4c^2\sigma^2}\right)\right] - \frac{f^2}{c^2} e^{-\frac{h^2T^2}{4c^2\sigma^2}}\right] \quad \ldots (7.93)$$

where S(x) is defined by (7.77).

The expression obtained by Beckmann and Spizzichino only contained the first term of (7.93). To examine the effect of the other terms a FORTRAN computer program was written to evaluate the reflectivity, using (7.93) and (7.39), together with the coordinate transformations of Appendix 4.1, and assuming that the total energy reaching the surface was $4\pi m E_o^2$.

A comparison of the results obtained by using only the first term of (7.93) with the results obtained by using all the terms of (7.93) showed that the second and third terms became significant when

(i) the value of R is small, e.g. < 0.5,

(ii) the difference $|\theta_2 - \theta_1|$ becomes large,

(iii) the ratio $\frac{T}{\sigma}$ approaches unity.

Table 7.1 shows the range of values of θ_2 for which (7.93) may be approximated by the first term only with an error of less than approximately 10 per cent.

T/σ	R	θ_1	Range
10	1.0	10°	$-45^\circ < \theta_2 < 55^\circ$
		40°	$-15^\circ < \theta_2 < 90^\circ$
		70°	$0^\circ < \theta_2 < 90^\circ$
10	0.5	10°	$-35^\circ < \theta_2 < 50^\circ$
		40°	$-15^\circ < \theta_2 < 75^\circ$
		70°	$35^\circ < \theta_2 < 90^\circ$
10	0.2	10°	$-30^\circ < \theta_2 < 35^\circ$
		40°	$0^\circ < \theta_2 < 60^\circ$
1	1.0	10°	$-15^\circ < \theta_2 < 30^\circ$

TABLE 7.1 The range of values of θ_2 for which (7.93) can be approximated by the first term only.

If the detector is set at the specular angle ($\theta_D = \theta_1$) then it can be shown, using the results of Appendix 4.1 that the reflected energy is given by

$$E_S = 4\pi m E_o^2 R^2 F(\theta_1, \theta_1, \rho''(0)) \cdot \mathrm{erf}\left(\frac{TL}{4\sigma R_o}\right) \mathrm{erf}\left(\frac{TM}{4\sigma R_o \cos\theta_1}\right) \quad \ldots (7.94)$$

There are two situations in which this result can be applied to the results discussed in Chapter 6.

(a) $\frac{T}{\sigma} \approx 1$ - in this case the dimensions of the detector system were such that

$$\left(\frac{TL}{4\pi R_o}\right)^2 << 1, \quad \left(\frac{TM}{4\sigma R_o \cos\theta_1}\right)^2 << 1$$

For $x^2 << 1$ the error function erf(x) may be approximated by (Abramowitz and Segun, 1968, p297)

$$\mathrm{erf}\ x \simeq \frac{2}{\sqrt{\pi}} \cdot x$$

so that, under these conditions (7.94) may be approximated by

$$\varepsilon_S \simeq 4\pi m E_o^2 R^2 F(\theta_1, \theta_1, \rho''(0)) \cdot \frac{T^2 LM}{4\pi\sigma^2 R_o^2 \cos\theta_1} \quad \ldots (7.95)$$

Since the shadowing function F is a slowly varying function of $\frac{T}{\sigma}$ we can see that

$$\varepsilon_S \propto \left(\frac{T}{\sigma}\right)^2 \quad \ldots (7.96)$$

Considering Table 6.4 shows that, for the first two lines of that table, the condition $\frac{T}{\sigma} \simeq 1$ is fulfilled.

Substituting the appropriate values in (7.96) we see that the theory predicts that the ratio of the energies reflected from the surface for these two values of $\frac{T}{\sigma}$ should be

$$\frac{\varepsilon_2}{\varepsilon_1} = \left(\frac{T_2}{T_1} \cdot \frac{\sigma_1}{\sigma_2}\right)^2 \approx 2 \ .$$

This predicted ratio agrees well with the results shown in Figure 6.14.

Equation (7.95) also predicts that $\varepsilon_S \propto \frac{1}{\cos\theta_1}$ for $\frac{T}{\sigma} \approx 1$. This prediction agrees to within 10 per cent with the results shown in Figure 6.5.

(b) $\frac{T}{\sigma} \approx 10$ - in this case equation (7.94) must be used directly. Since $\mathrm{erf}\left(\frac{TL}{4\sigma R_o}\right)$ varies slowly with $\frac{T}{\sigma}$, for the values of L and R_o relevant to the experimental results described in Chapter 6, we can see that the theory predicts that for $\frac{T}{\sigma} \approx 10$ the reflected energy ε_S should only vary slowly with $\frac{T}{\sigma}$. The results discussed in Section 6 tend to confirm this prediction.

7.12 Conclusions

The results of the previous sections suggest that the Kirchhoff approximation (equations (7.5), (7.6) and (7.7)) and the assumptions of Section 7.4 lead to results which agree qualitatively with experimental results for reflection from very rough surfaces at the specular angle. The theory also leads to results for smooth, perfectly reflecting surfaces

which agree with intuitive considerations. However, for very rough surfaces, the assumptions of Section 7.4 appear to be justified only over a limited range of angles and for surface materials with reflection coefficients ≈ 1.

APPENDIX 1 Some Atmospheric Processes Affecting Ozone

A.1.1 Dry Atmosphere

The most important reactions affecting the concentration of ozone in a dry atmosphere are listed below.

$$O_2 + h\nu \xrightarrow{\alpha_1} O(^3P) + O(^3P) \qquad 1750\text{Å} < \lambda < 2424\text{Å}$$

$$O_2 + h\nu \xrightarrow{\alpha_2} O(^1D) + O(^3P) \qquad \lambda < 1750\text{Å}$$

$$O_3 + h\nu \xrightarrow{\alpha_3} O_2 + O(^3P) \qquad 3100\text{Å} < \lambda < 11800\text{Å}$$

$$O_3 + h\nu \xrightarrow{\alpha_4} O_2 + O(^1D) \qquad \lambda < 3100\text{Å}$$

$$M + O(^3P) + O_2 \xrightarrow{k_1} M + O_3 \quad **$$

$$O(^3P) + O_3 \xrightarrow{k_2} O_2 + O_2$$

$$M + O(^3P) + O(^3P) \xrightarrow{k_3} M + O_2$$

$$O(^1D) + O_3 \xrightarrow{k_4} O_2 + O_2$$

$$O(^1D) + M \xrightarrow{k_5} O(^3P) + M$$

$$O(^1D) \xrightarrow{k_6} O(^3P) + h\nu$$

** M denotes any suitable molecule (in this case it would mostly be nitrogen) - this molecule is needed to conserve momentum.

The values of the rate coefficients have been measured by several workers - the values used in model atmosphere calculations by Hunt (1966,1971) are

$k_1 = 7.6 \times 10^{-35} \exp(\frac{890}{RT})$ - Benson and Axworthy (1965)

$k_2 = 5.6 \times 10^{-11} \exp(-\frac{5700}{RT})$ - Benson and Axworthy (1965)

$k_3 = 2.7 \times 10^{-33}$ - Reeves et al. (1960)

$k_4 = 10^{-11}$ - Fitzsimmons and Bair (1964)

$k_5 = 7 \times 10^{-11}$ - Zipf (1969)

$k_6 = 10^{-2}$ - Peterson et al. (1966)

The values of the absorption coefficients $\alpha_1, \alpha_2, \alpha_3, \alpha_4$ are discussed in Section 1.2.4.

A.1.2 Hydrogen-Oxygen Atmosphere

The reactions listed below have been tabulated by Nicolet (1964,1970), Norrish and Wayne (1965) and numerous other authors.

$$H + O_3 \xrightarrow{k_7} OH + O_2$$

$$OH + O(^3P) \xrightarrow{k_8} H + O_2$$

$$OH + O_3 \xrightarrow{k_9} HO_2 + O_2$$

$$OH + OH \xrightarrow{k_{10}} H_2O + O(^3P)$$

$$OH + HO_2 \xrightarrow{k_{11}} H_2O + O_2$$

$$H + HO_2 \xrightarrow{k_{12}} H_2 + O_2$$

$$H + HO_2 \xrightarrow{k_{13}} 2OH$$

$$O(^3P) + HO_2 \xrightarrow{k_{14}} OH + O_2$$

$$M + H + O_2 \xrightarrow{k_{15}} HO_2 + M$$

$$M + H + OH \xrightarrow{k_{16}} H_2O + M$$

$$M + H + H \xrightarrow{k_{17}} H_2 + M$$

$$HO_2 + HO_2 \xrightarrow{k_{18}} H_2O_2 + O_2$$

$$OH + H_2O_2 \xrightarrow{k_{19}} H_2O + HO_2$$

$$O(^3P) + H_2O_2 \xrightarrow{k_{20}} OH + HO_2$$

$$H + H_2O_2 \xrightarrow{k_{21}} H_2 + HO_2$$

$$O(^1D) + H_2 \xrightarrow{k_{22}} OH + H$$

$$O(^1D) + H_2O \xrightarrow{k_{23}} 2OH$$

$$M + O(^3P) + OH \xrightarrow{k_{24}} HO_2 + M$$

$$HO_2 + O_3 \xrightarrow{k_{25}} OH + 2O_2$$

$$O(^1D) + CH_4 \xrightarrow{k_{26}} CH_3 + OH$$

$$O(^3P) + H_2 \xrightarrow{k_{27}} H + OH$$

$$O(^3P) + CH_4 \xrightarrow{k_{28}} CH_3 + OH$$

$$H_2O + h\nu \xrightarrow{\alpha_5} H + OH \qquad \lambda < 2390\text{Å}$$

$$H_2O_2 + h\nu \xrightarrow{\alpha_6} 2OH \qquad \lambda < 5650\text{Å}$$

$$CH_4 + h\nu \xrightarrow{\alpha_7} CH_2 + H_2 \qquad \lambda < 2820\text{Å}$$

$$CH_4 + h\nu \xrightarrow{\alpha_8} CH + H + H_2 \qquad \lambda < 1360\text{Å}$$

The values of the rate coefficients used by Hunt (1966, 1971) are listed below

$k_7 = 2.6 \times 10^{-11}$ - Kaufman (1964)

$k_8 = 5 \times 10^{-11}$ - Kaufman (1964)

$k_9 = 5 \times 10^{-13}$ - Kaufman (1964)

$k_{10} = 2.8 \times 10^{-12}$ - Kaufman (1964)

$k_{11} = 10^{-11}$ - Kaufman (1964)

$k_{12} = 2 \times 10^{-13}$ - Clyne and Thrush (1963)

$k_{13} = 10^{-11}$ - Kaufman (1964)

$k_{14} = 10^{-11}$ - Kaufman (1964)

$k_{15} = 2.6 \times 10^{-33} \exp(\frac{1600}{RT})$ - Clyne and Thrush (1963)

$k_{16} = 2.5 \times 10^{-31}$ - Kaufman (1964)

$k_{17} = 2.6 \times 10^{-32}$ - Larkin and Thrush (1964)

$k_{18} = 3 \times 10^{-12}$ - Kaufman (1964)

$k_{19} = 4 \times 10^{-13}$ - Foner and Hudson (1962)

$k_{20} = 10^{-15}$ - Foner and Hudson (1962)

$k_{21} = 10^{-13}$ - Foner and Hudson (1962)

$k_{22} = 1.9 \times 10^{-10}$ - Young et al. (1968)

$k_{23} = 3 \times 10^{-11}$ - Biedenkapp et al. (1970)

$k_{24} = 1.4 \times 10^{-31}$ - Petersen and Krestschmer (1960)

$k_{25} = 10^{-14}$ (estimate only)

$k_{26} = 2.2 \times 10^{-10}$ - Young et al. (1968)

$k_{27} = 2.1 \times 10^{-11} \exp(\frac{9400}{RT})$ - Schofield (1967)

$k_{28} \quad 5.3 \times 10^{-11} \exp(-\frac{7950}{RT})$ - Schofield (1967)

Values of rate coefficients for the photo-dissociation processes are tabulated by Hunt (1971).

A.1.3 Reactions Involving Nitrogen and Nitrogen Compounds

$$NO + O_3 \longrightarrow NO_2 + O_2$$

$$NO_2 + O \longrightarrow NO + O_2$$

$$N + NO \longrightarrow N_2 + O$$

$$N + O_3 \longrightarrow NO + O_2$$

$$N + O_2 \longrightarrow NO + O$$

These reactions and a large number of reactions involving compounds such as NO, HNO_2, HNO_3, NO_2, NO_3, N_2O_5, N_2, N etc. have been tabulated by Crutzen (1971).

APPENDIX 2 Electronic Circuits for Night Round Photometers

A.2.1 Circuits for HAD 313

A.2.1.1 High Tension and Dynode Modulator Supplies

The circuit for this unit is shown in Figure A.2.1. The purpose of the circuit was to provide the negative high tension for the photomultipliers and also to provide a square wave of 100 volts, peak to peak, which, when applied to the selected dynode of the photomultiplier would modulate the photomultiplier current in order to take advantage of the low-drift characteristic of an A.C. amplifier system.

The basis of the circuit was a two-transistor, one-transformer converter in which, during one complete cycle, the flux density in the transformer core varies between the saturation value in one direction and the saturation value in the opposite direction. The operation of this type of circuit is described in detail in the RCA Silicon Power Circuits Manual (1967).

The voltage for the Dynode Modulator was taken straight from the output of the 560 turn secondary coil. The output of the other secondary coil was fed into a voltage doubling circuit to obtain the high tension voltage for the photomultiplier dynode chains. The running frequency of the converter was 1500 Hz; the current drain through each diode in the reverse-biassed state was of the order of 10^{-4} amps, so that the ripple voltage was negligible.

A.2.1.2 Dynode Chain Circuits

The dynode chain used in HAD 313, together with the

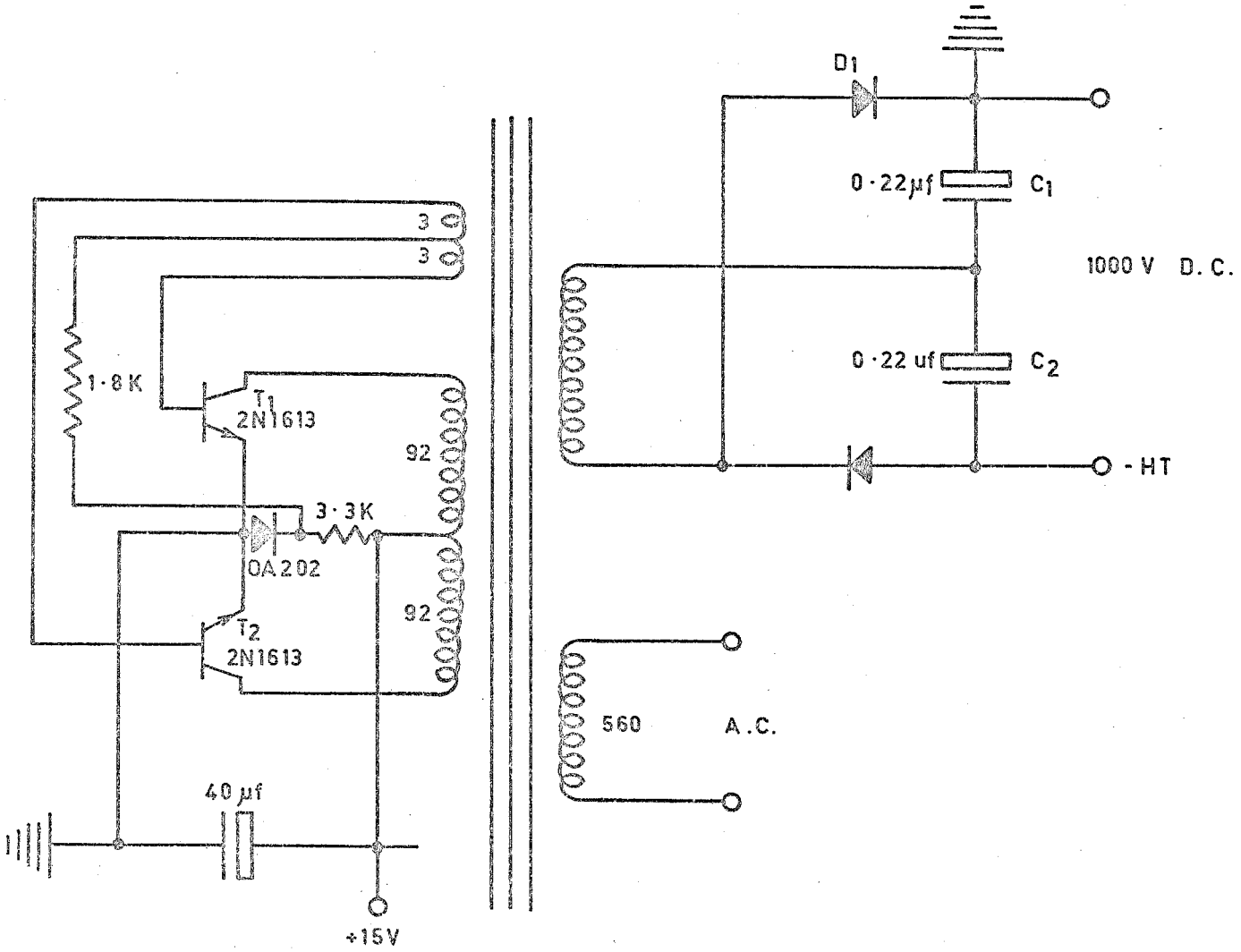

Figure A.2.1 Photomultiplier high tension supply and square wave supply for dynode modulator used in HAD313.

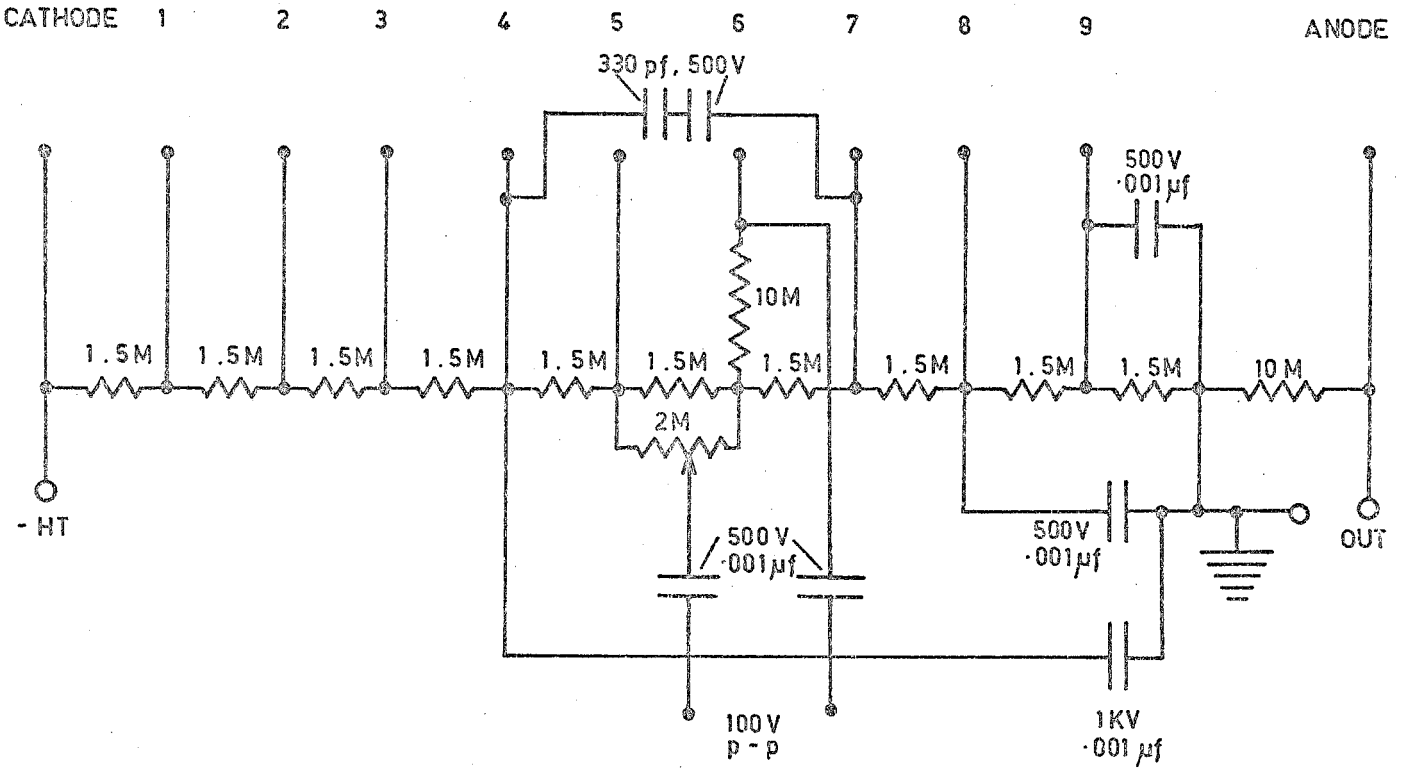

Figure A.2.2 Dynode chain used in HAD313 with facility for dynode modulation.

dynode modulation circuitry, is shown in Figure A.2.2. The most effective dynode for this modulation was found by Horton (1968) to be dynode number 6.

A.2.1.3 A.C. Amplifiers

The circuit for the amplifiers used on HAD 313 is shown in Figure A.2.3. The A.C. input signal is applied to the base of transistor T1 which is biassed by resistors R1a and R1b but which maintains a high input impedance through resistor R2. The output of T1 is cascaded through T2 onto an emitter load of resistor R3. The full signal is applied to a rectifying network C1, R4 and D1 and gives the output of stage 1. The signal at the emitter of T2 is A.C. coupled to the base of T3 and the gain of this stage is set by the magnitude of the A.C. coupled feedback resistor R5. The output in this case appears on the collector load and is similarly treated to the output of stage 1, supplying the output of stage 2 and the input to stage 3. Stage 3 is similar to stage 2.

The initial gain of stage 1, which may need to be altered depending on the sensitivity of the photometer, can be set by changing the input impedance through R6. Also in the input circuit is the temperature compensation net of M53 and R7.

Since the telemetry could only handle signals of less than 1.5 volts (any signal greater than this gave a false synchronous signal) all outputs were limited to 1.5 volts by the diodes

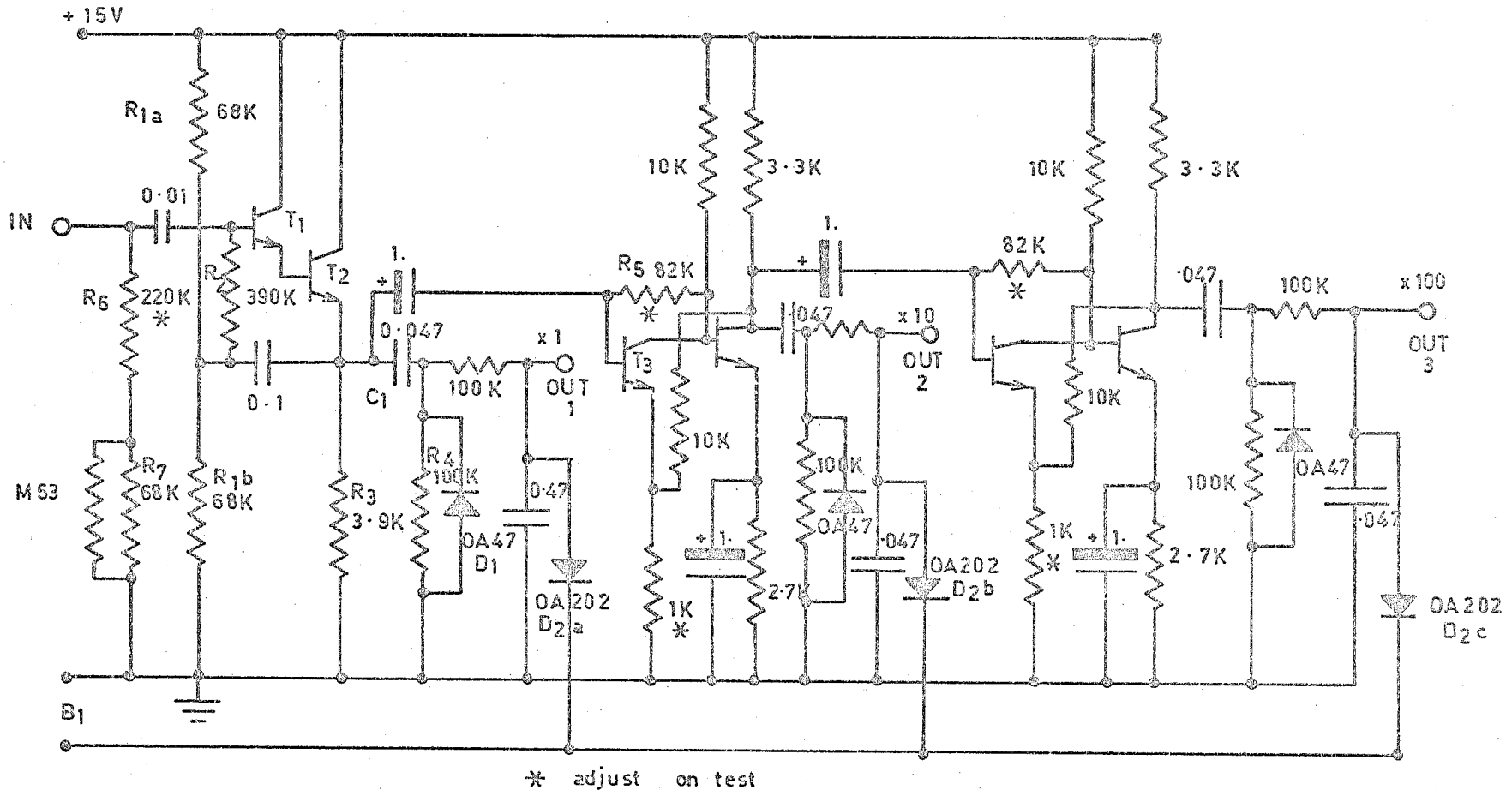

Figure A.2.3 Three stage amplifier. Transistors - 2N3694, Resistor - Ohms capacitance - μ farads.

D_{2a}, D_{2b} and D_{2c} and the battery B_1. Owing to the forward conducting characteristic of the diodes the signal applied to the telemetry could rise above 1.5 volts but not far enough to stimulate a sync signal.

A.2.2 Circuits for C104, C105 and C1014

A.2.2.1 High Tension Supply

The rapid advances in electronics technology and design concepts over the last few years resulted in the design of the high tension power supply unit being constantly modified as better components became available. The most recent development was the circuit flown in C1014, which is shown in Figure A.2.4.

The basic circuit is similar to that described in Appendix A.2.1, consisting of a one-transformer, two-transistor D.C. to D.C. converter. The additional circuitry, comprising the μA723C voltage regulator, etc., was added to improve the regulation of the supply. The earlier circuits were found to have appreciable amounts of ripple under load and this noise voltage was found to affect the performance of the photometer amplifiers. The situation was greatly improved by adding the extra circuitry shown in Figure A.2.4.

A.2.2.2 Dynode Chains

The dynode chains consisted of a string of 680KΩ resistors connected in such a way that the anode was close to

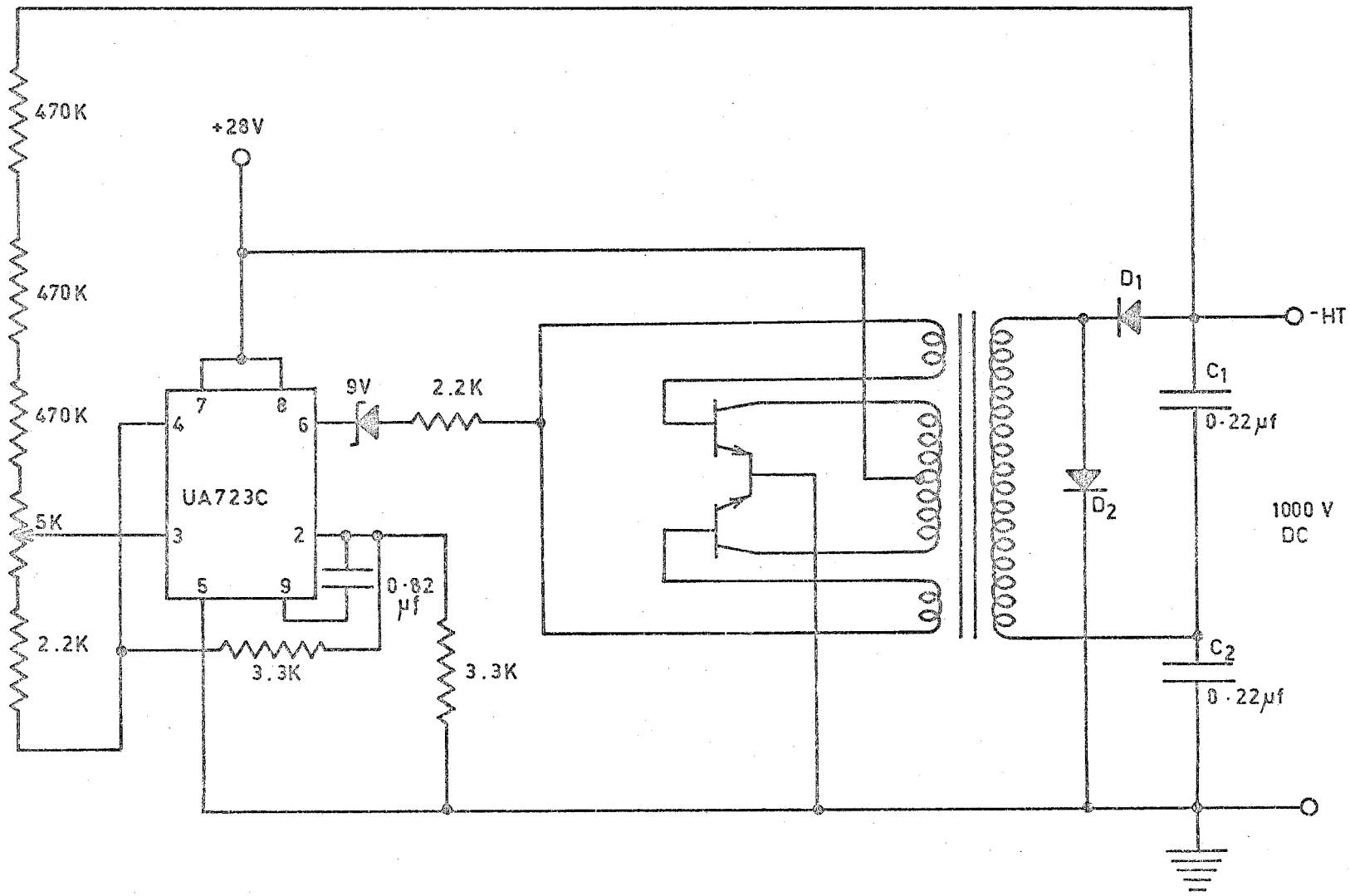

Figure A.2.4 Photomultiplier high tension power supply for C1014.

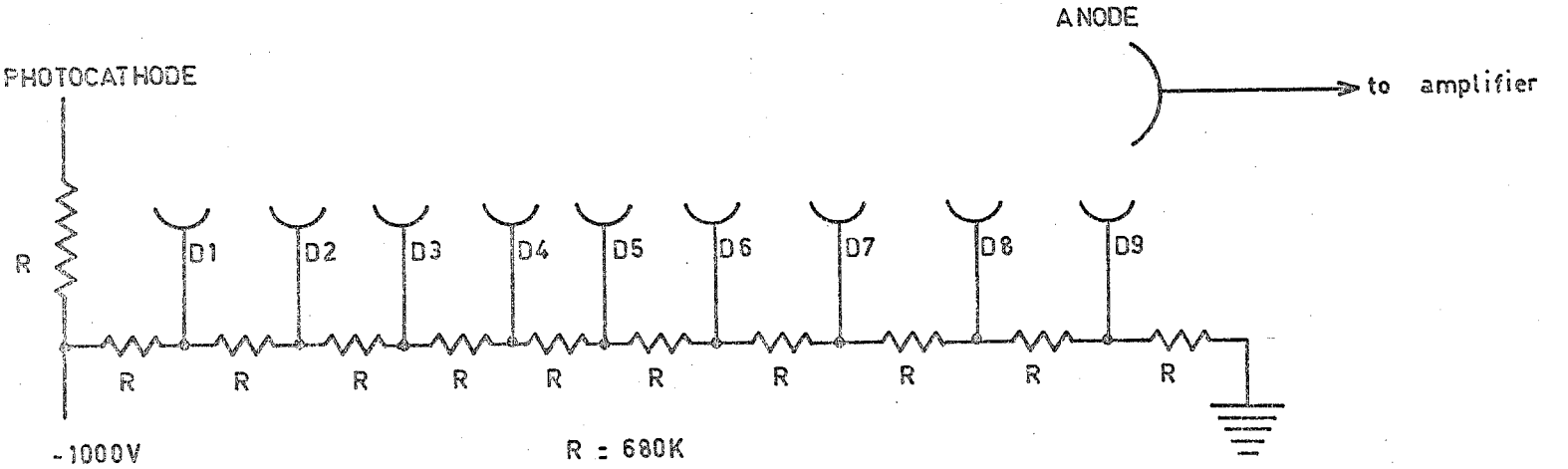

Figure A.2.5 Dynode chains used in C104, C105, C1014.

ground and the negative high tension was applied to the cathode end of the chain. This is shown in Figure A.2.5.

A.2.2.3 Amplifiers

The advent of stable D.C. operational amplifiers in the last few years meant that the A.C. amplifiers used in HAD 313 were redundant. The circuit shown in Figure A.2.3 was replaced by the much simpler one shown in Figure A.2.6.

For C1014 there was a special system flown to look at Lyman-α; the telemetry requirements for this experiment meant that there was only 1 telemetry channel available for each photometer, but the use of a new type of telemetry system with a maximum signal capability of -5 volts enabled a logarithmic amplifier covering 1 volt per decade of signal current to be used. The logarithmic amplifier circuit is shown in Figure A.2.7. To ensure that temperature effects were minimal the logarithmic element was kept at a steady temperature of 60° by means of an electronic heater.

The operation of the log amplifier is as follows. The voltage at the emitter of the transistor in the feedback loop of the P501 is proportional to the logarithm of the input current. The 5K potentiometer in the feedback loop of the µA741 is used to set the output so that a change of 1 volt occurs at the output when the input current changes by a factor of 10. The combination of the 2K potentiometer and the second transistor is a temperature compensation network to minimize

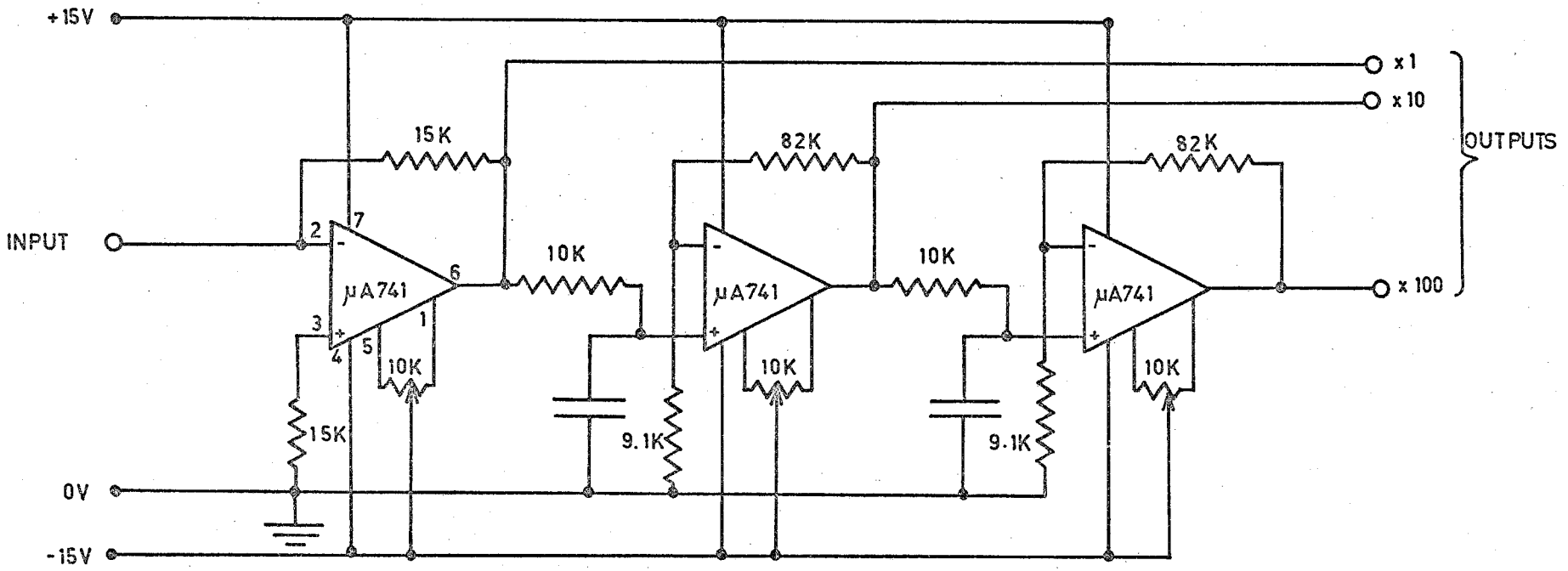

Figure A.2.6 Linear amplifier for C104 and C105.

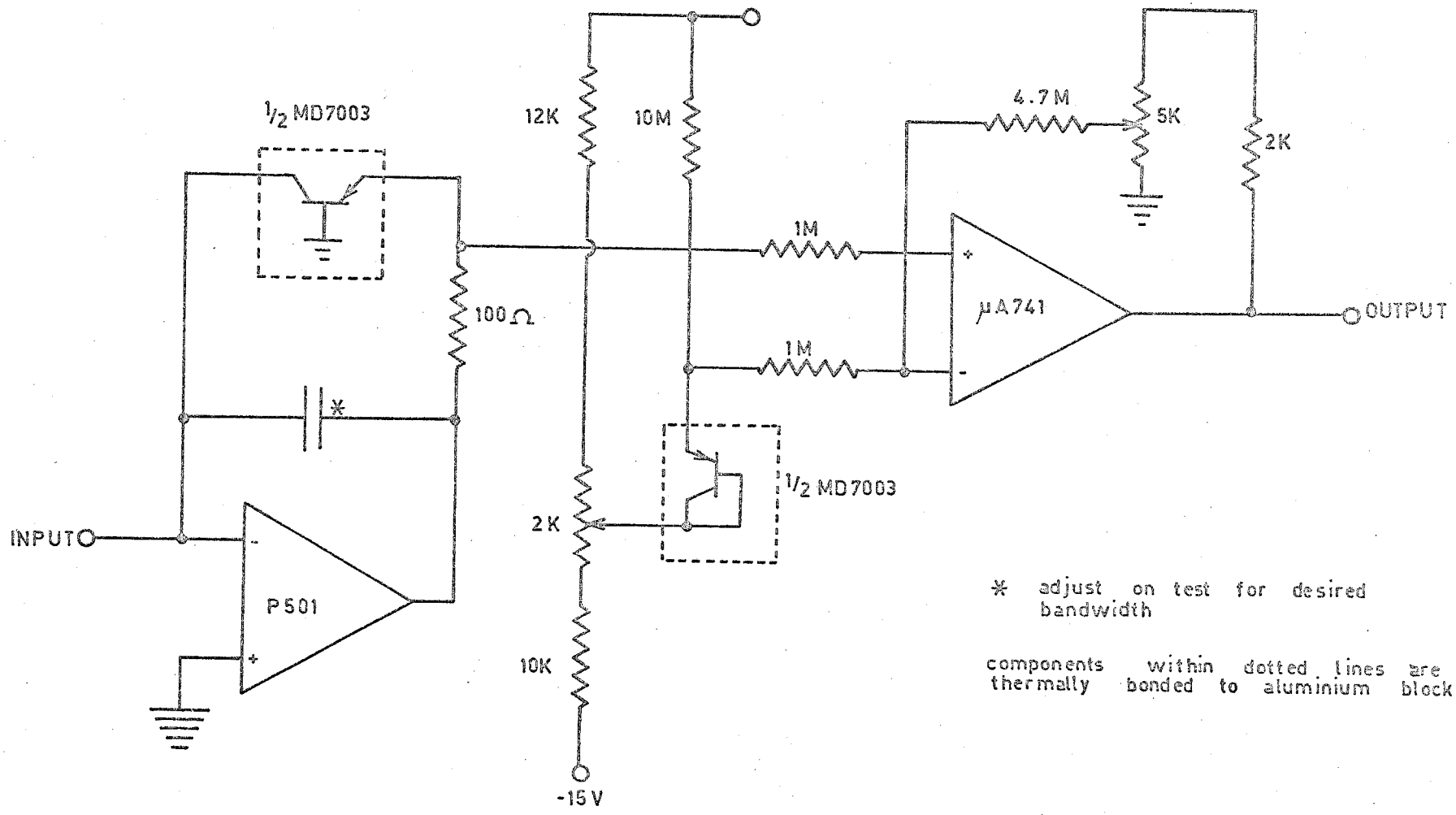

Figure A . 2 . 7 Logarithmic amplifier for C1014.

the effects of drift in the base-emitter voltage of the logarithmic element.

A.2.2.4 Aspect Sensor Amplifiers

For HAD 313 the aspect amplifier consisted of the first two stages of the photometer amplifier shown in Figure A.2.3.

For C104, C105 and C1014 it was decided that, as the important feature of the output of the aspect sensor was the time separation between the peaks and not the magnitude of the signal, a single stage amplifier could be used with a gain changing network which would reduce the gain of the amplifier for large input signals. This circuit is shown in Figure A.2.8; its operation is as follows. The first stage consists of a current-voltage converter (c.f. Figure A.2.6), which gave an output of 3.3 volts for an input current of 10 microamps. The output was fed into the gain changing network. Until the voltage reached the turnover point selected by R1 and R2 the OA202 diode is reverse-biassed so the output voltage equals the voltage at A. As soon as the voltage at A is such that the output of the second amplifier goes negative the OA202 starts to conduct and the output voltage is then determined by the network R3 and R4.

This system had the additional advantage that it required only one telemetry channel instead of the two needed for the aspect sensors on HAD 313.

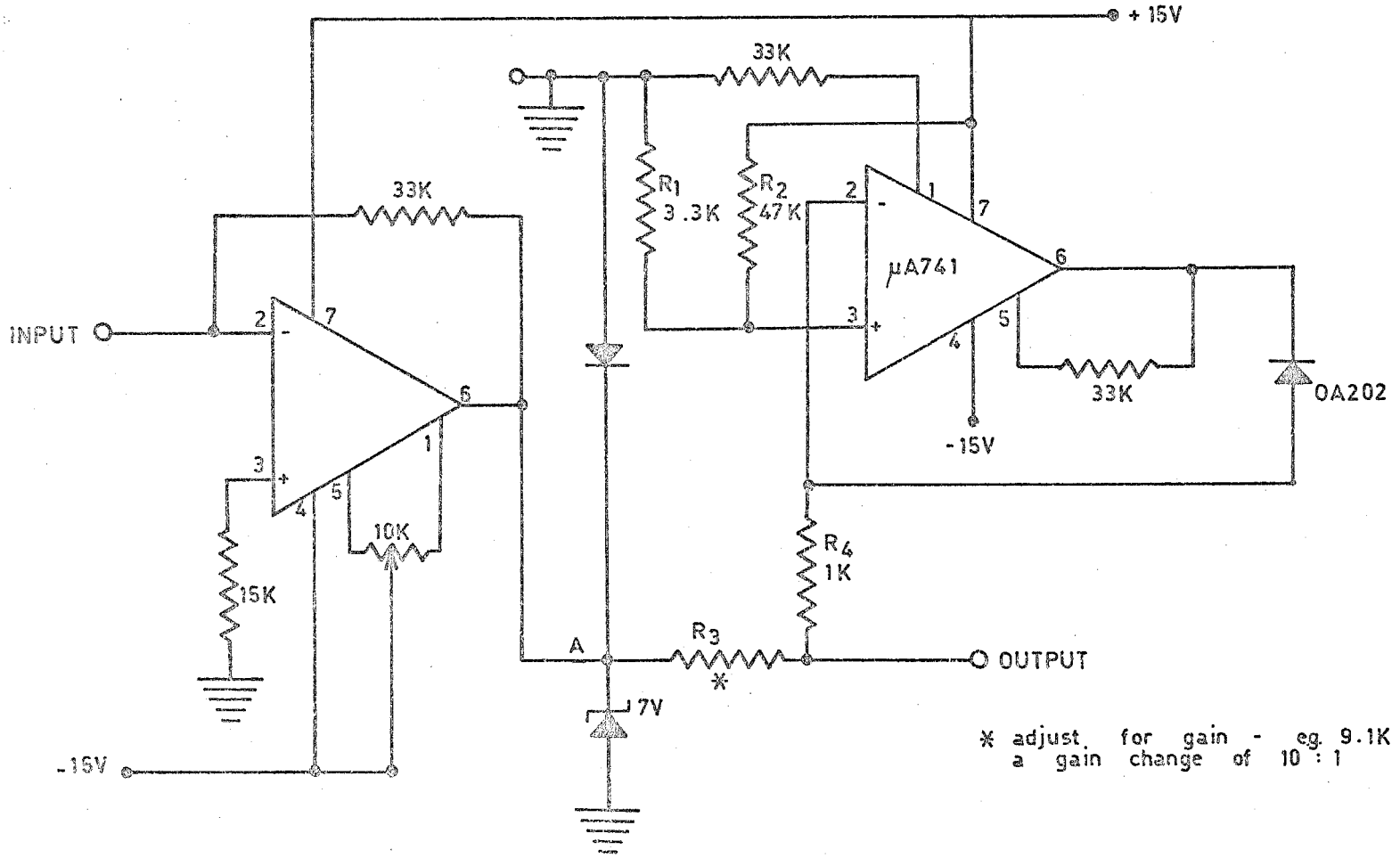

Figure A . 2 . 8 Aspect sensor amplifier for C104, C105 and C1014, with gain - changing network.

APPENDIX 3 The Logarithmic Dividing Unit

A.3.1 The Power Supplies

The wiring arrangements for the mains input and unregulated ±15 volt output are shown in Figure A3.1. Switch SA is the on-off switch for the mains voltage, while switch SB enables the entire unit to be floated with respect to mains earth, thus minimizing the chances of earth loops occurring.

The circuit diagrams for the 15 volt positive and negative regulators are shown in Figure A3.2. The output voltage for the positive regulator is adjusted by means of the 2.4K potentiometer. The output voltage for the negative regulator is adjusted by means of the 5K potentiometer.

A.3.2 The Integrator and Inverter Circuits

The integrator and inverter circuits are shown in Figure A3.3. For the integrator circuit the offset is adjusted as follows:- switch S2 is closed and the input open circuited - then, by adjusting the 1K potentiometer R5 the output offset can be reduced to zero. The switch S1 acts as a range-setter. On the highest range 9/10 of the input current is shunted through R2. On all other ranges the circuit functions as a normal integrator.

The dark current source is adjusted so that over several integrating cycles the mean signal due to the photomultiplier dark current averages out to zero.

The inverting stage is a simple unity-gain inverting

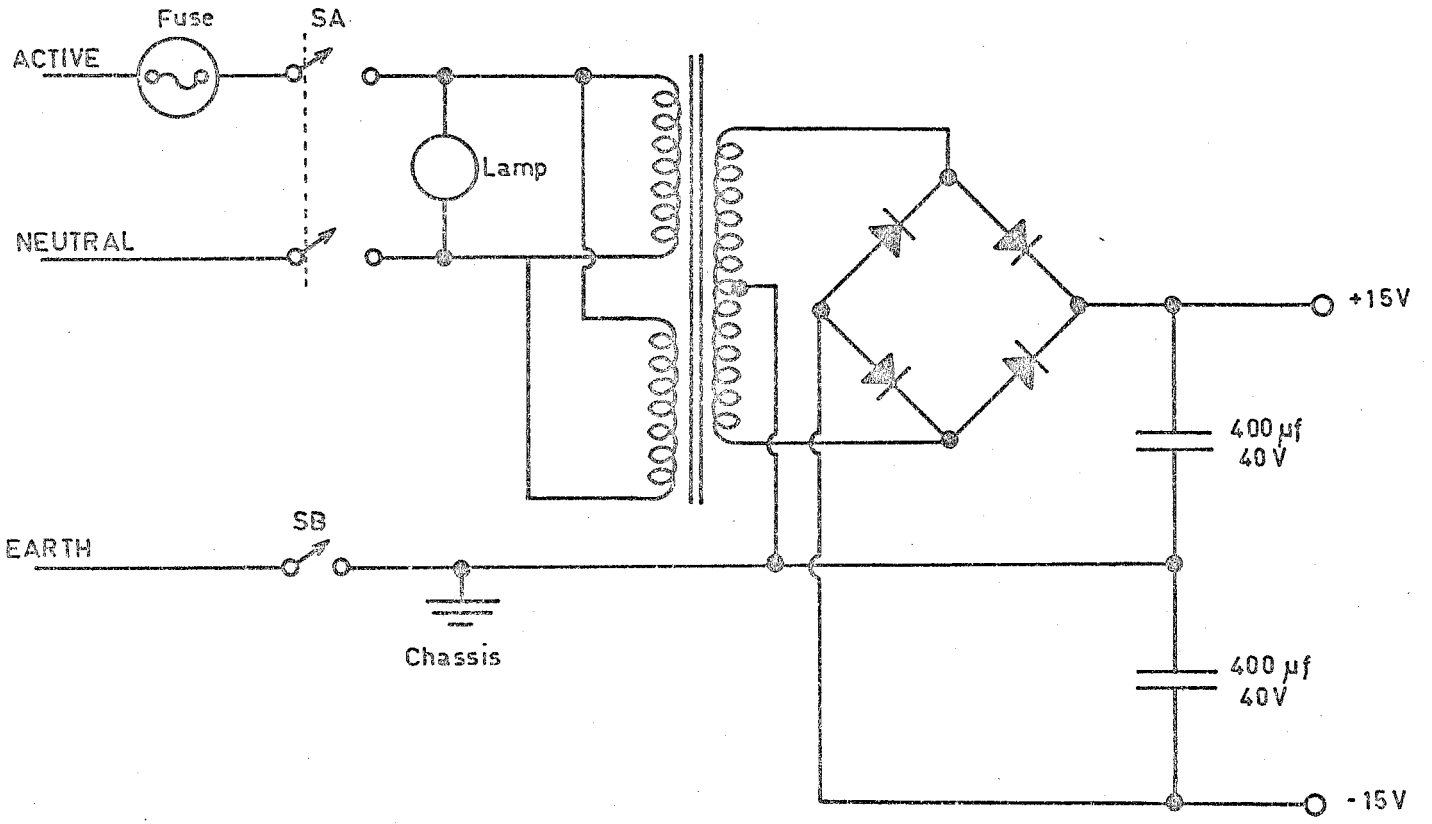

Figure A.3.1 Wiring arrangements for the mains input and unregulated ± 15 volt outputs.

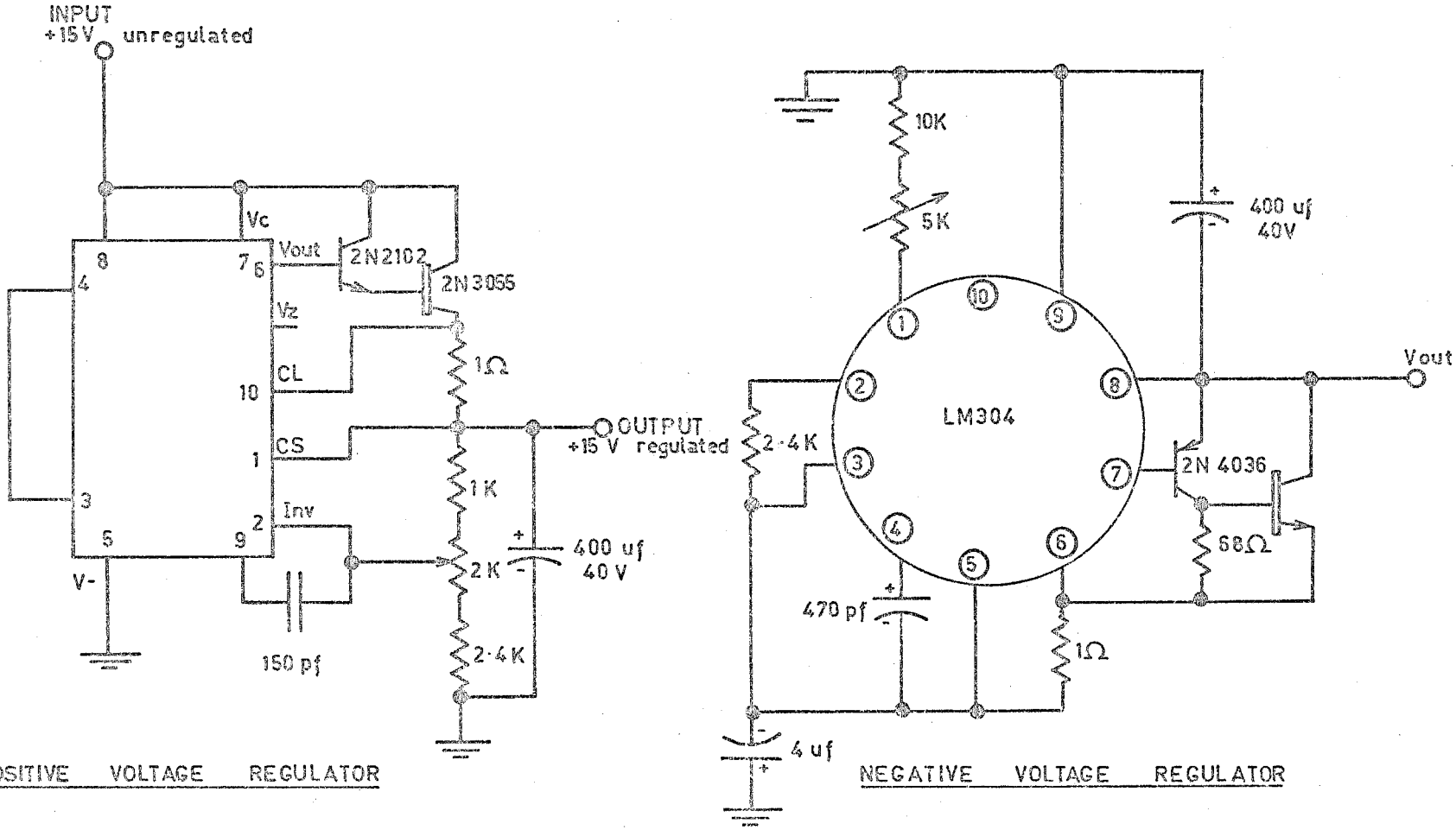

Figure A. 3 . 2 Circuit diagrams for the ± 15 volt regulators.

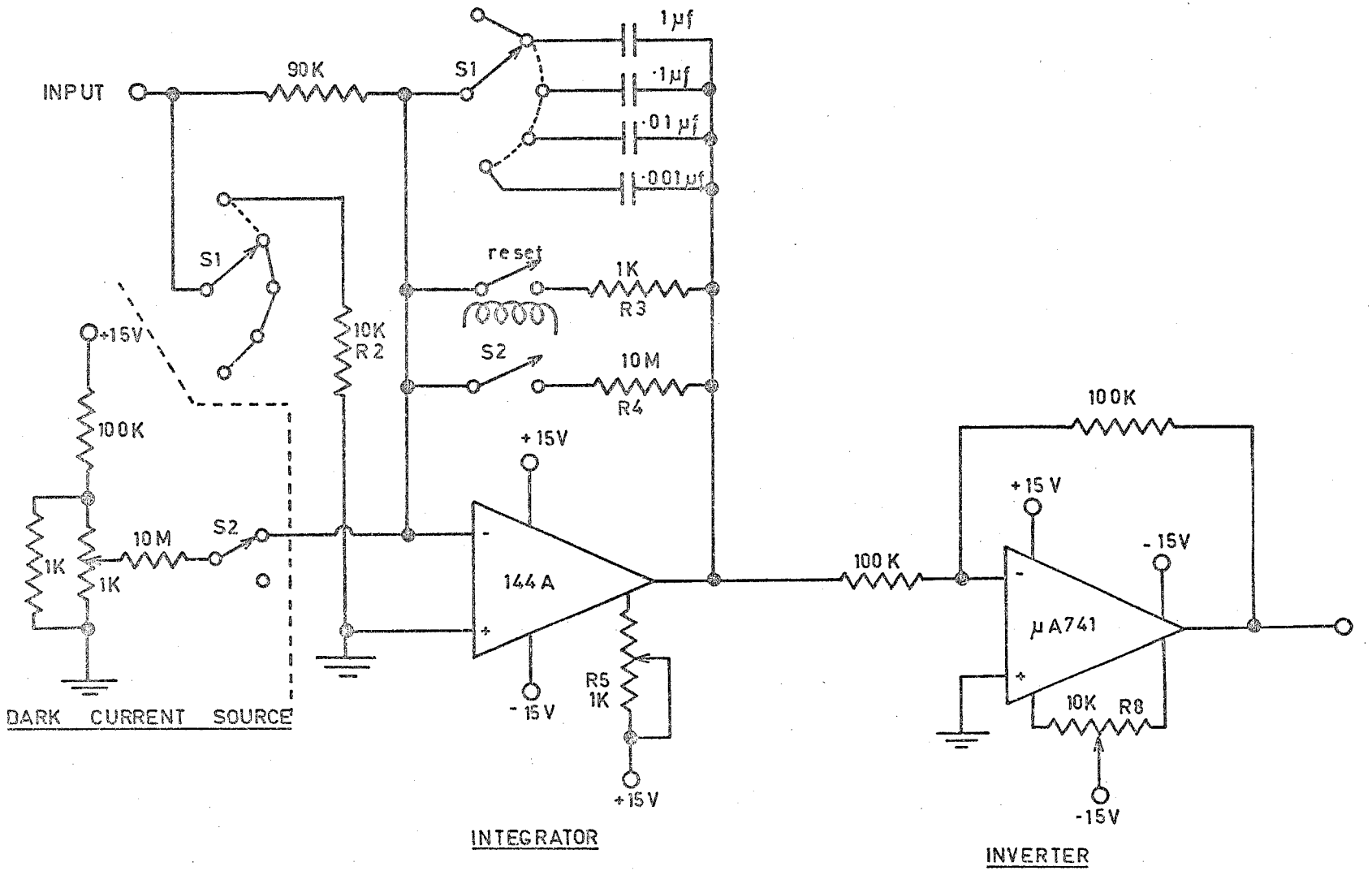

Figure A.3.3 Circuit diagram for the integrator and inverter circuits.

amplifier. The offset of the inverter is adjusted by adjusting the offset of the integrator as described above and then setting the output offset of the inverter to zero by means of the 10K potentiometer, R8.

A.3.3 The Logarithmic Amplifiers

The circuit for the logarithmic amplifiers is shown in Figure A3.4a. The offset of the logarithmic amplifier is adjusted by closing switch S5 and adjusting the output offset voltage to zero by means of the potentiometer R22. There are two of these amplifiers in the unit, one for the detector channel and one for the monitor channel. The transistor Q1 and its counterpart in the other log amplifier are mounted on the same semi-conductor chip to ensure that their temperature characteristics are as closely matched as possible.

A.3.4 The Subtractor

The subtractor circuit is shown in Figure A3.4b. The inputs are obtained from the outputs of the log amplifiers discussed in the previous section. The two resistors R_G and R_{TC} are mounted on the same substrate as the two transistors in the feedback loops of the log amplifiers - these four components comprise an Analogue Devices 751N Logarithmic Module. Resistor R_G is chosen so that the subtractor output changes by one volt when either input changes by a factor of 10, while R_{TC} is a temperature-dependent resistor chosen so that its temperature

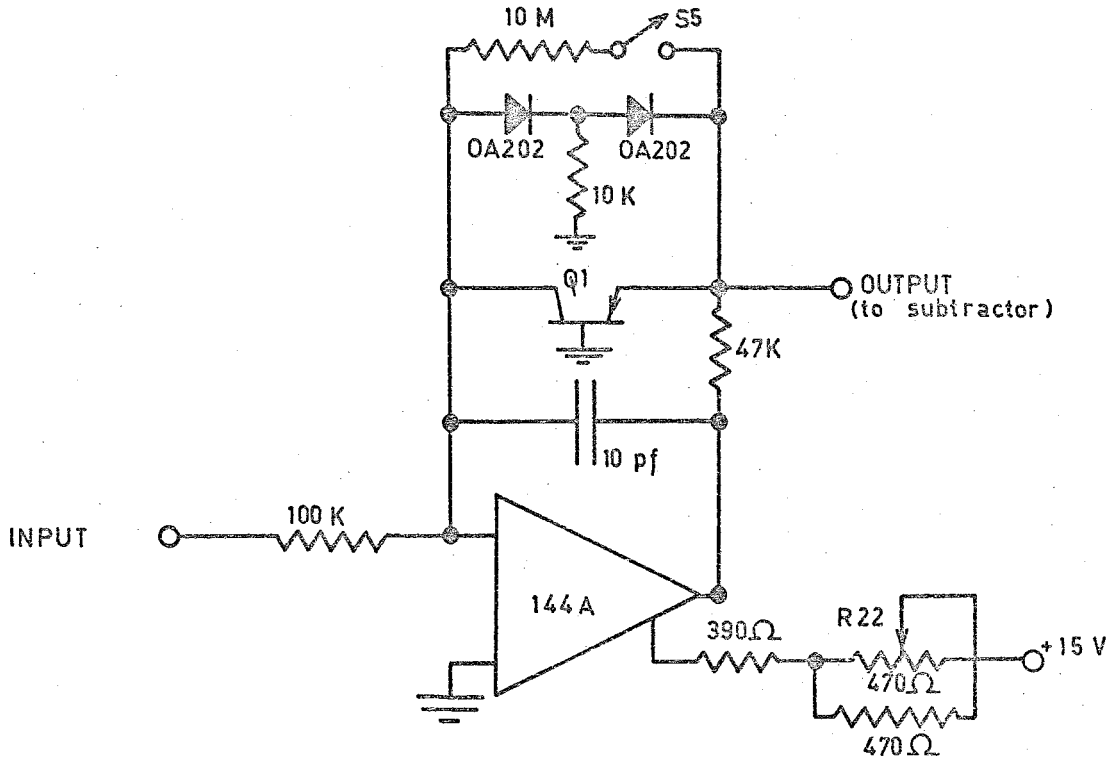

Figure A. 3 . 4 a Logarithmic amplifier circuit .

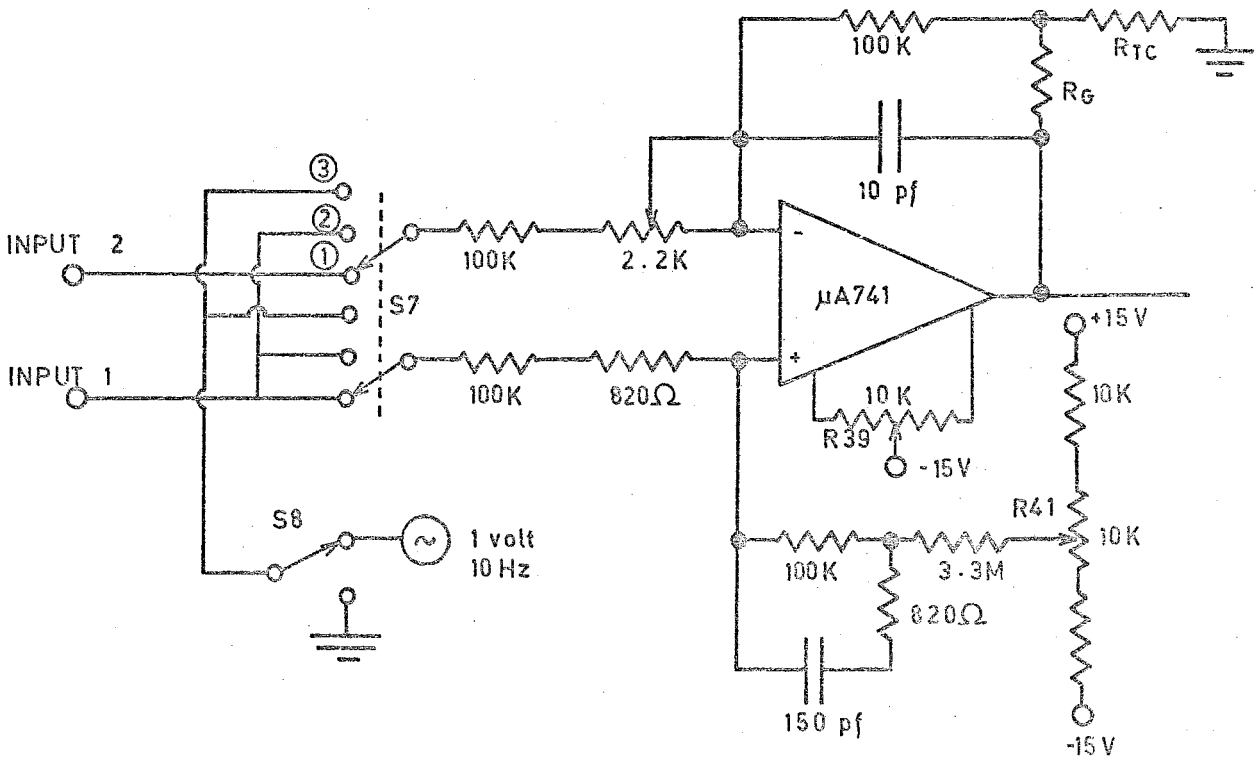

Figure A. 3 . 4 b Subtractor circuit .

coefficient is such as to cancel any difference in the temperature characteristics of the transistors in the two log amplifiers.

The subtractor is adjusted as follows:-

1) put switch S7 to position (3) and short both inputs to ground via switch S8; then adjust the output offset voltage to zero by means of R39.
2) put switch S7 to position (2) and put a time-varying signal into channel 1 (any current of suitable polarity and magnitude will suffice). Then adjust the potentiometer R41 until the drift in the subtractor output voltage is zero.
3) then adjust the potentiometer R32 until the output voltage from the subtractor is zero.

A.3.5 The Sample and Hold Circuit

The sample and hold circuit is shown in Figure A3.5. Switch S10 is activated by a relay - when S10 is closed the output voltage is equal to the input voltage (inverted) so that the circuit acts as a unity gain inverting amplifier. When S10 is open the arrangement of switches S9 and S10 ensures that current leakage across S10 is kept to a minimum - when S10 is open the output voltage remains steady at the value of the input voltage when S10 was last closed.

To adjust the offset switch S9 is switched to position 2 and the output offset of the sample and hold circuit is set to zero by means of potentiometer R45.

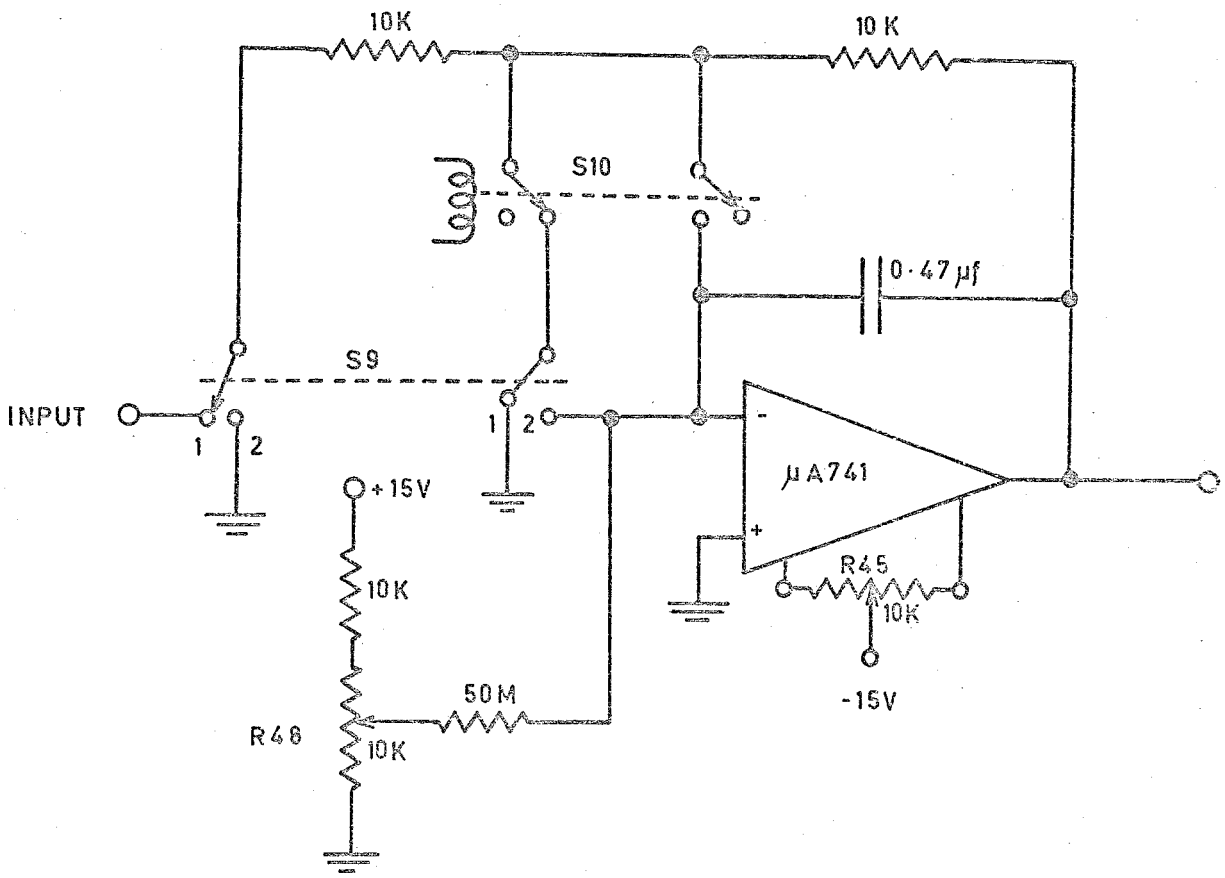

Figure A. 3 . 5 The sample and hold circuit.

To compensate for any drift in the output of the sample and hold switch S9 is put to position 1, a steady signal applied to the input and potentiometer R48 is adjusted until the output voltage remains steady.

A.3.6 The Control Pulse Circuitry

The circuits used to produce the sequence of pulses for controlling the sample and hold relay are shown in Figures A3.6 and A3.7. The design of these circuits was based on a series of multivibrator circuit designs by Malmstadt and Enke (1969).

The manual start circuit was added to enable the integrating cycle to be started externally by overriding the effect of the unijunction controlled astable multivibrator.

The relay drive circuits and the output circuits used for triggering the printer or digital voltmeter were designed so as not to overload any of the multivibrator outputs.

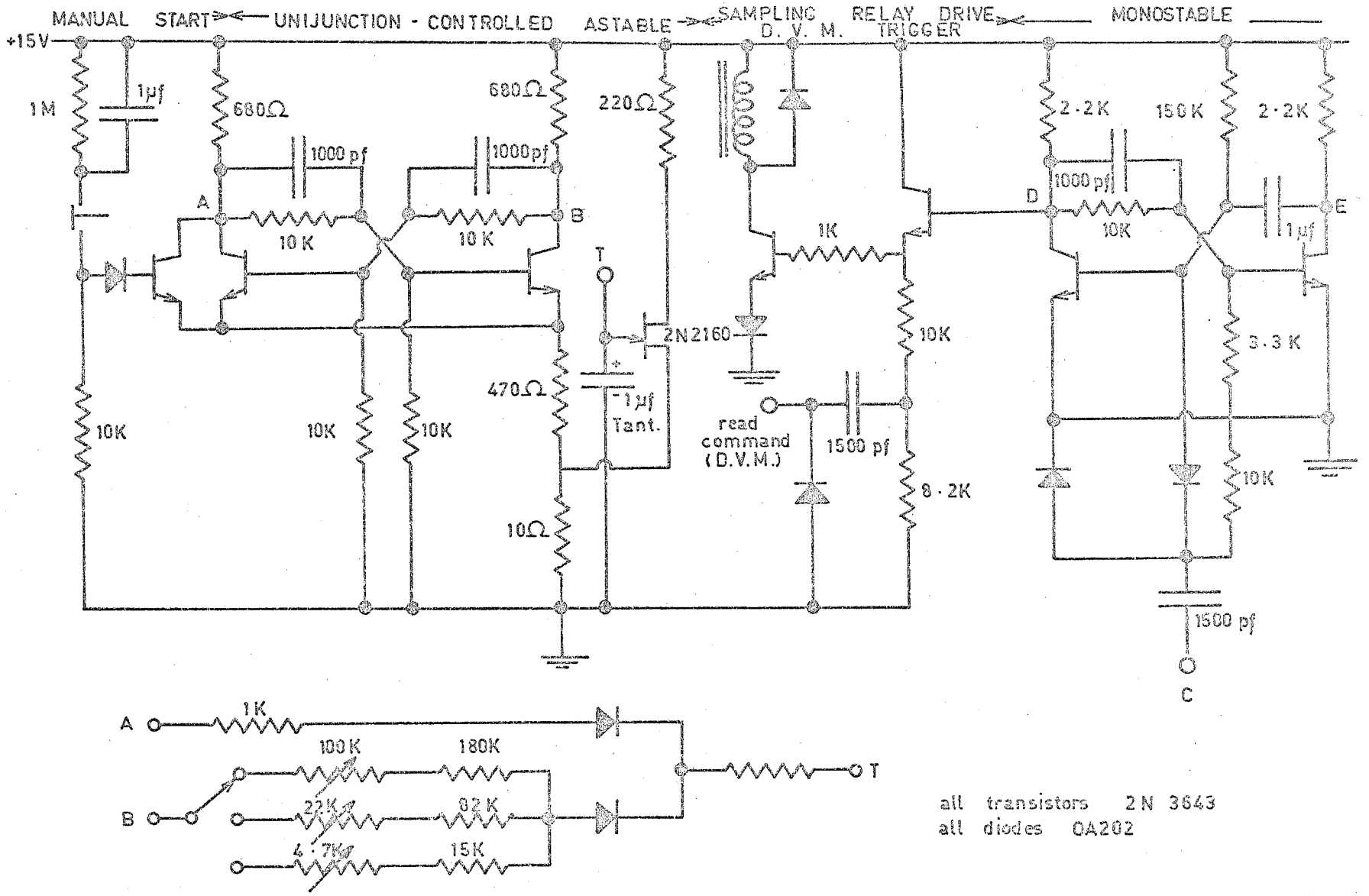

all transistors 2N 3643
all diodes OA202

Figure A.3.6 The first two stages of the control pulse circuitry. The letters A, B, C, D, E correspond to those in Figs. 7.5 and 7.6.

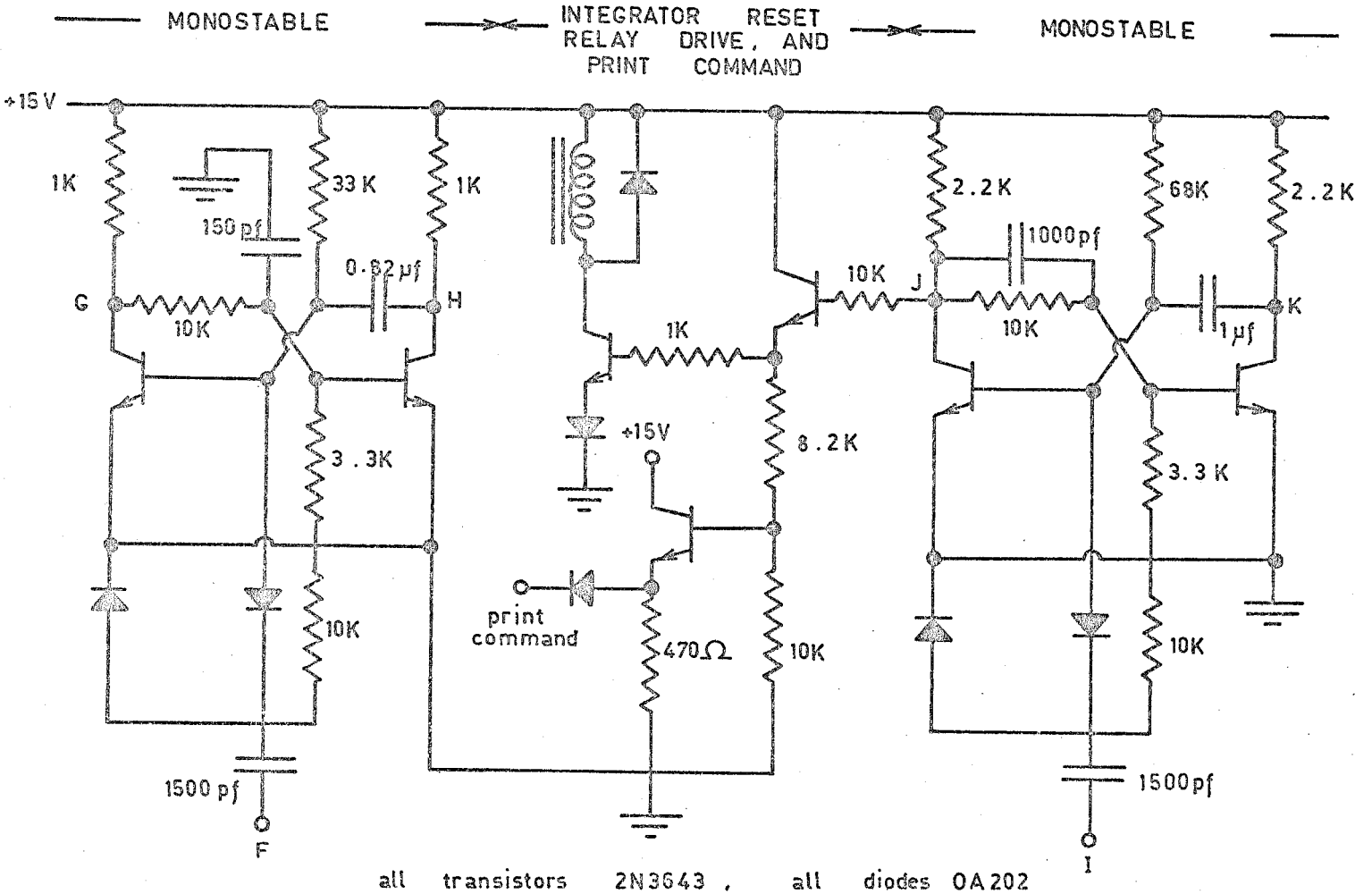

Figure A.3.7 The last two stages of the control pulse circuitry. The letters F, G, H, I, J, K correspond to those in Figs. 7.5 and 7.6.

APPENDIX 4 SOME USEFUL MATHEMATICAL RESULTS

A.4.1 Calculation of the Energy Reflected from a Smooth, Perfectly Reflecting Surface

The problem is to evaluate the right hand side of equation (7.35), viz.

$$(\varepsilon_s)_o = \left(\frac{kE_o lm}{\pi R_o}\right)^2 R_o^2 \int_\Omega \int w^2 \left[\frac{\sin(kla)}{kla} \cdot \frac{\sin(kmb)}{kmb}\right]^2 \sin\theta_2 d\theta_2 d\theta_3 \quad \ldots (A4.1)$$

This expression gives the total energy reaching the detector after reflection from a smooth surface. The notation is the same as that used in Chapter 7.

The integration can be carried out by transforming to a coordinate system which is defined with respect to the detector. Such a system of coordinates is shown in Figure A4.1 - the system X-Y has its origin at P, the central point of the detector surface. Since the experimental apparatus described in Chapter 5 did not allow the detector axis to be moved out of the plane of incidence we can restrict the discussion to the case where the direction of the detector axis is defined by the angular coordinates $(\theta_D, 0)$.

If the coordinates of P are denoted by $(R_o, \theta_D, 0)$ with respect to the reflecting surface, while the coordinates of Q (an arbitrary point on the detector surface) are denoted by (r, θ_2, θ_3) with respect to the reflecting surface and (X,Y) with

respect to the detector surface, then it can be seen from Figure A4.1 that

$$X\cos\theta_D = r\sin\theta_2 \cos\theta_3 - R_o\sin\theta_D \quad \ldots (A4.2)$$

$$Y = r\sin\theta_2 \sin\theta_3 \quad \ldots (A4.3)$$

and it can be shown in this case that

$$dA = R_o^2\sin\theta d\theta d\phi = \frac{R_o^2}{r^2} \cdot \frac{\cos\theta_D}{\cos\theta_2} \cdot dXdY \quad \ldots (A4.4)$$

where dA is a small element of area on the surface of the detector.

The quantities a and b in equation (A4.1) can now be written as

$$a = \frac{X}{r}\cos\theta_D + \frac{R_o}{r}\sin\theta_D - \sin\theta_1 \quad \ldots (A4.5)$$

$$b = \frac{Y}{r} \quad \ldots (A4.6)$$

Making these substitutions in (A4.1) leads to the result

$$(\varepsilon_s)_o = \left(\frac{kE_o lm}{\pi R_o}\right)^2 \cos\theta_D \int_{-L}^{L}\int_{-M}^{M} \frac{w^2}{\cos\theta_2} \cdot \left[\frac{\sin(\frac{kmY}{r})}{\frac{kmY}{r}}\right]^2 \cdot \left[\frac{\sin[kl(\frac{X}{r}\cos\theta_D + \frac{R_o}{r}\sin\theta_D - \sin\theta_1)]}{kl(\frac{X}{r}\cos\theta_D + \frac{R_o}{r}\sin\theta_D - \sin\theta_1)}\right]^2 \frac{R_o^2}{r^2} \cdot dXdY \quad \ldots (A4.7)$$

where

$$w = (1+R)\cos\theta_1 - (1-R)\cos\theta_2 \quad \ldots (A4.8)$$

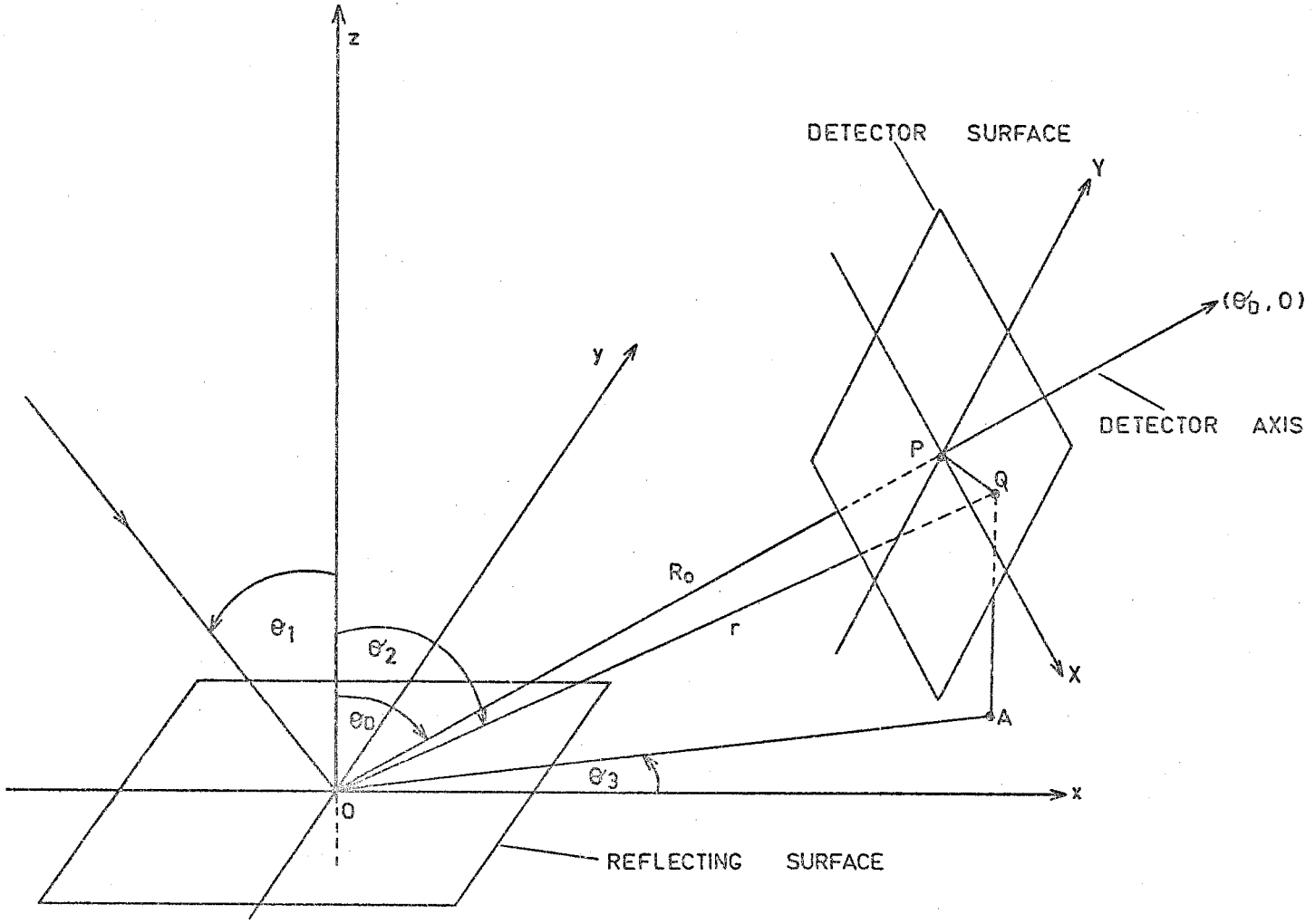

Figure A 4 . 1 The relation between the reflecting surface and the sensitive surface of the detector. A is the projection of Q on to the x - y plane.

$$\cos\theta_2 = \left(1 - \frac{(X\cos\theta_D + R_o\sin\theta_D)^2}{r^2} - \frac{Y^2}{r^2}\right)^{\frac{1}{2}} \qquad \ldots (A4.9)$$

R is the reflection coefficient of the surface, as described in Section 7.4, and 2L,2M are the dimensions of the detector surface.

The dimensions of the system described in Chapters 5 and 6 were

$k1 \simeq 10^5$
$km \simeq 10^4$
$R_o \simeq 5$ cms
$L \simeq 0.2$ cms
$M \simeq 0.2$ cms

Using these figures it can be seen that the following approximations can be made:-

$\cos\theta_2 \simeq \cos\theta_D$
$r \simeq R_o$

If we make use of these approximations and put $\theta_D = \theta_1$ then equation (A4.7) reduces to

$$(\varepsilon_s)_o = \left(\frac{kE_o 1m}{\pi R_o}\right)^2 \cdot 4\cos^2\theta_1 \int_{-L}^{L}\int_{-M}^{M} \left[\frac{\sin(\frac{kmY}{R_o})}{\frac{kmY}{R_o}}\right]^2 \cdot \left[\frac{\sin(\frac{k1X}{R_o}\cos\theta_1)}{\frac{k1X}{R_o}\cos\theta_1}\right]^2 \cdot dXdY \qquad \ldots (A4.10)$$

The dimensions of the system enable the limits of integration to be made infinite, since all the significant contributions

to the integral are made for values of X and Y such that $X \ll L$, $Y \ll M$.

Thus

$$(\varepsilon_s)_o \simeq \left(\frac{kE_o lm}{\pi R_o}\right)^2 \cdot 4\cos^2\theta_1 \int_{-\infty}^{\infty}\int_{-\infty}^{\infty} \left[\frac{\sin(\frac{klX}{R_o}\cos\theta_1)}{\frac{klX}{R_o}\cos\theta_1}\right]^2 \cdot \left[\frac{\sin(\frac{kmY}{R_o})}{\frac{kmY}{R_o}}\right]^2 \cdot dXdY \qquad \ldots (A4.11)$$

Now, $\int_o^{\infty} \left(\frac{\sin x}{x}\right)^2 dx = \frac{\pi}{2}$ (Gradshteyn and Ryzhik, 1965), so that, after suitable changes of variables, (A4.11) reduces to

$$(\varepsilon_s)_o \simeq \left(\frac{kE_o lm}{\pi R_o}\right)^2 \cdot 4\cos^2\theta_1 \cdot \frac{R_o}{kl\cos\theta_1} \cdot \frac{R_o}{km} \cdot \pi^2$$

or $$(\varepsilon_s)_o \simeq E_o^2 \cdot 4lm\cos\theta_1 \qquad \ldots (A4.12)$$

To check the accuracy of the approximations used in deriving (A4.10) from (A4.7) a computer program was written to evaluate (A4.7) numerically. It was found that (A4.12) was accurate to better than 0.1%.

A.4.2 Calculation of Averages for Normal Processes

This method of calculating averages involving normal processes (i.e. Gaussian processes) appears to have first been

applied to the problem under consideration by Hoffman (1955). The method is developed using the theory of stochastic processes, and the formal mathematical background is outlined by Papoulis (1965) and other authors.

The problem is to calculate the average value of expressions such as $\exp(ikcZ(x,y))$ where $Z(x,y)$ is a random function of x and y.

The variance $\sigma^2(x,y)$ of Z is defined by

$$\sigma^2(x,y) = \langle Z(x,y)^2 \rangle \qquad \ldots (A4.13)$$

while the covariance function $r(x,y,x',y')$ is defined by

$$r(x,y,x',y') = \langle Z(x,y)Z(x',y') \rangle \qquad \ldots (A.4.14)$$

(The notation is the same as in Chapter 7).

Any real, random function $Z(x,y)$, which is continuous over a finite region D, can be expanded in a series of orthogonal functions $\phi_{mn}(x,y)$ provided these functions satisfy certain conditions (e.g. completeness).

$$\text{i.e. } Z(x,y) = \sum_{m,n=1}^{\infty} a_{mn}\phi_{mn}(x,y) \qquad \ldots (A4.15)$$

$$\text{where } \int_D \int \phi_{mn}(x,y)\phi_{pq}(x,y)dxdy = \delta_{mp}\delta_{nq} \qquad \ldots (A4.16)$$

$$\text{and } \delta_{mp} = 1 \text{ , } m = p$$
$$= 0 \text{ , } m \neq p \qquad \ldots (A4.17)$$

$$\therefore\ r(x,y,x',y') = \sum_{m,n}\ \sum_{p,q} \phi_{mn}(x,y)\phi_{pq}(x',y') \left\langle a_{mn}a_{pq}\right\rangle$$

... (A4.18)

This last result can be greatly simplified by requiring that the a_{mn} be orthogonal, i.e.

$$\left\langle a_{mn}a_{pq}\right\rangle = 0\ ,\ m \neq p,\ n \neq q \qquad \ldots\ (A4.19)$$

Suppose we also assume that $\left\langle Z(x,y)\right\rangle = 0$. Then we must also have (from (A4.15))

$$\left\langle a_{mn}\right\rangle = 0 \qquad \ldots\ (A4.20)$$

It can be shown that if the a_{mn} in (A4.3) are orthogonal then the functions $\phi_{mn}(x,y)$ must satisfy the integral equation

$$\int_D\int r(x,y,x',y')\phi(x',y')dx'dy' = \lambda\phi(x,y) \qquad \ldots\ (A4.21)$$

for some value $\lambda = \lambda_{mn}$ of λ. Furthermore the variance of a_{mn} must equal λ_{mn}

$$\text{i.e.}\quad \left\langle a_{mn}^2\right\rangle = \lambda_{mn} \qquad \ldots\ (A4.22)$$

A proof of this result is given by Papoulis.

Using (A4.19) and (A4.22) in (A4.18) we have

$$r(x,y,x',y') = \sum_{m,n} \lambda_{mn}\phi_{mn}(x,y)\phi_{mn}(x',y') \qquad \ldots\ (A4.23)$$

Similarly $\sigma^2(x,y) = \sum_{m,n} \lambda_{mn}(\phi_{mn}(x,y))^2$ ... (A4.24)

These results can be applied in the following way:-

$$\left\langle e^{ikcZ(x,y)} \right\rangle = \left\langle \exp[ikc \sum_{m,n} a_{mn}\phi_{mn}(x,y)] \right\rangle$$

$$= \left\langle \prod_{m,n} \exp[ikca_{mn}\phi_{mn}(x,y)] \right\rangle \quad \ldots (A4.25)$$

where $\prod_{m,n} f_{mn}$ denotes the product of the f_{mn} taken over all values of f_{mn}.

Since the a_{mn} are orthogonal and each a_{mn} has mean zero, the a_{mn} are uncorrelated, which means that

$$\left\langle e^{ikcZ(x,y)} \right\rangle = \prod_{m,n} \left\langle \exp[ikca_{mn}\phi_{mn}(x,y)] \right\rangle \quad \ldots (A4.26)$$

If $Z(x,y)$ is a normal process then a_{mn} must also be a normal process, so that

$$\left\langle e^{ikcZ(x,y)} \right\rangle = \prod_{m,n} \exp[-\tfrac{1}{2}k^2c^2\lambda_{mn}(\phi_{mn}(x,y))^2]$$

$$= \exp[-\tfrac{1}{2}k^2c^2 \sum_{m,n} \lambda_{mn}(\phi_{mn}(x,y))^2]$$

$$= \exp[-\tfrac{1}{2}k^2c^2\sigma^2(x,y)] \quad \ldots (A4.27)$$

Similarly we can show that

$$\left\langle Z_x e^{ikcZ(x,y)} \right\rangle = ikc\exp[-\tfrac{1}{2}k^2c^2\sigma^2(x,y)]\frac{\partial}{\partial x}(\sigma^2(x,y))$$

... (A4.28)

$$e^{ikc(Z(x,y)-Z(x',y'))} = F \qquad \ldots (A4.29)$$

where

$$F = \exp[-\tfrac{1}{2}k^2c^2(\sigma^2(x,y) + \sigma^2(x',y') - 2r(x,y,x',y'))] \qquad \ldots (A4.30)$$

$$Z_x e^{ikc(Z(x,y)-Z(x',y'))} = ikc\left(\frac{\partial\sigma^2}{\partial x} - \frac{\partial r}{\partial x}\right)F \qquad \ldots (A4.31)$$

where

$$\sigma^2 = \sigma^2(x,y),\ r = r(x,y,x',y') \qquad \ldots (A4.32)$$

$$Z_x Z_{x'} e^{ikc(Z(x,y)-Z(x',y'))}$$

$$= \left(\frac{\partial^2 r}{\partial x \partial x'} + k^2c^2\left(\frac{\partial\sigma^2}{\partial x} - \frac{\partial r}{\partial x'}\right)\left(\frac{\partial\sigma'^2}{\partial x'} - \frac{\partial r}{\partial x}\right)\right)F \qquad \ldots (A4.33)$$

where

$$\sigma'^2 = \sigma^2(x',y') \qquad \ldots (A4.34)$$

If we assume that $Z(x,y)$ is a stationary, as well as Gaussian process, then

$$\sigma^2(x,y) = \sigma^2(x',y') = \sigma^2 = \text{const.} \qquad \ldots (A4.35)$$

Using (A4.35) the earlier results reduce to

$$e^{ikcZ(x,y)} = \exp[-\tfrac{1}{2}k^2c^2\sigma^2] \qquad \ldots (A4.36)$$

$$Z_x e^{ikcZ(x,y)} = 0 \qquad \ldots (A4.37)$$

$$\left\langle e^{ikc(Z(x,y)-Z(x',y'))}\right\rangle = \exp[-k^2c^2\sigma^2(1-\rho)] \qquad \ldots (A4.38)$$

$$\left\langle Z_x e^{ikc(Z(x,y)-Z(x',y'))}\right\rangle = ikc\sigma^2\frac{\partial\rho}{\partial x}\exp[-k^2c^2\sigma^2(1-\rho)] \qquad \ldots (A4.39)$$

$$\left\langle Z_x Z_{x'} e^{ikc(Z(x,y)-Z(x',y'))}\right\rangle = \sigma^2\left(\frac{\partial^2\rho}{\partial x\partial x'} + k^2c^2\sigma^2\frac{\partial\rho}{\partial x}\frac{\partial\rho}{\partial x'}\right) \cdot \exp[-k^2c^2\sigma^2(1-\rho)] \qquad \ldots (A4.40)$$

where $\rho = \rho(x,y,x',y') = \frac{1}{\sigma^2}r(x,y,x',y')$ ... (A4.41)

ρ is the auto-correlation function of the surface described by $Z(x,y)$ and is generally defined by

$$\rho(x,y,x',y') = \frac{\left\langle Z(x,y)Z(x',y')\right\rangle - \left\langle Z(x,y)\right\rangle\left\langle Z(x',y')\right\rangle}{\left\langle Z(x,y)^2\right\rangle} \qquad \ldots (A4.42)$$

APPENDIX 5 PUBLICATIONS

Carver, J. H., Horton, B. H., O'Brien, R. S. and Rofe, B. - 1971 - "Ozone determinations by lunar rocket photometry" - Planet. Space. Sci., 20, 217.

Carver, J. H., Horton, B. H., O'Brien, R. S., and O'Connor, G. G. - 1973 - "The ultraviolet reflectivity of the moon" - The Moon, (in press).

BIBLIOGRAPHY

Abramowitz, M., and Segun, I. E. - 1968 - "Handbook of Mathematical Functions" (Dover)

Ahmad, I. A., and Deutschman, W. A. - 1972 - Astron. J., 77, 692.

Allen, C. W. - 1962 - "Astrophysical Quantities" (Athlone Press), p.146.

Aro, T. O. - 1972 - J. Atmos. Terr. Phys., 34, 305.

Barth, C. A. - 1966 - Planet Space Sci., 14, 623.

Bates, D. R., and Nicolet, M. - 1950 - J. Geophys. Res., 55, 301.

Bazhulin, P. A., Kartashev, P. A., and Markov, M. N. - 1966 - Cosmic Research, 4, 530.

Beckmann, P. - 1966 - I.E.E.E. Transactions on Antennas and Propagation, AP-13, 253.

Beckmann, P., and Spizzichino, A. - 1963 - "The Scattering of Electromagnetic Waves from Rough Surfaces" (Pergamon Press).

Benson, S. W., and Axworthy, A. E. - 1965 - J. Chem. Phys., 42, 2615.

Bevington, P. R. - 1969 - "Data Reduction and Error Analysis for the Physical Sciences" (McGraw-Hill), Ch. 4.

Biedenkapp, D., Hartshorn, L. G., and Bair, E. J. - 1970 - Chem. Phys. Letters, 5, 379.

Brewer, A. W., and Milford, J. R. - 1960 - Proc. Roy. Soc. A., 256, 470.

Brinkmann, R. T., Green, A. E. S., and Barth, C. A. - 1966 - "A Digitalized Solar Ultraviolet Spectrum", NASA Tech. Report No. 32-951.

Carnahan, B., Luther, H. A., and Wilkes, J. O. - 1969 - "Applied Numerical Methods", (John Wiley and Sons).

Carver, J. H., Horton, B. H., and Burger, F. G. - 1966 - J. Geophys. Res., 71, 4189.

Carver, J. H., Horton, B. H., and Burger, F. G. - 1967 - Space Research, VII, 1020.

Carver, J. H., and Mitchell, P. - 1964 - J. Sci. Instrum., 41, 555.

Carver, J. H., Mitchell, P., Murray, E. L., and Rofe, B. - 1965 - Space Research VI, 373.

Chandrasekhar, S. - 1950 - "Radiative Transfer", (Clarendon Press)

Chung, D. H., Westphal, W. B., and Simmons, G. - 1970 - J. Geophys. Res., 75, 6524.

Clough, S. A., and Kneizys, F. X. - 1965 - AFCRL Research Paper 170.

Clyne, M. A. A., and Thrush, B. A. - 1963 - Proc. Roy. Soc. A; 275, 559.

Cospar International Reference Atmosphere - 1965 - p.5.

Craig, R. A. - 1965 - "The Upper Atmosphere - Meteorology and Physics", (Academic Press), p.184.

Crutzen, P. R. - 1971 - J. Geophys. Res., 76, 7311.

Davies, H. - 1954 - J. Elec. Eng. London, Part 4; 101, 209.

Detwiler, C. R., Garrett, D. L., Purcell, J. D., and Tousey, R. - 1961 - Ann. Geophys., 17, 263.

Dunkelmann, L., Hennes, J. P., and Fowler, W. B. - 1963 - Space Research, III, 1174.

Dutsch, H. U. - 1956 - Arch. Met. Wien., A9, 87.

Dutsch, H. U. - 1968 - Quart. J. Roy. Soc., 94, 483.

Dutsch, H. U., and Ling, C. - 1969 - Ann. Géophys., 25, 211.

Fielder, G. - 1967 - Nature, 215, 944.

Fielder, G., Guest, J. E., Wilson, L., and Rogers, P. S. - 1967 - Planet. Space Sci., 15, 1653.

Fitzsimmons, R. V., and Bair, E. J. - 1964 - J. Chem. Phys., 40, 451.

Foner, S. N., and Hudson, R. L., - 1962 - J. Chem. Phys., 36, 2681.

Friedman, H., Chubb, T. A., and Siomkajlo, J. N. - 1964 - Sounding Rocket Research Techniques, Instruction Manual (9); (I.Q.S.Y. Secretariat, London).

Friedman, R. M., Rawcliffe, R. D., and Meloy, G. E. - 1963 - J. Geophys. Res., 68, 6419.

Fung, A. K. - 1964 - J. Geophys. Res., 69, 1063.

Furukawa, P. M., Haagenson, P. L., and Scharberg, M. J. - 1967 - Nat. Center for Atmos. Res., Tech. Note 26.

Gehrels, T. - 1964 - ICARUS, 3, 491.

Gehrels, T., Coffeen, T., and Owings, D. - 1964 - Astron. J., 69, 826.

Gradshteyn, I. S., and Ryzhik, I. M. - 1965 - "Table of Integrals, Series and Products", (Academic Press), p.446.

Green, A. E. S., and Martin, J. D. - 1966 - in "The Middle Ultraviolet: Its Science and Technology", Ed. A. E. S. Green, (John Wiley and Sons), Ch. 7.

Greenman, N. N., Burkig, V. W., and Young, J. F. - 1967 - J. Geophys. Res., 72, 1355.

Griggs, M. - 1966 - in "The Middle Ultraviolet: Its Science and Technology", Ed. A. E. S. Green, (John Wiley and Sons), Ch. 4.

Grobecker, A. J. - 1971 - Ph.D. Thesis, Institute for Defence Analysis (U.S.A.), Science and Technology Division.

Hapke, B. W. - 1963 - J. Geophys. Res., 68, 4571.

Hapke, B. W. - April, 1965 - Paper presented at the Conference on the Nature of the Surface of the Moon, Goddard Space Flight Center, Maryland.

Hapke, B. W. - 1967 - ICARUS, 6, 277.

Hapke, B. W. - 1971 - in "Physics and Astronomy of the Moon", second edition, Ed. Z. Kopal, (Academic Press), Ch. 5.

Hapke, B. W., and Van Horn, H. - 1963 - J. Geophys. Res., 68, 4545.

Hays, P. B., and Roble, R. G. - 1973 - Planet Space Sci., 21, 273.

Hecht, H. G. - Sept. 11-12, 1967 - "Modern Aspects of Reflectance Spectroscopy", Proceedings of the American Chemical Society Symposium on Reflectance Spectroscopy.

Heddle, D. W. O. - 1963 - The Observatory, 83, 225.

Henderson, W. R. - 1971 - J. Geophys. Res., 76, 3166.

Hennes, J. P. - 1966 - J. Geophys. Res., 71, 763.

Hennes, J. P., and Dunkelmann, L. - 1966 - J. Geophys. Res., 71, 755.

Hering, W. S., and Barden, T. R. - 1964 - AFCRL Report 64-30 (II).

Hickman, D. R., and Nier, A. O. - 1972 - J. Geophys. Res., 77, 2880.

Hilsenrath, E. - 1971 - J. Atmos. Sci., 28, 295.

Hodgeson, J. A., Frost, K. J., O'Keefe, A. E., and Stevens, R. K. - 1970 - Analytical Chemistry, 42, 1795.

Hoffman, W. C. - 1955 - Quart. J. App. Maths., 13, 291.

Horton, B. H. - 1968 - Ph.D. Thesis, University of Adelaide.

Howard, J. N. - 1961 - Air Force Surveys in Geophysics, No. 142.

Hunt, B. G. - 1964 - Aust. Dept. of Supply, WRE Tech. Note PAD84.

Hunt, B. G. - 1965 - J. Atmos. Terr. Phys., 27, 133.

Hunt, B. G. - 1966 - J. Geophys. Res., 71, 1385.

Hunt, B. G. - 1971 - J. Atmos. Terr. Phys., 33, 1869.

Hunten, D. M. - 1967 - Space Sci. Reviews, 6, 493.

Inn, E. C. Y., and Tanaka, Y. - 1959 - Advances in Chemistry, 21, 263.

Jackson, E. D., and Wilshire, H. G. - 1968 - J. Geophys. Res., 73, 7621.

Johannessen, A., and Krankowsky, D. - May 1972 - Cospar Conference, Madrid, Paper L13.

Johnson, F. S., Purcell, J. D., and Tousey, R. - 1954 - in "Rocket Exploration of the Upper Atmosphere", ed. R. L. F. Boyd, (Pergamon Press), p.189.

Johnson, F. S., Purcell, J. D., Tousey, R., and Watanabe, K. - 1952 - J. Geophys. Res., 57, 157.

Kaufman, F. - 1964 - Ann. de Géophys., 20, 316.

Keneshea, T. J. - 1967 - AFCRL - 67 - 0221.

Klein, C. (Jr.) - 1972 - Earth-Science Reviews, 8, 169.

Kopal, Z. - 1969 - "The Moon" (Reidel Pub. Co., Holland).

Korolev, F. A., and Kulikov, O. F. - 1971 - Optics and Spectroscopy, 31, 442.

Kortüm, G. F. A. - 1969 - "Reflectance Spectroscopy", (Springer-Verlag), Ch. II.

Krasnopolsky, V. A., and Lebedinsky, A. I. - 1966 - Space Research, VII, 315.

Kulkarni, R. N., and Garnham, G. L. - 1970 - J. Geophys. Res., 75, 4174.

Kulkarni, R. N., and Pittock, A. B. - 1970 - Quart. J. Roy. Met. Soc., 96, 739.

Lane, A. P., and Irvine, W. M. - 1973 - Astron. J., 78, 267.

Larkin, F. S., and Thrush, B. A. - 1964 - Disc. Faraday Soc., 37, 112.

Lebedinsky, A. I., Krasnopolsky, V. A., and Krysko, A. A. - 1967a - Moon and Planets. 1, 59.

Lebedinsky, A. I., Aleshin, G. M., Iozenas, V. A., Krasnopolsky, V. A., Selivanov, A. S., and Zasetsky, V. V. - 1967b - Moon and Planets, 1, 65.

Lebedinsky, A. I., Krasnopolsky, V. A., and Aganina, M. U. - 1968 - Moon and Planets, 2, 47.

Lucke, R. L., Henry, R. C., and Fastie, W. G. - 1973 - Astron. J., 78, 263.

McCord, T. B. - 1969 - J. Geophys. Res., 74, 3131.

McCord, T. B., Charette, M. P., Johnson, T. V., Lebofsky, L. A., and Pieters, C. - 1972 - The Moon, 5, 52.

Malmstadt, H. V., and Enke, C. G. - 1969 - "Digital Electronics for Scientists", (Benjamin).

Marcus, A. H. - 1969 - J. Geophys. Res., 74, 5253.

Martynkevich, G. M. - 1972 - Cospar Conference, Madrid.

Miller, D. E., and Stewart, K. H. - 1965 - Proc. Roy. Soc. A., 288, 540.

Murgatroyd, R. J. - 1957 - Quart. J. Roy. Met. Soc., 83, 217.

Nicolet, M. - 1964 - Disc. Faraday Soc., 37, 7.

Nicolet, M. - 1970 - Ionospheric Research, Report No. 350.

Norrish, R. G. W., and Wayne, R. P. - 1965 - Proc. Roy. Soc. A., 288, 361.

O'Connor, G. G. - 1973 - Ph.D. Thesis, University of Adelaide.

Offerman, D., Pelka, K., and Von Zahn, U. - 1972 - Int. J. Mass Spectrom. and Ion Phys. 8, 391.

O'Keefe, J. A. - 1970 - J. Geophys. Res., 75, 6565.

O'Leary, B., and Briggs, F. - 1970 - J. Geophys. Res., 75, 6532.

Packer, D. M. - 1961 - Ann. de Géophys., 17, 67.

Paetzold, H. K., and Piscalar, F. - 1961 - Naturwissenschaften, 48, 474.

Papoulis, A. - 1965 - "Probability, Random Variables and Stochastic Processes", (McGraw-Hill), pp.457-459.

Petersen, H. L., and Kretschmer, C. B. - 1960 - U.S. Dept. Commerce, O.T.S., A.D. 283 044.

Peterson, V. L., Vanzandt, T. E., and Norton, R. B. - 1966 - J. Geophys. Res., 71, 2255.

Philbrick, C. R., Faucher, G. A., and Wlodyka, R. A. - 1971 - AFCRL - 71 - 0602, Environmental Research Paper No. 376.

Pikkarainen, T. - 1969 - Annales Academiae Scientiarum Fennicae, Ser. A, 6, Paper 316.

Poloskov, S. M., Lvova, A. A., and Mikirov, A. E. - 1967 - Space Research, VII, 1009.

Porteus, J. O. - 1963 - J. Opt. Soc. Amer., 53, 1394.

Ramahathan, K. R., and Dave, J. V. - 1957 - Annals of the I.G.Y., 5, 23.

Randhawa, J. S. - Mar. 1966 - U.S. Army Electronics Command Report ECOM-5039.

Randhawa, J. S. - July 1966 - U.S. Army Electronics Command Report ECOM-5064.

Randhawa, J. S. - 1970 - J. Geophys. Res., 75, 1693.

Randhawa, J. S. - 1971 - J. Geophys. Res., 76, 8139.

Rawcliffe, R. D., Meloy, G. E., Friedman, R. M., and Rogers, E. H. - 1963 - J. Geophys. Res., 68, 6425.

RCA Silicon Power Circuits Manual - 1967 - pp.147-186.

Read, H. H., and Watson, J. - 1963 - "Introduction to Geology", Vol. I, (MacMillan and Co.).

Reed, E. I. - 1968 - J. Geophys. Res., 73, 2951.

Reed, E. I., and Scolnik, R. - 1964 - N.A.S.A. Report X - 613 - 64 - 267.

Reeves, R. R., Manella, G., and Harteck, P. - 1960 - J. Chem. Phys., 32, 632.

Regener, E., Paetzold, H. K., and Ehmert, A. - 1954 - in "Rocket Exploration of the Upper Atmosphere", ed. R. L. F. Boyd, (Pergamon Press), p.202.

Regener, V. H. - 1960 - J. Geophys. Res., 65, 3975.

Ringwood, A. E. - 1970 - J. Geophys. Res., 75, 6453.

Samson, J. A. R. - 1967 - "Techniques of Vacuum Ultraviolet Spectroscopy", (John Wiley and Sons), p.313.

Sandercock, E. R. - 1967 - Ph.D. Thesis, University of Adelaide.

Schaefer, E. J., and Nichols, M. H. - 1964 - J. Geophys. Res., 69, 4649.

Schofield, K. - 1967 - Planet Space Sci., 15, 643.

Sissons, N. V. - March 1970 - Dept. of Supply Tech. Note HSA 153.

Smith, B. G. - 1967 - I.E.E.E. Transactions on Antennas and Propagation, AP-15, 668.

Smith, L. G., and Weeks, L. H. - 1965 - G.C.A. Tech. Report No. 65-10-N.

Stair, R., and Johnston, R. - 1953 - J. Res. Nat. Bur. Standards, 51, 81.

Stecher, T. P. - 1965 - J. Geophys. Res., 70, 2209.

Stergis, C. G. - 1966 - J. Atmos. Terr. Phys., 28, 273.

Subbaraya, B. H., Prakash, S., and Pareek, P. N. - 1972 - J. Atmos. Terr. Phys., 34, 1141.

Tanaka, Y., Inn, E. C. Y., and Watanabe, K. - 1953 - J. Chem. Phys., 21, 1651.

Tarasova, T. M. - 1963 - Planet Space Sci., 11, 437.

Thomas, R. J. - 1972 - Private Communication.

Tousey, R. - 1958 - Ann. de Géophys., 14, 186.

Twomey, S. - 1961 - J. Geophys. Res., 66, 2153.

Vassy, E. - 1937 - Ann. de Phys., 8, 679.

Venkateswaran, S. V., Moore, J. G., and Krueger, A. J. - 1961 - J. Geophys. Res., 66, 1751.

Walton, G. F. - 1957 - Annals of the I.G.Y., 5, 9.

Watson, G. N. - 1922 - "Theory of Bessel Functions", (Cambridge), p.394.

Weeks, L. H., and Smith, L. G. - 1968a - J. Geophys. Res., 73, 4835.

Weeks, L. H., and Smith, L. G. - 1968b - Planet Space Sci., 16, 1189.

Wendlandt, W. W., and Hecht, H. G. - 1966 - "Reflectance Spectroscopy", (Interscience Publishers).

Wildman, P. J. L., Kerley, M. J. and Shaw, M. S. - 1969 - J. Atmos. Terr. Phys., 31, 951.

Williamson, E. J., and Houghton, J. T. - 1965 - Quart. J. Roy. Met. Soc., 91, 330.

Wilshire, H. G., Stuart-Alexander, D. E., and Jackson, E. D. - 1973 - J. Geophys. Res. 78, 2379.

Wood, J. A. - 1970 - J. Geophys. Res., 75, 6497.

Wood, J. A., Marvin, U. B., Reid, J. B., Taylor, G. J., Bower, J. F., Powell, B. N., and Dickey, J. S. - 1971 - Smithson Astrophys. Obs., Special Report 333.

Young, R. A., Black, G., and Slanger, T. G. - 1968 - J. Chem. Phys., 49, 4758.

Zipf, E. C. - 1969 - Can. J. Chem., 47, 1863.